

ISSN en trámite



Geofísica Internacional

Revista Trimestral Publicada por el Instituto de Geofísica de la
Universidad Nacional Autónoma de México



México

Volume 52 Number 3
July - September
2013

— Geofísica Internacional —

Dr. José Francisco Valdés Galicia
Director of Instituto de Geofísica

Dr. Avto Gogichaishvili
President of Unión Geofísica Mexicana

Editor Chief

Dr. Servando De la Cruz-Reyna
Instituto de Geofísica, UNAM
sdelacrr@geofisica.unam.mx

Technical Editor

Mtra. Andrea Rostan Robledo
Instituto de Geofísica, UNAM
arostan@igeofisica.unam.mx

Editorial Board

Donald Bruce Dingwell
Earth and Environment
Ludwig Maximilian University of Munich,
Germany

Eric Desmond Barton
Departamento de Oceanografía
Instituto de Investigaciones Marinas, Spain

Jorge Clavero
Amawta Consultores, Chile

Gerhardt Jentzsch
Institut für Geowissenschaften
Friedrich-Schiller-Universität Jena, Germany

Peter Malischewsky
Institut für Geowissenschaften
Friedrich-Schiller-Universität Jena, Germany

François Michaud
Géosciences Azur
Université Pierre et Marie Curie, France

Olga Borisovna Popovicheva
Scobeltzine Institute of Nuclear Physics
Moscow State University, Rusia

Jaime Pous
Facultad de Geología
Universidad de Barcelona, Spain

Joaquín Rui
UA Science
University of Arizona, United States

Angelos Vourlidas
Solar Physics Branch
NASA Goddard Space Flight Center, United States

Théophile Ndougsa Mbarga
Department of Physics
University of Yaounde I, Cameroon

Associate Editors
José Agustín García Reynoso
Atmospheric Science Centro de Ciencias de la
Atmósfera UNAM, Mexico

Tereza Cavazos
Atmospheric Science
Departamento de Oceanografía Física CICESE,
Mexico

Dante Jaime Morán-Zenteno
Geochemistry
Instituto de Geología, UNAM, Mexico

Margarita López
Geochemistry
Instituto de Geología UNAM, Mexico

Avto Gogichaisvili
Geomagnetism And Paleomagnetism
Instituto de Geofísica UNAM, Mexico

Jaime Urrutia-Fucugauchi
Geomagnetism And Paleomagnetism
Instituto de Geofísica, UNAM, Mexico

Felipe I. Arreguín Cortés
Hydrology
Instituto Mexicano de Tecnología del Agua IMTA,
Mexico

William Lee Bandy
Marine Geology And Geophysics
Instituto de Geofísica UNAM, Mexico

Fabian García-Nocetti
**Mathematical And Computational
Modeling**
Instituto de Investigaciones en Matemáticas
Aplicadas y en Sistemas UNAM, Mexico

Graciela Herrera-Zamarrón
Mathematical Modeling
Instituto de Geofísica, UNAM, Mexico

Ismael Herrera Revilla
**Mathematical And Computational
Modeling**
Instituto de Geofísica UNAM, Mexico

Rene Chávez Segura
Near-Surface Geophysics
Instituto de Geofísica UNAM, Mexico

Juan García-Abdeslem
Near-Surface Geophysics
División de Ciencias de la Tierra CICESE, Mexico

Alec Torres-Freyermuth
Oceanography
Instituto de Ingeniería, UNAM, Mexico

Jorge Zavala Hidalgo
Oceanography
Centro de Ciencias de la Atmósfera UNAM,
Mexico

Shri Krishna Singh
Seismology
Instituto de Geofísica, UNAM, Mexico

Xyoli Pérez-Campos
Seismology
Servicio Sismológico Nacional, UNAM, Mexico

Blanca Mendoza Ortega
Space Physics
Centro de Ciencias de la Atmósfera, UNAM,
Mexico

Inez Staciari Batista
Space Physics
Pesquisador Senior Instituto Nacional de Pesquisas
Espaciais, Brazil

Roberto Carniel
Volcanology
Laboratorio di misure e trattamento dei segnali
DPIA - Università di Udine, Italy

Miguel Moctezuma-Flores
Satellite Geophysics
Facultad de Ingeniería, UNAM, Mexico

Assistance

Elizabeth Morales Hernández,
Management
eliedit@igeofisica.unam.mx



GEOFÍSICA INTERNACIONAL, Año 52, Vol. 52, Núm. 3, julio - septiembre de 2013 es una publicación trimestral, editada por la Universidad Nacional Autónoma de México, Ciudad Universitaria, Alcaldía Coyoacán, C.P. 04150, Ciudad de México, a través del Instituto de Geofísica, Circuito de la Investigación Científica s/n, Ciudad Universitaria, Alcaldía Coyoacán, C.P. 04150, Ciudad de México, Tel. (55)56 22 41 15. URL: <http://revistagi.geofisica.unam.mx>, correo electrónico: revistagi@igeofisica.unam.mx. Editora responsable: Andrea Rostan Robledo. Certificado de Reserva de Derechos al uso Exclusivo del Título: 04-2022-081610251200-102, ISSN: en trámite, otorgados por el Instituto Nacional del Derecho de Autor (INDAUTOR). Responsable de la última actualización Saúl Armendáriz Sánchez, Editor Técnico. Fecha de la última modificación: 30 de junio 2013, Circuito de la Investigación Científica s/n, Ciudad Universitaria, Alcaldía Coyoacán, C.P. 04150, Ciudad de México.

El contenido de los artículos es responsabilidad de los autores y no refleja el punto de vista de los árbitros, del Editor o de la UNAM. Se autoriza la reproducción total o parcial de los textos siempre y cuando se cite la fuente completa y la dirección electrónica de la publicación.



Esta obra está bajo una Licencia Creative Commons Atribución-NoComercial-SinDerivadas 4.0 Internacional.

Contents

Crustal structure and tectonic setting of the south central Andes from gravimetric analysis.

Cecilia Weidmann, Silvana Spagnotto, Mario Giménez, Patricia Martínez, Orlando Álvarez, Marcos Sánchez, Federico Lince Klinger

197

Characterization of ground motions using recurrence plots.

Silvia R. García, Miguel P. Romo, Jesús Figueroa-Nazuno

209

Geostatistical modeling of clay spatial distribution in siliciclastic rock samples using the plurigaussian simulation method.

Javier Méndez-Venegas, Martín A. Díaz-Viera

229

AVO analysis with partial stacking to detect gas anomalies in the GÜEPAJÉ-3D project.

Juan C. Mosquera, Alfredo Ghisays Alfredo Ghisays, Luis Montes

249

Geophysical-Archaeological Survey in Lake Tequesquitengo, Morelos, Mexico.

Roberto E. Galindo Domínguez, William L. Bandy, Carlos A. Mortera Gutiérrez, José Ortega Ramírez

261

Variability of extreme precipitation in coastal river basins of the southern Mexican Pacific region.

Nancy Pérez-Morga, Thomas Kretzschmar, Tereza Cavazos, Stephen V. Smith, Francisco Munoz-Arriola

277

Parallel Algorithms for Computational Models of Geophysical
Systems.

Antonio Carrillo-Ledesma, Ismael Herrera, Luis M. de la Cruz

Crustal structure and tectonic setting of the south central Andes from gravimetric analysis

Cecilia Weidmann*, Silvana Spagnotto, Mario Giménez, Patricia Martínez, Orlando Álvarez, Marcos Sánchez and Federico Lince Klinger

Received: December 20, 2011; accepted: February 14, 2013; published on line: June 28, 2013

Resumen

En el presente trabajo, a partir de datos gravimétricos terrestres, se preparó una carta de anomalías de Bouguer, la cual fue adecuadamente filtrada a fin de separar efectos gravimétricos someros y profundos. Con base en un modelo de densidad, mediante de técnicas de inversión gravimétrica, se modeló la discontinuidad corteza-manto y el basamento cristalino, respectivamente. De forma posterior, se evaluó el espesor elástico equivalente considerando la información de la discontinuidad de la corteza-manto y la carga topográfica. Se encontraron valores altos de espesor elástico T_e , al este de la precordillera Andina y al oeste de la sierra Pampeana de Velasco. Estos resultados son consistentes con los valores positivos de anomalía residual de Bouguer e isotáticos, lo que estaría indicando la presencia de rocas de alta densidad en corteza media a superior. Además, los análisis petrográficos y geoquímicos realizados en afloramientos en superficie indican un origen mantélico.

Palabras clave: gravedad, isostasia, espesor elástico equivalente, Andes centrales, modelo cortical, Sierras Pampeanas.

Abstract

Based on terrestrial gravity data, in this paper we prepared a map of Bouguer anomalies, which was filtered to separate shallow and deep gravity sources. Based on a density model and gravimetric inversion techniques, the discontinuous crust-mantle boundary and the top of crystalline basement were modeled. Subsequently, the equivalent elastic thickness (T_e) was evaluated, considering information from the crust-mantle discontinuity and topographic load, finding high T_e values in the eastern Andean foothills and west of the Velasco range. These results are consistent with the positive isostatic and residual Bouguer anomaly values, which suggest the presence of high-density rocks in the mid-to upper crust. In addition, petrographic and geochemical analysis conducted in surface outcrops suggest a mantle origin.

Key words: gravity, isostasy, equivalent elastic thickness, southern Andes, crustal model, Sierras Pampeanas.

C. Weidmann*
S. Spagnotto
O. Álvarez
M. Sánchez
F. Lince Klinger
Consejo Nacional de Investigaciones
Científicas y Técnicas, Argentina
*Corresponding author: ceciweidmann@yahoo.com.ar

M. Giménez
P. Martínez
CONICET
Instituto Geofísico Sismológico Volponi
Universidad Nacional de San Juan, Argentina

Introduction

The study area at the latitudes between 27°S and 30°S will be referred to as a part of the Southern Andes (Bohm *et al.*, 2002; Tassara and Yáñez, 2003). In this area the flat slab segment (27°S–33°30'S) has a strong active deformation, with a complex High Cordillera, a Precordillera thin-skinned belt and the thick-skinned Sierras Pampeanas (Ramos, 1999). These Sierras Pampeanas basement blocks uplifted during shallowing of the flat-slab since the Late Miocene. It records an initial migration of the magmatic arc by crustal erosion (Ramos, 1988), and a rapid migration associated with the shallowing of the subduction producing a volcanic front as far as 700 km from the trench during Quaternary times (Kay *et al.*, 1991).

The aim of our study is to examine the crustal structure in the research area on the basis of gravity-field modeling. Typically, the modeling of the gravity field involves the construction of a density model of the crust. Combined with the overlying topography, the density model constitutes the load acting on the crust. The internal crustal load is given by the integration along the crustal column of the modeled densities with respect to the reference crustal column. It follows that a density variation within the crust represents a variation in the load, and must be reflected in the isostatic response (Ebbing *et al.*, 2007, Braitenberg *et al.*, 2002).

The study of the isostatic state and of the regional rheological crustal properties is closely related to density modeling. Thus, isostatic modeling is useful for calculation of the isostatic state emplacing an independent constraint upon a given density model. Given the crustal load and the crustal structure, the study of the isostatic state permits modeling the rheological properties in terms of flexural rigidity and by making some assumptions regarding Poisson's ratio and Young's modulus, flexural rigidity can be interpreted in terms of elastic thickness. The flexural rigidity is an important parameter for the characterization of the crust.

Background

The geophysical background for the study area in this work is scarce, and moreover is limited to sparse 2-D seismic data and some deep refraction profiles made by YPF (Yacimientos Petrolíferos Fiscales) in the 1980's in the southeast part of the study region. Cristallini *et al.* (2004) determined the Moho to be 45 km deep, using profound seismic interpretation of parallel 27° South.

Results obtained from Introcaso *et al.* (2000) demonstrated that the shortening value for the present day Andes would be around 200 km, due

to present day compressive stresses and also found that in this region the Andean Cordillera is close to isostatic equilibrium. The CHARGE experiment (Chilean-Argentinian Geophysical Experiment), obtained Moho depths and Vp/Vs south of the study area, on a transect at 30°S, that suggest is a partially eclogitized lower crust under the Famatina and Cuyania terrains. Tassara *et al.* (2006) analyzed the geometry and characteristics of the Nazca plate and continental lithosphere, based on satellite gravity data. Tassara *et al.* (2007) also calculated the equivalent elastic thicknesses of South America using gravity, obtained from GRACE satellite.

In this paper, results of the gravimetric field interpretation are shown for the region between 27° and 30° of south latitude and 71° and 65° of west longitude (Figure 1), with the objective of understanding crustal characteristics and behavior that characterize it.

Geologic Setting

The complex history of the Andes started in the Palaeozoic with the accretion of Pacific micro-continental blocks to the western margin of Gondwana. At that time, the south-western coast of Gondwana was not far from the present-day Sierras Pampeanas in Argentina. The accretion of the terranes, with a new subduction zone forming along its western margin, belongs to the early Palaeozoic Famatinian tectonic cycle of Andean evolution. This subduction zone left a large accretionary prism preserved along the Pacific margin of Chile south of 25°S (Hervé *et al.*, 1981). In the second Gondwana tectonic cycle, the magmatic arc composed of granitoids and rhyolitic volcanic rocks was developed within this accretionary prism and in adjacent areas eastwards of it. The last evolutionary stage, the Andean tectonic cycle (Mesozoic to Cenozoic), is characterized by a major palaeogeographic change. The complex of backarc basins are associated with the arc developed on late Palaeozoic basement during the Jurassic–Early Cretaceous.

Subsequent subduction erosion removed large amounts of the accumulated Palaeozoic forearc. The Mesozoic–Cenozoic Andes, in contrast to the Palaeozoic Andes, lack evidence for the collision of major terranes and appear to be related to the tectonic erosion of the continental margin. The extraordinary feature of the Mesozoic evolution of the Andean orogen is the along-strike tectonic segmentation.

There are differences in the geological evolution, structural styles and behavior of the related magmatic arcs of various segments, as well as changes in the nature of the backarc basins (Mpodozis and Ramos, 1989 and references

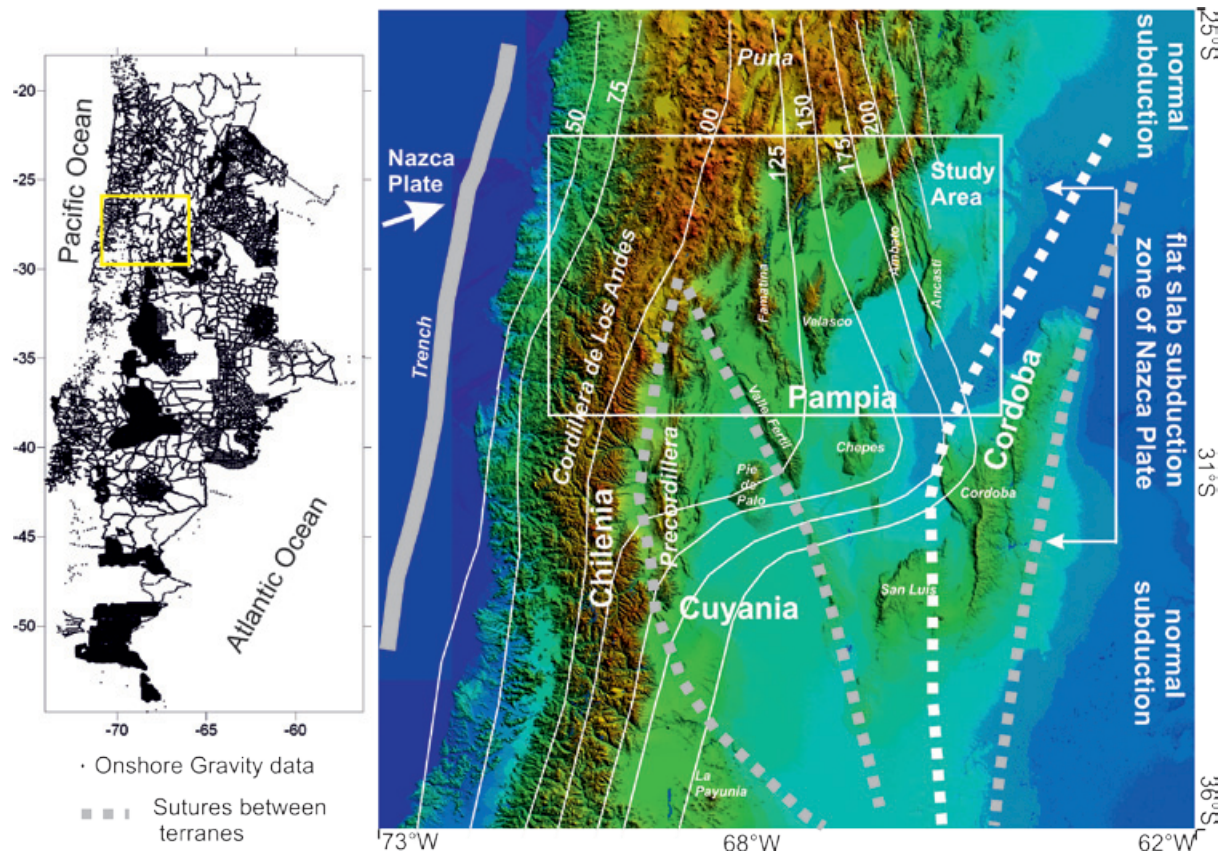


Figure 1. Location map of the study area. Solid lines show depth to the subducting Nazca plate. On the left the dots show locations of the gravity stations.

therein). Therefore, there must be two significant controls on the tectonic segmentation: the plate interactions and the pre-existing inhomogeneities of the South American plate (e.g. Jordan *et al.*, 1983). Thus, the Andes offer a great opportunity to understand and study the coupling of subduction and continental orogenesis. As proposed by various authors (e.g. Barazangi and Isacks, 1976; Jordan *et al.*, 1983; Mpodozis and Ramos; 1989; Cahill and Isacks, 1992), the Andes can be subdivided into several segments.

Methodology

The onshore gravity data set used for this work consists of a compilation of more than 7,500 gravity stations from several different sources. The observations were carried out over the past 20 years by the "Instituto Geofísico y Sismológico Volponi (IGSV)". Data of industry were provided through agreements with YPF (Argentina). Additional data was taken from: Araneda *et al.* (1999), Götze *et al.* (1990) and Chile.

This data compilation resulted in a rather inhomogeneous data set with large data gaps in some parts of the modeled region (Figure 2a). These gaps are mostly due to difficult access to

some of the areas under study. The complete Bouguer anomalies were calculated using a spherical Bouguer cap with a radius of 166.7 km, and densities of 2.67 g/cm³ (Hinze, 2003).

We used the ETOPO2 (<http://www.ngdc.noaa.gov/mgg/fliers/01mgg04.html>), for the digital elevation model. The normal gravity formula of 1967 was used and observations were tied to the IGSN71 gravity datum, which is still in use in South America. The Bouguer anomaly has an estimated accuracy of 2–5 mGal.

Separation of Gravimetric Sources

It is well known that the Bouguer anomaly contains the sum of gravimetric effects of different sources and there are many techniques that allow for a proper separation of such. Different frequency techniques were applied: band pass filter, upward continuation, surface trends, Butterworth filter (e.g. Blakely, 1995). Nevertheless, due to the powerful influence of the Andean root, the filter that proved to be most efficient, was obtained by a Butterworth filter with a cutoff of 300 km and filter order 8 (Blakely, 1995). Regional and residual gravity anomaly maps are presented in Figures 2a and 2b respectively.

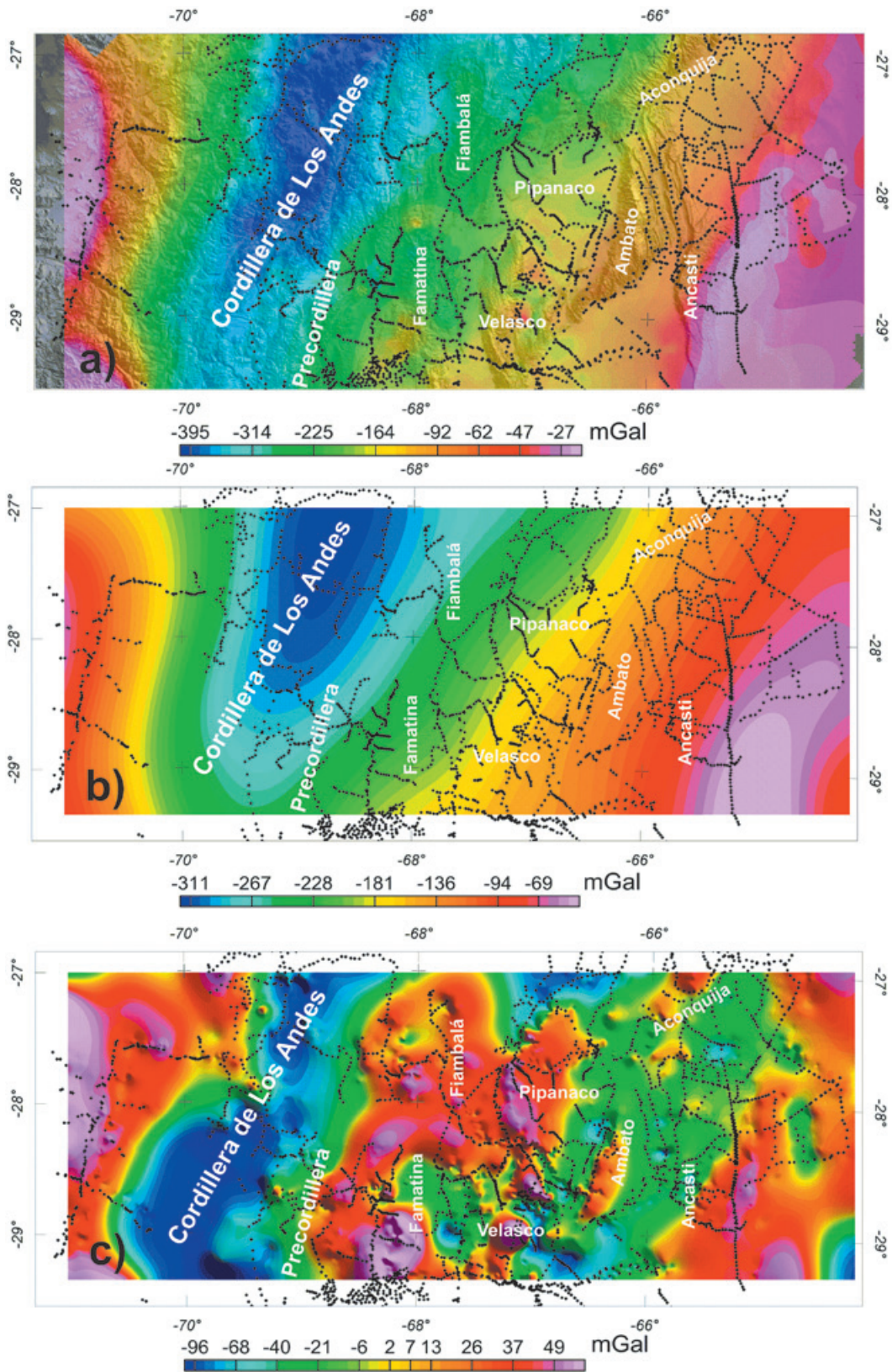


Figure 2. a) Bouguer anomaly map with the gravimetric stations, drawn on the digital elevation model. b) Bouguer regional anomaly, obtained through band pass filter. c) Bouguer residual anomaly obtained from the difference between a) and b).

Basement by Gravity Inversion

To estimate the depth to the crystalline basement, we calculated an inversion of the Bouguer residual anomaly (Figure 2c). Gravity modeling requires knowledge of densities of subsurface bodies, which can be approximated by using standard relationships between densities and seismic wave velocities of igneous and metamorphic rocks (Ludwig *et al.*, 1970; Brocher, 2005) or similar velocity-density relationships. Gardner *et al.* (1974) derive an empirical relationship between densities of commonly observed subsurface sedimentary rock and the velocities of propagation of seismic waves through the rocks. There are no deep boreholes in the area of study, so we used the "geological standard model" (Table 1), available seismic velocity model for the wells near the area of study and previous papers from: Götze and Kirchner, (1997); Ruíz and Introcaso (1999); Introcaso *et al.* (2000); Cristallini *et al.* (2004); Fromm *et al.* (2004); Gilbert *et al.* (2006); Giménez *et al.* (2006); Tassara *et al.* (2007); Giménez *et al.* (2009).

Table 1. Parameters of reference crustal model

Parameters	Values
Topographic Density	2.67 g/cm ³
Sediments Average Density	2.3 g/cm ³
Top Crust Density	2.7 g/cm ³
Medium Crust Density	2.8 g/cm ³
Lower Crust Density	2.9 g/cm ³
Lithosphere Mantle Density	3.3 g/cm ³
Crust Normal Thickness	35 km

We employ a software that uses fast Fourier transform (FFT) to compute the geological model response (Popowski *et al.* (2006). For this, all grids must be expanded in size and filled so they are periodic and eliminate edge effects (Blakely, 1995). Each layer is assigned density values (Table 1). The basement was assigned a value of 2.7 g/cm³ by extrapolating values obtained from seismologic studies by (Regnier *et al.*, 1994) for the Pie de Palo Range and the San Juan Precordillera. The values used for the crust and upper mantle are standard values used in previous studies by: Introcaso and Pacino (1988); Introcaso *et al.* (1992); Martinez and Introcaso (1999); Giménez *et al.* (2000).

When the area has rugged topography, care must be taken to ensure the depths to horizons of interest are reported relative to the datum of interest (Cordell, 1985). The topographical surface is the most practical frame of reference for measuring depths to density changes. Inversion

of the gravity field is calculated relative to a horizontal plane. In this work, the plane was at 7,000 m above sea level. The result of gravity inversion of the Bouguer residual anomaly calculated with GMSYS 3D and transformation to the depth below the topographic surface is the map of the top of the crystalline basement shown in Figure 3a.

Crust–Mantle discontinuity by Gravity inversion

To estimate the depth to the crust–mantle discontinuity we calculated an inversion of the Bouguer regional anomaly (Figure 2b), assuming a single boundary, with a density discontinuity across the Moho. The inverse calculation starts from the gravity field and attempts to obtain the causative density boundary, using an iterative algorithm developed by Braitenberg and Zadro, 1999. This method is analogous to the Oldenburg–Parker inversion approach of Oldenburg (1974). We used the parameters shown in Table 1. The density contrast between lower crustal and upper mantle was -0.4 g/cm³ (Woollard, 1959; Introcaso *et al.*, 1992; Introcaso, 1993; Giménez *et al.*, 2000). The result of the inversion model for the crust–mantle discontinuity is shown in Figure 3b.

Airy Isostatic Crustal of Model

Isostatic compensation requires that all topographical masses above the geoid height must be compensated, in accordance with the Airy hypothesis. To do this, we calculated the topographic load model from the digital terrain elevation averaged in blocks of 30 km x 30 km, in order to minimize short wavelengths. The parameters considered are the same as those used in the gravimetric inversion model (Table 1). The normal crustal thickness (Tn) considered was 35 km, the topographic load density was 2.67 g/cm³ and the crust–mantle density contrast was -0.4 g/cm³. The surface that hydrostatically compensates the masses located above the geoid can be seen in Figure 3c.

Airy Decompensated Isostatic Anomaly

Isostatic corrections can be used to remove the effect of roots or anti-roots of the crust produced by topographic heights or sedimentary basins, but do not solve the problems of crustal regions with high density. The reduction of this gravity field by the Moho for isostatic decompensating (Cordell *et al.*, 1991) is an attempt to remedy this.

The calculation of the decompensated isostatic gravity residual (Cordell *et al.*, 1991) was based on the local isostatic anomaly map (Figure 3c), continued upward to 40 km above sea level, resulting in a map showing long wavelength

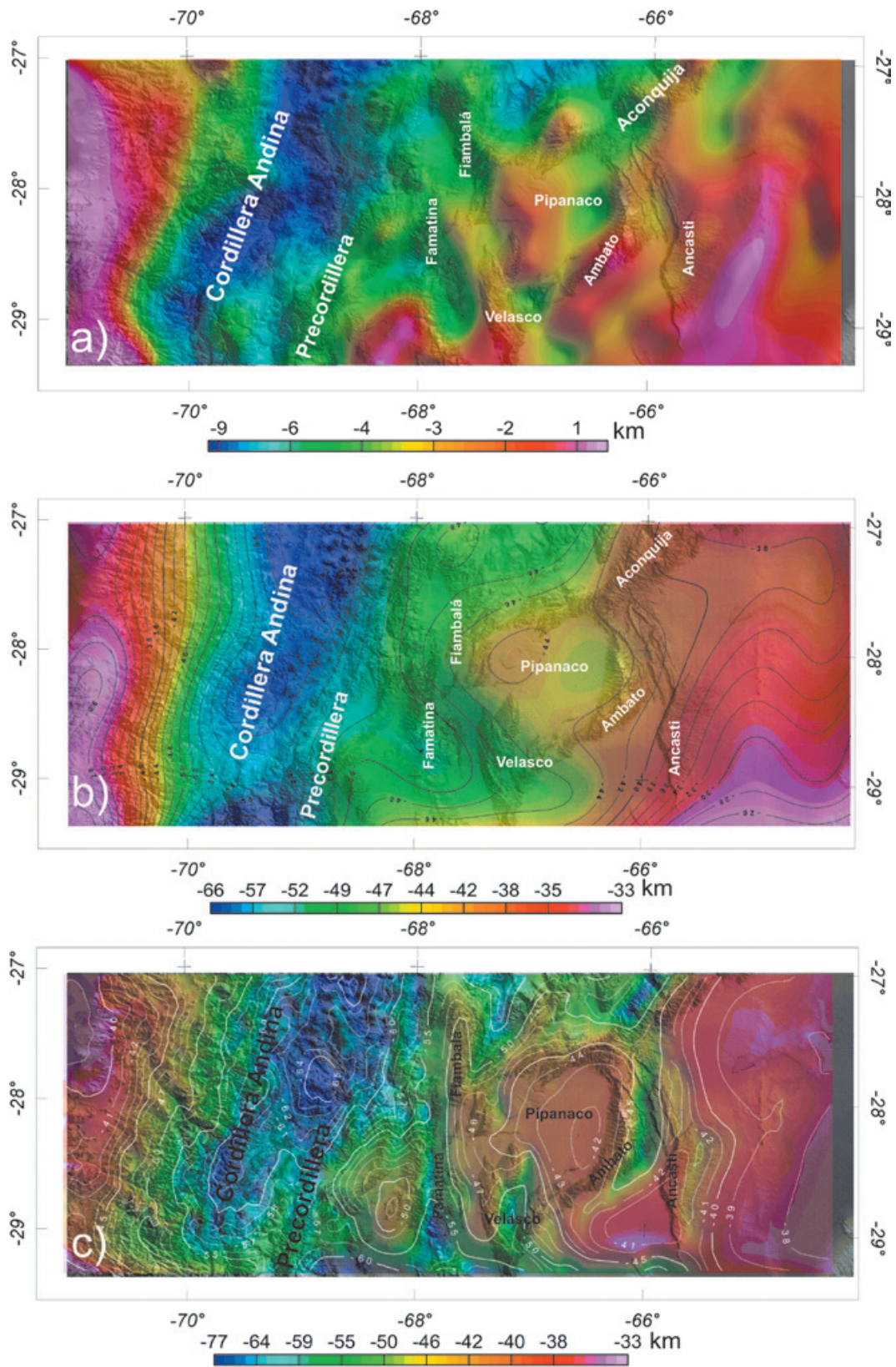


Figure 3. a) Top of basement, obtained by gravimetric inversion of the Bouguer anomaly map, based on the parameters in Chart 1. b) Crust-mantle depth obtained by gravimetric inversion of Bouguer regional anomaly. c) Isostatic model compensated on the Airy hypothesis of the crust-mantle boundary.

effects, which were subtracted from the isostatic anomaly itself (Figure 3c), in order to obtain the uncompensated isostatic anomaly (Figure 4a).

Elastic Lithospheric Thickness

The parameter that characterizes the apparent flexural strength of the lithosphere is the flexural rigidity (D), which is commonly expressed through the elastic thickness of the lithosphere (Te). The flexural rigidity of the plate is defined in terms of Young’s modulus (E), Poisson’s ratio (ν), and the elastic thickness (Te), with the following equation:

$$D = \frac{ET_e^3}{12(1 - \nu^2)}$$

In order to study the lithospheric properties in this region, elastic thickness (Te) was estimated (Figure 4). We used the Lithoflex software (Braitenberg and Zadro, 2007) to calculate flexural rigidity by inverse modeling, allowing for high spatial resolution.

For the inverse flexure calculation application the following are required: a crustal load and the crust-mantle discontinuity. The crustal flexural rigidity is then obtained from the condition that the flexure model with the known loads matches the assumed crustal thickness model. By means of this procedure it is possible to divide the crust into areas of differing Te, which can be geologically significant.

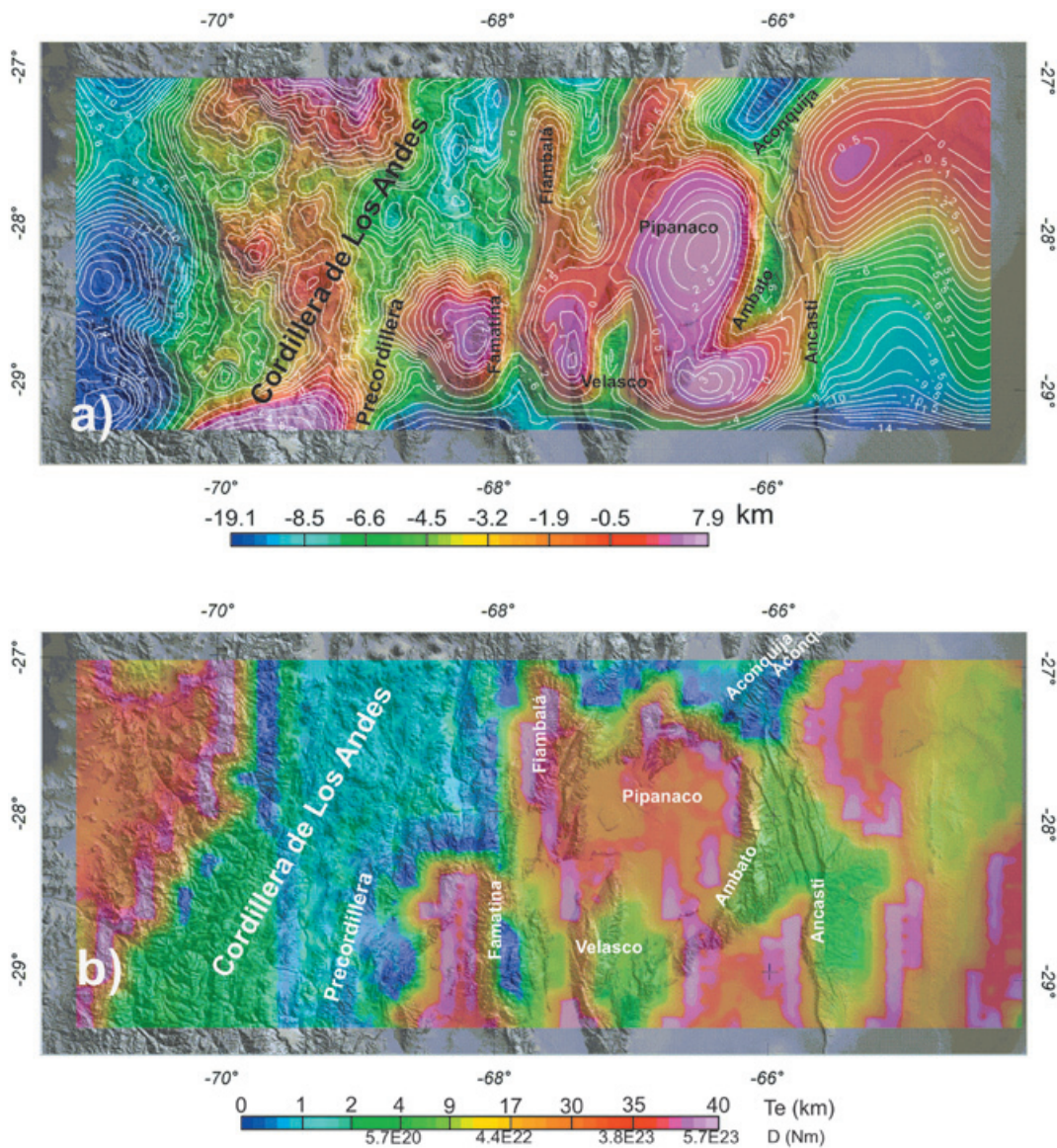


Figure 4. a) Isostatic anomaly. b) Effective elastic thickness map (Te) and flexural rigidity (D).

The densities used in the calculations are (Table 1), for masses above sea level, density equal to 2.67 g/cm³; upper crustal density: 2.7 g/cm³; lower crustal density: 2.9 g/cm³; upper mantle density: 3.3 g/cm³. The Bouguer anomaly was inverted considering a normal crust thickness of 35 km.

Using the Bouguer anomaly field for the gravity inverse calculations we obtained a gravimetric crust–mantle discontinuity (Figure 3b). In order to model the gravity crust–mantle discontinuity in terms of an isostatic model, the equivalent elastic thickness (T_e) is allowed to vary in the range $1 < T_e < 40$ km. The elastic thickness is constant over moving windows of 35 km x 35 km size. The window size was chosen by evaluating the wavelength of the main visible geological structures.

The flexure was calculated with standard values of Young's modulus (10^{11} N/m²) and a normal Poisson's ratio of 0.25; crust and mantle densities were 2.9 g/cm³ and 3.3 g/cm³ respectively (Figure 4b).

Results

The Bouguer anomaly map (Figure 2a) shows the influence of the Andean root that causes a negative gradient centered on the Andes Cordillera axis. Filters were applied to separate the different wavelengths of gravity features. We obtained two maps, 1) a regional trend map (Figure 2b) that would respond primarily to the crust–mantle discontinuity geometry, and 2) a residual Bouguer anomaly map, linked to short and medium wavelengths (Figure 2c) that could be related to the middle and upper crustal densities.

Considering that we used a 2.67 g/cm³ density for the Bouguer correction, the positive values of Bouguer residual anomaly observed (Figure 2c); indicate the presence of denser bodies than the reference value. Negative values would correspond to lighter rocks. The Precordillera area and the northeast (Figure 2c) reveal positive anomalies. In general, positive residual anomaly values suggest the presence of mantle involvement in the generation of felsic rocks from parental magmas (Dahlquist *et al.*, 2010). This model supposes the fusion of continental lithosphere by intrusion of asthenospheric magma.

These dense bodies could be layered residual crustal melts or remnants of asthenospheric material (which led to the melting of the continental lithosphere).

The upper crust base model (Figure 3a) clearly shows the existence of dense bodies located a few kilometers from the surface, as interpreted

in the residual Bouguer anomaly map (Dahlquist *et al.*, 2010).

Figure 3b reflects the geometry of the crust–mantle interface, which presents maximum values below the Andean axis (66 km), close to 35 km on the eastern edge of the study area. The Cordillera de Los Andes is associated with a pronounced crustal "root", whereas beneath the range of the Sierra de Famatina and Sierras Pampeanas, the crustal thickness decreases significantly.

The Airy isostatic model (Figure 3c) indicates a hypothetical surface of the crust–mantle interface, produced by assuming that the topographic masses are in local hydrostatic equilibrium. Results obtained by the inversion of the regional Bouguer anomaly gravimetric model (Figure 3b), are significantly different from the isostatic model (Figure 3c) especially in the regions of: Fiambalá, Más, Aconquija ranges and Pípanaco basin.

To verify this isostatic imbalance, we calculated the decompensated isostatic anomaly (Figure 4a) in which the long-wavelength isostatic anomaly effects were removed (Cordell *et al.*, 1991). The obtained results respond to heterogeneities located in the upper crust. We observed that this map shows optimal consistency with the residual Bouguer anomaly.

On the other hand, the results obtained in the calculation of equivalent elastic thickness (T_e) indicate those as Tassara and Yanez (2003), expected from previous work: Stewart and Watts (1997); Sá (2004); Pérez-Gussinyé (2004); Tassara *et al.* (2007); Sacek and Ussami (2009). The Andean domain values are lower than 10 km, indicating that the crust that contains the Andean Cordillera has a low flexural rigidity, close to local compensation. On the contrary, there are high values of T_e on a strip that extends from the Western edge of the Sierra de Velasco to the North of the Sierra de Tinogasta (across the regions of Vinchina, Villa Castelli, Jagué and Los Pozuelos) and to the East, under the Ancasti Sierras and Pípanaco basin. These high values of T_e and D , are consistent with the positive residual anomalies observed in Figure 2c and Figure 4a which favors the hypothesis with areas of high density and higher flexural rigidity.

Previous studies suggested the presence of dense bodies in the crust, which could be interpreted as eclogitized crust (Ramos, 2009). However, those studies put the eclogite at the base of the crust, but in this interpretation, dense masses would be located within the middle to upper crust. Another alternative was proposed by Astini *et al.* (2009), focusing on Central Andes rifting stage in the early Carboniferous

to late Permian. Crustal extension with rotated basement blocks, rift sedimentation and thinning associated with differentiated rhyolitic and basandesitic magmatism (are associated with a more basic residue deposited in the lower crust). Astini *et al.* (2009) point out that during the early Carboniferous, the Sierras Pampeanas area contained numerous Type A granitic bodies with mantle contamination, implying that on a regional scale, asthenospheric ascent could be explained by rifting, which would have obscured Sanrafaelic shortening (Figure 5). We believe that this model of tectonic evolution is compatible with the results obtained from gravimetric analysis.

Conclusions

The gravity models presented in this paper show that the crustal structure in the southern Central Andes is not homogeneous. The observed gravity

anomalies are interpreted to be produced by medium to short wavelength bodies, which are interpreted as intrusions placed in the middle to upper crust. Isotopic results in the region also suggest the presence of mantle source magmas that could be remnants of asthenospheric material fused with continental lithosphere, generating granitic magmas that are presently exposed on the surface. Dense material from the mantle (magma type A) would have been intruded during crustal stretching in the Early Carboniferous. Associated thinning and differentiated rhyolitic and basandesitic magmatism, leaving the denser bodies in the lower crust. The configuration of granitic bodies with mantle contamination might have been obscured during the Sanrafaelic shortening. Some of these bodies are visible on the surface and others can be identified by their high density.

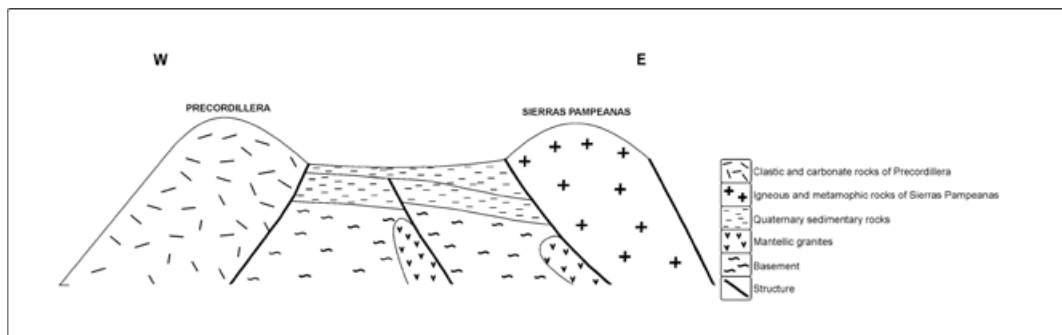


Figure 5. Schematic profile of the crust.

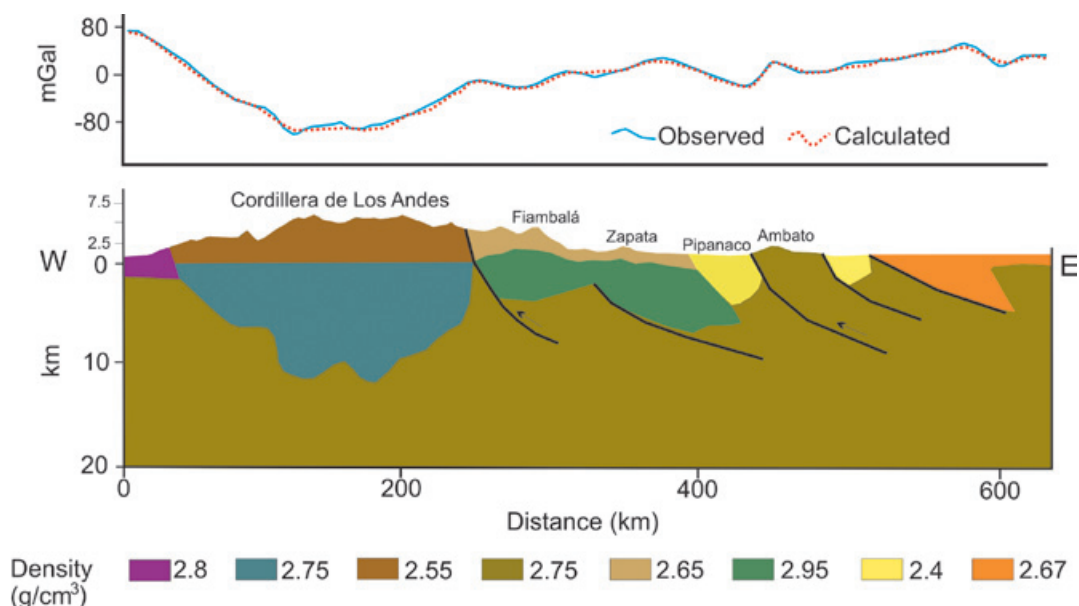


Figure 6. 2D density model.

Acknowledgments

We are grateful to CONICET, Consejo Nacional de Investigaciones Científicas y Técnicas, for the fellowships granted and the Agencia Nacional de Promoción Científica y Tecnológica, Project PICT- 2007-01903 and CICITCA-UNSJ for their economic support.

Bibliography

- Araneda M., Avendaño M.S., Schmidt S., Gotze H.J., Muñoz J., 1999, Hoja Puerto Montt: Carta gravimétrica de Chile. Subdirección Nacional de Geología. SERNAGEOMIN, CHILE. 16pag.
- Astini R.A., Martina F., Ezpeleta M., Dávila F.M., Cawood P.A., 2009, Chronology from rifting to foreland basin in the Paganzo Basin (Argentina), and a reappraisal on the Eo- and Neohercynian tectonics along Western Gondwana. *Actas, XII Congreso Geológico Chileno, Santiago, S9-010*, 40-43.
- Barazangi M., Isacks B., 1976, Spatial distribution of earthquakes and subduction of the Nazca plate beneath South America, *Geology*, 4, 686-692.
- Blakely R.J., 1995, Potential theory in gravity and magnetic applications. Cambridge University Press, 441.
- Bohm M., Lüth S., Asch G., Bataille K., Bruhn C., Rietbrock A., Wigger P., 2002, The Southern Andes between 36°S and 40°S latitude: seismicity and average velocities, *Tectonophysics*, 356, 275-289.
- Braitenberg C., Zadro M., 1999, Iterative 3D gravity inversion with integration of seismologic data. Proceedings of the 2nd Joint Meeting IAG and Ige C, Trieste, Italy. *Bollettino di Geofisica Teorica ed Applicata*, 40, 2.
- Braitenberg C., Ebbing J., Götze H.J., 2002, Inverse modeling of elastic thickness by convolution method - the eastern Alps as a case example. *Earth Pl. Sci. Lett.*, 202, 387-404.
- Braitenberg C., Zadro M., 2007, Comparative analysis of the free oscillations generated by the Sumatra-Andamans Islands 2004 and the Chile 1960 earthquakes, *Bulletin of the Seismological Society of America*, doi: 10.1785/0120050624, 97, (1A), S6-S17.
- Brocher T.M., 2005, Empirical relations between elastic wave speeds and density in the Earth's crust, *Bulletin of the Seismological Society of America*, 95, 2081-2092.
- Cahill T., Isacks B.L., 1992, Seismicity and the shape of the subducted Nazca plate, *J. Geophys. Res.*, 97, 17503-17529.
- CHARGE, 2000-2002, Experimento sísmológico (www.geo.arizona.edu/CHARGE)
- Cordell L., 1985, Techniques, applications, and problems of analytical continuation of New México aeromagnetic data between arbitrary surfaces of very high relief [abs.], Proceedings of the International Meeting on Potential Fields in Rugged Topography, Institute of Geophysics, University of Lausanne, Switzerland, *Bulletin*, 7, 96-99.
- Cordell L., Zorin Y.A., Keller G.R., 1991, The decompensative gravity anomaly and deep structure of the region of the Rio Grande rift, *J. Geophys. Res.*, 96, 6557-6568.
- Cristallini E.O., Comínguez A.H., Ramos V.A., Mercerat E.D., 2004, Basement double-wedge thrusting in the northern Sierras Pampeanas of Argentina (278S), Constraints from deep seismic reflection, in K. R. McClay, ed., Thrust tectonics and hydrocarbon systems: AAPG Memoir, 82, 65-90.
- Dahlquist J., Alasino P.H., Nelson Eby G., Galindo C., Casquet C., 2010, Fault controlled Carboniferous A-type magmatism in the proto-Andean foreland (Sierras Pampeanas, Argentina), Geochemical constraints and petrogenesis. *Lithos*, 115, 65-81.
- Ebbing J., Braitenberg C., Wienecke S., 2007, Insights into the lithospheric structure and tectonic setting of the Barents Sea region from isostatic considerations, *Geophys. J. Int.*, 171, 1390-1403.
- Fromm R., Zandt G., Beck S.L., 2004, Crustal thickness beneath the Andes and Sierras Pampeanas at 30°S inferred from Pn apparent phase velocities, *Geophys. Res. Lett.*, 31, doi:10.1029/2003GL019231.
- Gardner G., Gardner L.W., Gregory A.R., 1974, Formation velocity and density, The diagnostic basics for stratigraphic traps. *Geophysics*, 39, 6, 770-780.
- Gilbert H., Beck S., Zandt G., 2006, Lithospheric and upper mantle structure of Central Chile and Argentina. *Geophys. J. Int.*, 165, 383-398.
- Giménez M.E., Martínez M.P., Bustos G., Jordan T., Lince Klinger F., Mallea M.; Girardi Gallego Guardia A., 2006, Evaluación del Movilismo Hidrostático del Valle De La Rioja, La Rioja-

- Argentina. *Revista Ciencias - FCFN- UNSJ*, Año 10, 1, 3-11.
- Giménez M., Martínez M.P., Introcaso A., 2000, A Crustal Model based mainly on Gravity data in the Area between the Bermejo Basin and the Sierras de Valle Fértil- Argentina. *J. South American Earth Sci.*, 13, 3, 275-286.
- Giménez M., Martínez P., Jordan T., Ruiz F., Lince Klinger F., 2009, Gravity characterization of the La Rioja Valley Basin, Argentina. *Geophysics*, 74, 3, B83-B94 ISSN-00168033.
- Götze H.J., Lahmeyer B., Schmidt S., Strunk S., Araneda M., 1990, Central Andes Gravity Data Base. *Eos*, 71, 401-407.
- Götze H.J., Kirchner A., 1997, Interpretation of gravity and geoid in the Central Andes between 20° and 29°S. *J. South Am. Earth Sci.*, 10, 2, 179-188.
- Hervé F., Davidson J., Godoy E., Mpodozis C., Covacevich V., 1981, The Late Paleozoic in Chile: Stratigraphy, structure and possible tectonic framework. *Anais da Academia Brasileira de Ciencias*, 53, 2, 362-373.
- Hinze W.J., 2003, Bouguer reduction density, why 2.67. *Geophysics*, 68, 5, 1559-1560.
- Introcaso A., 1993, El Levantamiento de Los Andes Centrales involucrando Manto Superior anómalo. III Congreso Internacional da sociedade Brasileira de Geofísica. Rio de Janeiro, 2, 1043-1047.
- Introcaso A., Pacino M.C., 1988, Modelo gravimétrico de corteza y manto superior bajo el segmento argentino-chileno en la Latitud 32° sur. V Congreso Geológico Chileno, II, F63-F76.
- Introcaso A., Pacino M.C., Fraga H., 1992, Gravity, isostasy and Andean crustal shortening between latitudes 30°S y 35°S. *Tectonophysics*, 205, 31-48.
- Introcaso A., Pacino M.P., Guspí F., 2000, The Andes of Argentina and Chile: Crustal configuration, Isostasy, Shortening and Tectonic features from Gravity Data. *Temas de Geociencia*, 5, 31. UNR Editora.
- Jordan T.E., Isacks B., Ramos V.A., Allmendinger R.W., 1983, Mountain building in the Central Andes, *Episodes*, 1983,(3), 20-26.
- Kay S.M., Mpodozis C., Ramos V.A., Munizaga F., 1991, Magma source variations for mid to late Tertiary volcanic rocks erupted over a shallowing subduction zone and through a thickening crust in the Main Andean Cordillera (28°-33°S), in Harmon, R.S. and Rapela, C., eds, *Andean Magmatism and its Tectonic Setting*, Geological Society of America Special Paper, 265, 113-137.
- Ludwig W.J., Nafe J. E., Drake C.L., 1970, Seismic refraction.
- Martínez M.P., Introcaso A., 1999, Sierra Pampeana de Valle Fértil. Provincia de San Juan. Análisis Estructural a partir de datos Gravimétricos. UNR Editora. *Temas de Geociencia*, 2, 80.
- Mpodozis C.; Ramos V.A., 1989, The Andes of Chile and Argentina. In *Geology of the Andes and its relation to hydrocarbon and mineral resources* (Ericksen, G.E.; Cañas, M.T.; Reinemund, J.; editors). Circum-Pacific Council for Energy and Mineral Resources, *Earth Sciences Series*, 11, 59-90.
- Oldenburg D.W., 1974, The inversion and interpretation of gravity anomalies. *Geophysics*, 39, 526-536.
- Pérez-Gussinyé M., Lowry A.R., Watts A. B., Velicogna I., 2004, On the recovery of the effective elastic thickness using spectral methods: examples from synthetic data and the Fennoscandian shield, *J. Geophys. Res.*, 109, B10409.
- Popowski T., Connard G., French R., 2006, GMSYS-3D: 3D Gravity and Magnetic Modeling for OasisMontaj-User Guide, Northwest Geophysical Associates, Corvallis, Oregon.
- Ramos V.A., 1988, The tectonics of the Central Andes: 30° to 33°S latitude, in Clark, S., Burchfiel, D., (eds), *Processes in continental lithospheric deformation*, *Geological Society of America Special Paper*, 218, 31-54.
- Ramos V., 1999, Plate tectonic setting of the Andean Cordillera, *Episodes*, 22, 3, 183-190.
- Ramos V.A., 2009, Anatomy and global context of the Andes: Main geologic features and the Andean orogenic cycle, in Kay, S.M., Ramos, V.A., and Dickinson, W.R., eds., *Backbone of the Americas: Shallow Subduction, Plateau Uplift, and Ridge and Terrane Collision*: Geological Society of America Memoir, 204.
- Regnier M., Chiu J., Smalley R., Isacks B., Araujo M., 1994, Crustal Thickness variation in the Andean Foreland, Argentina, from Converted Waves. *Bulletin of the Seismological Society of America*, 84, 4, 1097-1111.

- Ruiz F., Introcaso A., 1999, Geophysical evidences of crustal ancient junction in Desaguadero-Bermejo megafault (San Juan-La Rioja Province, Argentina). *Acta Geodetica et Geophysica Hungarica*. Sopron.
- Sà N.C., 2004, Livre-docência. Universidade de São Paulo, USP, Brasil. Título: O campo de gravidade, o geóide e a estrutura crustal na América do Sul, Ano de obtenção.
- Sacek V., Ussami N., 2009, Reappraisal of the effective elastic thickness for the sub-Andes using 3-d finite element flexural modelling, gravity and geological constraints. *Geophys. J. Int.*, 179, 2, 778-786.
- Stewart J., Watts A.B., 1997, Gravity anomalies and spatial variations of flexural rigidity at mountain ranges, *J. Geophys. Res.*, 102, B3, 5327-5352.
- Tassara A., Yañez G., 2003, Relación entre el espesor elástico de la litósfera y la segmentación tectónica del margen andino (15-478S), *Revista Geológica de Chile*, 30, 2, 159-186.
- Tassara A., Götze H.J., Schmidt S., Hackney R., 2006, Three-dimensional density model of the Nazca plate and the Andean continental margin. *J. Geophys. Res.*, 111, doi: 10.1029/2005JB003976.
- Tassara A., Swain C., Hackney R., Kirby J., 2007, Elastic thickness structure of South America estimated using wavelets and satellite-derived gravity data. *Earth Pl. Sci. Lett.*, 253, 17-36.
- Woollard G.P., 1959, Crustal structure from gravity and seismic measurements: *J. Geophys. Res.*, 64, 10, 1521-1544.

Characterization of ground motions using recurrence plots

Silvia R. García*, Miguel P. Romo and Jesús Figueroa-Nazuno

Received: February 27, 2012; accepted: January 10, 2013; published on line: June 28, 2013

Resumen

Los modelos matemáticos tradicionales relacionados con el análisis de los terremotos son lineales y en algunos casos son incapaces de predecir determinados comportamientos, porque los datos que modelan pueden ser altamente no lineales y complejos. En este trabajo se describe la implementación de un método alternativo para el análisis sísmico en series de tiempo. La herramienta Mapas de Recurrencia (MR) permite el reconocimiento y el tratamiento de las aceleraciones medidas. Un Mapa de Recurrencia (MR) obtenido de datos sísmicos permite una interpretación más eficiente de los movimientos del suelo y la aplicación de esta explicación a la definición de estratigrafía y de las tendencias de respuesta. Los atributos no lineales obtenidos a partir del análisis de Mapas de Recurrencia se pueden utilizar como filtros para revelar patrones, o en combinación para predecir una propiedad sísmica. La caracterización automatizada de datos sísmicos, basada en los atributos sísmicos no lineales, podría rescribir las reglas de interpretación del fenómeno sísmico. El objetivo de este trabajo es establecer una metodología para la aplicación práctica de la dinámica no lineal en el reconocimiento de patrones sísmicos, un campo de la ingeniería desafiante y en constante evolución.

Palabras clave: mapas de recurrencia, series de tiempo sísmicas, caos análisis no lineal, movimientos fuertes de terreno, periodo fundamental del suelo, vibraciones en masas de suelo.

Abstract

The current analysis of earthquakes is typically based on linear mathematical models that may fail to describe and forecast particular behaviors, because in many cases the data complexity may induce a highly non linear behavior. In this paper the implementation of an alternative method for seismic time series analysis is presented. The RPs (Recurrence Plots) enables recognition and treatment of measured accelerations. An RP obtained from seismic data allows a more efficient interpretation of the ground motions and this explanation contributes to characterize materials and responses. The nonlinear attributes from RPs analysis can be used as filters to reveal patterns or be combined to predict a seismic property. Automated seismic data characterization, based on nonlinear seismic attributes, could rewrite the rules of earthquake phenomena interpretation. The objective of this work is to establish a new methodology for practical application of nonlinear dynamics in seismic pattern/attributes recognition, an evolving and challenging engineering field.

Key words: recurrence plots, seismic time series, nonlinear analysis chaos, strong ground motions, soil natural periods, soil vibrations.

S. R. García*
M. P. Romo
Coordinación de Geotecnia
Instituto de Ingeniería
Universidad Nacional Autónoma de México.
Ciudad Universitaria
Apartado Postal 70-472
México D.F., México

*Corresponding author: sgab@pumas.iingen.unam.mx

J. Figueroa-Nazuno
Laboratorio de Computación Paralela y Distribuida
Centro de Investigación en Computación
Instituto Politécnico Nacional
Av. Juan de Dios Bátiz
Apartado Postal 75-476
México, D.F., México

Introduction

Data analysis often requires the drawing of meaningful conclusions about complicated systems using time-series data from a single sensor. The problem is rather complex because there usually exists simultaneously overabundance and lack of data: megabytes of time-series data about one parameter but no information regarding other important quantities. Data-mining techniques (Fayyad, 1996) provide some useful ways to deal successfully with the sheer volume of information that constitutes one part of this challenge. The second part is much harder. If the target system is highly complex say, a sudden release of strain/energy accumulated during extensive time intervals in the upper part of the Earth in the form of seismic waves radiated out in all directions from the source region through the Earth's interior and recorded at large distances by sensitive seismographs, but only a few of its important properties (e.g., surface acceleration) is sensor accessible, the data analysis procedure would appear to be fundamentally limited.

Figure 1 shows a simple example of the kind of problem that this work addresses: a mechanical spring/mass system and two time-series data sets gathered by sensors that measure the position and velocity of the mass. This system is linear: it responds in proportion to changes. Pulling the mass twice as far down, for instance, will elicit an oscillation that is twice as large, not one that is $2^{1.5}$ as large or $\log 2$ times as large. A pendulum in contrast reacts according to a non linear relationship: if it is hanging straight down, a small change in its angle will have little effect, but if it is balanced at the inverted point, minor changes have significant effects in its response. This distinction is extremely important to science in general and for data analysis in particular. If the system under examination is linear, data analysis is comparatively straightforward and the tools are well developed. The data can be characterized by using statistics (mean, standard deviation, etc.), fit curves to them (functional approximation), and plot various kind of graphs to aid understanding of the behavior. If a more-detailed analysis is required, the system can be represented in an "input + transfer function \rightarrow output" manner using any of a wide variety of time- or frequency-domain models. This kind of formalism admits a large collection of powerful reasoning techniques, such as superposition and the notion of transforming back and forth between the time and frequency domains.

Nonlinear systems pose an important question to intelligent data analysis. Not only they are ubiquitous in science and engineering, but their

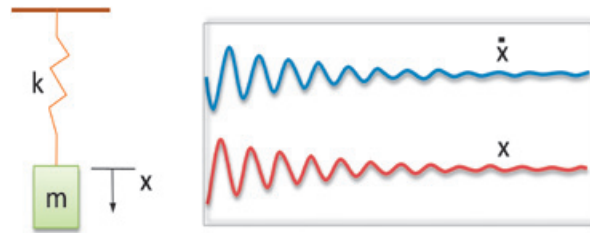


Figure 1. A spring/mass system and the vertical position and velocity time series (measured by two sensors)

mathematics is also vastly harder and many standard time series analysis techniques simply do not apply to nonlinear problems. Real systems exhibit broad band behavior which makes that many traditional signal processing operations become useless. Non linear problems cannot be decomposed in the standard "input + transfer function \rightarrow output" manner, nor can the noise be removed by simply low-pass filter data. The concept of a discrete set of spectral components does not make sense in many nonlinear problems, so using transforms to move between time and frequency domains does not work.

Another common complication in data analysis is *observability*: access to enough information to fully describe the system. The spring/mass system in Figure 1, for instance, has two state variables, the position and velocity of the mass, and both of them can be measured in order to know the state of the system. But for complex problems, the question is how to identify all of the internal state variables of the system and infer their values from the signals that can be observed. Geoseismic (geotechnical and seismological) procedures require accurate conclusions about reconstructed dynamics because fully observable systems are rare in geotechnical and earthquake engineering practice; as a rule, many often, most of a system's state variables either are physically inaccessible or cannot be measured with available sensors.

Based on the existing parameters, countless *seismic attributes* (measurements derived from seismic data) has been defined and introduced in seismic exploration (Sheriff, 1991; Brown, 1996; Chen and Sidney, 1997; and Eastwood, 2002). Many of these attributes play exceptionally an important role in interpreting and analyzing data (Chopra and Marfurt, 2005) however, many questions remain unanswered about the effectiveness and practicality of using these conventional (linear and stationary) techniques on earthquake phenomena. In this work a more useful time-series analysis procedure is presented.

The aim of this investigation is to apply the concepts of chaos theory to global characterization

of the soil deposits through the structures of the two-dimensional images, Recurrence Plots (Eckmann *et al.* 1986) constructed from acceleration time series. The RPs-methodology proposed here, general and practical, uses the structures of the accelerograms for a "topological" interpretation of the data. Through visualization and quantitative assessment of these configurations, the manifestations of soil (heterogeneous materials vibrating) can be described. We demonstrate the potential capability of RPs using events recorded in Mexico City (rock and soft-soil deposits) during minor and extreme seismic events.

Studying Complex Systems

When a researcher must deal with large data sets, the expert should adopt or develop specific analyses for classification, visualization, understanding and manipulation of the time series in order to understand more about the underlying system and to determine the direction of future research. Traditional methods of time series analysis come from the well-established field of digital signal processing (Abarbanel, 1996). One of the most familiar and widely used tools is the Fourier transform. Indeed, many traditional methods of analysis, visualization, or processing uses the Fourier transform in order to change a set of linear differential equations into an algebraic problem where powerful

methods of matrix manipulation may be used. However, these methods are designed to deal with a restricted subclass of possible data. The data is often assumed to be stationary -that means, independent of time. It is also assumed that the dynamics are fairly simple, both low-dimensional and linear. Compound this with the additional assumptions of low noise and a non broad-band power spectrum, then it can be seen that a very limited class of data is implied. With experimental nonlinear data, as the ground accelerations measured during an earthquake, this traditional signal processing methods may fail because the system dynamics are, at best, complicated, and at worst, extremely noisy.

An example to illustrate this point is depicted in Figure 2. Fourier transform is applied to data (acceleration time series) from a soft soils deposit (site named as SCT) when is affected by seismic load (four events). If natural period (fundamental frequency), stratigraphy and topographical/geometrical conditions are held constant (same recording station) then the differences between the response representations must be related with the fault mechanism, magnitude, distance (source-site) and directivity. See the spectra of two events from the same seismogenic zone (epicenters circled together that means for practical purposes, same fault, distance and radiation pattern) shown in Figure 2a. The frequency content is very similar and the obvious

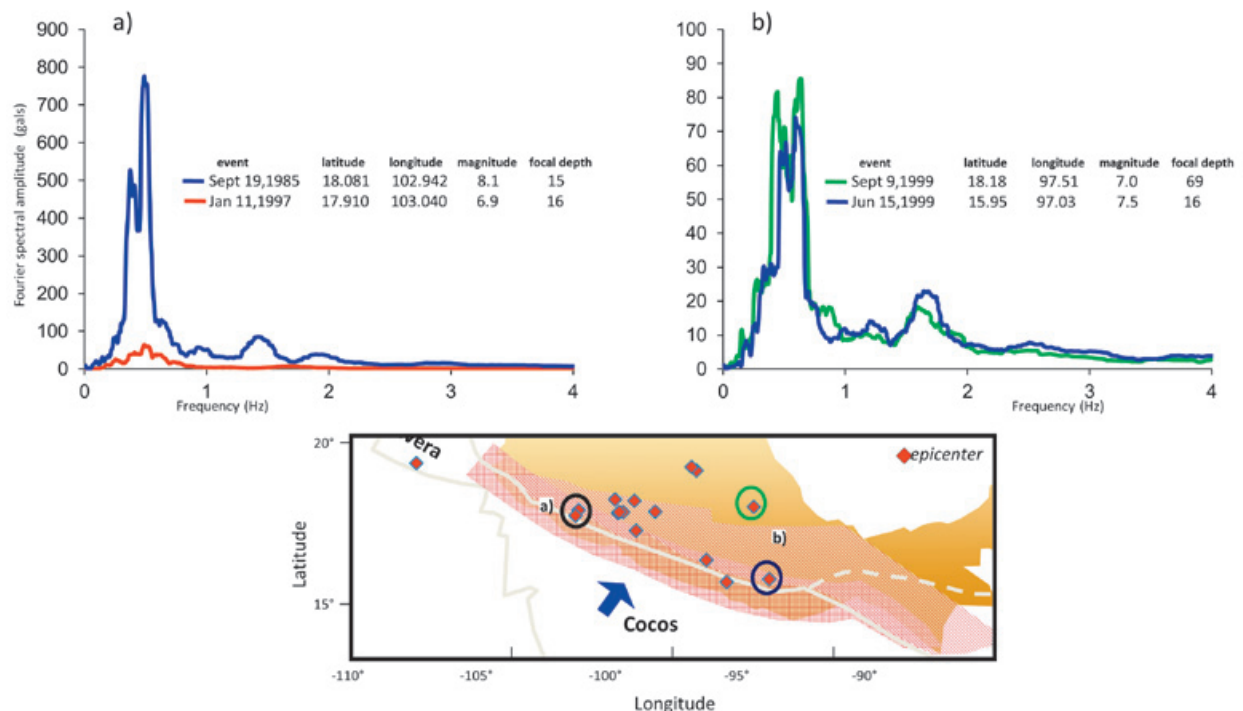


Figure 2. Fourier spectra examples from Mexico City seismic recordings, site: SCT (Lake zone, soft soils)

difference between these representations is the intensity level. What additional variables (if any) are needed to explain the remarkable distance between shaking energies? In Figure 2b two responses due to seismic events generated by different fault mechanisms, thus having dissimilar directivities and distances, are shown. As can be seen, these Fourier representations have very similar frequency-intensity distribution and it can be assumed that they might produce the same structural or architectural damage. Since they result from very different seismic activity, which conditions or parameters must be defined in order to justify the strong similitude between these responses? In these cases, the transformation to the frequency domain is restrictive and many important geological and seismic aspects could be ignored or misinterpreted.

What is needed is an alternative and reliable recording-based approach to explore, to characterize and to quantify earthquake-induced effects. Analysis from a nonlinear dynamics perspective may yield more fruitful results; still, this is not a straightforward task. Calculation of empirical global nonlinear quantities, such as Lyapunov exponents and fractal dimension, from time series data is known to often yield erroneous results (Ding *et al.*, 1993; Parlitz, 1992). The literature is replete with examples of poor or erroneous calculations and it has been shown that some popular methods may produce circumspect results (Eckmann and Ruelle, 1992; Vastano and Kostelich, 1986). Limited data set size, noise, nonstationarity and intricate dynamics are presented as additional complications. The concerns about the data are compounded by concerns about analysis. It is expected that the following consistent synthesis of the RP-analysis will enable researchers to perform studies more efficiently and more confidently. Thus it is encouraged that first at all, the user familiarizes him with the background and the methodology before attempting any analysis. To make the paper self-contained, some key concepts of Chaos Theory and Recurrence Plots are presented in the following paragraphs.

Chaos Attractor

State Space Description

The state of a system is defined as the value of the smallest vector such that at time t_0 it completely determines the system behavior for any time $t \geq t_0$ (Cao, 1997). The components of the state vector \bar{x} are called state variables. The evolution of a system can be visualized as a path in state space. Since a dynamical system must contain memory elements, integrators can be used to describe the state space representation.

The evolution of the state space can therefore be described with the following equations:

$$\dot{\bar{x}}(t) = f(\bar{x}, \bar{u}, t) \quad (1)$$

$$\bar{y}(t) = g(\bar{x}, \bar{u}, t) \quad (2)$$

where \bar{u} and \bar{y} are the system input and output respectively. This set of differential equations completely describes the system. The collection of all possible states is called the phase space. Thus, the phase space is a subset of the state space.

Equilibrium Points, Periodic Solutions, Quasiperiodic Solutions and Chaos.

As time goes to infinity, the asymptotic behavior of a system that is not purely noise-driven can be categorized as being one of four general types: equilibrium points, periodic solutions, quasiperiodic solutions, or chaos (Horai *et al.*, 2002).

An equilibrium point can be either stable or unstable. Stable equilibrium points are called sinks, and unstable points are called sources. A sink causes that near trajectories move towards the self-sink with an increase in time, and this is an example of an attractor. When a trajectory precisely returns to itself, the system has a periodic solution with a fixed period T . The value of T is the time needed to reach the same point in state space again. A limit cycle is an example of an attractor that has a periodic solution. The period of a quasiperiodic system is not fixed, i.e. the phase space is formed by the sum of periodic solutions that have periods whose ratio is irrational.

Lorenz (Lorenz, 1963) discovered the first example of a chaotic attractor while searching for the solution of a weather prediction model. Qualitatively speaking, a chaotic attractor is an attractor that is not of the previous three types. A system of this type is very dependent on initial conditions, i.e. two points in state space that are separated by a small distance will diverge exponentially as the system evolves. Thus, the term "chaotic" describes a dynamical property of a system.

Modeling the Attractor

Having established that a system contains a chaotic attractor, the process can be modeled by reconstructing the state space. Two methods are available: the method of delays and principal component analysis. We will not give a detailed description of principal component analysis

because in this investigation the method of delays is used. Thus, we refer the reader interested on the former method to Broomhead and King (1986).

Mutual Information. Frasier and Swinney (Fraser and Swenney, 1986) proposed mutual information method to obtain an estimate for delay time, τ (March *et al.*, 2005). Mutual information provides a general measure for the dependence of two variables, thus, the value of τ for which the mutual information goes to zero is preferred. Additional arguments for choosing the first zero can be found in (Saussol and Wu, 2003).

Mutual information is a measure found in the field of Information Theory. Let S be a communication system with s_1, s_2, \dots, s_n a set of possible messages with associated probabilities $P_s(s_1), P_s(s_2), \dots, P_s(s_n)$.

The entropy H of the system is the average amount of information gained from measuring s and it is defined as

$$H(S) = -\sum_i P_s(s_i) \log P_s(s_i) \quad (4)$$

For a logarithmic base of two, H is measured in bits. Mutual information measures the dependency of $x(t+T)$. Let $[s, q] = [x(t), x(t+T)]$, and consider a coupled system (S, Q) . Then, for sent message s and corresponding measurement s_i ,

$$\begin{aligned} H(Q|s_i) &= -\sum_j P_{q|s}(q_j|s_i) \log [P_{q|s}(q_j|s_i)] \\ &= \sum_j \frac{P_{sq}(s_i, q_j)}{P_s(s_i)} \log \frac{P_{sq}(s_i, q_j)}{P_s(s_i)} \end{aligned} \quad (5)$$

where $P_{q|s}(q_j|s_i)$ is the probability that a measurement of q will result in q_j , subject to the condition that the measured value of s is s_i . Next we take the average uncertainty of $H(Q|s_i)$ over s_i ,

$$\begin{aligned} H(Q|s_i) &= \sum_i P_s(s_i) H(Q|s_i) \\ &= -\sum_{i,j} P_{sq}(s_i, q_j) \log \frac{P_{sq}(s_i, q_j)}{P_s(s_i)} \end{aligned}$$

$$= H(S, Q) - H(S) \quad (6)$$

with

$$H(S, Q) = -\sum P_{sq}(s_i, q_j) \log P_{sq}(s_i, q_j) \quad (7)$$

The reduction of the uncertainty of q by measuring s is called the mutual information $I(S, Q)$ which can be expressed as

$$I(Q, S) = H(Q) - H(Q|S) \quad (8)$$

$$= H(Q) + H(S) - H(S, Q) = I(S, Q) \quad (9)$$

where $H(Q)$ is the uncertainty of q in isolation. If both S and Q are continuous, then

$$I(S, Q) = \int P_{sq}(s, q) \log \frac{P_{sq}(s, q)}{P_s(s)P_q(q)} ds dq \quad (10)$$

If s and q are different only as a result of noise, then $I(S, Q)$ gives the relative accuracy of the measurements. Thus, it specifies how much information the measurement of x_i provides about x_{i+j} . The mean and variance of the mutual information estimation can be calculated (Takens, 1981). Although mutual information guarantees decorrelation between x_k and x_{k+t} and between x_{k+t} and x_{k+2t} , it does not necessary follow that x_k and x_{k+2t} are also uncorrelated (Afraimovich *et al.*, 2003).

False Nearest Neighborhoods. Mutual information gives an estimate for τ_s , but does not determine the embedding dimension d . The Takens' Theorem (Takens, 1981) states that an m -dimensional attractor will be completely unfolded with no self-crossings if the embedding dimension is chosen larger than $2m$. In this work, the method of false nearest neighbors is used for finding a good value for d (Afraimovich, 1997).

The method is based on the idea that two points close to each other (called neighbors) in dimension d , may in fact not be close at all in dimension $d+1$. This can happen when the lower dimensional system is simply a projection of a higher dimensional system, and it is unable to completely describe the system. Thus, the algorithm searches for "false nearest neighbors" by identifying candidate neighbors, increasing

the dimension, and then inspecting the candidate neighbors for false ones. When no false neighbors can be identified, it is assumed that the attractor is completely unfolded and d , at this point, taken as the embedding dimension.

Recurrence Analysis

In our daily life we make predictions that are not based on the evaluation of long and complicated sets of mathematical equations, but rather on two crucial facts: i) similar situations often evolve in a similar way; ii) some situations occur over and over again. The first fact is linked to certain determinism in many real world systems. Chaos theory has taught us that some systems - although deterministic- are very sensitive to fluctuations and even the smallest perturbations of the initial conditions can make a precise prediction on long time scales impossible. The second fact is fundamental to many systems and it is probably one of the reasons why life has developed memory. Experience allows remembering similar situations, making predictions and, hence, helps to survive. But remembering similar situations is only helpful if a system returns or recurs to former states. Such a recurrence is a fundamental characteristic of many dynamical systems and it can indeed be used to study their properties.

The set of nonlinear dynamic techniques, called Nonlinear Time Series Analysis (Kantz and Schreiber, 1997), can be classified into metric, dynamical, and topological tools. The metric approach depends on the computation of distances on the system's attractor. The dynamical approach deals with computing the way nearby orbits diverge by means of estimating Lyapunov exponents. Topological methods are characterized by the study of the organization of the strange attractor, and they include close returns plots and Recurrence Plots (Eckmann *et al.*, 1986).

Recurrence Plots

RPs are intricate and visually appealing. They are also useful for finding hidden correlations in highly complicated data. In this work the RP-analysis is extended, formalized, and systematized in a meaningful way that is based both in theory and experiments and that targets both quantitative and qualitative properties for its geotechnical and seismological application.

In this section, we briefly outline some of the basic features of RPs and describe how an RP of an experimental data set can be generated. The standard first step in this procedure is to reconstruct the dynamics by embedding the one-dimensional time series in a d_E -dimensional reconstruction space using the method of delay

coordinates. Given a system whose topological dimension is d , the sampling of a single state variable is equivalent to projecting the d -dimensional phase-space dynamics down onto one axis.

Loosely speaking, embedding is akin to "unfolding" those dynamics, albeit on different axes (Packard *et al.*, 1980; Takens, 1981). Given a trajectory in the embedded space, finally, an RP is constructed by computing the distance between every pair of points (y_p, y_j) using an appropriate norm and then shading each pixel (i, j) according to that distance. The process of constructing a correct embedding is the subject of a large body of literature and numerous heuristic algorithms and arguments. Abarbanel (1995) gives a good summary of this extremely active field.

a) Delay Coordinate Embedding. To reconstruct the dynamics, we begin with experimental data consisting of a time series:

$$\{x_1, x_2, \dots, x_N\} \tag{11}$$

Delay-coordinate reconstruction of the unobserved and possibly multi-dimensional phase space dynamics from this single observable x is governed by two parameters, embedding dimension d_E and time delay τ . The resultant trajectory in R^{d_E} is:

$$\{y_1, y_2, \dots, y_m\} \tag{12}$$

where $m = N - (d_E - 1)\tau$ and

$$y_k = \left(x_k, x_{k+\tau}, x_{k+2\tau}, \dots, x_{k+(d_E-1)\tau} \right) \tag{13}$$

for $k=1, 2, \dots, m$. Note that using $d_E=1$ merely returns the original time series; one dimensional embedding is equivalent to not embedding at all. Proper choice of d_E and τ is critical to this type of phase-space reconstruction and must therefore be done wisely; only "correct" values of these two parameters yield embeddings that are guaranteed by the Takens Theorem (Takens, 1981; Packard *et al.*, 1980; Sauer *et al.*, 1991) to be topologically equivalent to the original (unobserved) phase-space dynamics.

Assuming that the delay-coordinate embedding has been correctly carried out, it is natural to assume that the RP of a reconstructed trajectory bears great similarity to an RP of

the true dynamics. Furthermore, we expect any properties of the reconstructed trajectory inferred from this RP to be true of the underlying system as well. This is, in fact, the rationale behind the standard procedure of embedding the data before constructing a RP.

B) Constructing the Recurrence Plot. RPs are based upon the mutual distances between points on a trajectory, so the first step in their construction is to choose a norm D . In this work the maximum norm is used, although in one dimension the maximum norm is, of course, equivalent to the Euclidean p -norm. We chose the maximum norm for two reasons: for ease of implementation and because the maximum distance arising in the recurrence calculations (the difference between the largest and smallest measurements in the time series) is independent of embedding dimension d_E for this particular norm. This means that we can make direct comparisons between RPs generated using different values of d_E without first having to re-scale the plots. Next, we define the recurrence matrix A as follows:

$$A(i, j) = D(y_i, y_j), 1 \leq i, j \leq m \tag{14}$$

follows

$$D(y_i, y_j) = \max_{1 \leq k \leq d_E} |x_{i+(k-1)\tau} - x_{j+(k-1)\tau}| \tag{15}$$

The time series spans both ordinate and abscissa and each point (i, j) on the plane is shaded according to the distance between the two corresponding trajectory points y_i and y_j (Figure 3). The pixel lying at (i, j) is color-coded according to the distance. For instance, if the 117th point on the trajectory is 14 distance units away from the 9435th point, the pixel lying at $(117, 9435)$ on the RP will be shaded with the color that corresponds to a spacing of 14.

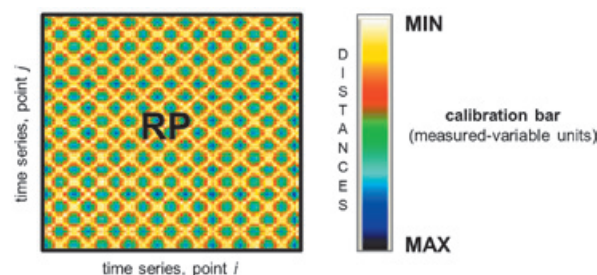


Figure 3. RP graphical description

Figure 4 shows RPs generated from very different data sets: from a time series derived by sampling the function $\sin t$ until a noise series. The colors on these plots range from white-yellow for very small spacing to dark blue for large inter-point distances (see calibration bar in Figure 3). With this in mind, the sine-wave RP is relatively easy to understand; each of the “blocks” of color simply represents half a period of the signal. The lower RPs in the Figure 4 (see the ECG, Lorenz and Rössler RPs, for example), generated from chaotic data sets, are far more complicated, although they too have block-like structures resembling what might be expected from a periodic signal. These signals, though, are not periodic, so the repeated structural elements in the plot request a deeper explanation. The recurrent inter-point distances (repeated colors) are not straightforwardly related with the signals but it seems that some kind of determinism is presented in the behaviors. The RPs could be categorized following the knowledge about the systems that generated the signal and the particular array of the repeated structures. Alternatively, recurrence points for the white noise (at the bottom of Figure 4) are simply distributed in a homogeneous random pattern, signifying that the variable lacks of deterministic structures.

C) Structures in RPs. As already mentioned, the initial purpose of RPs was to visualize trajectories in phase space, which is especially advantageous in the case of high dimensional systems. RPs yield important insights into the time evolution of these trajectories, because typical patterns in RPs are linked to a specific behavior of the system. Following the phase space characteristics, the path in the correlation dimension curve and the large scale patterns in RPs, designated as *typology*, the RPs structures can be classified as *homogeneous*, *periodic*, drift and disrupted ones (Marwan, 2003):

- *Homogeneous* RPs are typical of systems in which the relaxation times are short in comparison with the time spanned by the RP. An example of such an RP is that of a stationary random time series. See the uniformly distributed white noise example shown in Figure 4.
- Periodic and quasi-periodic systems have RPs with diagonal oriented, periodic or quasi-periodic recurrent structures (diagonal lines, checkerboard structures). Figure 4 shows the RP of the sine signal, example of a periodic system. Irrational frequency ratios cause more complex quasi-periodic recurrent structures (see the ECG, Lorenz, Rössler and sun spots examples); however, even for oscillating

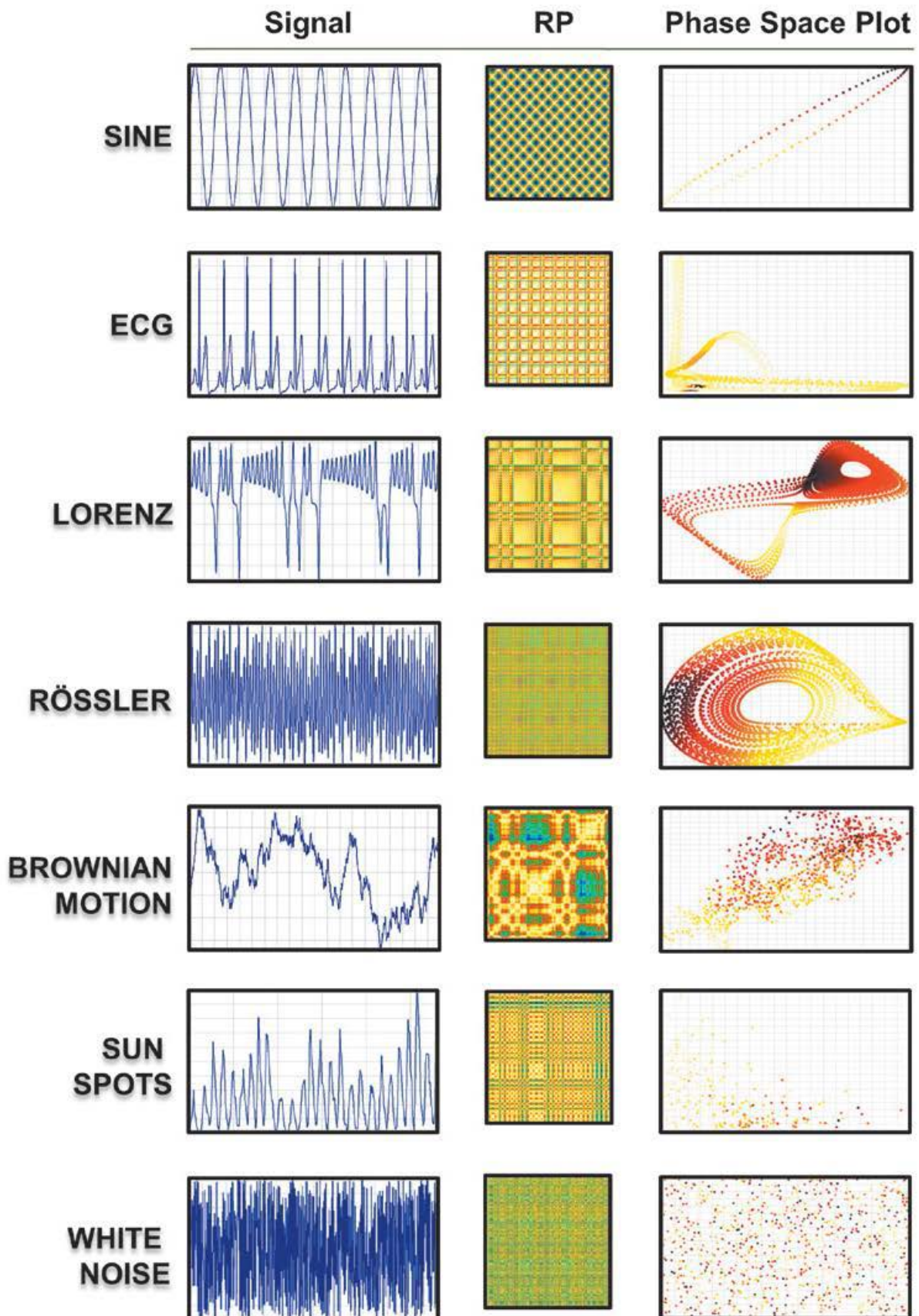


Figure 4. Examples of Recurrence Plots and Phase Space Plots of different data sets.

systems whose oscillations are not easily recognizable, RPs can be very useful.

- A drift is caused by systems with slowly varying parameters, i.e. non-stationary systems. The RP pales away from the line of identity, LOI (the main diagonal line in a RP, $R_{i,j}=1$).
- Abrupt changes in the dynamics as well as extreme events cause *white areas or bands* in the RP, for example the Brownian motion (Figure 4). RPs allow finding and assessing extreme and rare events easily by using the frequency of their recurrences.

A closer inspection of the RPs reveals also the *texture* or small-scale structures (Eckmann *et al.*, 1987), which can be typically classified in single dots, diagonal lines as well as vertical and horizontal lines (the combination of vertical and horizontal lines obviously forms rectangular clusters of recurrence points); in addition, even bowed lines may occur (Marwan, 2003; Eckmann *et al.*, 1987):

- Single, isolated recurrence points can occur if states are rare, if they persist only for a very short time, or fluctuate strongly.

- A diagonal line $R_{i+k,j+k} \equiv 1 \left| \begin{matrix} l-1 \\ k=0 \end{matrix} \right|$ (where l is the length of the diagonal line) occurs when a segment of the trajectory runs almost in parallel to another segment for l time units:

- A vertical (horizontal) line $R_{i,j+k} \equiv 1 \left| \begin{matrix} v-1 \\ k=0 \end{matrix} \right|$ (with v the length of the vertical line) marks a time interval in which a state does not change or changes very slowly:

The state is trapped for some time. This is a typical behavior of laminar states (intermittency) (Marwan *et al.*, 2002).

- *Bowed lines* are lines with a non-constant slope. The shape of a bowed line depends on the local time relationship between the corresponding close trajectory segments.

Table 1. Typical patterns in RPs and their meanings (modified from [30]).

	Pattern	Meaning
(1)	Homogeneity	The process is stationary
(2)	Fading to the upper left and lower right corners	Non-stationary data; the process contains a trend or a drift
(3)	Disruptions (white bands)	Non-stationary data; some states are rare or far from the normal; transitions may have occurred
(4)	Periodic/quasi-periodic patterns	Cyclicities in the process; the time distance between periodic patterns (e.g. lines) corresponds to the period; different distances between long diagonal lines reveal quasi-periodic processes
(5)	Single isolated points	Strong fluctuation in the process; if only single isolated points occur, the process may be an uncorrelated random or even anti-correlated process
(6)	Diagonal lines (parallel to the LOI)	The evolution of states is similar at different epochs; the process could be deterministic; if these diagonal lines occur beside single isolated points, the process could be chaotic (if these diagonal lines are periodic, unstable periodic orbits can be observed)
(7)	Diagonal lines (ortogonal to the LOI)	The evolution of states is similar at different times but with reverse time; sometimes this is an indication for an insufficient embedding
(8)	Vertical and horizontal lines / clusters	Some states do not change or change slowly for some time; indication for laminar states
(9)	Long bowed line structures	The evolution of states is similar at different epochs but with different velocity; the dynamics of the system could be changing

RPs of paradigmatic systems provide an instructive introduction into characteristic typology and texture but the visual interpretation of RPs requires some experience. To summarize the explanations about typology and texture, we present a list of features and their corresponding interpretation in Table 1.

RPs of Seismic Recordings

A set of acceleration time series recorded in the soft soils of the Mexican metropolis are used to study its chaotic nature. We first define the soil systems and then we classify the behavior and propose a nonlinear label.

Data base

The recorded responses on the surface of 11 soft soils (clays) and 4 stiff deposits within the urban area of Mexico City conform the signals used in this study. These sites are located on the lacustrine basin where soils were deposited by air or water transportation (very soft clay

formations with large amounts of microorganisms interbedded by thin seams of silty sand), some others are product of volcanic effusions that took place within the last one million years (fly ash and volcanic glass) and there are stations on a third type of soils that are considered firm or materials rock-like. Based on this material characterization and the historical seismic behavior, the Mexico valley has the geotechnical microzonation. This map is taken as a means of gaining broad insight into the surface motion of a particular site. The elastic natural periods T_n (key parameter in ground motions categorization) of the sites included in the database vary from $T_n=1$ s to $T_n=4.2$ s (Table 2).

The 9 events selected (Table 3), having at least 100 s and high signal-to-noise ratios, are representative of the tectonic regions (different source mechanism) that affects the valley. The set is denser in events from the subduction of the Cocos Plate into the Continental Plate because they are associated to the most damaging shocks.

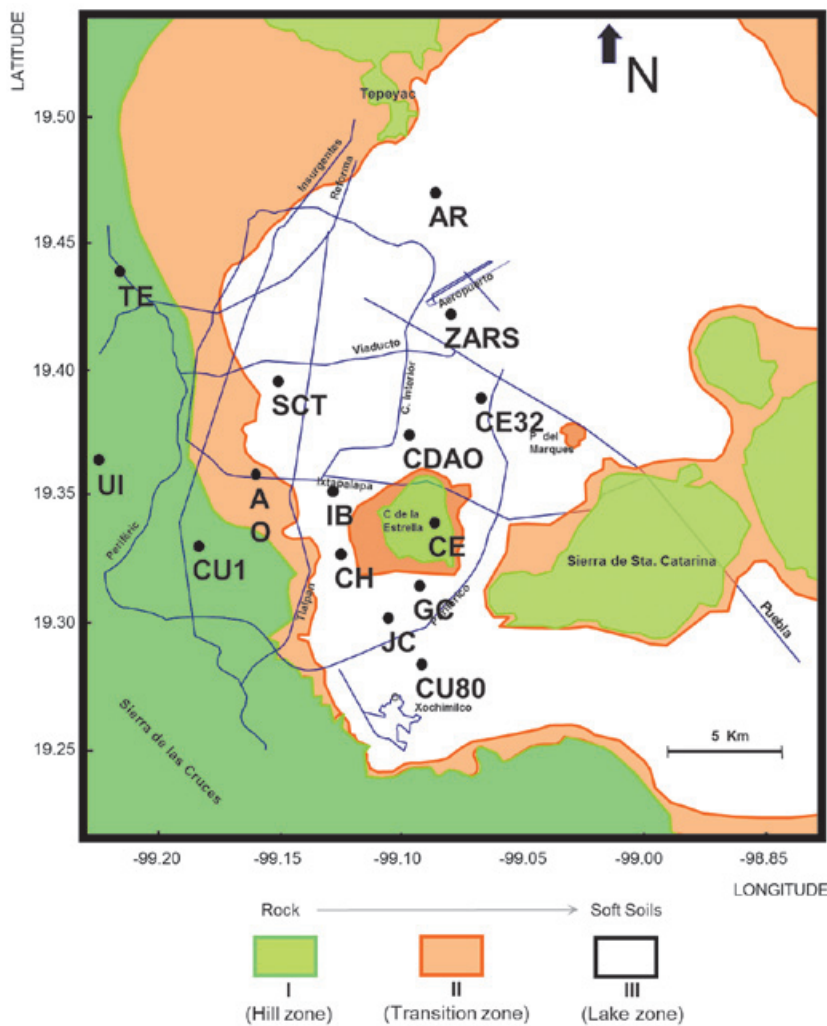


Figure 5. Mexico City zonification.

Table 2. Sites included in this study.

Site	Geotechnical Zone	T_n (s)
AR	Lake zone	3.8
AO	Transition zone	1.0
CE	Hill zone	0.5
CE32	Lake zone	4.1
CDAO	Lake zone	3.6
CH	Transition zone	1.0
CU1	Hill zone	0.5
CU80	Lake zone	3.8
GC	Lake zone	2.0
IB	Lake zone	1.5
JC	Lake zone	3.0
SCT	Lake zone	1.5
TE	Hill zone	0.5
UI	Hill zone	0.5
ZARS	Lake zone	3.3

Regular and chaotic ground motions

Information accumulated over the last four decades has firmly established that the singular geotechnical environment that prevails in Mexico City is the one most important factor to be accounted for in explaining the huge amplification of seismic movements. Also, observational evidence has made it clear that seismic movements within the Basin of Mexico can differ considerably from one site to the other (Romo and Seed, 1986). The statutory regulations have tried to take into account these facts but still there are dangerous doubts about the outcome patterns. The purpose of the following analysis is to illustrate an alternative

way in which the oscillations can be described and to provide a qualitative understanding of the complex system responses.

RPs-Typology (large scale)

Examples of RPs obtained from accelerograms recorded during the earthquakes listed in Table 2, are shown in Figure 6. One intriguing and puzzling characteristic of the RPs is the structural similitude that they exhibit with different seismic and site conditions. Evaluating RPs constructed from accelerograms recorded during the same event on different site conditions (Figure 7), one question is obligated: do soft soils and rocks, when are excited by the same seismic force, have alike movements? On the other hand, keeping constant the soil properties (dividing the database in a subset of soft soils and a subset of rock deposits) and varying the seismic inputs (events), the RPs structures are exceptionally comparable (Figure 8) and the query is evident: do earthquake mechanism, distance (from epicenter to the site) and transmission pattern have significant impact on the way the materials vibrate?

Answering these questions using the large scale is a difficult task and requires the use of restricting assumptions in order to explain the behaviors and response trends. It is important to point out that the conventional time series analysis tools works on this scale.

Through a deep inspection of the RPs and using nonlinear concepts we can say that the ground structures (soft and stiff, homogeneous and heterogeneous deposits) when are affected by seismic forces, in a macro scale, evolve in a similar way. The time evolution of the ground accelerations exposes well defined white areas and cold bands (green/blue strips), hallmark in nonstationary systems. The combination of

Table 3. Database seismic events.

Date (day/month/year)	LAT	LONG	Magnitude (max)	Focal Depth (km)
9/19/1985	18.081	102.942	Ms = 8.1	15
9/19/1985	18.024	103.057	Mb = 6.2	20
5/11/1990	17.046	100.84	Mc = 5.3	12
10/24/1993	16.54	100.84	Ms = 6.6	19
9/14/1995	16.31	98.88	Mc = 7.3	22
2/25/1996	15.83	98.25	Ms = 6.9	3
1/11/1997	17.91	103.04	Ms = 6.9	16
6/21/1999	17.99	101.72	Mb = 6.0	54
9/30/1999	15.95	97.03	Ms = 7.5	16

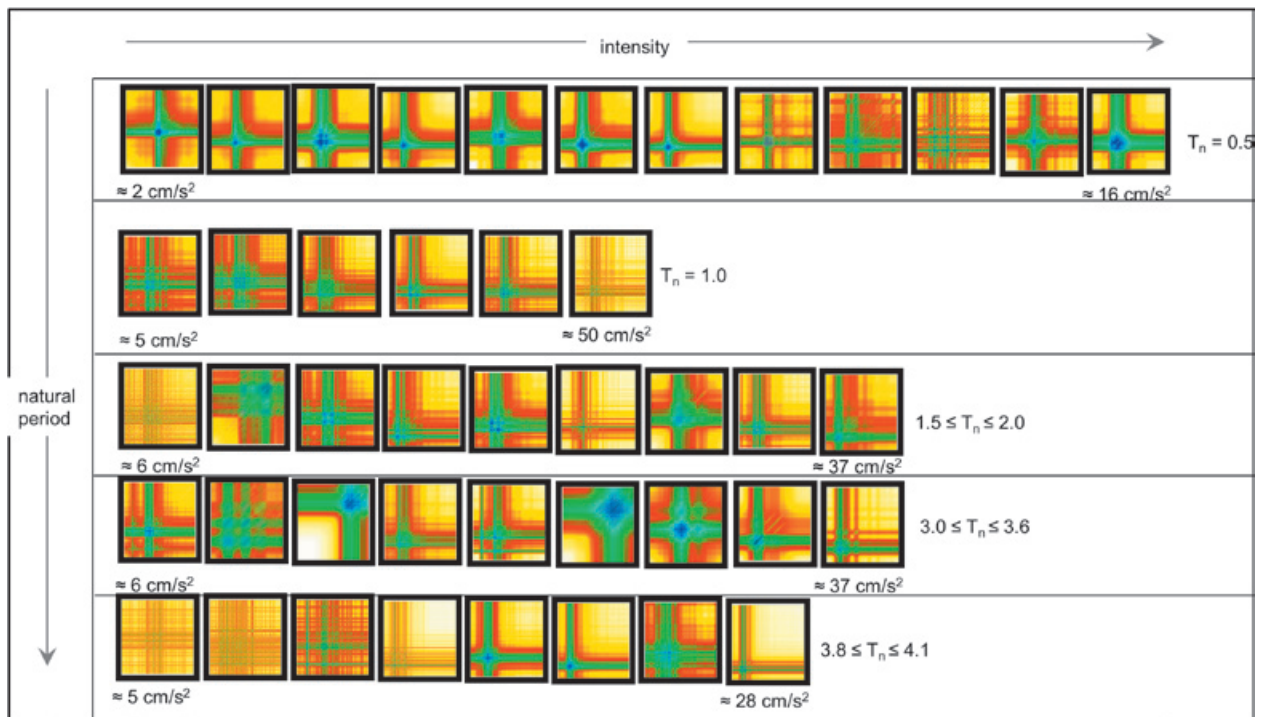


Figure 6. Some examples of RPs, different soils conditions and input seismic intensity.

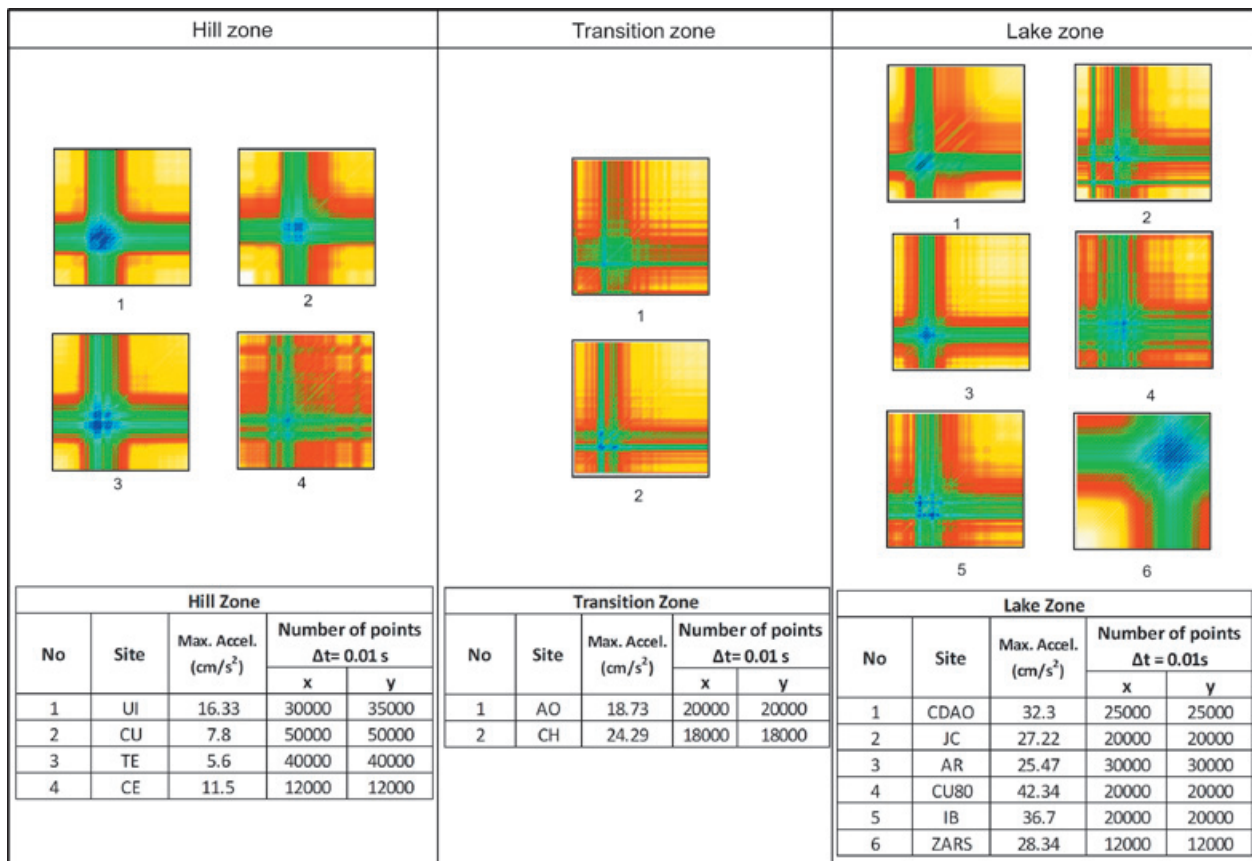


Figure 7. Examples of RPs from an event (30/09/99) on different geotechnical zones.

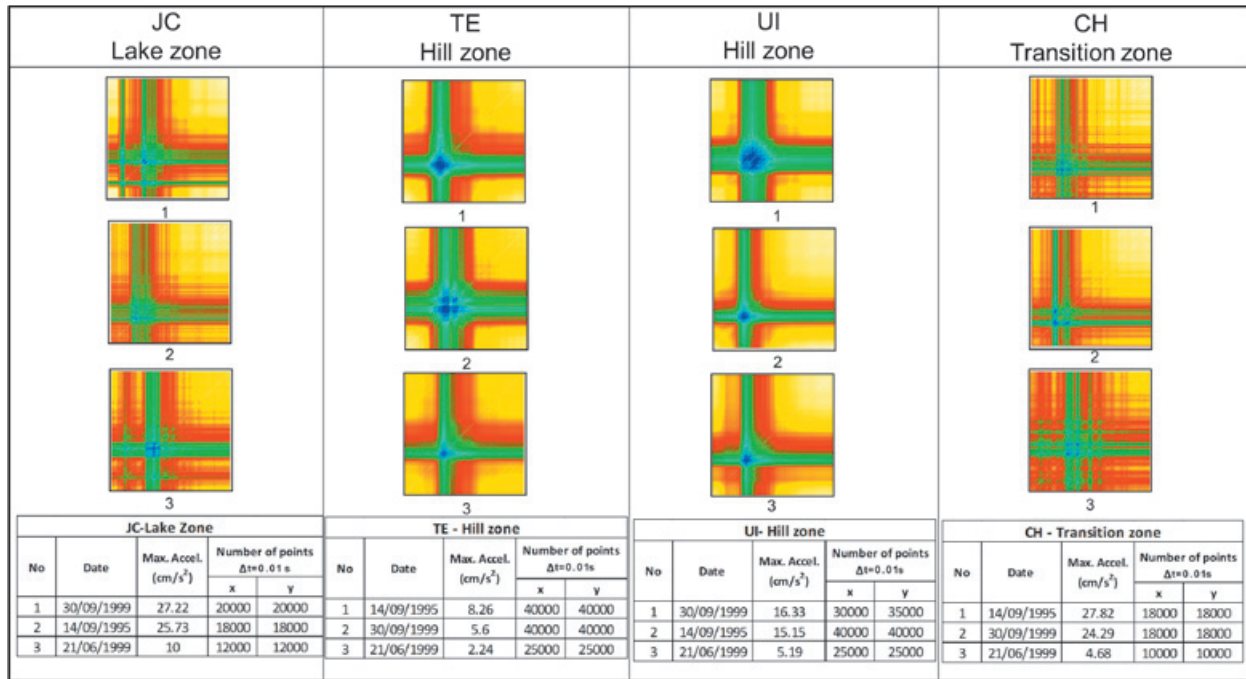


Figure 8. Examples of RPs calculated for each site varying input conditions (event).

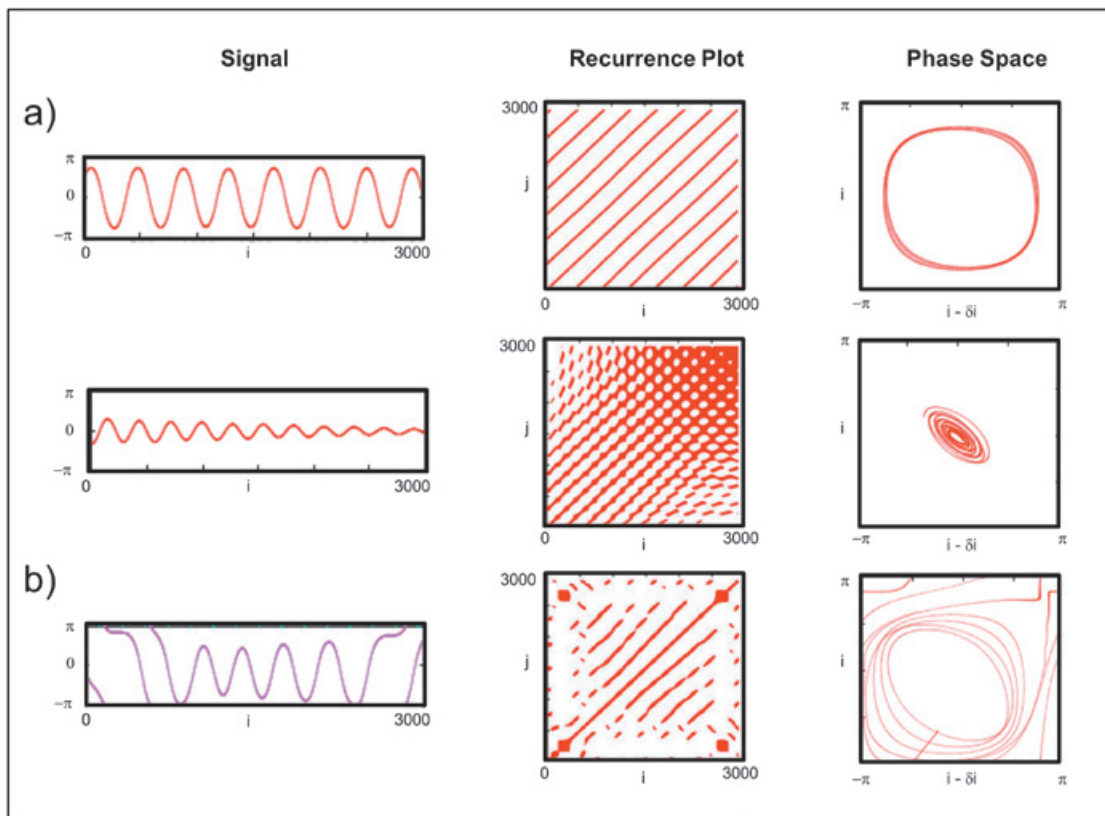


Figure 9. Pendulum behavior.

vertical and horizontal strips forms rectangular clusters where the maximum accelerations are located. Because of the abrupt changes between the beginning, the intense and the final part of the movements, a ground motion can be defined as an event that contain extreme sub-events (maximum accelerations) where the ground conditions are anomalous for some seconds to then vanish until the movement finishes. The number of clusters that appears in the RPs is the recurrence of the sub-events. The study of vertical RP structures makes the identification of trapping time (seconds that soil and rocks are being truly perturbed) possible.

To better understand the complexity of the ground motions, compare the RPs calculated from seismic time series with those from a pendulum's oscillation and damped vibration (low drive frequencies) depicted in Figure 9a. The ground response is very far from the deterministic behavior of this apparently simple device. See the RP in Figure 9b, the drive frequency is raised and the attractor undergoes a series of bifurcations (the pendulum is oscillating in a chaotic manner) but even in this regime the pendulum's RP manifests as seemingly structured with almost-periodic patterns. None of the RPs of accelerograms can be related with the patterns of the pendulum's attractors. The underlying process in seismic ground motions seems much more complex and it cannot be directly labeled as "deterministic", "chaotic" or "random".

The RPs-vertical structures displayed by the layered natural materials should be related with intermittence. In dynamical systems the intermittence is the alteration of phases of seemingly periodic systems. The apparent periodic phases of the ground behavior are not quite, but only nearly periodic. Thus, rather than a truly-periodic series of values, the data are apparently periodic but where the chaotic nature of the system becomes apparent after certain ground acceleration is reached. It is very important to point out that intermittence is more patent during large earthquakes, and a probably reason, which looks a paradox, is that the energy released from the source is not permanently continuous on time, there are relax intervals in between without important seismic wave arrivals from the source. Therefore the intermittence in accelerograms could be considered as a random sequence of episodes of seismic wave arrivals and episodes of free soil vibrations.

In a modeling scenario where the system was composed of many kilometers of crust (the outermost layer of the earth) from the source of seismic activity to the station where the measurement instrument registers the acceleration of a point on the ground surface (Figure 10), soils and rocks can be classified as nonlinear devices because they become activated when their reaction potential crosses a certain threshold. The activity of large formations of geological ma-

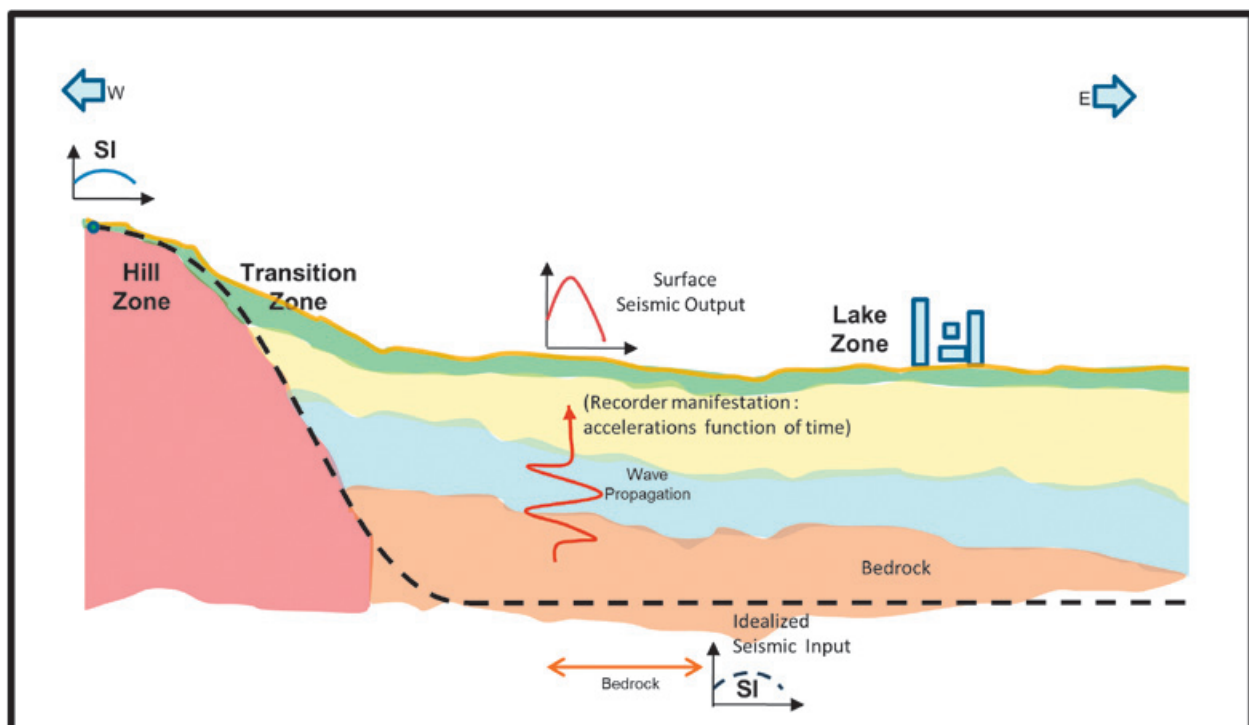


Figure 10. Transmission of seismic waves through the different geotechnical zones.

materials (soils and rocks) is macroscopically measurable in the accelerogram which results from a spatial integration of many reaction potentials (the environment interacting) but what is needed in the earthquake engineering is a description of the particular nonlinear devices (soil and rock deposits) through this macro manifestation, and this is the main advantage of RPs over the time-series analysis tools.

RPs-Texture (small scale)

Delay-coordinate embedding produces clean, easily analyzable pictures of the ground dynamics and the results suggest that the dynamical behavior of the soils/rocks is very high-dimensional (Table 3). This implies that the system is probably influenced by variables that can be hardly identified or that are beyond the limits of our current understanding (Strogatz, 2000). However, a proper definition of initial conditions permits characterizing the system evolutions and extracting meaningful (for engineering purposes) conclusions about the behavior of this complex natural structure.

Zooming into the RPs, the soil response can be studied from the clear and suggestive signatures in the clusters. The width of the vertical band indicates the time in which the *intense* state does not change or changes very slowly. The strong ground accelerations are trapped for some seconds (the cluster base) and because this extreme situation is not an isolated point (rare) the possibility that this alteration had been produced by noise is eliminated. In this *intense* time, periodic, chaotic or random

patterns can be recognized and the parameters range over which the system is stable and where the trajectories are divergent could be identified.

Harmonics in soft soils oscillations. Observe the Figure 11. These clusters in the third column were obtained from accelerograms registered in soft soils deposits. These examples show diagonal oriented recurrent structures that can be related with the vibration of one degree of freedom 1D oscillator. Due to space restrictions only some examples are showed, but they are representative of the structures displayed for the whole soft-soils set.

Assuming that during *intermittence* soft soils behave as a 1D oscillator, the period of soil vibration during the semi-sinusoidal oscillation (in this investigation called T_{ss}) can be obtained from the distance between diagonals (Figure 12). For a same site, no important degradation is observed in T_{ss} , even when the records came from different intensity, frequency and duration input conditions. Beyond the scope of this work is the discussion about the impact of the differences between T_{ss} and T_n in the aseismic design, but no doubt exists that the T_{ss} values are more authentic than those obtained from spectral analyses and many important conclusions about nonlinearity and site effects must be re-evaluated using these findings.

Chaotic vibrations in stiff soils structures. The clusters in the first column of Figure 11 are far more complicated. The checkboard structures and the upward diagonal lines result from strings of vector patterns repeating themselves multiple

Table 4. Examples of time delays and embedding dimensions.

Site	14/09/1995		21/06/1999		30/09/1999	
	Delay	Dimension	Delay	Dimension	Delay	Dimension
SCT	100	10	60	26	80	53
CDAO	68	38	51	35	67	53
CU	59	9	30	58	91	39
TE07	97	44	43	40	100	41
UI	46	59	26	60	40	46
ZARS	29	56	32	51	34	51
AO	45	1	12	18	31	20
CE	52	10	17	21	44	19
CH	24	20	11	22	25	24
CU8	/	/	4	26	32	23
GC	38	22	12	22	12	22
IB	34	21	13	1	47	24
JC	41	22	12	23	37	24

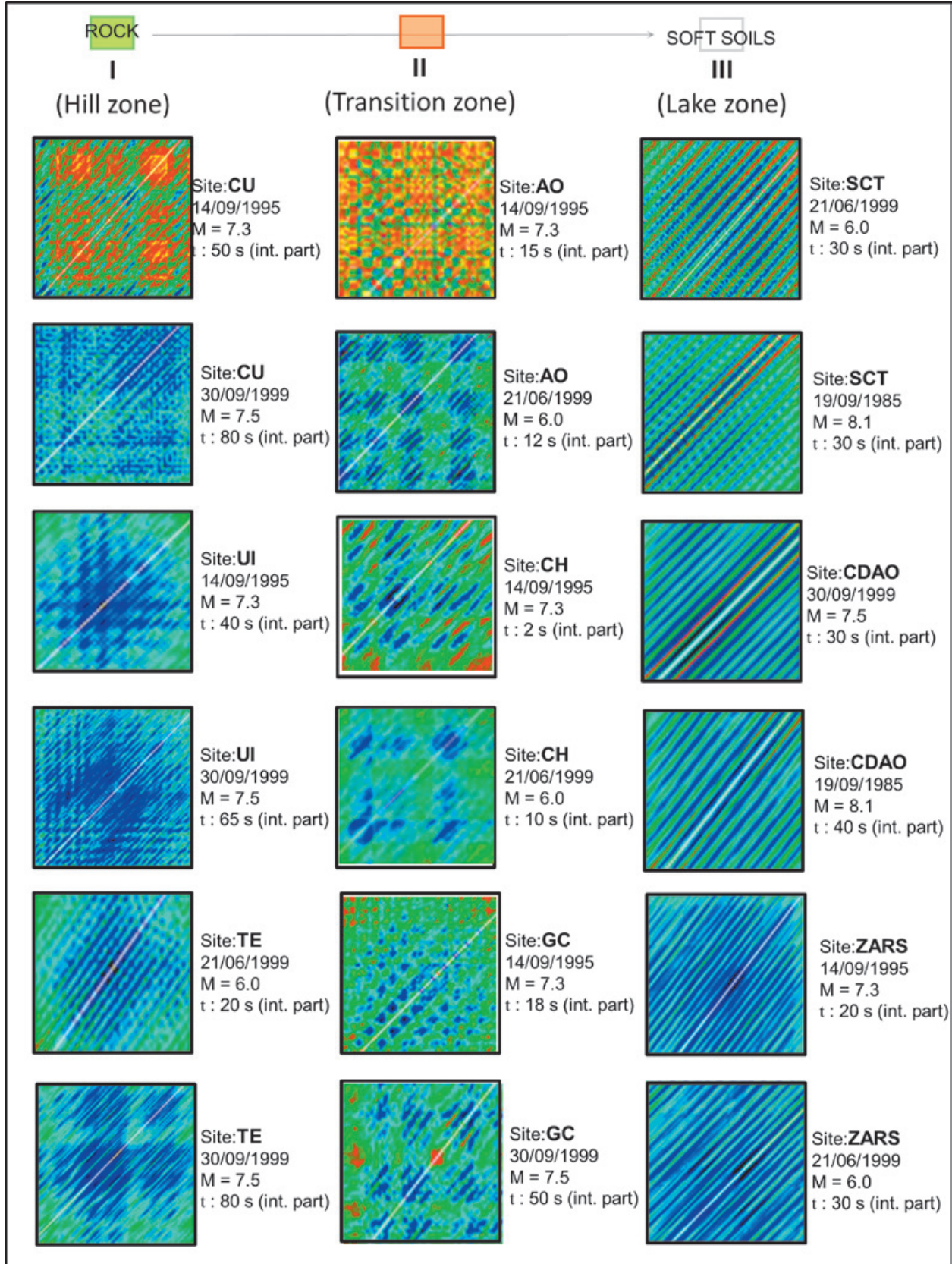


Figure 11. RPs Clusters, some examples of periodic and chaotic patterns.

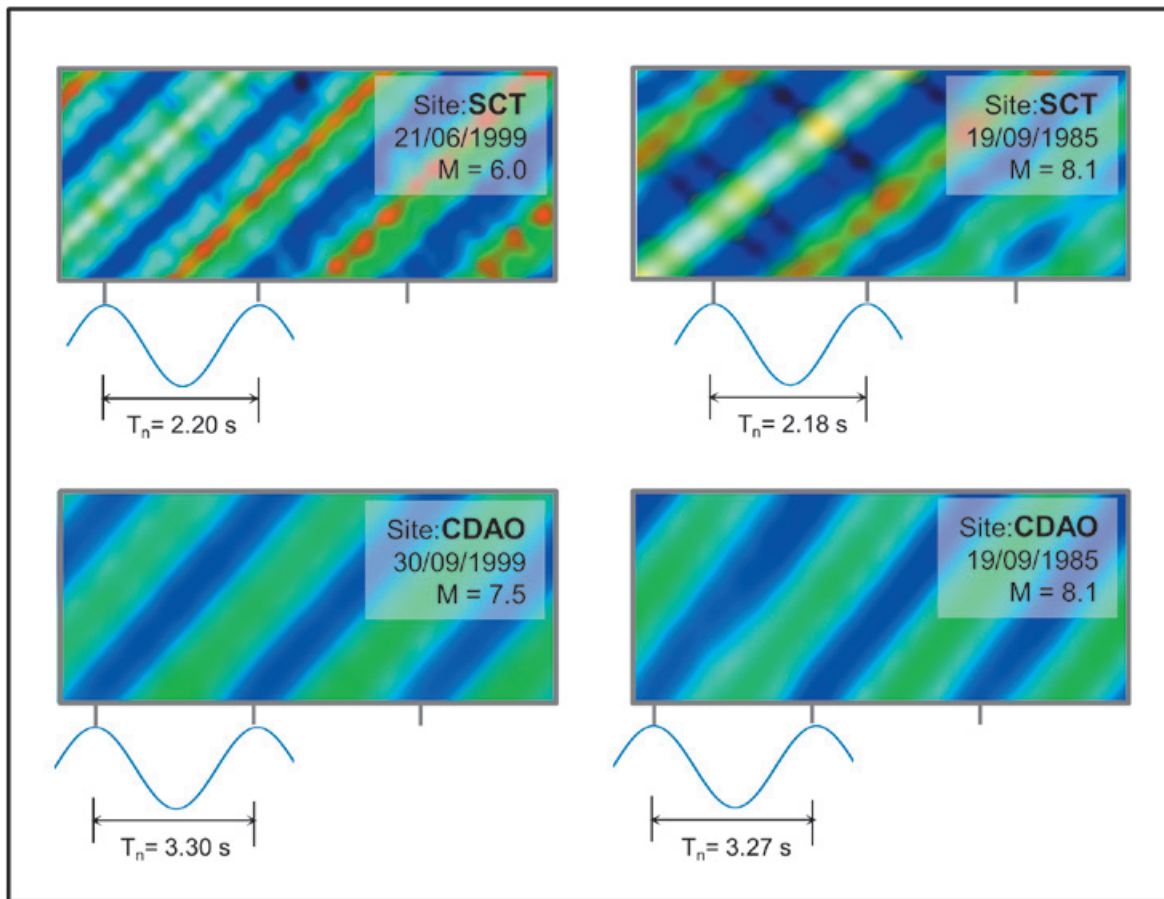


Figure 12. Period of sinusoidal oscillations for SCTan CDAO sites.

times down the dynamics. This type of recurrent structure indicates that the dynamics is visiting the same region of an attractor at different times; therefore, the presence of diagonal lines indicates that deterministic rules are present in the dynamics. The set of lines parallel to the main diagonal is the signature of determinism, however, it is not so clear as in soft-soils (e.g., the size of the lines being relatively short among a field of scattered recurrent points), i.e., the RPs contain subtle patterns not easily ascertained by visual inspection.

Although the blocklike structures resembling to what might be expected from a periodic signal, the rock-like materials exhibit a complex recurrent behavior with irregular cyclicities that qualifies them as dynamical systems and their behavior as typical for nonlinear or chaotic systems. This means that the deposits in Hill zone are highly sensitive to initial conditions, e.g. small differences in directivity, fault mechanism or distance, yield widely diverging outcomes.

As in many natural systems, the geological materials constitute systems that can be called

deterministic, meaning that their future behavior is fully determined by their initial conditions, with no random elements involved. The deterministic nature of rock (stiff materials) systems does not make them predictable. The rock-like deposits behavior can be described as deterministic chaos, or simply chaos.

Random signature in Transition zone. The clusters from sites, whose stratigraphy is erratic or not clearly defined, are distributed in a homogeneous random pattern, signifying that the random variable (accelerations) lacks of deterministic structures (see second column in Figure 11).

It seems that the location of the seismic source has not a strong influence on the characteristic of the RPs-clusters. From these observations we can conclude that seismic soil response is controlled by the dynamics of the fault that governs the time episodes of energy release, but the magnitude, the epicentral distance and the focal depth are not parameters that can fully categorize the random behaviors and *Transition* topologies in the RPs.

Conclusions

Based on the findings of this study, recorded accelerograms on soils and rocks should be considered as a sequence of episodes of seismic wave arrivals alternated with free soil vibrations episodes, behavior related with *intermittence*.

If we associate the clusters size with the concept of *effective acceleration*, the RPs can help to determine which level of acceleration is most closely related to structural response and to damage potential of an earthquake and which is its duration. The different durations are consequence, following with the assumption of *intermittence*, of the arrival of seismic waves at the end of the earthquake that excite soil/rock layers and which are attenuated (or amplified) depending of the periods and corresponding damping materials. It has been noticed, from the analyzed cases (different fault mechanisms, epicentral distances and magnitudes), that there are no significant differences between soil and rock time evolutions (macroscale). The study of the alteration of phases in RPs drives to the conclusion that soils and rocks deposits responses can be characterized only in the intense part of the time series. Soft soils deposits progress from quasi-periodic to periodic oscillations as the amplitude of the seismic responses exceeds certain acceleration thresholds. RPs of stiff materials, in general, display more complicated structures but they resemble chaotic movements for the universe of initial conditions analyzed. Despite being chaotic, the trajectory are actually quite organized, contrary to the RPs from erratic stratigraphies (Transition zone) whose are very close to being completely random.

The inconsistency between soil amplification theories and accelerographic measurements for large earthquakes could be re-interpreted through Chaos theory: Geological materials are systems that evolve in a similar way, so the amplification ratios should not be studied in the macro scale (even in the frequency domain). The deposits studied can be linked to certain determinism but they are very sensitive to initial conditions. The slightest change in initial conditions (stiffness material and intensity of the seismic waves arrivals, between the most important) or noise may cause the system to enter a very different trajectory.

This investigation permits to conclude that due to the inherent nonlinearities, the linear analysis techniques either fail or become meaningless to describe seismic responses and the spectral relations derived from these preprocessing techniques do not produce meaningful results.

Even if nowadays the consideration of non-linear seismic attributes is not necessary, it is undeniable that it will be needed in the future.

The future will see more multidimensional attributes with geotechnical, geological and seismological significance and a greater reliance on multi-attribute analysis. These trends are leading to automatic pattern recognition techniques for geoseismic analysis, able to rapidly characterize large volumes of data, or retrieve subtle details hidden in the data. Our aim is to propose a robust qualitative/quantitative method capable to identify and to characterize the seismic time series to be exploited in analysis and design procedures. Like search engines help you locate information on the worldwide web, the nonlinear tools built in your data viewer would locate features in your seismic records, as a "seismic search engine".

Bibliography

- Abarbanel H.D., 1995, Analysis of Observed Chaotic Data. 1st ed., *Springer-Verlag*, New York.
- Afraimovich V., Chazottes J.R., Saussol B. , 2003, Pointwise dimensions for Poincaré recurrences associated with maps and special flows, *Discrete Conti. Dynam. Syst. A* 9 (2) 263–280.
- Afraimovich V., 1997, Pesin's dimension for Poincaré recurrences, *Chaos* 7 (1) 12–20.
- Broomhead D.S. and King G.P., 1986, On the Qualitative Analysis of Experimental Dynamical Systems in `Nonlinear Phenomena and Chaos` ed. S. Sarkar, Adam Hilger: Bristol 113 – 144
- Brown A. R. , 1996, Seismic attributes and their classification, *The Leading Edge*, 15, 1090.
- Cao L., 1997, Practical method for determining the minimum embedding dimension of a scalar time series, *Physica D*, 110, 1–2, 43–50.
- Chen Q., Sidney S., 1997, Seismic attribute technology for reservoir forecasting and monitoring, *The Leading Edge*, 16, 5, 447–448.
- Chopra S., Marfurt K. J., 2005, Seismic attributes: A historical perspective, *Geophysics*, 70, 5, 3S0–28S0.
- Ding M., Grebogi C., Ott E. , Sauer T., Yorke J. A., 1993, Plateau onset for correlation dimension: When does it occur?, *Phys. Rev. Lett.* 70, 3872–3875.

- Eastwood J. , 2002, The attribute explosion, *The Leading Edge*, 21, 994.
- Eckmann J.P., Kamphorst S.O., Ruelle D., 1987, Recurrence plots of dynamical systems, *Europhys. Lett.* 5, 973–977.
- Eckmann J.P., Oliffson Kamphorst S., Ruelle D., and Ciliberto S., 1986, Lyapunov exponents from a time series, *Phys. Rev. A* 34, 4971.
- Eckmann J.P., Ruelle D. , 1992, Fundamental limitations for estimating dimensions and Lyapunov exponents in dynamical systems, *Physica D*, 56, 185-187.
- Fraser A. M. and Swinney H. L., 1986, Independent coordinates for strange attractors from mutual information, *Phys. Rev. A* 33 1134-1140.
- Fayyad U., Piatetsky-Shapiro G., Smyth P., Uthurusamy R., 1996, *Advances in Knowledge Discovery and Data Mining*, 1st ed., MIT Press.
- Horai S., Yamada T. , Aihara K., 2002, Determinism analysis with isodirectional recurrence plots, *IEEE Trans. Inst. Electric. Eng. Jpn. C* 122 (1) 141–147.
- Kantz H., Schreiber T., 1997, *Nonlinear Time Series Analysis*, Cambridge University Press, Cambridge.
- Lorenz E.N., 1963, Deterministic nonperiodic flow, *J. Atmos. Sci.* 20, 130–141.
- March T.K., Chapman S.C., Dendy R.O., 2005, Recurrence plot statistics and the effect of embedding, *Physica D* 200,1–2, 171–184.
- Marwan N., 2003, Encounters with neighbours—current developments of concepts based on recurrence plots and their applications, Ph.D. Thesis, University of Potsdam.
- Marwan N., M.H. Trauth, M. Vuille, J. Kurths, 2003, Comparing modern and Pleistocene ENSO-like influences in NW Argentina using nonlinear time series analysis methods, *Clim. Dynam.* 21 (3–4) 317–326.
- Marwan N., Wessel N., Meyerfeldt U., Schirdewan A., Kurths J., 2002, Recurrence plot based measures of complexity and its application to heart rate variability data, *Phys. Rev. E* 66 (2).
- Packard N.H., Crutchfield J.P., Farmer J.D., Shaw R.S., 1980, Geometry from a Time Series, *Phys. Rev. Lett.*, 45- 9, 712-716.
- Parlitz U., 1992, Identification of true and spurious Lyapunov exponents from time series *Int. J. Bifurcat. Chaos*, 2, 155–165.
- Sauer T., Yorke J.A., Casdagli M., 1991, Embedology, *J. Stat. Phys.* 65(3/4), 579-616.
- Saussol B., Wu J., 2003, Recurrence spectrum in smooth dynamical systems, *Nonlinearity* 16-6, 1991–2001.
- Sheriff R. E., 1991, *Encyclopedic dictionary of exploration geophysics*, 3rd ed., SEG.
- Strogatz S.H., 2000, *Nonlinear dynamics and chaos*, Perseus Publishing, Cambridge, S.H.
- Takens F. , 1981, Detecting strange attractors in turbulence, in: D. Rand, L.-S.Young (Eds.), *Dynamical Systems and Turbulence*, Lecture Notes in Mathematics, 898, Springer, Berlin, pp. 366–381.
- Vastano J.A. , Kostelich E.J., 1986, Comparison of algorithms for determining Lyapunov exponents from experimental data, in *Dimensions and Entropies in Chaotic Systems*, Mayer-Kress G. eds, New York, Springer-Verlag, 100-107 pp.

Geostatistical modeling of clay spatial distribution in siliciclastic rock samples using the plurigaussian simulation method

Javier Méndez-Venegas* and Martín A. Díaz-Viera

Received: March 03, 2012; accepted: February 21, 2013; published on line: June 28, 2013

Resumen

Con el fin de implementar esquemas de recuperación secundaria y mejorada en formaciones terrígenas complejas como los depósitos turbidíticos, el conocimiento de la distribución espacial de los granos de lutitas es un elemento crucial para la predicción del flujo de fluidos. Debido a que la interacción de los granos de lutitas con el agua puede provocar que éstas modifiquen su tamaño y/o forma, lo que causaría taponamiento de los espacios porosos y consecuentemente impacto en el flujo. En el presente trabajo, se propone una metodología para la simulación estocástica de la distribución espacial de granos obtenida a partir de imágenes de microscopio electrónico de barrido de muestras de rocas siliciclásticas. El objetivo de la metodología es obtener modelos estocásticos que permitan investigar el comportamiento de los granos de lutitas bajo diferentes condiciones de interacción físico-químicas y regímenes de flujo, y que sirvan de referencia para obtener propiedades petrofísicas (porosidad y permeabilidad) efectivas a escala de núcleo. Para la simulación estocástica espacial de los granos se utiliza el método plurigaussiano, el cual se basa en el truncado de varias funciones aleatorias Gaussianas estándar, lo cual permite manejar de manera adecuada la proporción de cada categoría y las relaciones de dependencia espacial cuando se tiene más de dos categorías o clases de grano. Los resultados muestran que los medios porosos estocásticamente simulados utilizando el método plurigaussiano reproducen adecuadamente las proporciones, las estadísticas básicas y tamaños de las estructuras de los poros presentes en las imágenes de referencia estudiadas.

Palabras clave: Geoestadística, medios porosos, monogaussiano, plurigaussiano, distribución espacial, rocas siliciclásticas.

Abstract

In order to implement secondary and enhanced oil recovery processes in complex terrigenous formations as is usual in turbidite deposits, a precise knowledge of the spatial distribution of shale grains is a crucial element for the fluid flow prediction. The reason of this is that the interaction of water with shale grains can significantly modify their size and/or shape, which in turn would cause porous space sealing with the subsequent impact in the flow. In this work, a methodology for stochastic simulations of spatial grains distributions obtained from scanning electron microscopy images of siliciclastic rock samples is proposed. The aim of the methodology is to obtain stochastic models would let us investigate the shale grain behavior under various physico-chemical interactions and flux regimes, which in turn, will help us get effective petrophysical properties (porosity and permeability) at core scale. For stochastic spatial grains simulations a plurigaussian method is applied, which is based on the truncation of several standard Gaussian random functions. This approach is very flexible, since it allows to simultaneously manage the proportions of each grain category in a very general manner and to rigorously handle their spatial dependency relationships in the case of two or more grain categories. The obtained results show that the stochastically simulated porous media using the plurigaussian method adequately reproduces the proportions, basic statistics and sizes of the pore structures present in the studied reference images.

Key words: Geostatistics, porous media, monogaussian, plurigaussian, spatial distribution, siliciclastic rock.

J. Méndez-Venegas
Instituto de Geofísica
Universidad Nacional Autónoma de México
Del. Coyoacán 04510
México D.F.
*Corresponding author: lemendez84@yahoo.com.mx

M. A. Díaz-Viera
Programa de Recuperación de Yacimientos
Instituto Mexicano del Petróleo
Del. Gustavo A. Madero.

Introduction

The porous media characterization is a fundamental problem in areas of knowledge such as soil sciences, hydrogeology, oil reservoir, etc. Owing to the fact that the more precise knowledge one has about the porous media structure, the better the accuracy in predicting effective petrophysical properties such as porosity, permeability, capillary pressure and relative permeabilities.

In particular, in the oil industry understanding the petrophysical properties concerning the rock formation is a crucial element in reservoir management, since it allows us to accurately model the mechanisms that govern the recovery of hydrocarbons and consequently serve to propose and implement optimal secondary and enhanced recovery processes.

The aim in this work is to model the spatial grains distributions in rock samples from siliciclastic reservoir formations. As it is well known, the siliciclastic rocks are of sedimentary origin, usually formed in situ and were generated by erosion processes, transportation and deposition. Sedimentary rocks are formed by a packed grain structure that constitute the solid matrix and a pore system that is the space not occupied by the grains. The grains of the siliciclastic rocks are composed mainly of minerals such as quartz, clays, feldspars and other heavy minerals.

Usually the characterization of porous media is reduced to the study of just two categories (see section Stochastic Porous Media Reconstruction Methods), i.e. it is modeled as two phase media consisting only by rock matrix and pore space and ignoring the complex mineralogy distribution of grains that constitute the porous matrix.

Clay swelling occurs when water-base filtrates from drilling, completion, workover or simulation fluids enter the formation. Clay swelling can be caused by ion exchange or changes in water salinity. However, only clays that are directly contacted by the fluid moving in the rock will react. The nature of the reaction depends on the structure of the clays and their chemical state at the moment of contact. The most common swelling clays are smectite and smectite mixtures that create an almost impermeable barrier for fluid flow when they are located in the larger pores of a reservoir rock.

The clay swelling yields a direct impact in the reduction of pore space, and consequently in the porosity, but at the same time the spatial modification of porosity produces an alteration of the rock permeability. This is considered as a type of formation damage in which absolute rock permeability is reduced because of the alteration of clay equilibrium.

The absolute permeability is a fundamental petrophysical property of rocks and it is defined as the ability to flow or transmit fluids through a rock, conducted when a single fluid, or phase, is present in the rock. The permeability can be related with the pore space connectivity.

In this paper a novel and general methodology for stochastically reconstruction of mineralogy distribution applying the plurigaussian simulation method which far as we know it is first introduced to simulate the spatial grain distribution. In particular, the proposed methodology is applied to the clay spatial distribution in rock samples from heterogeneous siliciclastic formations to evaluate the variation of their petrophysical properties, such as porosity and permeability during a swelling process.

A brief historical review of stochastic reconstruction methodologies for porous media in the first section of this paper is presented. After that, the data and methodology used for the reconstruction of the mineralogy of the porous medium are described. Subsequently, details of the geostatistical analysis of the data are shown. The results of the stochastic simulations are discussed in the following section and finally the conclusion and further work are given in last section.

Stochastic porous media reconstruction methods: a brief review

The stochastic approach has been used for porous media reconstruction at pore scale in the past 20 years. The stochastic models that have been developed are basically geostatistics, which model the spatial dependency structure present in the rock structure. In particular, to represent porous media from sedimentary rock samples has been modeled the spatial distribution of grains (rock matrix) and pores (pore space). It is possible to generate a 3D model of the pore space by statistical information produced by analysis of 2D thin sections.

In their works, Adler *et al.* (1990) and Adler and Thovert (1998) applied the truncated Gaussian or monogaussian simulation method (Xu and Journel, 1993; Galli *et al.*, 1994) for a porous media reconstruction from image analysis of 2D thin sections of Fontainebleau sandstone. In the truncated Gaussian method a Gaussian random function is generated and thresholded to retrieve the binary phases (pore space and rock matrix) with the correct porosity and correlation function. This method can also be extended to include more phases, such as clay.

A greater flexibility can be achieved by using the method of simulated annealing (Yeong and

Torquato 1998a,b; Manwart *et al.* 2000; Talukdar and Torsaeter 2002; Capek *et al.* 2008, Politis *et al.* 2008). Rather than being restricted to one- and two-point correlation functions, the objective function used can be made to match additional quantities such as multi-point correlation functions, lineal-path function or pore size distribution function. Incorporating more higher-order information into the objective function, such as the local percolation probability, would most likely improve the reconstruction further, but that would also increase the computational cost of the method significantly. Although this reconstruction procedure has been more successful, the resulting images do not always capture the connectivity of pore space.

Another reconstruction methods preserving the pore size distribution, is the superposed spheres. Dos Santos *et al.* (2002) developed the method for reconstruct a medium upholding this statistic. The method calculates the number of spheres in order to reconstruct a given porous media, saving it is the porosity. Each sphere superposes neighboring spheres according to a user defined parameter. This method presents good results for connectivity, although it does not preserves the autocorrelation function.

Thovert *et al.* (2001) and Hilfer and Manswart (2001 and 2002) introduced a method that is a hybrid between the statistical and object-based methods. They verified their method using a 3D Fontainebleau sample and reported that the local percolation probability was found to be significantly better in comparison with the traditional simulated annealing. Here, local percolation probability is applied to characterize the porous media topology as a measure of connectivity (Vogel, 2002).

In their work, Casar-González and Suro-Pérez (2000, 2001 and 2003) applied the indicator simulation method and a hybrid between the multiple-point statistics and simulated annealing method. They verified their method using a carbonate rocks and reported that the results are statistically equivalent to the real porous media, i. e. both approaches reproduce correctly the histogram and the spatial variability.

Strebelle (2002) suggested a statistical algorithm in which the multiple-point statistics were inferred from exhaustive 2D training images of equivalent reservoir structures and then used to reconstruct the reservoir, adhering to any conditioning data. This method was applied successfully to both fluvial and more complex patterned reservoirs. The ability to reproduce any pattern makes this method highly attractive for reconstructing complex porous media like carbonates.

Okabe and Blunt (2005 and 2007) have used this algorithm to reconstruct a 3D Fontainebleau sandstone from a 2D training image. Although the granular structure is not as well reproduced as in object-based methods, the local percolation probability is significantly better reproduced than that achieved by other methods such as Gaussian field techniques.

In previous works about porous media reconstruction, those have been modeled as two phase media consisting only by rock matrix and pore space and ignoring the complex mineralogy distribution of grains that constitute the porous matrix. This approach possesses the disadvantage that it does not consider the mineralogical composition of the rock and consequently, these models cannot account for the chemical interaction of fluids with minerals present in the rock and even more they do not consider the dynamic alteration of petrophysical properties resulting of diagenetic processes.

In this paper we are proposing to apply the plurigaussian simulation method to simulate the spatial distribution of the mineralogical heterogeneity in the porous matrix. The choice of plurigaussian method is based on its flexibility to represent complex spatial dependencies of multiple phases. To our knowledge this method has not been applied before for this purpose. In particular, here we present the application to a case study for the distribution of clays in siliciclastic rocks. Such a model could be used to quantify the dynamic modification of the petrophysical properties of siliciclastic rocks when occur the swelling phenomenon of clays.

Data and methods

The main goals of this work are to model the geometry of the pore space by simulating grain spatial distribution from images taken in siliciclastic rock samples, as well as, the spatial distribution of clays present in the solid matrix, using spatial stochastic simulations. The procedure is applied in two successive stages. First are simulated two categories: matrix and the pore space, and subsequently is made the simulation of the mineralogy of interest.

For simulating the clay spatial distribution, we can consider two cases: the first case (case 1) is made under the assumption that clay present in the rock are allogenic, i.e., clay fragments are originally formed in other location but were transported and deposited in the pore space, therefore, clays occupy a portion of the pore space; while in the second case (case 2), clay is considered authigenic, which means that the clay was formed together with the rock and it is part of the rock matrix composition.

The images used as input data are obtained by scanning electron microscopy in backscatter electron mode. The sample preparation is similar to the one used for preparation of thin sections using light microscopy and consists of the following: the sample was impregnated with epoxy resin and polished on one side once the epoxy has hardened.

The process of extracting pores, clays and rock matrix from images of scanning electron microscopy is simpler, compared to the process for thin sections. A color thin section image contains three gray-level images in RGB space, while in scanning electron microscopy only one gray-level image is involved. In images of scanning electron microscopy, the rock matrix can be subdivided into ranges associated with different minerals using the atomic density contrast. For example, the pore space is associated with the darker gray tone because of the fact that the epoxy resin possesses smaller atomic density compared with the minerals contained in the matrix.

In the porous-media stochastic model are considered three categories: pore space, clay grains and rock matrix, where in the rock matrix category are included the rest of (no clay) mineralogies. A segmentation procedure developed by Fens (2000) enables automatic extraction of pore, clay and rock matrix categories. This procedure is based on fitting three Gaussian functions to the gray-level histogram. In images of scanning electron microscopy the gray-values represent atomic density. Prior to processing and analyzing, these gray-values have to be calibrated which takes place using a set of standards with known gray-values. This calibration is essential to make quantitative use of the data provided by the analysis. The calibration standards used here are taken from Fens (2000) and consisted of artificial reservoir rock samples that contain only quartz and epoxy.

The total gray-value range in images of scanning electron microscopy can be divided in sub-ranges. In Figure 1 the color bar below the histogram shows the division in these sub-ranges representing pores, clays, quartz, feldspar and the heavy minerals. Two-level thresholding is used to extract the pixels in each range of gray-values. Thresholding is an image-to-image transformation, in this case a transformation from a gray-value image to a binary image (Fens, 2000).

In the case study presented, we used an image of a sandstone block obtained with the procedure described above (Figure 2), which was taken of the PhD thesis of T. Fens (Fens, 2000). The image size is 2 x 2 mm with a resolution of 256 x 256 pixels,

with a pixel size equal to 0.0078 mm. In the image of Figure 2 the same five categories are clearly visible: quartz, clays, feldspars, heavy minerals and pore space. In what follows this image will be referred as the reference image.

According to the objectives of this work, the reference image was initially segmented in three categories: pore space, clays and rock matrix; the last one grouped in single category: quartz, heavy minerals and feldspars (Figure 3). The resulting image has the same size as the reference image and will help us compare the simulations obtained in the latter stages of the modeling procedure. For the case 1, the reference image is segmented in two categories: black and white; where in black is represented rock matrix and in white are combined pore space and clays (Figure 4). For the case 2 is, it is applied the same procedure, but now in black are grouped rock matrix and clays while pore space is represented in white (Figure 5).

Additionally, the Euler characteristic is calculated to compare the connectivity presented in reference image versus simulations obtained. The Euler characteristic gives positive values for poorly connected structures and negative values for more connected structures (Vogel, 2002; Wu *et al.* 2006).

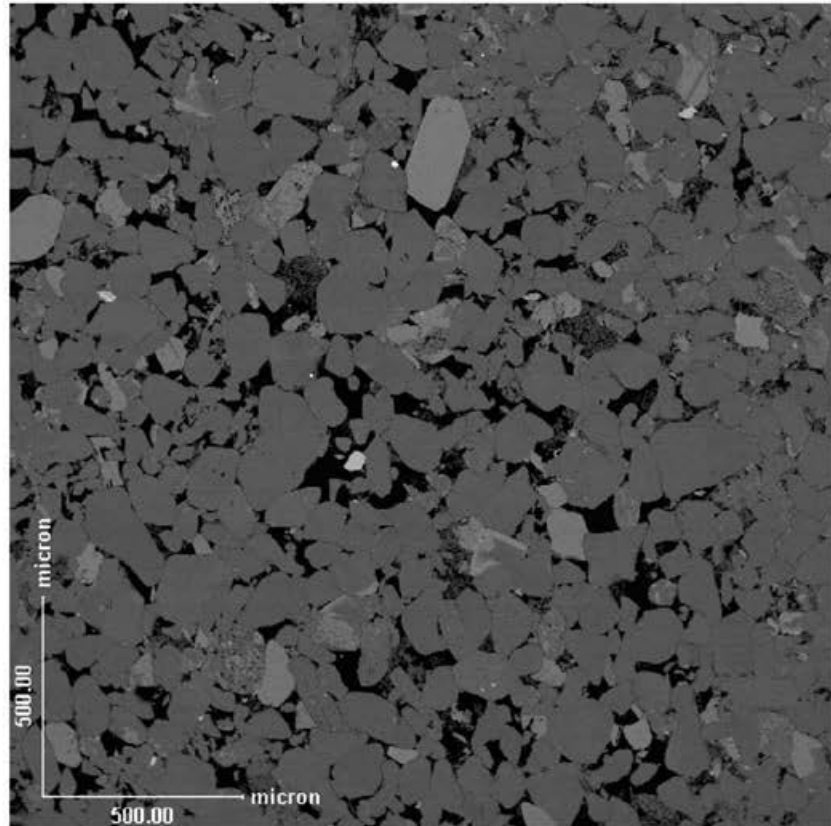
The calculation the Euler characteristic is a function of pore size (diameter), complete methodology for calculation of this characteristic is presented in Vogel (2002).

The exploratory analysis of the data is an essential phase in any practical statistical analysis. In general, it is a combination of statistical and graphical techniques that allows verifying the hypothesis that has to fulfill data sample to apply any statistical procedure. In a geostatistical analysis, it is required that the data sample fulfills the following:

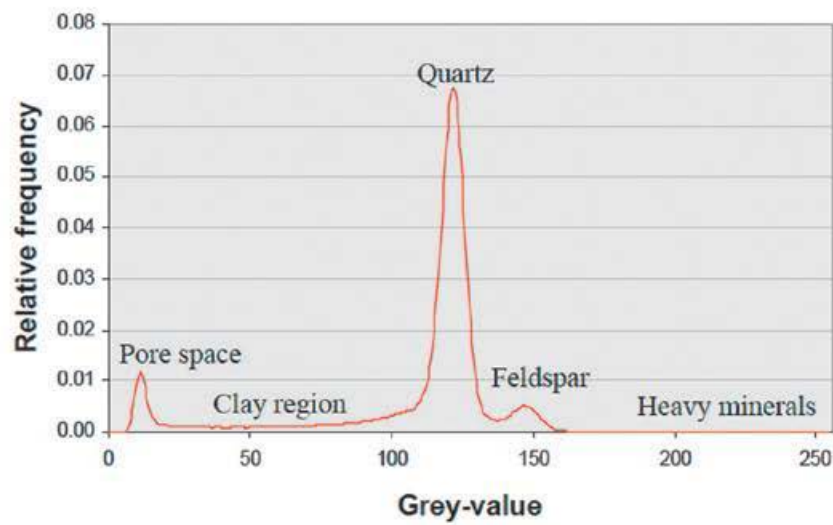
- a) Data sample is normally distributed or at least symmetrical.
- b) Data sample must not show a significant trend; at least the intrinsic hypothesis has to be satisfied.
- c) There are not distributional neither spatial outliers.

A series of techniques that are recommended to verify the above assumptions are listed below

1. Basic statistics (mean, median, variance, quartiles, skewness).
2. Graphics (histogram, box plot, scatter plot, QQ plot).



Grey-value histogram



Ranges for thresholding



Figure 1. Image of a shaly sandstone (top) and the gray-value histogram calculated from an image (bottom) (Fens, 2000).

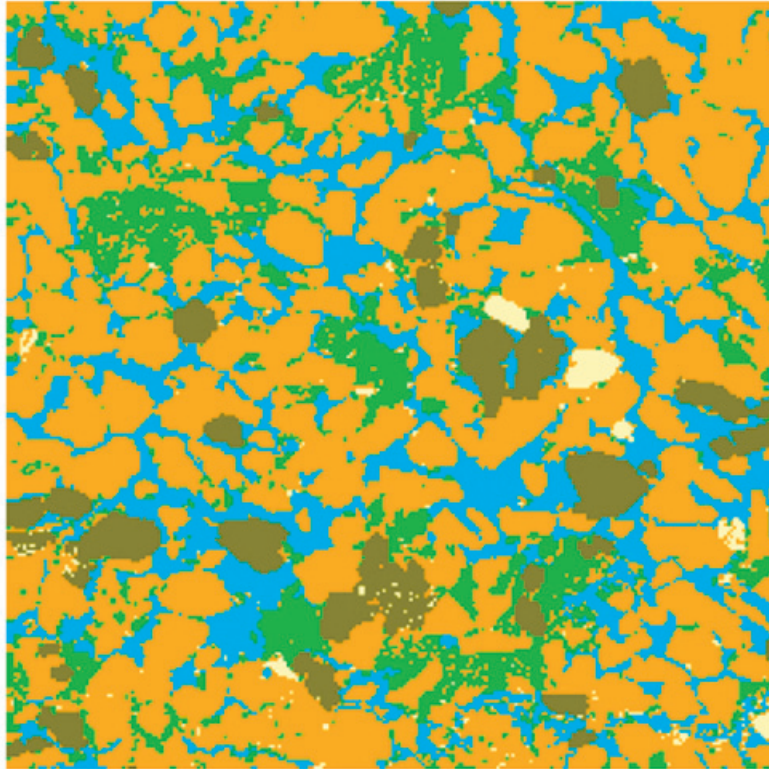


Figure 2. Reference image: quartz (orange), clays (green), pore space (blue), feldspars (dark green) and heavy minerals (white) (Fens, 2000).

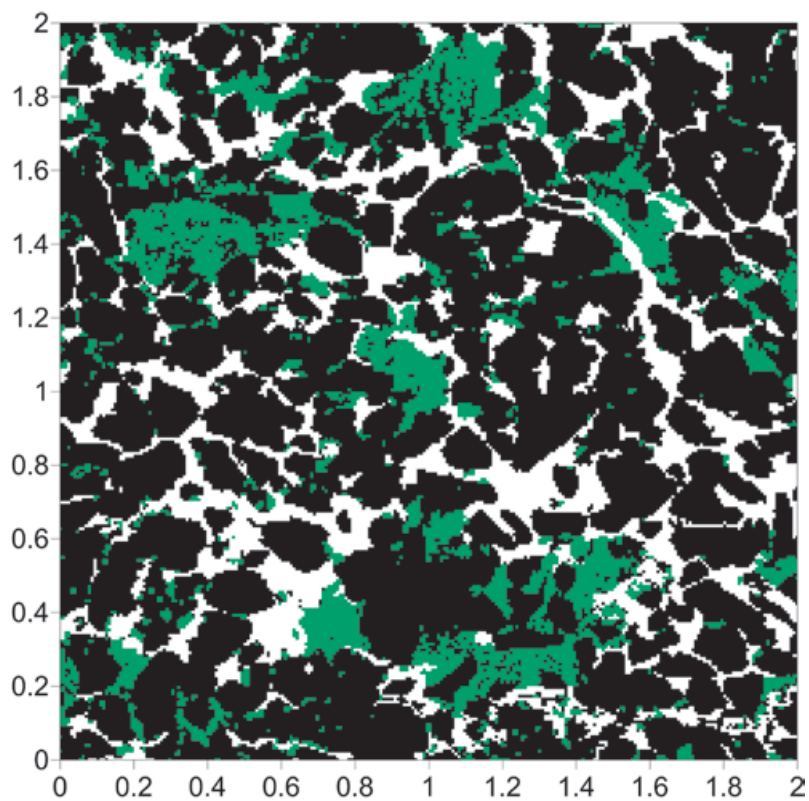


Figure 3. Segmentation of the Figure 2, rock (black), clays (green) and pore space (white).

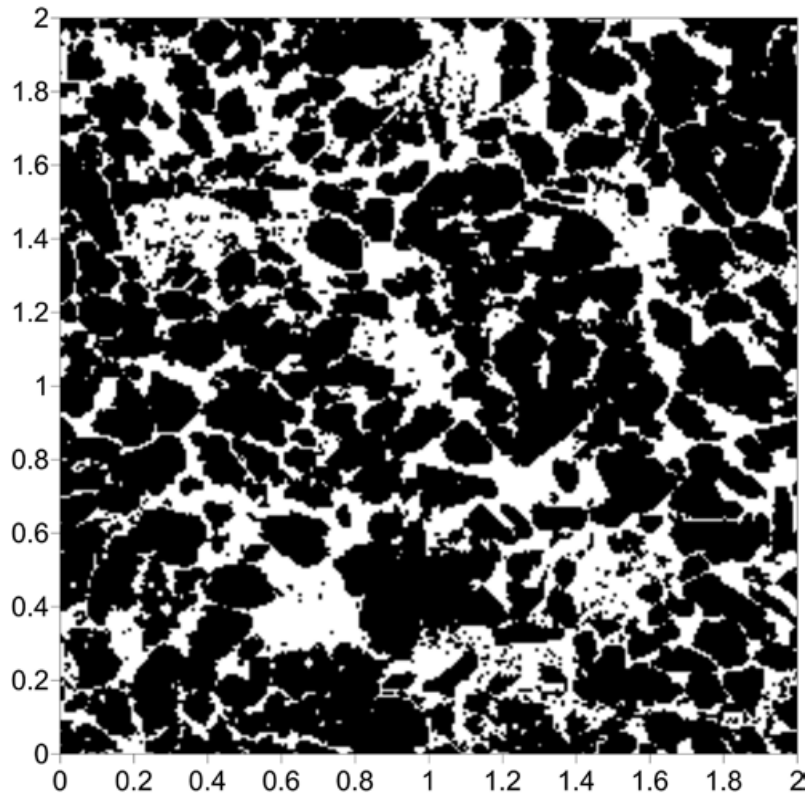


Figure 4. Binary representation of the Figure 3, in black rock matrix and in white pore space and clays.

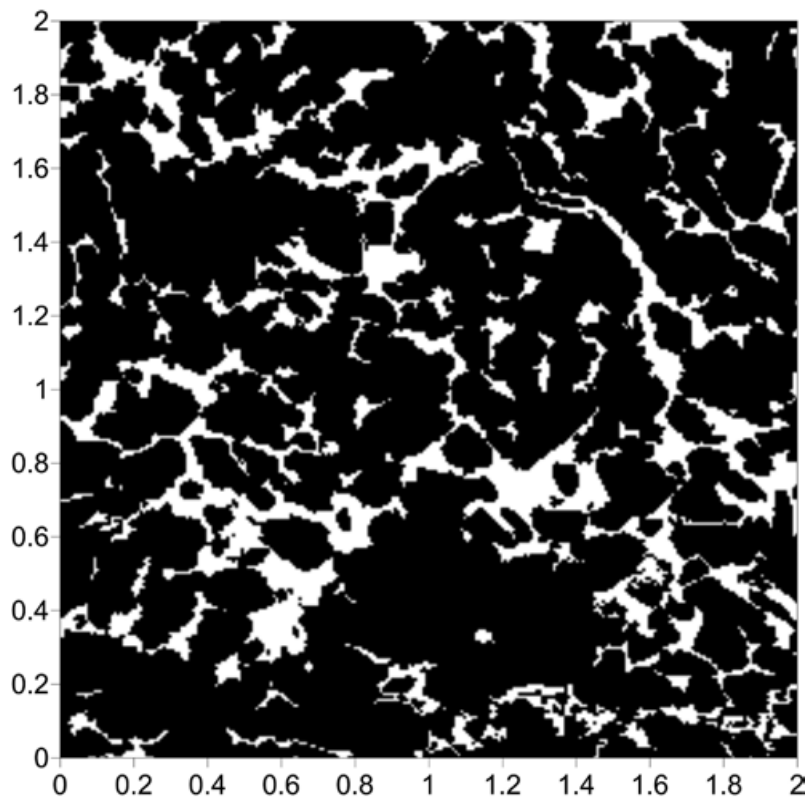


Figure 5. Binary representation of the Figure 3, in black rock matrix and clays and in white pore space.

Once the results of the application of these techniques are analyzed decisions can be taken to modify the data (applying transformations, excluding observations, etc.) to meet the main assumptions as far as possible or simply to take into account those assumptions that are not satisfied when the analysis is done (Armstrong and Delfiner, 1980).

The variographic or structural analysis is the most important part of the geostatistical analysis. Its aim is to model the underlying spatial structure in the data sample. In accordance to the degree of stationarity existent the data analyzed, a variogram or a covariance function can be used to determine the structure of spatial dependence. In this paper we use the variogram because it is less restrictive from the point of view of the degree of stationarity. In summary, a variographic analysis consists of the estimation of the sample variogram and to finding the variogram model that better fits it.

The variogram function is defined as follows:

$$\begin{aligned} \gamma(\underline{h}) &= \frac{1}{2} \text{Var} \left(Z(\underline{x} + \underline{h}) - Z(\underline{x}) \right) \\ &= \frac{1}{2} E \left[\left(Z(\underline{x} + \underline{h}) - Z(\underline{x}) \right)^2 \right] \end{aligned} \quad (1)$$

The most common variogram estimator $\hat{\gamma}(\underline{h})$ is given by:

$$\hat{\gamma}(\underline{h}) = \frac{1}{2N(\underline{h})} \sum_{i=1}^{N(\underline{h})} \left[Z(\underline{x}_i + \underline{h}) - Z(\underline{x}_i) \right]^2 \quad (2)$$

where $N(\underline{h})$ is the number of observations pairs ($Z(\underline{x})$ and $Z(\underline{x}+\underline{h})$) and $h = \|\underline{h}\|$ is the separation distance between them.

Geostatistical simulations consist in generating multiple realizations $Z_s(\underline{x})$ of a random function statistically equivalent, which means that each of the realizations has the same statistical properties that are attributed to the random function $Z(\underline{x})$. In practice we do not know with certainty the statistical properties of the random function $Z(\underline{x})$, therefore usually we only generate realizations that are at least statistical equivalent to the first and second-order moments present in the sample values of the random function $Z(\underline{x})$.

Stochastic simulation method

A random function Z is a family of random variables $Z(\underline{x})$ where \underline{x} belongs to \mathbb{R}^d or some subset of it. In

the one dimensional case, we prefer to speak of a stochastic process. In this work, the resulting segmented image can be viewed as a discrete or categorical random function. There are a large variety of simulation methods of categorical random functions, grouped into two families: the object models and the cells models (Chilès, 1999; Lantuejoul, 2002).

In object models each category is associated with a certain geometric shape (object) and are based on Poisson point processes, while in the cells models, a cell can take the value of one category and are based on the truncation of Gaussian random functions. Here we will use the second family of simulation methods to investigate the application.

The implementation of simulation of cells requires to characterize the discrete random function in terms of the spatial relationship of their categories, for which geostatistical analysis is done which consists of getting the proportions of occurrences of each category, the basic statistics and its variogram or the semivariance function, which is a dependence measure or spatial autocorrelation.

The proportions are calculated by dividing the sum of pixels of a given category between the total of pixels of the image, while the variogram is estimated by considering the value of the lag or interval equal to the size of the image pixel.

The proportions and the variogram obtained by categories are used as parameters in the spatial stochastic simulation method that is chosen.

Here, as a stochastic simulation method for simulating mineralogy distribution is applied the truncated plurigaussian simulation method (Galli *et al.*, 1994; Le Loc'h and Galli, 1997; Armstrong *et al.*, 2003). This method is a generalization of the truncated Gaussian simulation method, also known as monogaussian simulation method (Xu and Journel, 1993; Galli *et al.*, 1994). These methods are used to simulate categorical or discrete variables, such as geological facies. The principle of these methods consists on firstly to simulate one or several standard Gaussian random functions along the study domain and afterwards they are truncated following certain spatial relationship rules in order to produce a categorical variable.

The truncated Gaussian simulation method is based only one Gaussian random function and it is summarized in Figure 6. The image (top-left) represents the standard Gaussian random function with a Gaussian model, the image (top-right) shows the histogram of a standard Gaussian distribution with two cut-offs, -0.67 and 0.12,

and their respective proportion (25%, 30% and 45%). The image on the bottom, values below -0.67 are green facies, values above 0.12 are red facies and intermediate values are yellow facies. This image also shows the main limitations of the truncated Gaussian method: the anisotropy is the same for all facies and the yellow facies can touch the other two facies, but the green facies and the red facies never touch. If three or more facies were simulated in this way, they would occur in a fixed order, i.e., the method makes a hierarchy of phases when we have three or more phases.

The truncated plurigaussian method is used in the case of three or more phases and when not have a ordering between them. This method overcomes the limitations of the truncated Gaussian method, that is to say, while the truncated Gaussian only use one Gaussian random function in the truncated plurigaussian any number of Gaussian random functions may be used.

Figure 7 illustrates the truncated plurigaussian method for the case of two Gaussian random functions $Z_1(x)$ and $Z_2(x)$, the two Gaussian random functions used are presented at the top. The Gaussian random function on the left has its long range in the 45° while the other Gaussian random function has its long range in the 135° . The spatial relationships and contacts between units are

defined by a truncation rule, this truncation rule is symbolized by a flag. The bottom (left) show the flag, which shows that there are five facies, where the facies 1,2,3,4 and facies 1,2,4,5 are in touch at the same time and the facies 3 cannot enter in contact with the facies 5. The flag also tells us the proportion of each facies in the resulting simulation. The final simulation is obtained by modeling the horizontal axis of the flag by the first Gaussian random function, while the vertical axis of the flag is modeled using the second Gaussian random function. i. e. If $Z_2 < Z_{2B}$ and $Z_1 < Z_{1A}$, the facies is coded as green; if $Z_2 > Z_{2B}$, the facies is classified as blue; if $Z_2 < Z_{2A}$ and $Z_1 < Z_{1A}$, the facies is orange; if $Z_2 > Z_{2A}$, $Z_2 < Z_{2B}$ and $Z_1 < Z_{1B}$, the facies is coded as red and if $Z_2 > Z_{2A}$, $Z_2 < Z_{2B}$, $Z_1 > Z_{1A}$ and $Z_1 > Z_{1B}$, the facies is yellow.

The truncated Gaussian method was used in the first stage, for the second stage there are three phases where all the phases considered are in contact with each other simultaneously therefore this method was discarded.

To perform the second stage, the truncated plurigaussian method was chosen because this method through the flag can control the contacts and proportions of more than two categories in a suitable way, which is the case of the present work.

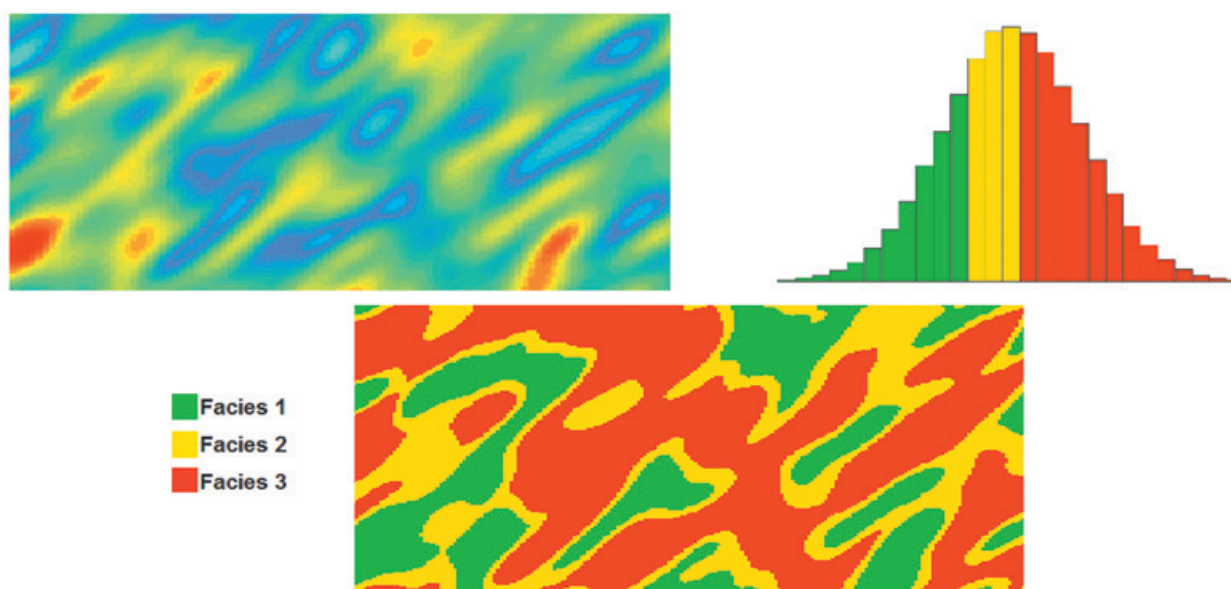


Figure 6. The truncated Gaussian method. Standard Gaussian random function has a Gaussian model (top- left), the histogram of a standard Gaussian distribution (top- right) and facies realization generated by truncated Gaussian method (bottom).

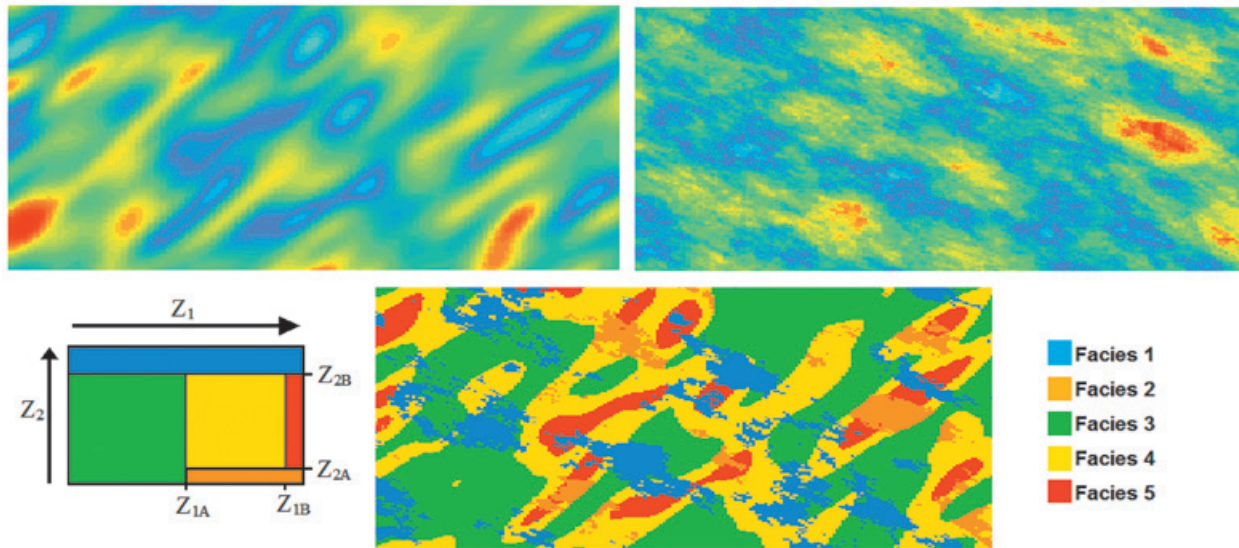


Figure 7. The truncated plurigaussian method. Standard Gaussian random function $Z_1(x)$ has a Gaussian model (top- left), standard Gaussian random function $Z_2(x)$ has a spherical model (top- right), example of a truncation rule for five facies (bottom- left) and Facies realization generated by truncated plurigaussian method (bottom-center).

Truncated plurigaussian simulation method requires the following steps:

1. Determination the thresholds at which the different standard Gaussian random function are truncated and the variogram model for each Gaussian random function.
2. Simulation of a realization of each Gaussian random function with the variogram model.
3. Application of the thresholds to the Gaussian realizations to obtain truncated plurigaussian simulation.

A detailed description of the mathematical fundamentals underlying the truncated Gaussian and plurigaussian methods can be found in Armstrong *et al.* (2003) and Lantuejoul (2002).

Geostatistical analysis

The monogaussian and plurigaussian method was applied using the reference image. During

the data exploratory analysis, several statistical parameters were computed (Table 1 and Table 2); these will be used to see to what degree the simulations reproduce the statistics of the original information. This analysis concluded that the data have no outliers or trend, which was important to identify because it affects the computation of the variogram and, therefore, the model fit.

Variograms were calculated and subsequently a model was adjusted to each one of them using weighted least squares. The model with the lowest sum of squares errors was chosen and it was validated using cross validation. The leave-one-out method (Journel and Huijbregts, 1978) was used for cross-validation; which involves removing each one of the samples and estimating the value at that point using the kriging equations and the variogram model obtained. As a result, a map of the differences between actual and estimated values is obtained.

The variograms were calculated under the assumption that the information has no trend or anisotropy. These assumptions were corroborated by obtaining the variograms, because they do not have a quadratic growth and comparing the variograms in different directions, they do not show significant differences in sill, nor in range.

Figures 8, 9 and 10 show variograms for pore space (case 1 and case 2) and clays. To every variogram obtained a model was adjusted, the collection of which are presented in Table 3.

Table 1. Proportions of each category.

Category	Figure 4	Figure 5	Figure 3
Pore space	34.60%	19.90%	19.90%
Rock	65.40%	80.10%	65.40%
Clays			14.70%

Table 2. Basic statistics of the reference image.

Statistics	Figure 4	Figure 5	Figure 3
Minimum	0.000	0.000	0.000
First quartile	0.000	1.000	1.000
Medium	1.000	1.000	2.000
Third quartile	1.000	1.000	2.000
Maximum	1.000	1.000	2.000
Mean	0.661	0.799	1.460
Variance	0.224	0.160	0.649
Standard Deviation	0.473	0.400	0.806

Table 3. Fitted models variograms for the three variable.

Variable	Model	Nugget	Sill	Practical Range (mm)
Pore space (case 1)	Exponential	0.013	0.210	0.081
Pore space (case 2)	Exponential	0.000	0.160	0.075
Clays	Exponential	0.027	0.091	0.135

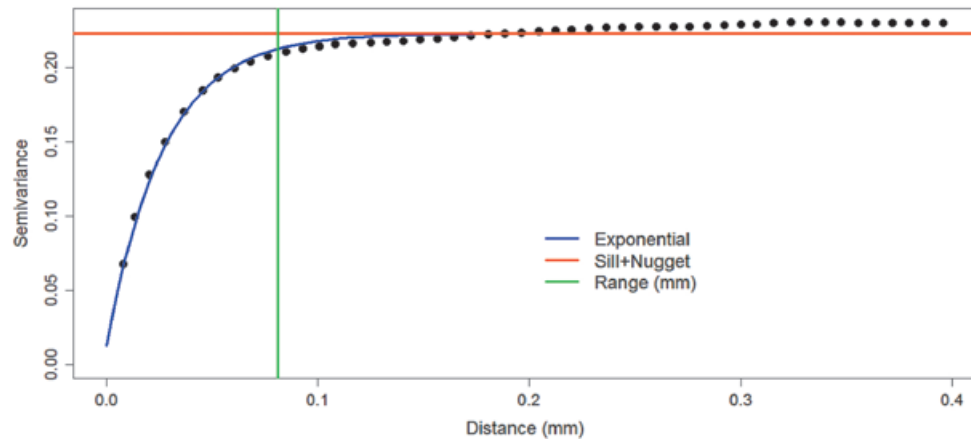


Figure 8. Estimated and fitted variogram model of pore space variable (case 1).

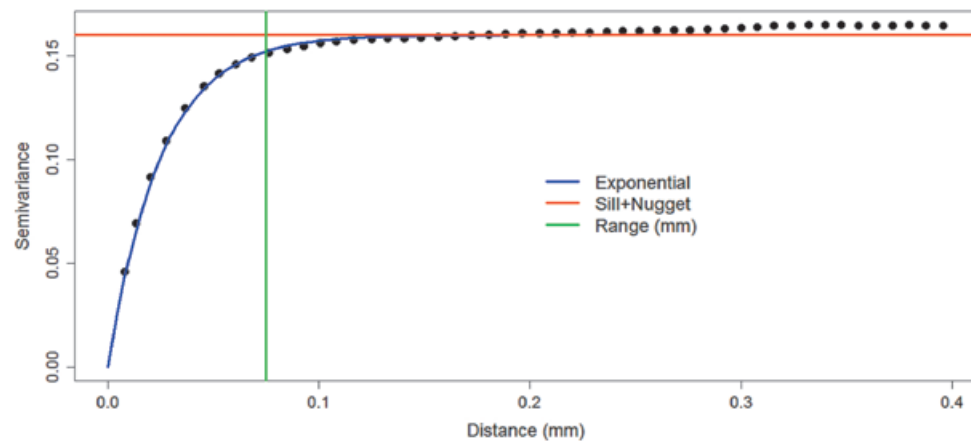


Figure 9. Estimated and fitted variogram model of pore space variable (case 2).

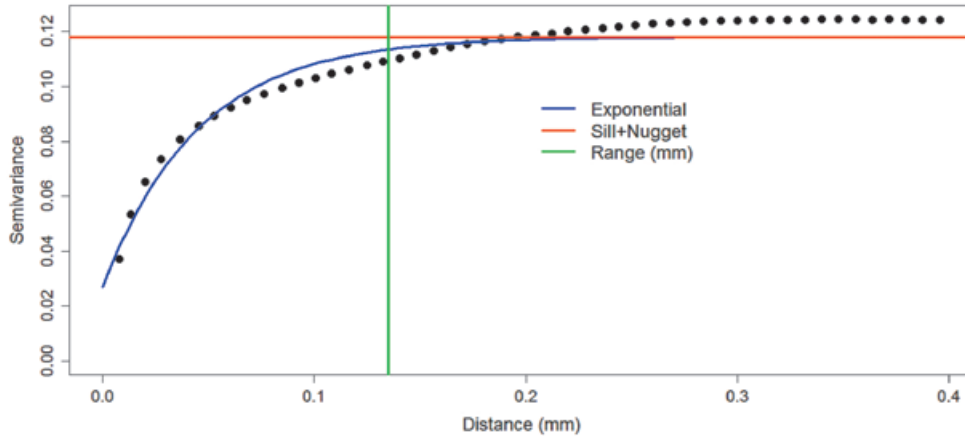


Figure 10. Estimated and fitted variogram model of clays variable.

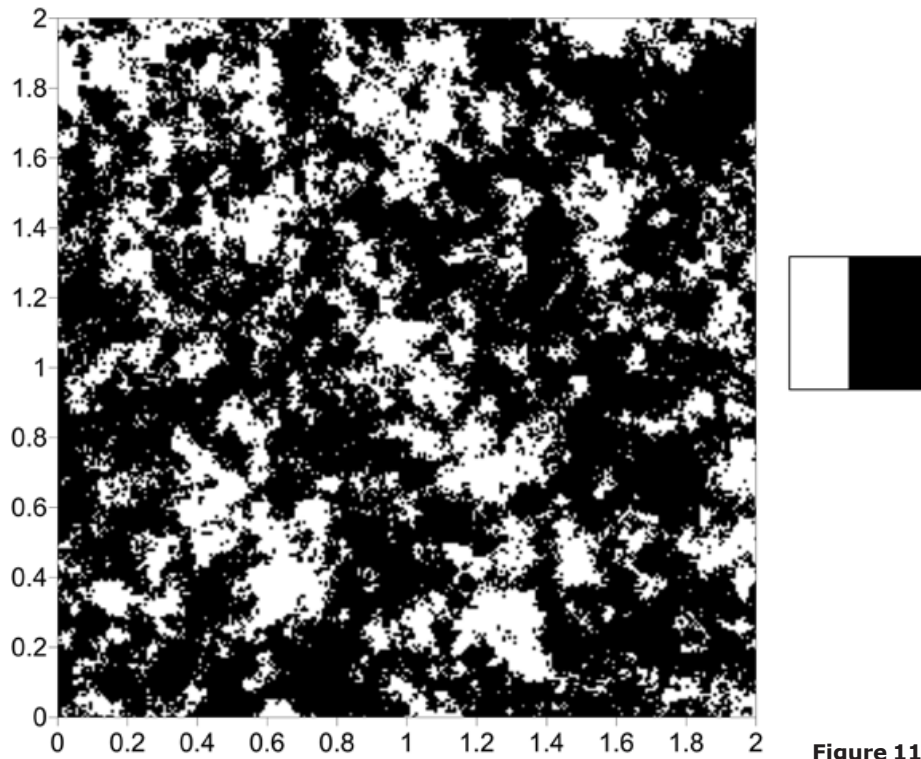


Figure 11. Pore space simulation (case 1).

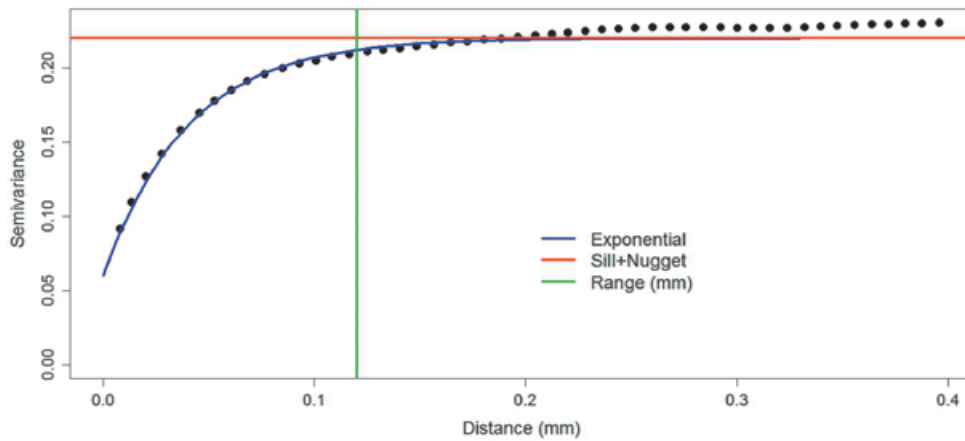


Figure 12. Estimated and fitted variogram model of the simulation of pore space (case 1).

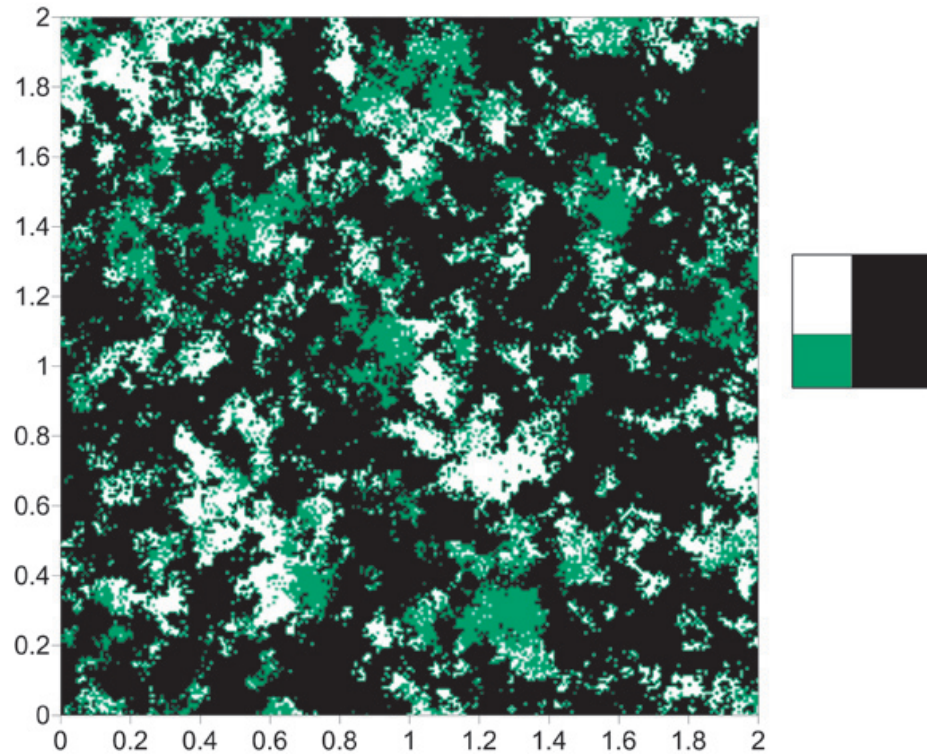


Figure 13. Clay distribution simulation (case 1).

Simulation results

For simulating the first stage (case 1), we used the proportions of Figure 4 and the pore space model of Table 4. The simulation result is shown in Figure 11. Figure 11 shows on the right the flag used in the simulation. The flag only have two divisions (pore space “white” and rock “black”); the division indicates the proportion of the category in the final simulation (left).

In the second stage, consider the proportions of Figure 3. The flag used is shown in Figure 13 (right). The model used in the first Gaussian

random function is the same as that used in stage 1; for the second Gaussian random function, we used the clays model (Table 3). The simulation result of this stage is shown in Figure 13.

The right of Figure 13 shows the flag, where according to the proposed case, first the pore and rock matrix is formed and then the clays, i.e. in the simulation of the first stage (Figure 11), the clays are integrated within the pore space. This is done by including another category within the category that was occupied by the pore space in the flag of the first stage. The final simulation is shown at the left of Figure 13.

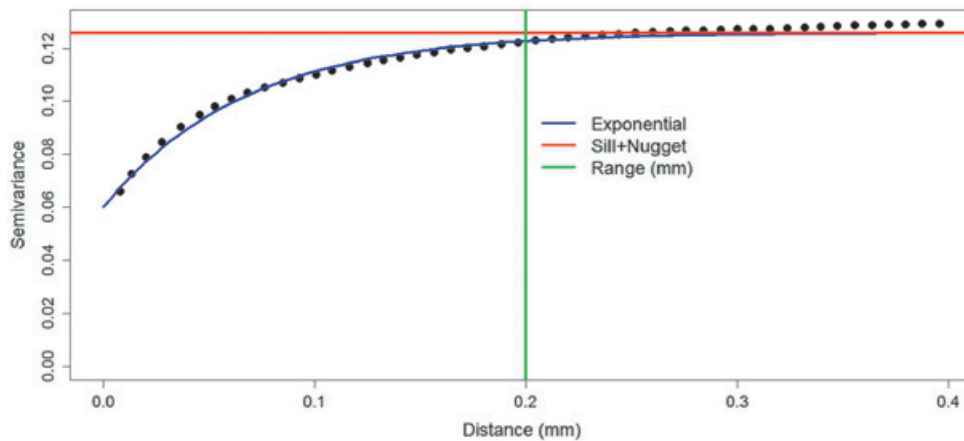


Figure 14. Estimated and fitted variogram model of the simulation of clays (case 1).

Table 4. Proportions of the reference image and the simulations of case 1.

Category	Figure 4	Figure 11	Mean of simulation	
			10	100
Pore space	34.6%	34.11%	33.89%	33.8%
Rock	65.4%	65.89%	66.11%	66.2%
Category	Figure 4	Figure 13	Mean of simulation	
			10	100
Pore space	19.9%	19.57%	19.39%	19.5%
Rock	65.4%	65.89%	66.11%	66.2%
Clays	14.7%	14.54%	14.5%	14.3%

Table 5. Fitted variograms models for the outcomes of the simulation.

Variable	Model	Nugget	Sill	Practical range (mm)
Pore space (case 1)	Exponential	0.06	0.16	0.12
Clays (case 1)	Exponential	0.06	0.066	0.2

Table 6. Basic statistics of the reference image and the simulations of case 1.

Category	Figure 4	Figure 11	Figure 3	Figure 13
Minimum	0.000	0.000	0.000	0.000
First quartile	0.000	0.000	1.000	1.000
Medium	1.000	1.000	2.000	2.000
Third quartile	1.000	1.000	2.000	2.000
Maximum	1.000	1.000	2.000	2.000
Mean	0.661	0.659	1.460	1.463
Variance	0.224	0.224	0.649	0.640
Standard Deviation	0.473	0.474	0.806	0.800

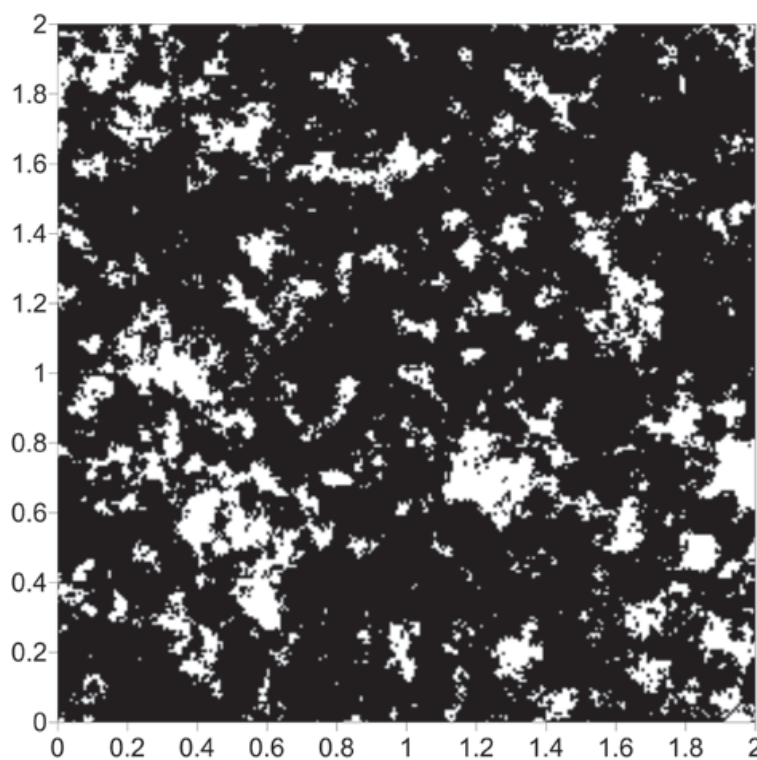


Figure 15. Pore space simulation (case 2).

Figure 4 is the reference image of the simulation of the first stage (Figure 11). Table 4 (column 2 and 3) shows the proportions of the reference image and the simulation. The simulation adequately reproduces the image proportions, basic statistics (Table 6) and the variogram models (Table 5 and Figure 12), when models are reproduced, indicating that the simulation reproduces properly the sizes of the structures.

The result of the second stage (Figure 13) is compared with the reference image (Figure 3). Table 4 (columns 4 and 5) and Table 6 show the proportions and basic statistics of the reference image and the simulation.

Figure 15 shows the simulation of the first stage (case 2), the ingredients of the simulation

with the proportions of Figure 5 and the pore space model (Table 3).

Table 7 (columns 2 and 3) and Table 8 show respectively the proportions and basic statistics of the reference image and the simulation. Variogram models for the simulation are presented in Table 9 and Figures 16 and 18.

The simulation of the second stage (Figure 17) is comparable to Figure 3. Table 7 (column 4 and 5) and Table 8 present the proportions and statistics of the image and the simulation. In both phases of this case the proportions, statistics and the sizes of the structures, present in the reference images, are well reproduced.

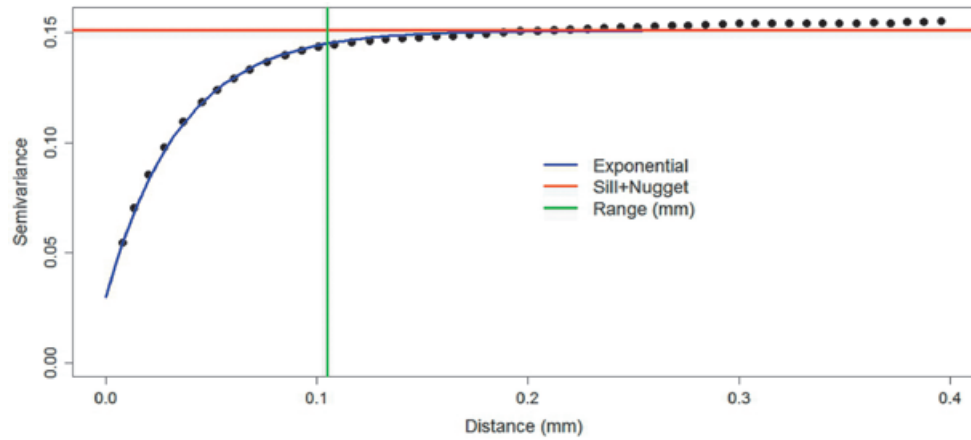


Figure 16. Estimated and fitted variogram model of the simulation of pore space (case 2).

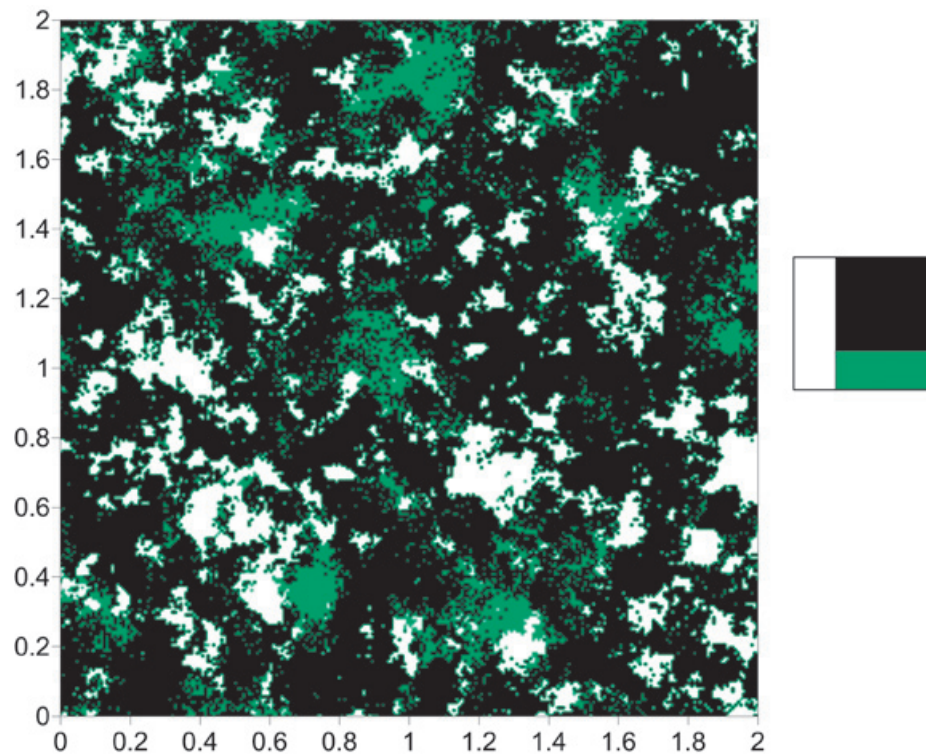


Figure 17. Clay distribution simulation (case 2).

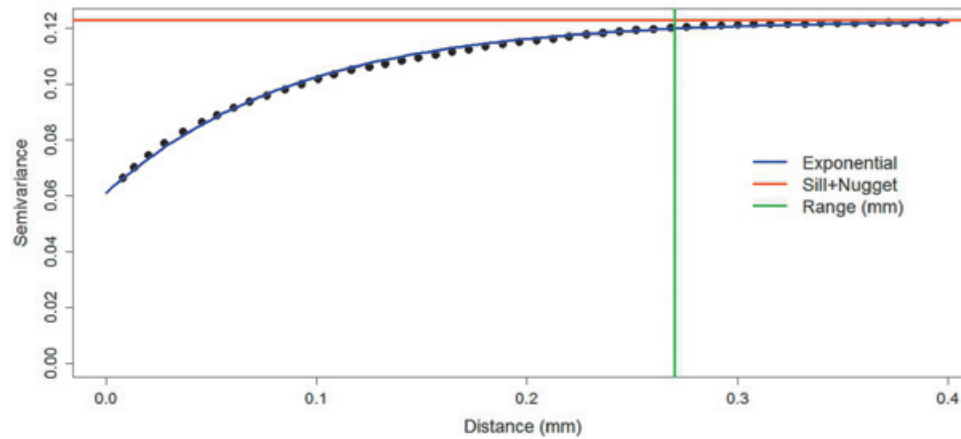


Figure 18. Estimated and fitted variogram model of the simulation of clays (case 2).

Table 7. Proportions of the reference image and the simulations of case 2.

Category	Figure 4	Figure 15	Mean of simulation	
			10	100
Pore space	19.90%	18.8%	18.52%	18.44%
Rock	80.10%	81.2%	81.48%	81.56%

Category	Figure 4	Figure 17	Mean of simulation	
			10	100
Pore space	19.90%	18.8%	18.52%	18.44%
Rock	65.40%	67.48%	67.69%	67.8%
Clays	14.70%	13.72%	13.79%	13.76%

Table 8. Basic statistics of the reference image and the simulations of case 2.

Category	Figure 5	Figure 15	Figure 3	Figure 17
Minimum	0.000	0.000	0.000	0.000
First quartile	1.000	1.000	1.000	1.000
Medium	1.000	1.000	2.000	2.000
Third quartile	1.000	1.000	2.000	2.000
Maximum	1.000	1.000	2.000	2.000
Mean	0.799	0.812	1.460	1.487
Variance	0.160	0.153	0.649	0.626
Standard Deviation	0.400	0.391	0.806	0.800

Table 9. Fitted variograms models for the outcomes of the simulation.

Variable	Model	Nugget	Sill	Practical range (mm)
Pore space (case 2)	Exponential	0.03	0.121	0.105
Clays (case 2)	Exponential	0.061	0.062	0.27

Table 9 shows the Euler characteristic values obtained for the reference figure and all simulations. In the table 9 all the values are greater than or equal to zero, so that it can be concluded that both the reference image as the simulations are similarly connected.

Figures 19, 20 and 21 compare the Euler characteristic of the reference images with their

respective simulation. The figures show the plots of the Euler characteristic versus the diameter measured in pixels of the reference images and their respective simulation. In the three cases a very close qualitative behavior is observed. This fact could be interpreted that the simulation method reproduces quite well the connectivity behavior of reference images.

Figure 19. Comparison the Euler characteristic presented in Figure 4 versus Figure 11.

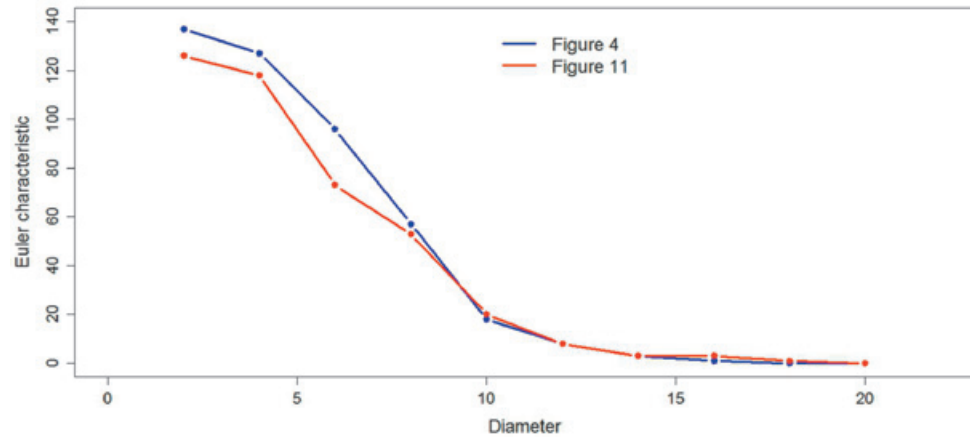


Figure 20. Comparison the Euler characteristic presented in Figure 5 versus Figure 15.

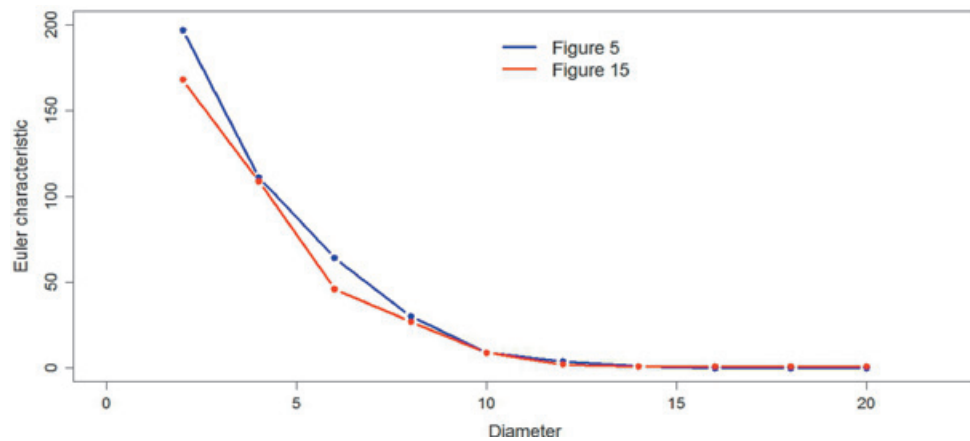


Figure 21. Comparison the Euler characteristic presented in Figure 3 versus Figures 13 and 17.

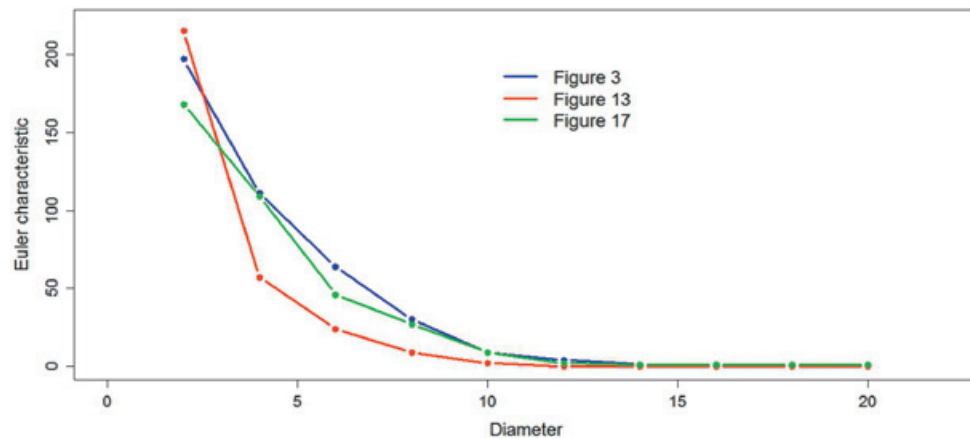


Table 10. Euler characteristic of reference images and simulations.

Diameter	2	4	6	8	10	12	14	16	18	20
Figure 3	197	111	64	30	9	4	1	0	0	0
Figure 4	137	127	96	57	18	8	3	1	0	0
Figure 5	197	111	64	30	9	4	1	0	0	0
Figure 11	126	118	73	53	20	8	3	3	1	0
Figure 13	215	57	24	9	2	0	0	0	0	0
Figure 15	168	109	46	27	9	2	1	1	1	1
Figure 17	168	109	46	27	9	2	1	1	1	1

Conclusions

This work is part of a line of research that attempts to investigate the impact of the interaction of reservoir fluids within themselves and/or injected chemicals on the petrophysical properties of the rock (porosity, permeability, relative permeability, etc.; and consequently in the patterns of fluid flow through the rock), and the changes in occupied volume by the clays at pore scale.

The results presented are preliminary. However it has been found that the simulations using the plurigaussian method adequately reproduces the proportions, basic statistics and sizes of the structures present in the studied reference images. Moreover, apparently the plurigaussian method reproduces the connectivity present in the corresponding reference image.

Although the work presented is restricted to 2D images, the methodology can be extended to 3D to achieve the reconstruction of the geometry of the porous medium, allowing a more adequate estimation of petrophysical properties.

As a future work it should be considered to combine the plurigaussian method with other methods, as might be a multipoint geostatistical simulation method (Okabe and Blunt, 2005 and 2007).

Bibliography

- Adler P.M., Thovert J.F., 1998, Real porous media: Local geometry and macroscopic properties, *Applied Mechanics Reviews*, 51, 537-585.
- Adler P.M., Jacquin C.G., Quiblier J.A., 1990, Flow in simulated porous media. *International Journal of Multiphase Flow*, 16, 4, 691-712.
- Armstrong M., Delfiner P., 1980, Towards a more robust variogram: case study on coal. Fontainebleau: Springer.

Armstrong M., Galli A., Le Loc'h G., Geffroy F., Eschard R., 2003, Plurigaussian Simulations in Geosciences. Springer, Berlin, 160 pp.

Capek P., Hejtmánek V., Brabec L., Zikánová A., Kocirík M., 2008, Stochastic Reconstruction of Particulate Media Using Simulated Annealing: Improving Pore Connectivity, Transport in Porous Media, 76, 2, 179-198.

Casar-González R., Suro-Pérez V., 2000, Stochastic imaging of vuggy formations. 2000 SPE International Petroleum Conference and Exhibition, Villahermosa, México. SPE 58998.

Casar-González R., Suro-Pérez V., 2001, Two procedures for stochastic simulation of vuggy formations.. 2001 SPE Latin American and Caribbean Petroleum Conference and Exhibition, Buenos Aires, Argentina. SPE 69663.

Casar-González R., 2003, Modelado estocástico de propiedades petrofísicas en yacimientos de alta porosidad secundaria. Tesis Doctoral. Facultad de Ingeniería, División de Estudios de Posgrado, Universidad Nacional Autónoma de México, Mexico.

Chilès J.P., Delfiner P., 1999, Geostatistics: Modeling Spatial Uncertainty. New York: Wiley.

Dos Santos L.O.E., Philippi P.C., Fernandes C.P., Gaspari H.C., 2002, Reconstrução tridimensional de microestruturas porosas com o método das esferas sobrepostas, in: Proceedings of the ENCIT 2002, Caxambu - MG, Brazil - Paper CIT02-0449.

Fens T., 2000, Petrophysical Properties from Small Rock Samples Using Image Analysis Techniques. Ph.D. thesis. Netherlands: Delft University Press.

- Galli A., Beucher H., Le Loc'h G., Doligez B., HeresimGroup, 1994, The pros and cons of the truncated gaussian method. *Geostatistical Simulations*, 217-233. Dordrecht: Kluwer.
- Hilfer R., Manwart C., 2001, Permeability and conductivity for reconstruction models of porous media, *Physical Review E.*, 64, 021304-021307.
- Lantuejoul C., 2002, *Geostatistical Simulation: Models and Algorithms*. Berlin: Springer.
- Le Loc'h G., Galli A., 1997, Truncated plurigaussian method: theoretical and practical points of view. *Geostatistics Wollongong*, 1, 211-222, Dordrecht: Kluwer.
- Manwart C., Torquato S., Hilfer R., 2000, Stochastic reconstruction of sandstones, *Physical Review E.*, 62, 41, 365-371.
- Okabe H., Blunt M., 2005, Pore space reconstruction using multiple point statistics. *Petroleum Science and Engineering*, 46, 121-137.
- Okabe H., Blunt M., 2007, Pore space reconstruction of vuggy carbonates using microtomography and multiple-point statistics. *Water Resources Research*, 43.
- Politis M., Kikkinides E., Kainourgiakis M., Stubos A., 2008, Hybrid process-based and stochastic reconstruction method of porous media. *Microporous and Mesoporous Materials*, 110, 92-99.
- Strebelle S., 2002, Conditional simulation of complex geological structures using multiple-point statistics, *Mathematical Geology*, 34, 1-21.
- Talukdar M.S., Torsaeter O., 2002, Reconstruction of chalk pore networks from 2D backscatter electron micrographs using a simulated annealing technique, *Journal of Petroleum Science Engineering*, 33, 265-282.
- Thovert J.F., Yousefian F., Spanne P., Jacquin C.G., Adler P.M., 2001, Grain reconstruction of porous media: Application to a low-porosity Fontainebleau sandstone. *Physical Review E.*, 63, 061307-061323.
- Vogel H.J., 2002, Topological characterization of porous media. In: *Morphology and Condensed Matter - Physics and Geometry of Spatially Complex Systems*. Mecke, K., and Stoyan, D. (eds.), *Lecture Notes in Physics*, 600, 75-92.
- Wu K., Van Dijke M., Couples G., Jiang Z. Ma, J., Sorbie K., Crawford J., Young I., Zhang X., 2006, 3D Stochastic Modeling of Heterogeneous Porous Media - Applications to Reservoir Rocks. *Transport in Porous Media* 65, 443-467.
- Xu W., Journel A.G., 1993, GTSIM: Gaussian truncated simulations of reservoirs units in a W. Texas carbonate field. SPE 27412.
- Yeong C.L.Y., Torquato S., 1998a, Reconstructing random media. *Physical Review E.*, 58, 1, 495-506.
- Yeong C.L.Y., Torquato S., 1998b, Reconstructing random media II Three-Dimensional from Two-Dimensional Cuts, *Physical Review E.*, 58, 1, 224-233.

AVO analysis with partial stacking to detect gas anomalies in the GÜEPAJÉ-3D project

Juan C. Mosquera*, Alfredo Ghisays and Luis Montes

Received: March 03, 2012; accepted: April 01, 2013; published on line: June 28, 2013

Resumen

La técnica AVO con apilados parciales se aplicó en un campo gasífero para detectar presencia de gas al tope de la Formación Ciénaga de Oro (FCO) usando apilados parciales del programa sísmico terrestre Güepajé-3D y apoyado con registros del pozo Ayombe-1.

Mediante la técnica de sustitución de fluidos se simuló el reemplazamiento de gas por agua para conocer la sensibilidad de la respuesta sísmica al cambio del fluido en un segmento del pozo Ayombe-1. Se observó una anomalía clase I al tope de la FCO, aun cuando las respuestas de sustituir gas por agua fueron muy similares al aplicar la técnica AVO con apilados parciales se observaron anomalías AVO clase I al tope de la FCO en los pozos con gas Ayombe-1 y Güepajé-1 y ninguna en el pozo seco Güepajé-3. A pesar de tener gas, en el pozo Güepajé-2 los resultados permiten diferenciar entre una incipiente anomalía clase I y ninguna.

Al usarse en el volumen sísmico del Proyecto Güepajé-3D la técnica suministra un mapa de indicador directo de gas que se correlaciona con estructura de la superficie al tope de la FCO.

Pueden factores líticos como compactación, cementación y presencia de carbonatos supra yaciendo la FCO, así como la variabilidad en el espesor variable de las capas parcial y totalmente saturadas al tope de la FCO, generar anomalías en zonas con baja probabilidad de tener gas.

Palabras clave: caso histórico, modelado de pozo, tendencia de fondo, anomalía de AVO, factor de fluido, apilados parciales, Güepajé-3D.

Abstract

We applied analysis AVO with partial stacking to an onshore gas field in order to detect gas at the top of the Ciénaga de Oro formation (FCO), by using seismic gathers of the Güepajé-3D project. The technique was supported by petrophysical analysis of the Ayombe-1 well.

The sensitivity of seismic response to changes in the saturating fluid was evaluated by fluid substitution technique in an interval of the Ayombe-1 well. As a result, a class I AVO anomaly at the top of the FCO was observed, even though the gas and water responses were similar.

After applying AVO with partial stack technique at the top of FCO, AVO class I anomalies were observed in the Ayombe-1 and Güepajé-1 gas wells and none in the dry Güepajé-3 well. In spite of being reported with gas, the results in the Güepajé-2 well indicated any to an incipient class I anomaly related to a weak seismic response associated to gas.

When the technique was applied to the seismic volume of the Güepajé-3D Project, a map of the direct gas indicator was obtained. The map shows a high correlation with the structural surface at top of FCO. Lithic factors such as compaction, cementation and carbonate overlaying the FCO and variable thickness of partial and full saturated layers, may cause anomalies in zones unlikely to contain gas.

Key words: case history, well modeling, background trend, AVO anomaly, fluid factor, partial stacks, Güepajé-3D.

J.C. Mosquera*
Petrobras Colombia Ltd.
Carrera 7 Núm. 71-21. Piso 17
Bogotá, Colombia
**Corresponding author: juanmosque@yahoo.com*

A. Ghisays
Universidad del Atlántico
Facultad de Ciencias básicas
Km. 7. Vía Puerto Colombia
E-mail: alfredoghisays@mail.uniatlantico.edu.co

L. Montes
Universidad Nacional de Colombia
Departamento de Geociencias
Carrera 30 Núm. 45 - 03
Ed. Manuel Ancizar, Of. 326
Bogotá, Colombia
E-mail: lamontesv@unal.edu.co

Introduction

The elastic nature of rocks, depends on lithology and fluid content in pores, (Koefoed, 1955; Gassmann, 1951).

Bright spots in stacked sections were associated with gas accumulation, and later extended to related oil anomalies. Hilterman (1975) retook Koefoed's work, by analyzing how amplitude varies with incidence angle before stacking to predict lithology. As in bright spot cases, AVO anomalies were associated to gas but the possibility of using such methodology to indicate the presence of oil was foreseen.

AVO analysis was applied to localize hydrocarbon reserves and to diminish the risk of exploratory projects. Although the number of successful wells increased, dry wells with this type of anomalies were still reported. Ostrander (1984) published a method applied to prestack sections to discern anomalies caused by sandstones with or without gas. Rutherford and Williams (1989) characterized three different seismic anomalies produced by hydrocarbons (class I, phase change class II, and bright spot class III). AVO analysis gained a new impulse with the contributions of Hilterman (1975) and Smith and Gidlow (1987), who established the concepts of Intercept and Gradient, and introduced the analysis of Intercept and Gradient images separately. In the linear relationship between seismic amplitudes and squared sine of reflecting angles, the Gradient represents the slope and the Intercept the reflecting coefficient. Rutherford and Williams (1989) and Castagna (1997), proposed classifying AVO anomalies in four classes according to Intercept and Gradient values. Rosa *et al.* (1999) introduced the Elastic Impedance concept, based on using volumes partially stacked by range of angles together with the visualization and analysis of images of Gradients and Intercept, (Connolly, 1999).

The partial stack technique has been widely applied in elastic and simultaneous inversion to estimate physical properties (Maver and Bolding, 2004) and velocities by constraining the inversion with borelog information (Wei *et al.*, 2006).

AVO with partial stack technique is part of the corporate knowledge in some companies; however, there are no related publications to date. In the study area some confidential AVO studies have been performed using 2D seismic lines. We applied this technique to a seismic volume of the Güepajé-3D project, supported with well log analysis. Some zones with anomalies associated to gas at the top of the FCO were identified. Factors such as compaction, cementation and carbonates in rocks that overlay the FCO, together with variable thickness layers partially or fully

saturated, may cause anomalies in zones with unlikely gas presence.

Location

The Güepajé – Ayombe seismic 3D program is located in an area that includes the municipalities of San Pedro and the Guaimaral and Canutalito police Inspections, in the Department of Sucre, Colombia, as seen on the map in Figure 1.

The seismic dataset covers an area of 112 km², of which, 64 km² are located in the Magangué block, 41 km² in the Ayombe block and 7 km² in La Creciente block. In 1992 gas was discovered in the FCO in the Güepajé-1 well and some gas samples were reported in the Middle Porquero and in the Lower Porquero formations. By the end of 1992 the Ayombe-1 well, drilled at a distance of 6.5 km north of the Güepajé-1 well, reported gas in the FCO (Sánchez, 1993).

In 1993 the Güepajé-2 well was drilled at 2.9km NNW from the Güepajé-1 well, suggesting gas field continuity in the same units of the Güepajé-1 well. By the end of 1993 the Güepajé-3 well was drilled at 5 Km South from the Güepajé-1 well, where the target FCO sandstones were found argillaceous without gas.

Geology

The Lower Magdalena Valley basin (VIM acronym in Spanish) is located in the Northwest of Colombia, where oblique subduction along the Romeral fault system has formed a trans-pressure and trans-tension deformation since the Late Cretaceous to date (Barrero *et al.*, 2008). From top to base, the stratigraphic column in the area contains the formations of Corpa (Pleistocene-Upper Pliocene), Tubará (Upper Miocene), Porquero (Upper and Lower Miocene), Ciénaga de Oro (Oligocene-Lower Miocene) and the basement (Pre Miocene). The Porquero formation is divided in Upper and Lower units with a thin microfossil carbonate level at bottom.

The petroleum system source rock is a very thick shale from Early Miocene (Porquero Lower Formation), rich in both organic material and type II kerogen. The FCO has an upper unit with a high type III organic material content with the generation window in the deepest areas of the basin. The reservoir consists of FCO sandstones and limestones with net thickness around 90 m and 15% of average porosity. The seal rock is formed by the Lower Porquero shales and the FCO shales. The Tubará formation also acts as seal unit. Different types of structural traps emboss the potential of this basin such as traps associated to top closures in faults related to contractions, anticline closings in the lower part of normal

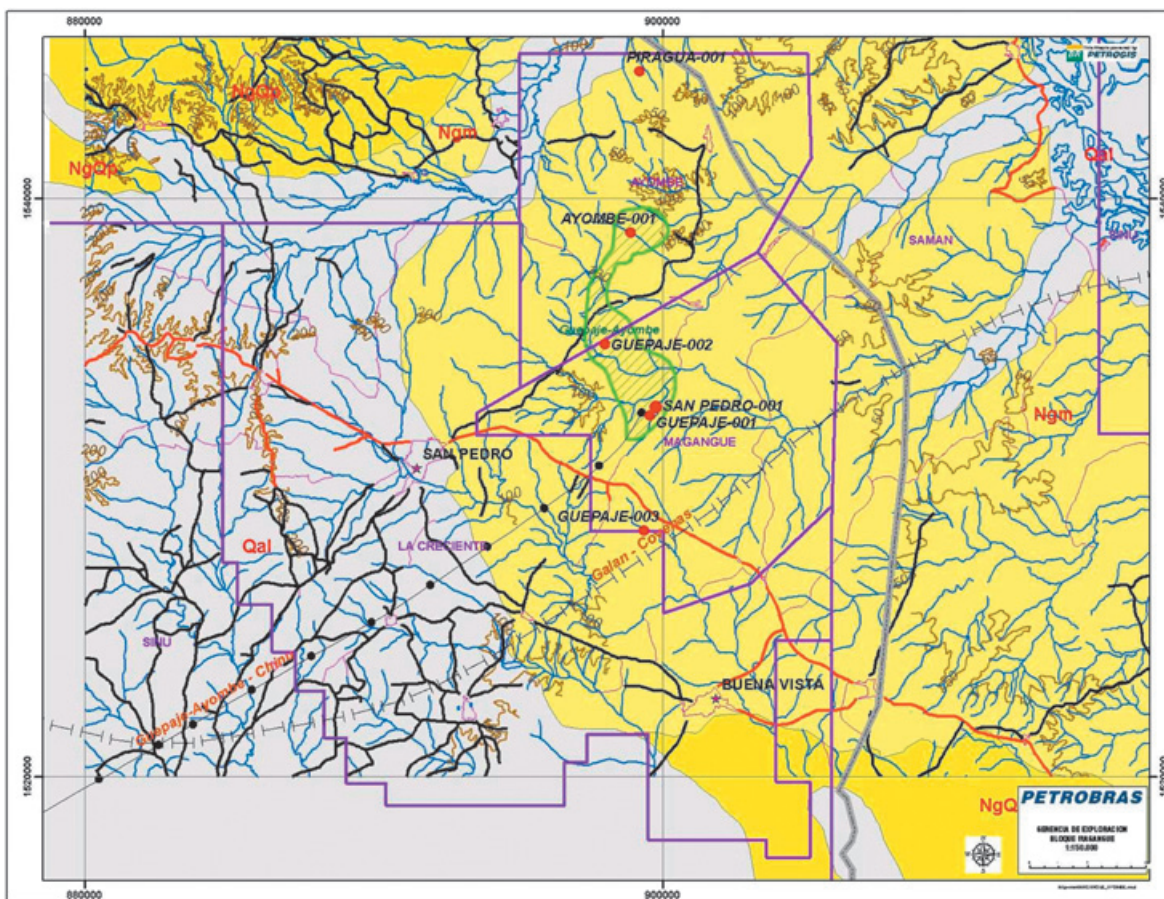


Figure 1. Map of the study area, including Magangué, Ayombe and La Creciente blocks.

faults, structures related to geometries in bloom generated by transpression, and rollovers in the hanging blocks of normal listric faults. Stratigraphic traps are also a potential in carbonate rocks and a submarine range of turbidites.

Active source rocks in generation/expulsion phase are present in an extensive area in the so called Plato sub-basin. The API gravity for oil generated inside the basin varies between 30° to 52°. The sulphur content is too low whereas the paraffin's concentration is relatively high. Several geo-chemical parameters indicate that most of the oil was originated in a relatively dioxic proximal siliciclastic environment. The most probable migration occurred along the network of fractures and faults planes (Barrero *et al.*, 2008).

The tops of the Tubará, Upper and Lower Porquero, Ciénaga de Oro formations and also Basement were interpreted in the migrated sections; such events were tied up with the Ayombe-1 well check shot, as seen in the Figure 2.

In the seismic section, the Corpa formation overlays the Tubará formation which has a moderately variable thickness and presents

medium to strong reflections with parallel to sub-parallel layers dipping to the SWS; its seismic character is consistent with its high sandstones content through the section. The Porquero Superior formation, composed of shales, presents a variable thickness and weak reflectors.

The Ayombe -1 well logs were correlated with the seismic dataset of the Güepajé-3D program, which had a 30m x 30m bin and 30 nominal fold. The seismic volume was processed up to a prestack migrated volume (PSTM) applying a special process sequence for AVO by angles range, the volume was interpreted as seen in the inline of Figure 2. The Figure 3B shows a detailed structural interpretation at the top of the FCO. The FCO has a variable thickness ranging from a few to 200 meters with a 100m thickness average in the area.

Theory

The wave behavior at a discontinuity between two semi infinite elastic media is determined by the Zoeppritz equations, guaranteeing both displacement and stress continuity on the two opposite sides. These equations were approximated by Shuey (1985) through the expression:

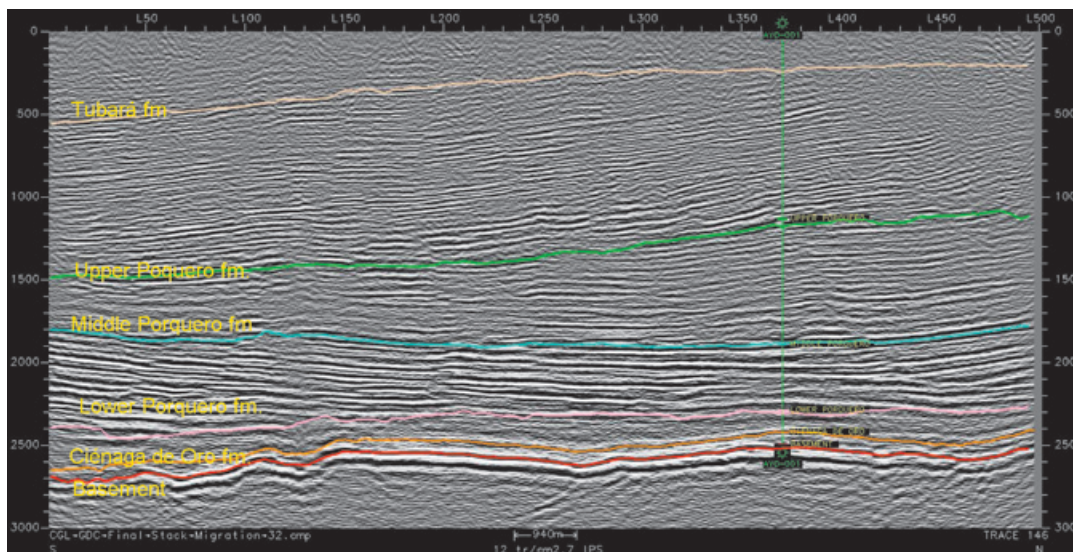


Figure 2. The Tubará, Porquero Superior, Porquero Medio, Porquero Inferior, Ciénaga de Oro formations and Basement, are interpreted from the youngest at the top to the oldest at the bottom.

$$\begin{aligned}
 A(\theta) = & \underbrace{\frac{1}{2} \left(\frac{\Delta V_P}{\alpha} + \frac{\Delta \rho}{\rho} \right)}_{\theta \leq 10^\circ} \\
 & + \underbrace{\left(\frac{1}{2} \frac{\Delta V_P}{\alpha} - 4 \left(\frac{\beta}{\alpha} \right)^2 \frac{\Delta V_S}{\beta} - 2 \left(\frac{\beta}{\alpha} \right)^2 \frac{\Delta \rho}{\rho} \right)}_{\theta \leq 35^\circ} \sin^2 \theta \\
 & + \underbrace{\frac{1}{2} \left(\frac{\Delta V_P}{\alpha} \right) (\tan^2 \theta - \sin^2 \theta)}_{\theta \leq 45^\circ}
 \end{aligned} \tag{1}$$

where ρ is average density, and α and β are P and S wave average velocities, ΔV_S , ΔV_P and $\Delta \rho$ are velocity and density changes from one media to another, θ is the reflection angle and A is the amplitude of the reflected wave. For θ lesser than 35° the equation 1 is approximated to

$$A(\theta) = I + G \sin^2 \theta \tag{2}$$

Where I is the Intercept and is the Gradient. According to equation 2 and in case of near offsets, i.e. $10^\circ < \theta < 20^\circ$, the amplitudes shall be renamed as $A_M(\theta) = I + G \sin^2 \theta_M$. In case of far offsets, i.e. $20^\circ < \theta < 35^\circ$, the amplitudes shall be $A_F(\theta) = I + G \sin^2 \theta_F$.

After manipulating and solving them, the following is obtained:

$$I = A_M - \left(\frac{A_F - A_M}{\sin^2 \theta_F - \sin^2 \theta_M} \right) \sin^2 \theta_N \tag{3}$$

by:

$$G = A_M \left(\frac{1}{\sin^2 \theta_M - \sin^2 \theta_N} \right) - A_N \left(\frac{1}{\sin^2 \theta_F - \sin^2 \theta_M} \right) \tag{4}$$

By using the equations 3 and 4, the Intercept and Gradient are correlated in a section, where the data located along the straight line defines the trend (background) whereas those others are orthogonally deviated to it (Figure 4B). The deviation is used as a fluid factor indicator (Smith & Gidlow, 1987) and is given by:

$$F_F = \frac{\Delta V_P}{\alpha} - M \frac{\beta}{\alpha} \frac{\Delta V_S}{\beta} \tag{5}$$

M corresponds to the slope of the relationship $V_P = 1.16V_S + 1360$, established by Castagna *et al.* (1984) from sonic and seismic measurements in mudrocks.

Modeling the Ayombe-1 well

In the Ayombe-1 well, the analyzed 2357–3340m interval includes the Lower Porquero and Ciénaga de Oro formations and the Basement, along with Gamma Ray (GR), Resistivity (HRS), Sonic (DT8D) and Density (RHOB) logs were run. Although the shear velocity log was not acquired in this well, a pseudo shear velocity profile was

calculated by the Greenberg-Castagna method (1992). The complete sets of logs, including the estimated pseudo shear log, are shown in figure 3A.

A well logs analysis in the 2357-3371 m interval provided the following results. The GR log shows a sandstone-shale pattern. The Resistivity log indicates a 40% - 60% gas saturation range in the 3210 to 3228 m interval, a 10% to 20% gas saturations range in the 3228 to 3232 m interval and 100% water saturation between 3232 m and 3362 m deep. In depth, Poisson's relation log tends to decrease but arriving at the top of FCO (gas reservoir at 3210 m) it falls abruptly and rises immediately to continue its former decreasing trend.

The top of FCO is clearly identified by the abrupt changes in Resistivity, GR, Density and Sonic logs as observed in Figure 3A. Observable breaks around 3130 m in GR, Resistivity, Density and Sonic logs tend to point out the top of carbonate level overlaying the FCO.

To match the seismic volume along the well, a synthetic seismogram was obtained by the convolution of a wavelet extracted from the seismic volume with the product of multiplying Sonic by Density logs, after depth to time conversion. The Figure 3B depicts the stack section in the vicinity of the Ayombe-1 well along the 2100 - 2500m interval. It is observed how the seismogram ties the Ciénaga de Oro, the Lower Porquero and part of the Upper Porquero formations.

In the next step, some synthetic seismograms were generated with angles from 0° to 40°

varying each 2°, to observe how the amplitude changes with the reflecting angle. An obtained seismogram is seen in Figure 4A, where amplitude is characterized by a positive intercept (peak) that decreases with an angle (negative gradient) at the top of the FCO fm. Using seismic data at the top of FCO in the vicinity of the well, the Intercept-Gradient cross plot was generated (Figure 4B).

The linear regression through data clustered in the upper polygon defines the background or the non anomalous data. The estimated straight line, with a slope of 1.156, intercepts the abscissa in 0.0015. The points which are not aligned with the background are considered anomalous, i.e. those ones within the below irregular hexagon, are identified as a class I anomaly.

This kind of anomaly characterizes layers overlaying lower impedance rocks that might generate dim spots in stacked section because hydrocarbon reduces the reservoir - seal impedance contrast.

The fluids substitution was simulated in the 3210-3228 m interval (40% - 60% gas saturated) and the 3232-3362 m interval (100% water saturated), using the Biot - Gassmann equations. The obtained responses in both cases are characterized by negative Gradients and positive Intercepts, although the amplitudes are always higher in the 100% water saturation case than in the partially saturated gas case, as noted in Figure 5. The Gamma Ray, Resistivity, Density, Vs and Vp responses, in both the partially and fully saturated cases, are shown in Figure 6.

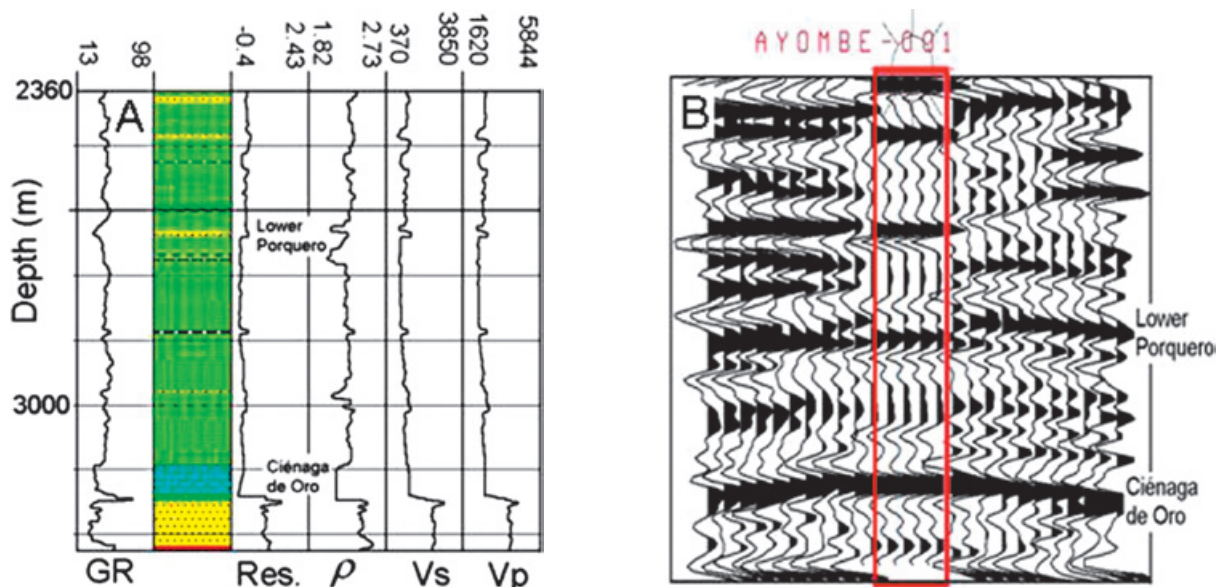


Figure 3. A) The Interval of 2357m of depth to the bottom of the Ayombe-1 well with borehole logs. B) The synthetic seismograms in the inset tie up the seismic section.

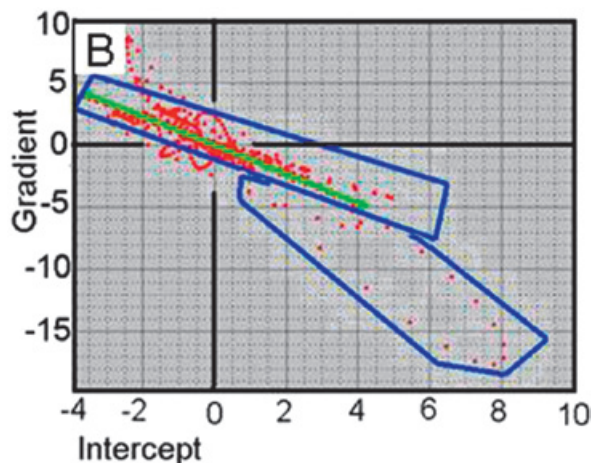
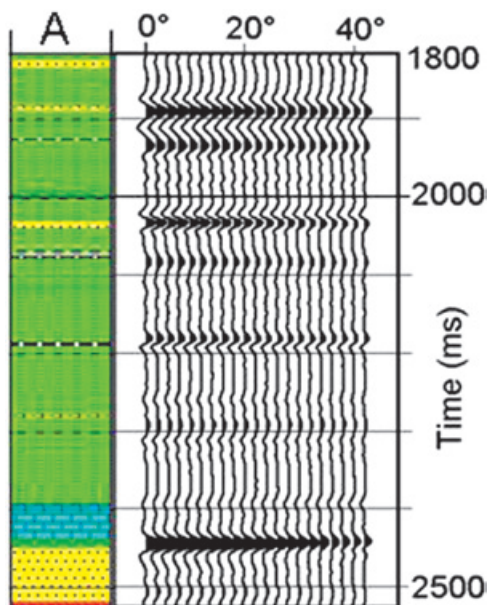


Figure 4 A) At the top of the FCO fm. the amplitude decreases with the angle. B) Data in the IV quadrant indicates a class I anomaly at the top of the FCO fm.

In the 100% water saturation case, when water fills up pores in rock matrix at the top of FCO, the following was observed. The Gamma Ray log remains unchanged because its response does not depend on fluids in pores. The Resistivity log falls quickly due to the gas is more resistive than water. The Density log increases because water is denser than gas. The shear velocity remains the same because liquids cannot be sheared, whereas acoustic wave velocity increases due to the fact that liquids are not compressible.

The 33m of seismic resolution at 3200m depth impedes to discriminate the transition zone with 80%-90% gas saturation and with a 23m thickness. Therefore, the top of the fully saturated water zone cannot be picked out. Besides, possible tuning related to absence of frequencies at far offsets might increase the uncertainty.

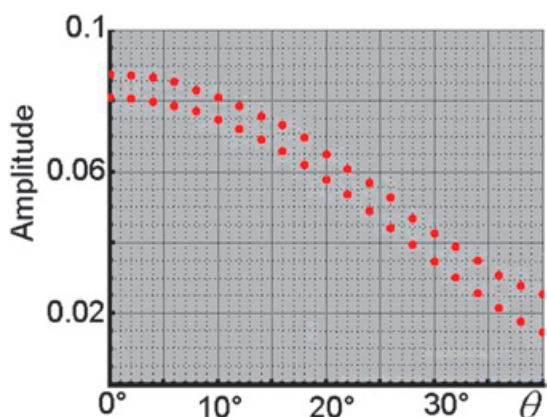


Figure 5. In the partially and fully saturated cases, at the top of the FCO, the amplitude decreases with the angle.

Partial stack AVO analysis

The partial stacks of near offsets (0°-10° range angle), mid offsets (10°-20°) and far offsets (20°-37°) were initially generated. Although, the near offset stack was not considered in this analysis because of the very low signal to noise ratio. The obtained partial stacks together with stacking velocities were used to calculate the Gradient (Figure 7A) and the Intercept (Figure 7B) sections.

In order to restrict the analysis at the top of the FCO, only those data inside the boxes of figures 7A and 7B were correlated. As a result, the obtained cross correlation graph was inserted in Figure 8A. Using the same straight line that established the background at the top of the FCO, an orthogonal deviation section was generated, Figure 8B. At the top of the FCO in the vicinity of Ayombe-1 well a green color and a tiny red color are observed (indicated by an arrow), which according buttons at right of Figure 8B indicates IV to III quadrant and hence a weakly class II to a class I anomaly. This result agrees with the result obtained by

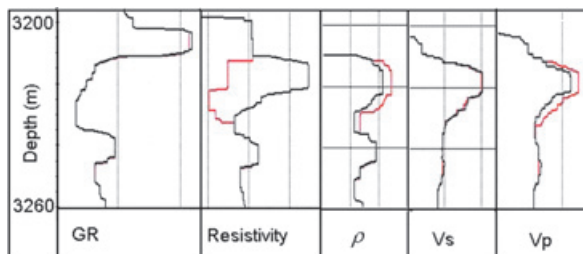


Figure 6. Logs at the top of FCO partially (in black) and fully saturated (in red) cases.

previous well modeling. This partial stack AVO methodology was applied to seismic traces belonging to three 2D seismic lines that crossed or were very close to the three wells Güepajé-1 (line 160), the Güepajé-2 (line 244) and the Güepajé-3 (line 28). Consequently, the three deviation sections associated to the mentioned lines were obtained, focusing on target zones in vicinities of the three considered wells. The analysis of the deviation sections of the line 160 at top of FCO in Güepajé-1 well (indicated by an arrow) identified III to IV quadrant pointing out a class II to a class I anomaly (Figure 9A). In the deviation section of the line 244 at the top of the FCO in Güepajé-2 well (marked with an arrow) no anomaly was identified Figure 9B. Finally an incipient class I anomaly was detected in the deviation section of the line 28 in the Güepajé-3 well, see the arrow in Figure 9C. Up to this point, the partial stack AVO methodology has been applied to 2D seismic data and after having verified its robustness with well logs, the technique was used on 3D seismic volume to detect anomalies associated to gas over the surface defining the top of the FCO.

The mid and far offset stacks at the top of the FCO surface previously obtained were used

to generate the Intercept (Figure 10A) and the Gradient (Figure 10B) maps associated to this surface. In the Intercept map, positive values are observed in the vicinity of the Ayombe-1 (>0.249), Güepajé-1 (>0.436), Güepajé-2 (>0.037) and Güepajé-3 (>0.096) wells, with color ranging from green to brown in the colors scale. In the Gradient map negative values are observed in zones around the locations of the four considered wells. The values of -4.66 for Ayombe-1, -0.40 for Güepajé-1, -1.88 for Güepajé-2 and -1.29 for Güepajé-3 ($\gg -1.29$) wells are associated to colors ranging from white to red. The anterior results, and the Gradient and Intercept values around wells, are in agreement with those supplied by the petrophysical analysis and the 2D seismic analysis formerly done. In both maps the 2480 ms contour line highlights the gas-water contact (GWC) obtained by extrapolating these contacts in the wells.

Finally, an orthogonal deviation map used as a fluid indicator map was obtained, in Figure 11, using as reference background the same straight line established for the Ayombe-1 well. In this map, anomalous values are indicated by colors ranging from green to red. It is notable the

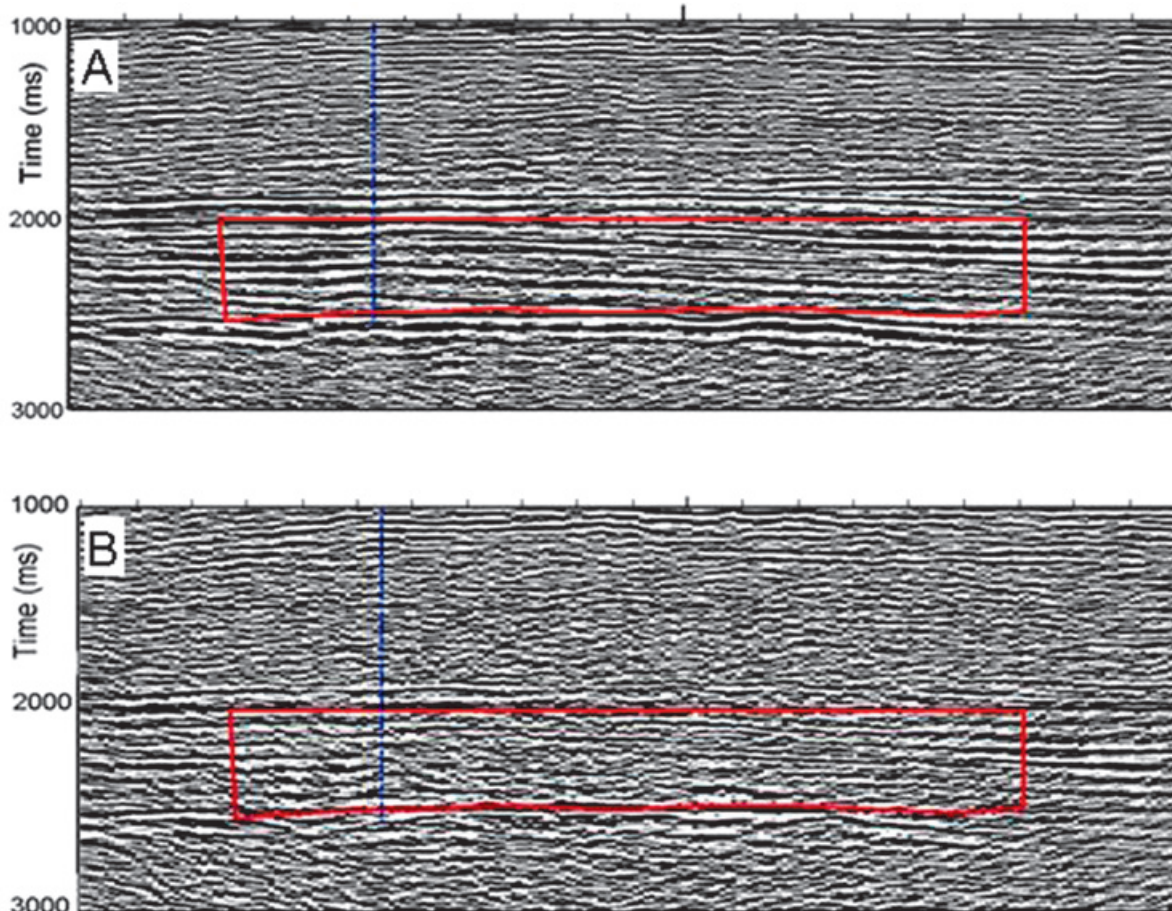


Figure 7. In the Line 370, the polygon surrounds the target in A) the mid offset stack and B) the far offset stack.

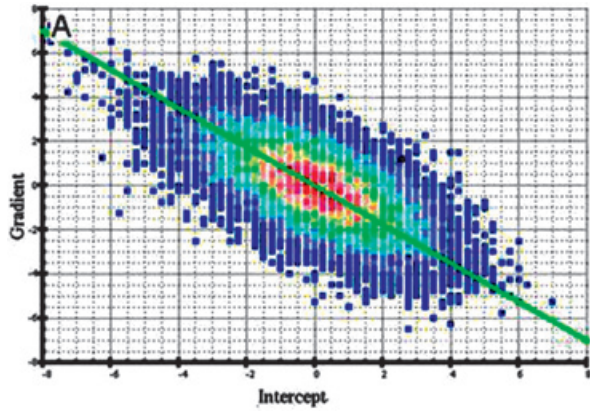


Figure 8. A) Gradient vs. Intercept cross plot B) In the orthogonal deviation section, at the top of FCO (by a white arrow) in the Ayombe-1 well (in blue) a green color is observed indicating a 4th AVO quadrant and hence a class I anomaly.

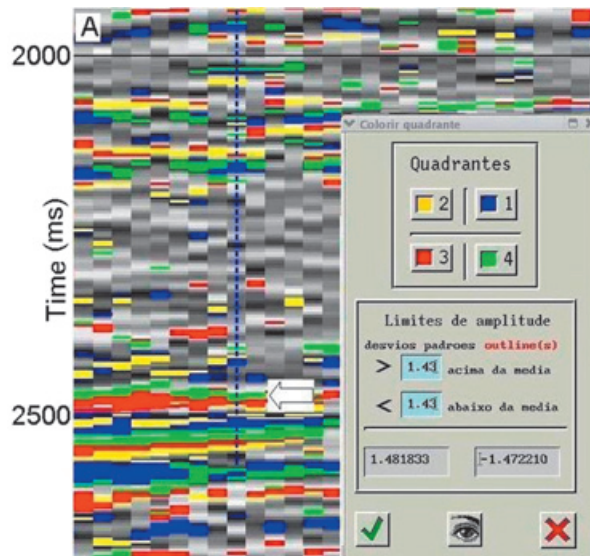
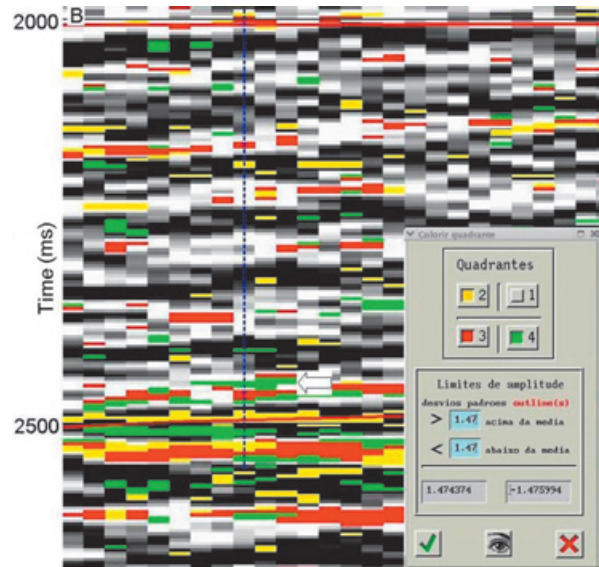
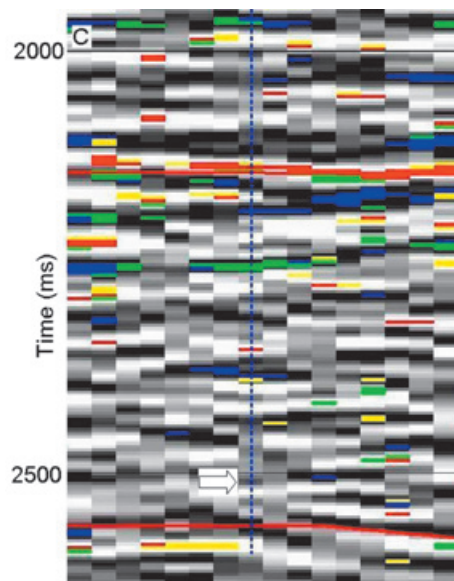
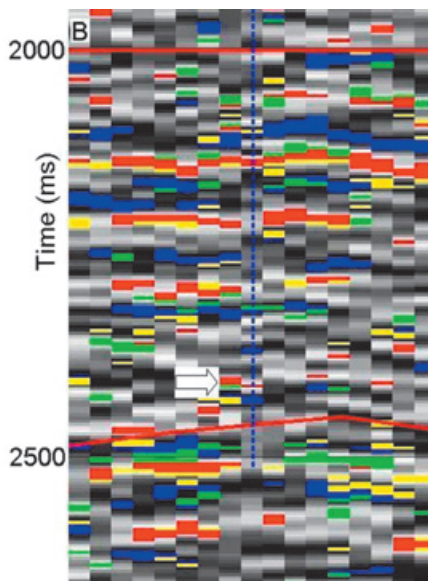


Figure 9. In each orthogonal deviation section a white arrow indicates A) at the top of the FCO a class I anomaly in line 160 B) a weak class I anomaly in line 244 and C) no anomaly in line 28.



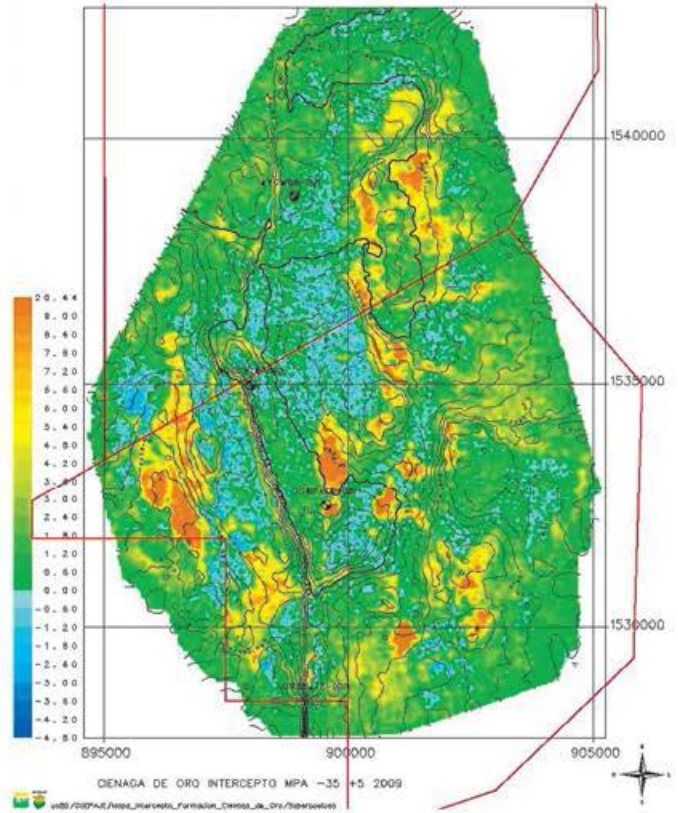
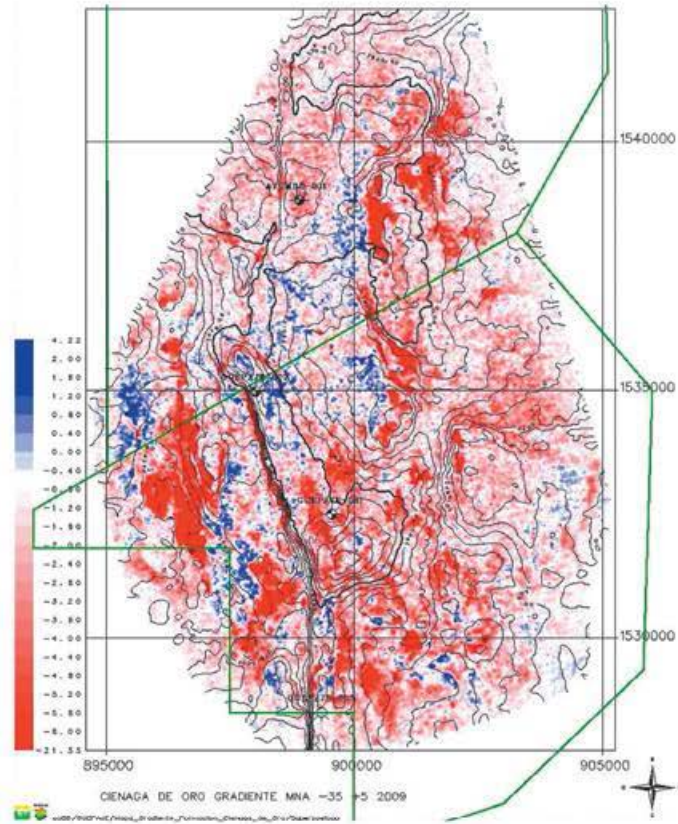


Figure 10. Maps of A) Intercept and B) Gradient at top of the Ciénaga de Oro formation. The bold contour at 2480 ms indicates the gas-water contact.

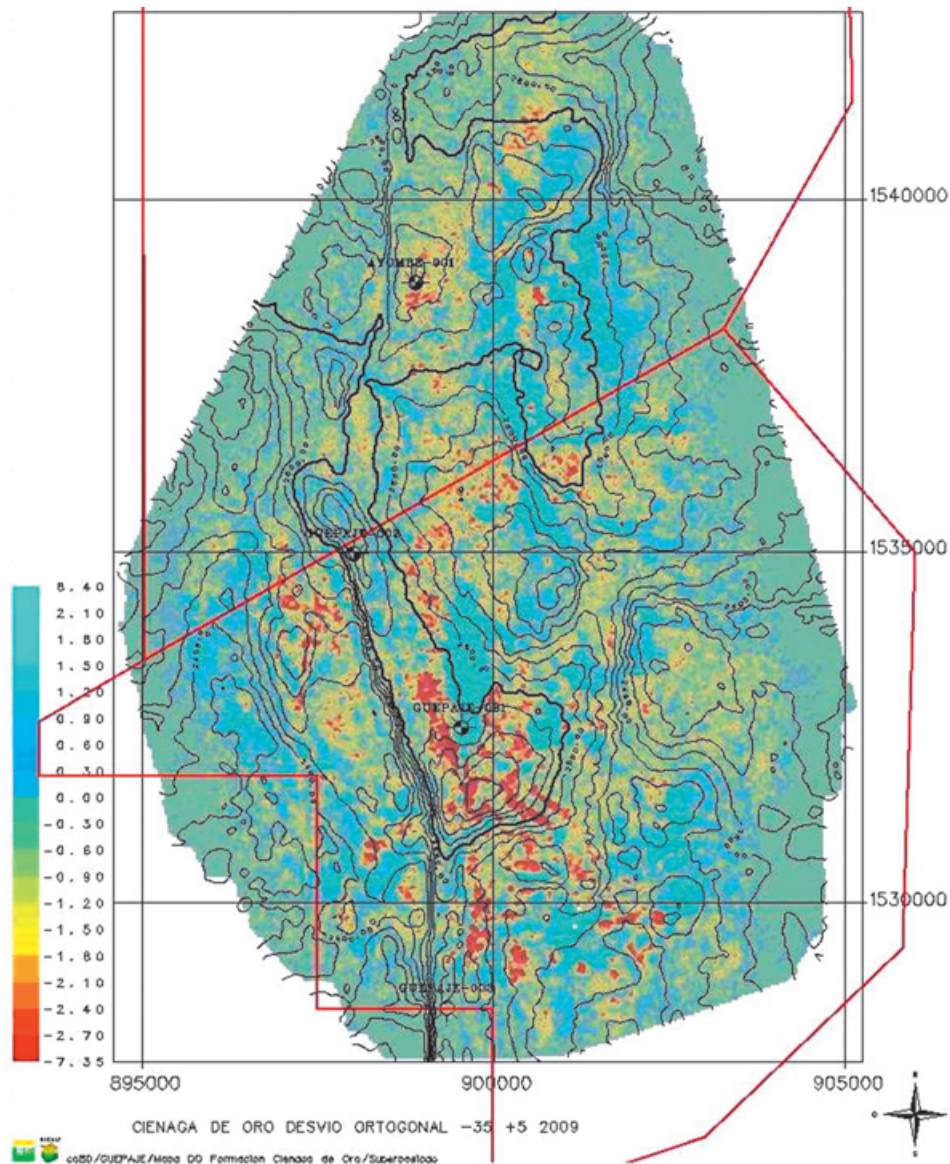


Figure 11. Orthogonal deviation map at top of FCO with the gas-water contact contour in bold at 2480 ms.

presence of negative orthogonal deviation values, with values below -1.6 in Ayombe-1 (-1.88) and Güepajé-1 (-2.66) which can be considered highly anomalous and also values above -1.6 in Güepajé-2 (-1.33) and Güepajé-3 (-0.23) which are closer to the background line.

A structural map of the surface at the top of the FCO was created, enhancing the GWC and shallowest zones, seen in Figure 12A. In order to relate the structural map with the orthogonal anomaly map, another map was created which includes only deviation anomalous values below -1.6, represented by red dots in Figure 12B. In the Ayombe-1 and Güepajé-1 wells the anomalies observed in Figure 12B indicate gas presence which agrees with observed AVO anomalies and

test drilling. Besides, a weak anomaly in the vicinity of Güepajé-2 and no anomaly at Güepajé-3 wells were observed. The correlation between the two maps shows anomalies concentrated in the zone enclosed by 2480 ms curve and in the highest areas of folded surface. Even though, there are deviation anomalies in deep areas of the folded surface.

This adverse result might be due to factors such as influence of lithology, since the top FCO is under a varying thick carbonate level. Therefore, the AVO response would be stronger than by presence of gas. Besides, variable thickness of both partial and full saturated layers in the study area may enforce tuning at the top of the FCO, obscuring the procured results.

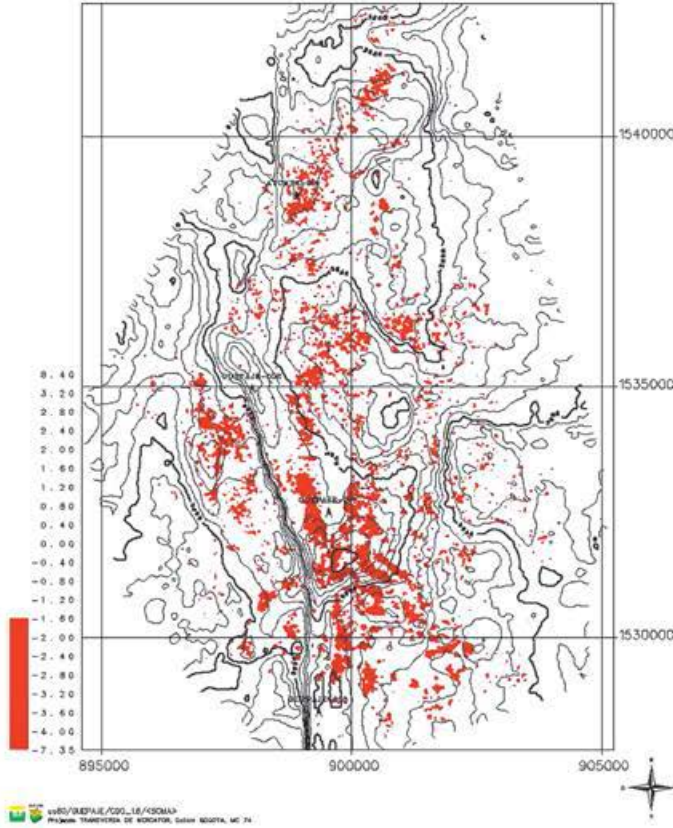
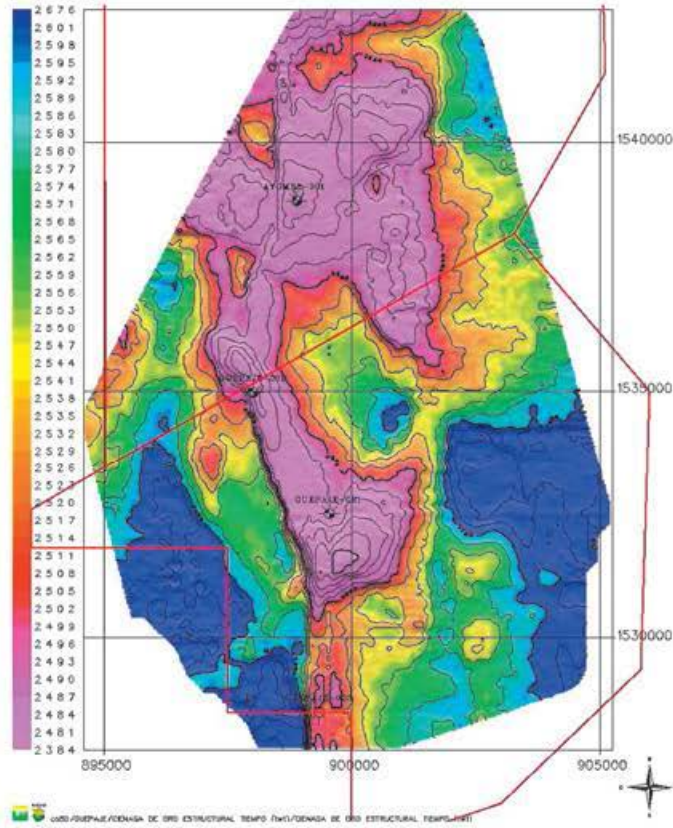


Figure 12. A) Structural map at the top of FCO correlated with B) gas anomaly map.

Conclusions

A class I AVO anomaly was identified at the top of a gas saturated zone in the Ciénaga de Oro formation by AVO modeling of the Ayombe-1 well, that showed that up to 40°, would not have a phase change occur in the presence of gas.

The AVO analysis in four 2D lines which cross or are close to the four wells, found no anomaly in the proven dry Güepajé-3 well, and class I anomalies in the Güepajé-1 and Ayombe-1 gas wells. Even with gas presence, no anomaly was observed in the Güepajé-2 well.

The substitution of gas by water in the Ayombe-1 well provided similar responses, this along with the observed anomalies point out the low sensitivity of AVO analysis for gas detection in this area.

After applied to the seismic volume of the Güepajé-3D Project, the AVO with Partial stack technique provided a gas indicator map which correlated well the structural map of the surface at top of FCO. Some anomalies were observed in zones with low probability of gas presence. This adverse result might be due to lithic factors, e.g. the carbonate layer that overlies the FCO as also the unknown varying thickness distribution in the partially and the fully saturated layers at the top of the FCO.

The technique uses stacked data with a better signal to noise ratio allowing a fast evaluation of possible anomalies in seismic sections and in maps, and besides facilitates to use a direct indicator of hydrocarbons. Its main disadvantage is its minor content of frequency, associated to the NMO stretch and losses by absorption. A dipolar sonic log would provide reliable results by diminishing the uncertainty to estimate shear wave velocity.

Acknowledgments

The authors thank PETROBRAS for the technical support rendered and for the information supplied to the project. Also, thanks to the Universidad Nacional de Colombia where the research was developed. This paper is a product of the Master's thesis in Geophysics of the Geologist Juan C. Mosquera.

Bibliography

Barrero D., Pardo A., Vargas, C., Martínez, J., 2008, Colombian Sedimentary Basins: Nomenclature, Boundaries and Petroleum Geology, New Proposal, Agencia Nacional de Hidrocarburos, Bogotá.

- Castagna J., Swan H, 1997, Principles of AVO crossplotting, *The Leading Edge*, 16, 337-342.
- Castagna J., Batzle M., Eastwood R, 1984, Relationships between compressional wave and shear wave velocities in clastic silicate rocks, *SEG Expanded Abstracts*, 3, 582-584.
- Connolly P, 1999, Elastic impedance, *The Leading Edge*, 18, 438-452.
- Gassmann F, 1951, Elastic waves through a packing of spheres, *Geophysics*, 16, 673-685.
- Greenberg M., Castagna J., 1992, Shear wave velocity estimation in porous rocks: theoretical formulation, preliminary verification and application, *Geophys. Prosp.*, 40, 195-209.
- Hilterman F., 1975, Amplitudes of seismic waves: a quick look, *Geophysics*, 40, 745-762.
- Koefoed O., 1955, On the effect of Poisson's ratio of rock strata on the reflection of plane waves, *Geophys. Prosp.*, 3, 381-387.
- Maver K., Bolding K., 2004, Simultaneous AVO inversion for accurate prediction of rock properties, *Offshore Technology Conference*, Houston, TX., OTC 16925.
- Ostrander W., 1984, Plane - wave reflection coefficients for gas sands at non-normal angles of incidence, *Geophysics*, 49, 1637-1648.
- Rosa A., Santos P., Campos R., 1999, AVO analysis with the elastic impedance concept, *VI International Congress of the Brazilian Geophysical Society*, Rio de Janeiro, 3-6.
- Rutherford S., Williams R., 1989, Amplitude versus offset variations in gas sands, *Geophysics*, 54, 680-688.
- Sánchez J., 1993, Informe Interno Final del Pozo Ayombe-1, Empresa Colombiana de Petróleos - ECOPETROL, 21.
- Shuey R., 1985, A simplification of the Zoeppritz equations, *Geophysics*, 50, 609-614.
- Smith G., Gidlow P., 1987, Weighted stacking for rock property estimation and detection of gas, *Geophys. Prosp.*, 35, 993-1014.
- Wei X., Jiang X., Booth D., Liu Y., 2006, The inversion of seismic velocity using a partial-offset stack with well-log constraints. *J. Geophys. Eng.*, 3, 50-58.

Geophysical-Archaeological Survey in Lake Tequesquitengo, Morelos, Mexico

Roberto E. Galindo Domínguez*, William L. Bandy, Carlos A. Mortera Gutiérrez and José Ortega Ramírez

Received: September 7, 2012; accepted: February 25, 2013; published on line: June 28, 2013

Resumen

En agosto del 2009 se llevó a cabo una prospección geofísica subacuática con fines arqueológicos en el Lago de Tequesquitengo, en el Estado de Morelos. El objetivo del trabajo fue localizar y delimitar los restos del pueblo que yace sumergido en el fondo del lago desde mediados del siglo XIX. Se realizó la adquisición y mapeo de datos magnéticos, batimétricos de ecosondeo monohaz y se obtuvieron imágenes de sonar de barrido lateral de 200 KHz. Para el posicionamiento de la embarcación durante la prospección se empleó un sistema de navegación marina GPS. A excepción de los restos de las estructuras culturales más grandes visibles en las imágenes de sonar, los resultados magnéticos fueron más útiles para delimitar la extensión del pueblo sumergido. Los datos muestran anomalías con longitud de onda corta alrededor y en las inmediaciones de la iglesia sumergida. Asimismo, las anomalías con los componentes de longitud de onda en la banda más corta están agrupadas en el área adyacente inmediata al este de la iglesia. Los componentes de longitud de onda corta sólo se observan alrededor de la iglesia y no en el resto del área prospectada, por lo que proponemos que éstos corresponden a restos culturales pertenecientes al pueblo sumergido.

Palabras clave: Lago de Tequesquitengo, México, Geofísica, Arqueología, Magnética.

Abstract

In August 2009, a marine geophysical survey was conducted in Lake Tequesquitengo (located in the state of Morelos, Mexico) to delineate the extent of the remains of a small town that has been submerged since the mid 19th century. The survey consists of the acquisition and mapping of magnetic, single beam bathymetric and side-scan sonar data. A dual receiver marine GPS navigation system was used to position the boat during the survey. Except for the larger structural remains that are visible on the side scan sonar images, the magnetic anomaly map proved to be most useful in delineating the extent of the town. These anomalies exhibit short wavelength components in the area surrounding a submerged church, with the shortest wavelength components being confined to the area immediately east of the church. These short wavelength components are only observed near the church; therefore, we propose that they delineate the buried remnants of the submerged town.

Key words: Lake Tequesquitengo, Mexico, Geophysics, Archaeology, Magnetic.

R. E. Galindo Domínguez*
W. L. Bandy
C. A. Mortera Gutiérrez
Instituto de Geofísica,
Universidad Nacional Autónoma de México,
Ciudad Universitaria
Delegación Coyoacan, 04510
México D.F., México
**Corresponding author: rgalindo@geofisica.unam.mx*

J.Ortega Ramírez
Geophysics Laboratory
Instituto Nacional de Antropología e Historia
México D.F., México

Introduction

Marine geophysical techniques are useful to locate and map archaeological sites submerged in lakes (e.g. Cassavoy and Crisman, 1988; Crisman, 2005). However, few such studies have been attempted in Mexican lakes, many of which may contain significant archaeological remains and artifacts. In August 2009, the first marine geophysical-archaeological survey within Lake Tequesquitengo, located in Morelos, Mexico (Figure 1), was undertaken by students and investigators from the Instituto de Geofísica, UNAM. Since the middle part of the 19th century, a small colonial-style town has been submerged in the southernmost part of this lake where the church tower and some of its walls and columns are still observed. These structures have been previously mapped; however, the full extent of the town has yet to be determined. The purpose of the study is to define using geophysical methods (total field magnetic, bathymetry, and side scan sonar) the extent of the submerged town. The results should prove useful for planning future archaeological dives in this area.

Preliminary results of this work have been presented in Galindo *et al.* (2009), Galindo (2012) and in the thesis of Galindo (2011). Herein we present these results in a more concise, readily available form along with previously unpublished results of an analysis of the spatial wavelength components of the magnetic anomalies.

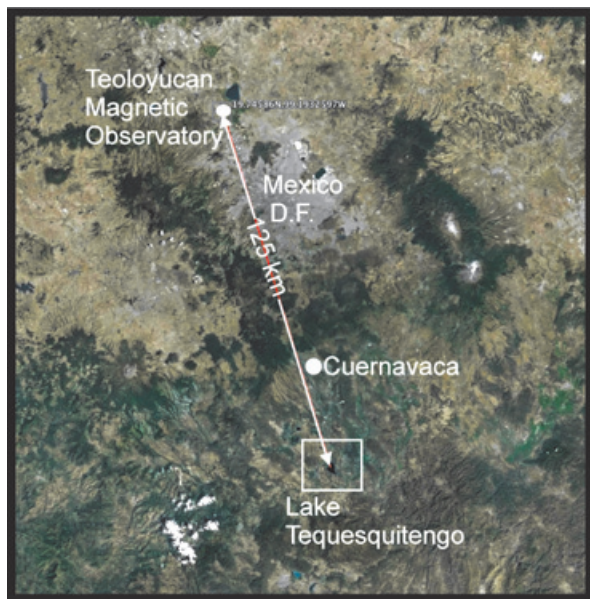


Figure 1. Location of Lake Tequesquitengo south of Cuernavaca and the Teoloyucan Magnetic Observatory located in the NW corner of Mexico D.F. (Background map from Google Earth).

Previous Work

The most prominent cultural remains are associated with a submerged church located within the southernmost part of Lake Tequesquitengo (Figure 2). The church lies on a small bathymetric high at about 2057160m N, 471940m E (UTM zone 14Q): which is the position of the navigation buoy marking the bell tower as determined using a single frequency GPS. With the exception of equipment testing, no detailed geophysical survey has been previously conducted in the lake. However, two separate groups have conducted professional underwater archaeological surveys (dive surveys) in the area around the church. In the latter part of 1987, the PROTEO group (Lowenstein *et al.*, 1991) began a 5-year, systematic survey ("Proyecto Pueblo Hundido de Tequesquitengo") of the area around the submerged church. They found a major concentration of cultural remains located in a 20m x 20m area (400 m² area) corresponding to the remains of the church (the bell tower, walls, columns, etc.). They also report a second area of cultural remains, which they called "La Casa del Cura" (possibly the remains of the Presbytery), located 15 meters north of the bell tower, which covers an area of about 200 m². The plan, constructed by the PROTEO group, of the structures found in the area of the church tower and their relation with the Presbytery is presented in Figure 3a. The area encompassing both structures is roughly 55m in the N-S direction by 45 m in the E-W direction (Figure 3b).

The second group of investigators, headed by Biologist Virginia Urbieta, extended the search area of the PROTEO group (Figure 4). They found cultural remains (e.g., columns, remains of walls and a small shelter, etc.) in the area surrounding the sites mapped by PROTEO. Specifically, remains were mapped up to 30 meters north of the Presbytery and up to 30 meters south and west of the bell tower. Thus, the results of the archaeological dives have established that cultural remains exist for a distance of at least 60 meters north of the bell tower, 40 meters south of the bell tower, 40 meters west of the bell tower, and 15 meters east of the bell tower: an area of about 5,500 m². Of importance to our study is that Urbieta's group detected the upper parts of some buried structures east and NE of the church; thus, it is quite possible that the remains extend farther from the mapped area, especially in the deeper parts of the lake located to the east and northeast of the church where artifacts may be completely covered by sediments.

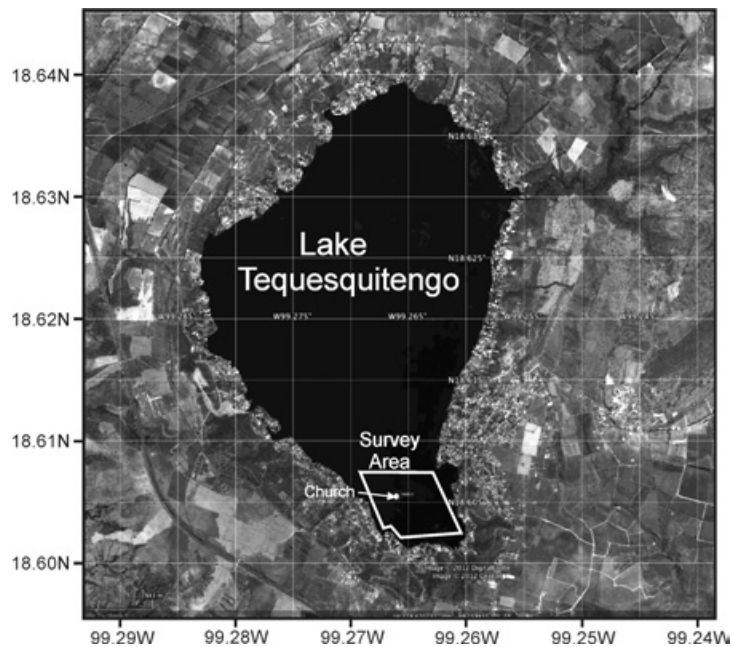


Figure 2. Location map of the survey area and submerged church (Background map from Google Earth).

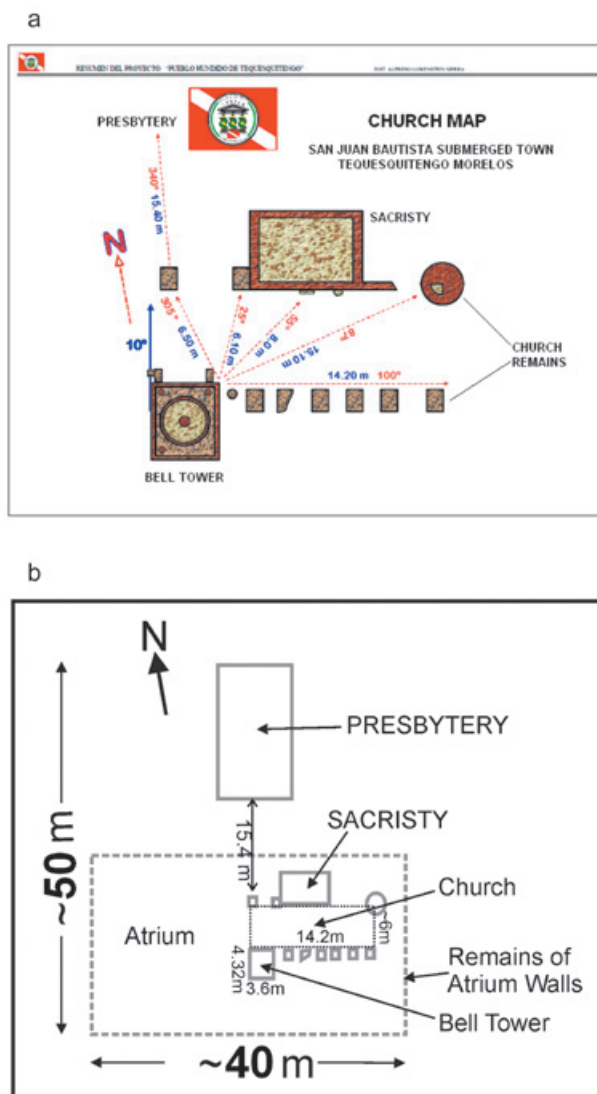


Figure 3. Archaeological site plans illustrating the relative positions of the major structural remains. A) San Juan Bautista Church as mapped during the PROTEO surveys (Lowenstein *et al.*, 1991). B) Church and Presbytery.

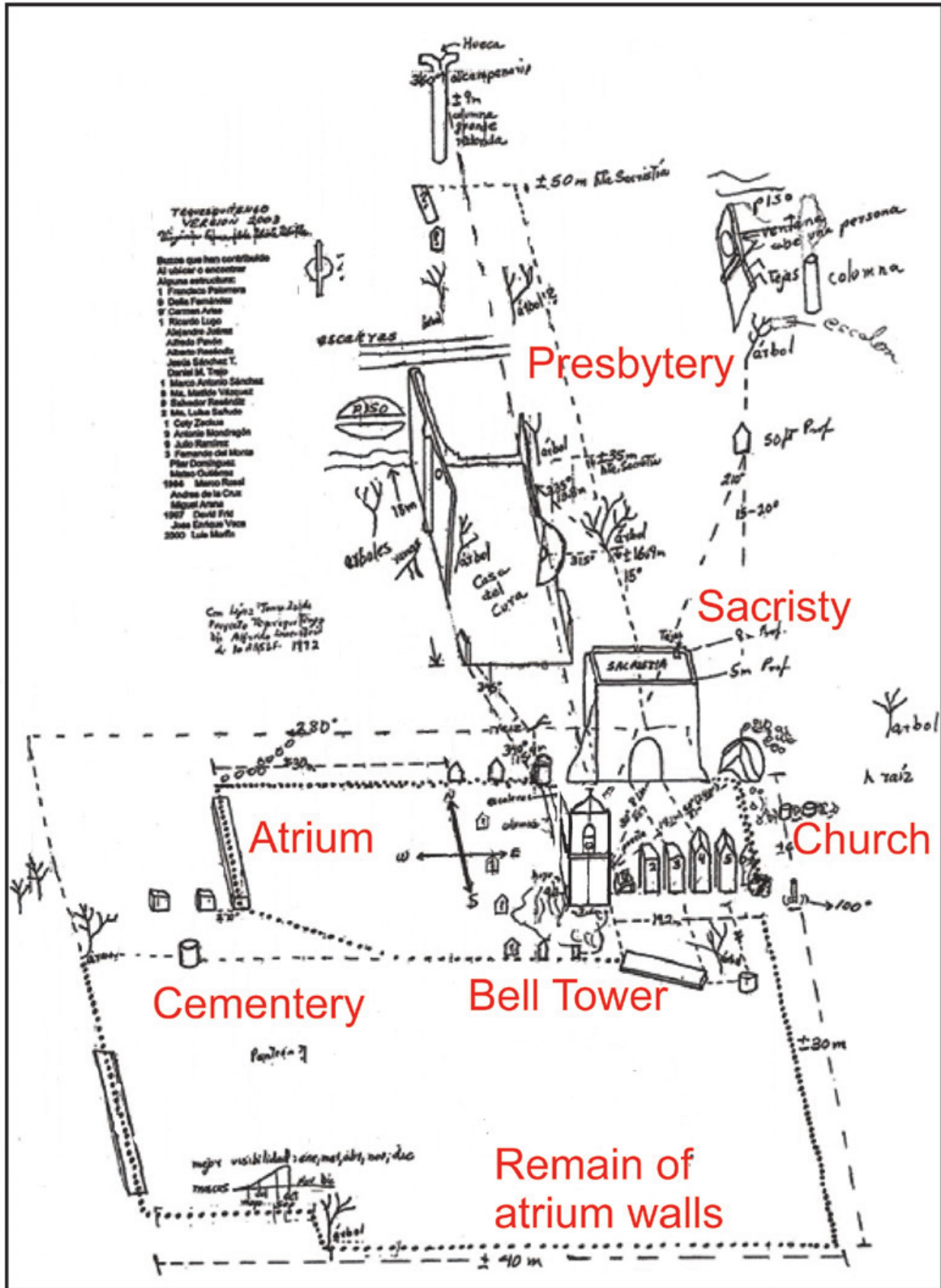


Figure 4. Map of the church and surrounding areas as determined by the group headed by Virginia Urbieto (unpublished map graciously provided by Virginia Urbieto).

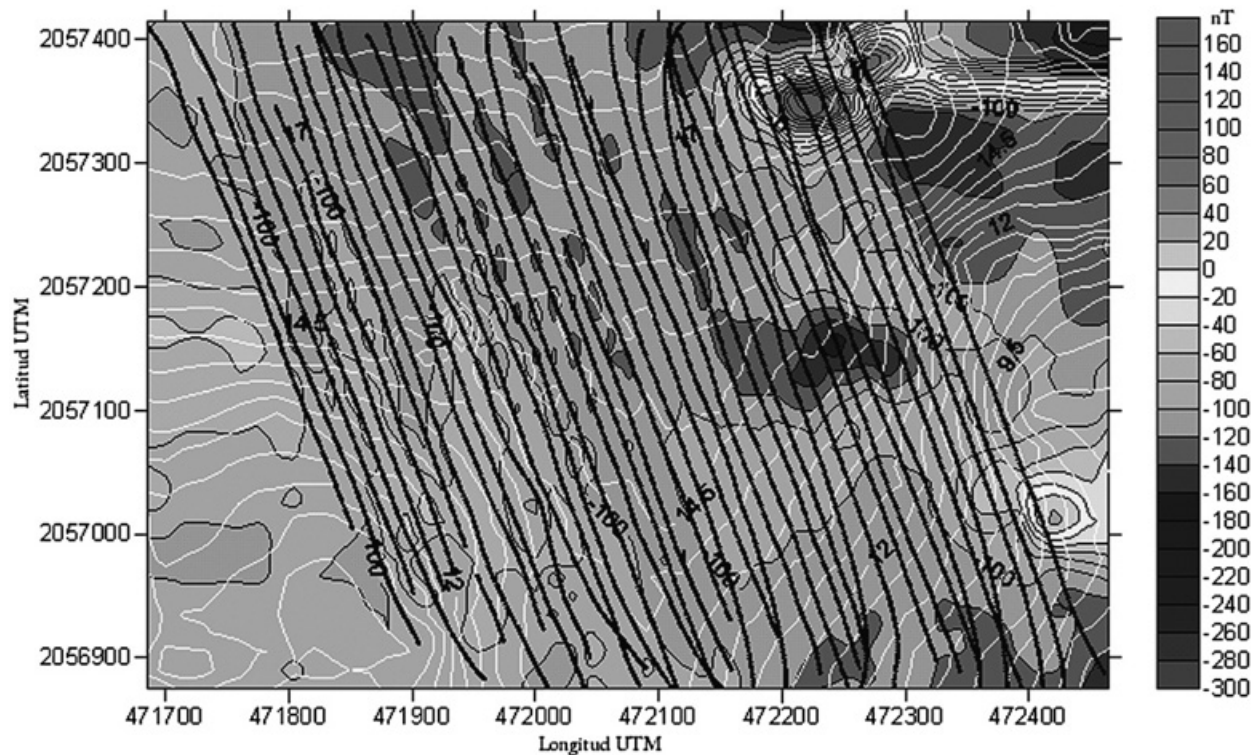


Figure 5. Survey lines superimposed on the magnetic contour map (black-shaded contours) and bathymetric contours (white contours) constructed from the data collected during the survey.

Geophysical Survey

The main survey covered an area of 284,640 m² in the southernmost part of the lake (Figure 2). Total field magnetic measurements, bathymetry, side scan sonar data collected along 36 parallel lines oriented at an azimuth of 339° were used in the present analysis (Figure 5). The profiles have an average length of 593 meters with a planned line spacing of 15 meters.

The boat used in the survey was the "Barracuda" (Figure 6) which was graciously provided by the port captain of Tequesquitengo. The position of the ship during the survey was determined using the *Kongsberg* SEAPATH20 dual GPS receiver, marine navigation system which provides the boats heading, position and speed. The navigation data was displayed in real time using the Nobeltec navigation program which was used by the captain as a helmsman's display, which helps the captain to keep the boat on the survey line.

The total field magnetic data was collected using the *Geometrics Model G877* marine proton precession magnetometer, which has a resolution of 0.1 nT (Breiner, 1973). The sensor, which is connected to the recording computer by an electrical/strength cable, was towed a distance of 50 meters behind the boat

to minimize the magnetic noise generated by the boat and its' motor. Non-metal floats were mounted to the cable to keep the sensor at a depth of 1 meter so that the cable and sensor would not hit the lake bottom during turns nor snag on submerged objects. The magnetic data was recorded at a sampling rate of 2 seconds using the *Geometrics Mag Log Lite* program. This program also calculates and records the position of the magnetic sensor using the Ship's navigation data. Magnetic data was not recorded



Figure 6. Photo of the "Barracuda" taken during installation of the equipment.

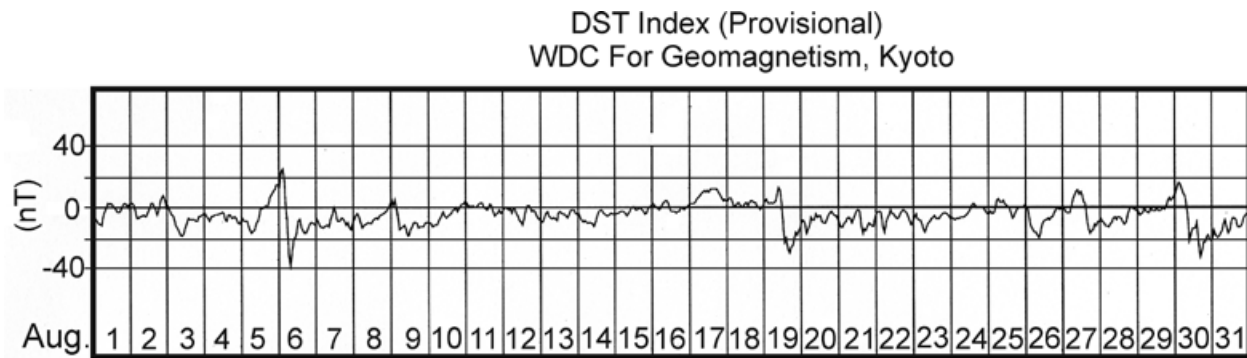


Figure 7. Graph of the equatorial DST Index versus time (GMT) for August 2009. Data obtained from the Kyoto Observatory [<http://swdcwww.kugi.kyoto-u.ac.jp/dstdir/index.html>].



Figure 8. Photographs of the survey equipment. Left side, EA600 echosounder transducer. Right side, Sidescan sonar transducers.

while the boat was turning to the next line. During the survey, the DST (Disturbance Storm Time) index data from the Kyoto observatory, Japan, was periodically checked to make sure that no magnetic storm was occurring during data acquisition. The plot (Figure 7) of the DST index for August 26 and 27, 2009 illustrates that the data collected during our survey were not perturbed by any magnetic storms.

Bathymetric data and side scan sonar data was obtained using the *Kongsberg EA 600* (Kongsberg, 2004, 2007) combination single beam echo-sounder and side-scan sonar system. The frequency of the two side-scan transducers is 200 KHz (Figure 8). The transducer for the echo-sounder can be driven at either 38 or 200 KHz; during the survey the 200 KHz option was used.

Total Field Magnetic Data Processing

A contour map of the raw uncorrected total field magnetic measurements of the survey is presented in Figure 9a. In addition to the

magnetic field produced by the cultural artifacts of the town (which is what we are interested in), the raw data measured by the proton precession magnetometer includes a component due to the Earth's main field, a component due to the Sun which causes fluctuations (diurnal variations) in the Earth's magnetic field by inducing currents in the ionosphere (Otaola, et al., 1993; Blakely, 1996), a component due to the ships' heading (or sensor orientation), and a component due to other ship effects (which we assume to be small as the sensor was towed 50 meters behind the boat). Thus, to determine the magnetic field produced by the cultural artifacts, we must first remove all the other components as best we can, or in other words, we must reduce the measured values to magnetic anomalies.

Removal of the Earth's main field (IGRF)

The first step in the reduction of the raw data is to remove the contribution of the Earth's main field. This is accomplished by estimating the value of the Earth's main field at the location and time of each measurement using model 11 (IAGA, Working Group V-MOD, 2010) of International Geomagnetic Reference Field (IGRF11) and removing this value from the measured value. The Fortran source code of the IGRF11 subroutine was obtained from <http://www.ngdc.noaa.gov/IAGA/vmod/igrf.html>. A main driver was written to adapt the subroutine for use in reducing marine data. Figure 9b presents a contour map of the total field data corrected for the contribution of the Earth's main field.

Correction for Diurnal Variations

The next step in the reduction procedure is to remove the diurnal variations from the IGRF-corrected values. To accomplish this, the total field magnetic data for the survey dates were obtained from the magnetic observatory at Teoloyucan (a permanent magnetic observatory maintained by the Instituto de Geofísica, UNAM)

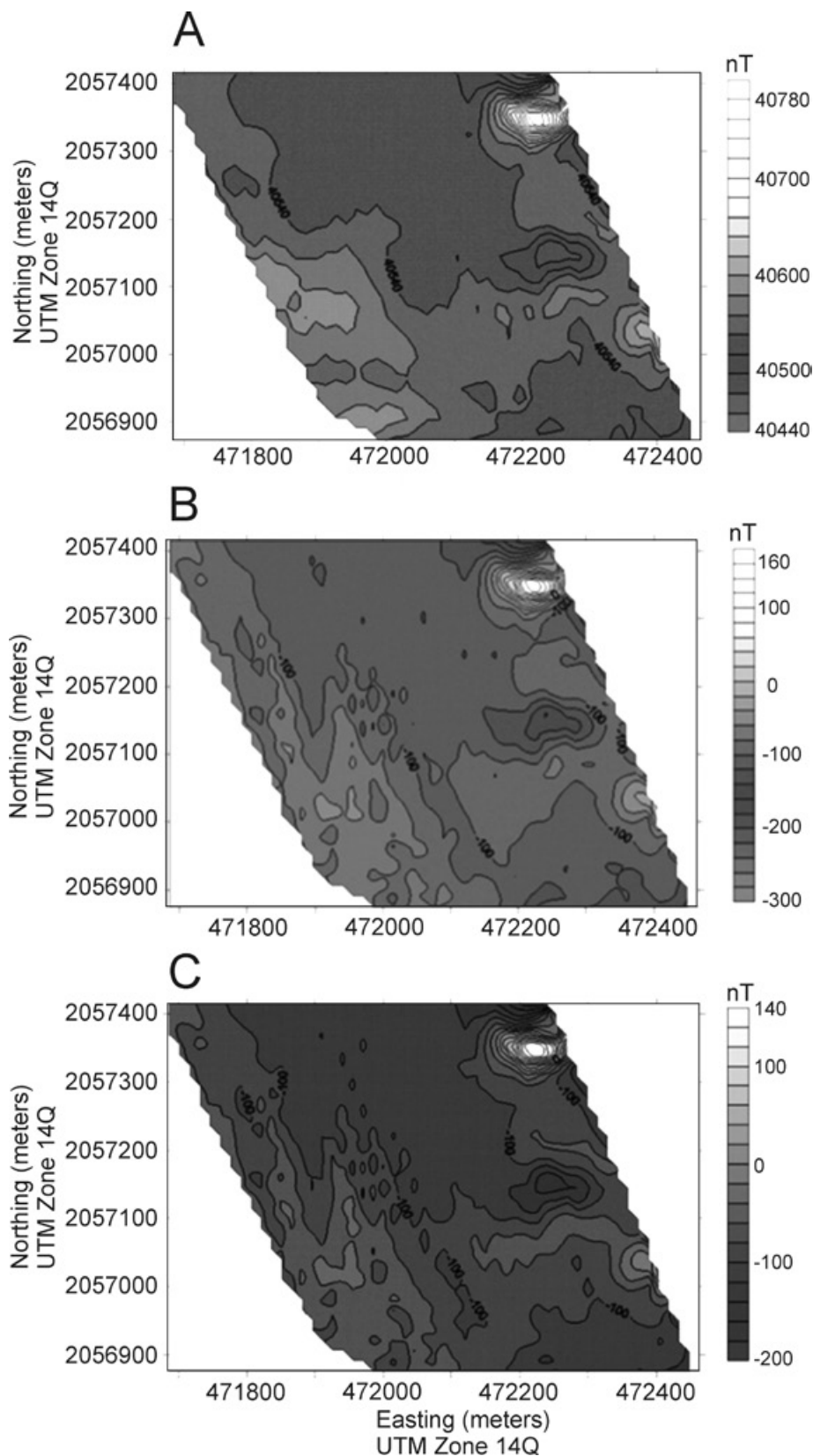


Figure 9. Contour maps of the magnetic data at three processed stages. A) A contour map of the raw uncorrected total field magnetic measurements. B) Contour map of the total field data corrected for the contribution of the Earth's main field. C) Contour map of the total field values corrected for both the IGRF and diurnal variations.

which is located at $19^{\circ} 44' 45.100''\text{N}$, $99^{\circ} 11' 35.735''\text{W}$, 125 km from Lake Tequesquitengo (Figure 1). These data were corrected for the IGRF again using the IGRF11 model for the Earth's main field and the high frequency components of the Teoloyucan data were removed by fitting a polynomial (magnetic value as a function of time) to the data. The resulting values are assumed to represent the low frequency diurnal variations at the survey area. Each measured value was then corrected using the polynomial value corresponding to the time of the measurement. A contour map of the total field values corrected for both the IGRF and diurnal variations is presented in Figure 9c.

Correction for Ship's Heading

The procedure used herein to make the heading corrections is based on the mis-tie correction algorithm of Bandy *et al.* (1990), modified so that it could be applied to grids (Bandy *et al.*, manuscript in preparation). The procedure is as follows. The survey is separated into two groups of lines, all lines in each group having roughly the same overall heading, and hence the same heading error. The two data groups

are gridded separately using the exact same grid specifications for both grids, and the mean difference between the two grids is determined. The heading corrections are then applied by adding one half of the mean difference to the data of one of the group and subtracting one half of the mean difference from the data of the other group (similar to equations 15a and 15b of Bandy *et al.*, 1990). The corrected data of the 2 groups are then re-combined and the entire data set is gridded. A contour map of the final magnetic anomalies (i.e. after correcting the raw data for the Earth's main field, diurnal fluctuations and ship's heading) is presented in Figure 10. The area marked by the rectangle is the area where the principle cultural remains, such as the church, have been found and mapped during previous dive surveys. The area enclosed by the circle is interpreted from the magnetic characteristics to be the area most likely to contain additional cultural artifacts. It is interesting to note (Figures 9 and 10) that the magnetic signature of this zone has been progressively clarified at each step of the reduction of the raw data to anomaly values as is expected if the signature is due to real sources.

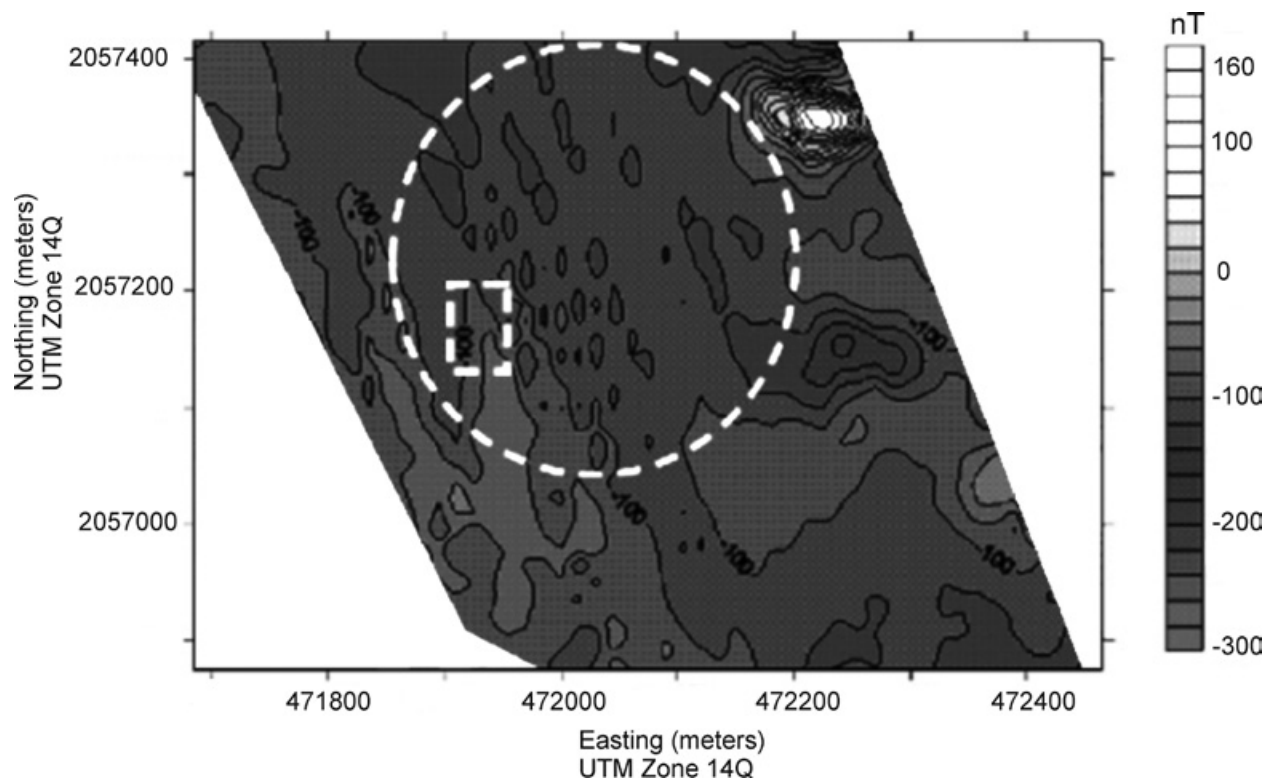


Figure 10. Contour map of the final magnetic anomalies (i.e. after correcting the raw data for the Earth's main field, diurnal fluctuations and ship's heading). The rectangle delineates the area mapped by previous dive surveys. The area enclosed by the dashed circle is the area that we propose to contain cultural remains.

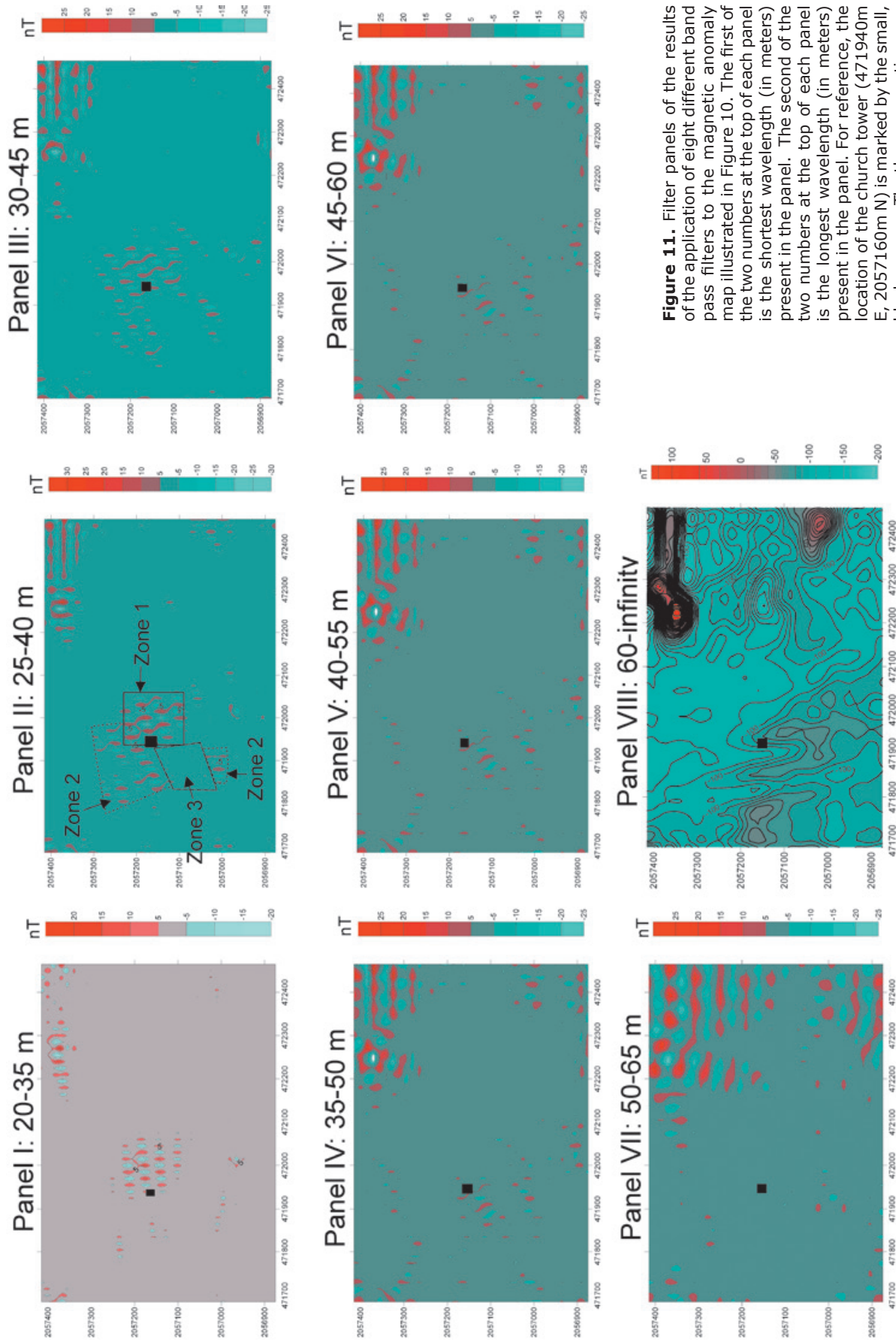


Figure 11. Filter panels of the results of the application of eight different band pass filters to the magnetic anomaly map illustrated in Figure 10. The first of the two numbers at the top of each panel is the shortest wavelength (in meters) present in the panel. The second of the two numbers at the top of each panel is the longest wavelength (in meters) present in the panel. For reference, the location of the church tower (471940m E, 2057160m N) is marked by the small, black squares. The three magnetic zones surrounding the church are illustrated in panel II. See text for more details.

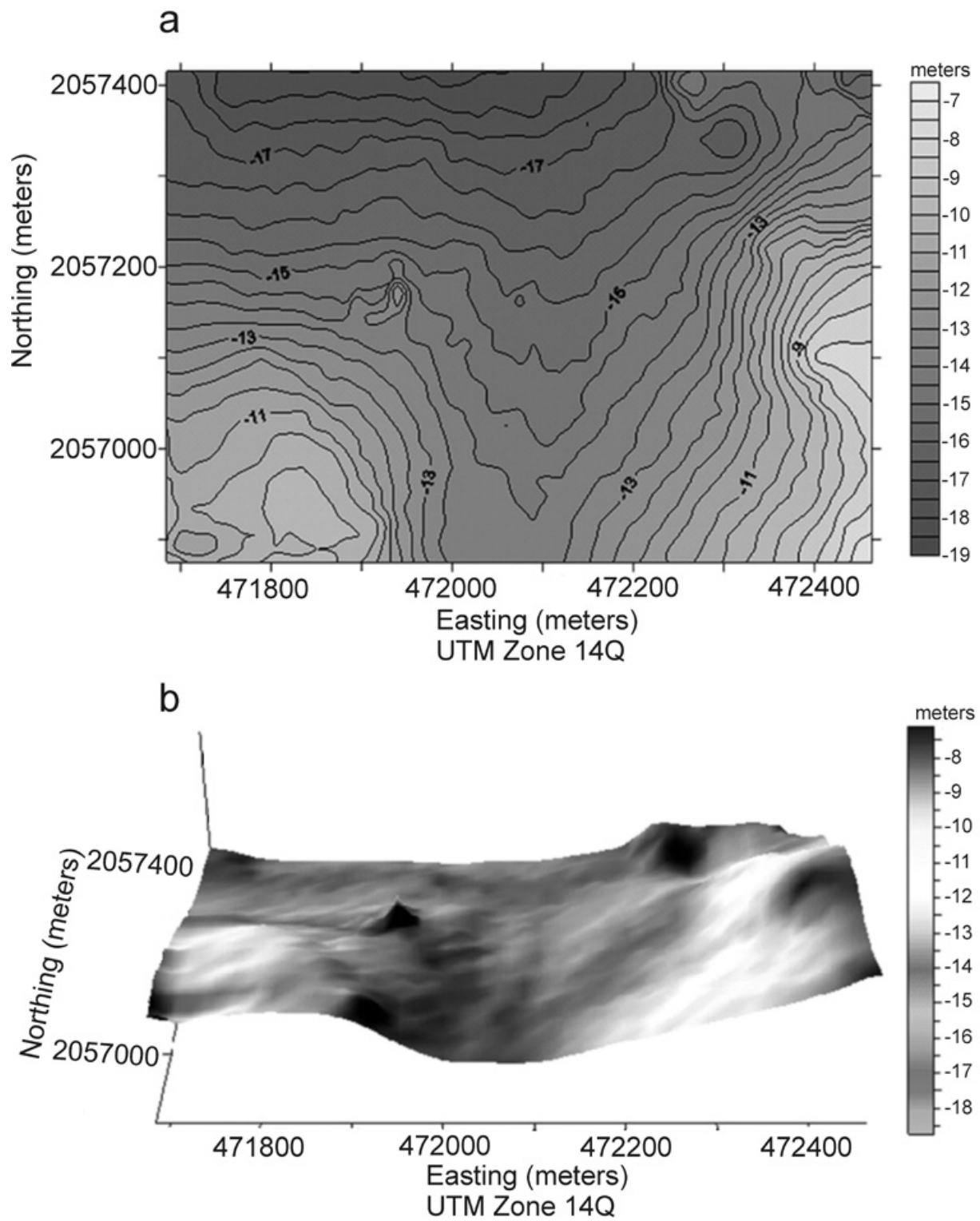


Figure 12. Newly constructed bathymetric map of the survey area. A) Contour representation. B) 3-D surface representation. Note the small high to the west where the remains of the church are located.

Frequency Filtering

Wavelength filtering was applied to the gridded data which was used to produce the map shown in Figure 10 to better isolate those anomalies associated with the remains of the town. The spacing between grid nodes was in all cases 15 meters to coincide with the spacing between survey lines. Thus, the minimum resolvable component wavelength is 30 meters. Filtering was accomplished using the program FFTFIL which is included in the Potential-Field geophysical software version 2.0 obtained from the United States Geological Survey (Hildenbrand, 1983; Cordell *et al.*, 1992).

Figure 11 illustrates the application of eight different trapezoidal, band pass filters. The two numbers at the top of each panel are the limits of the wavelengths which are entirely removed by the filter. In all filters, a 5 meter linear ramp has been applied at each end of the filter. Thus, for example, in the filter used to produce Panel IV wavelengths between 40 and 45 meters were passed with no reduction of amplitude, and frequencies less than 35 meters and greater than 50 meters were completely removed. Also shown in the panels is the location of the church tower (filled square) for reference.

Bathymetry and side scan sonar images of the site

Single beam echo-sounder bathymetric data and side scan sonar images were collected concurrent with the magnetic data using the Kongsberg EA-600 echo sounder including its side scan option. The bathymetric contour map and surface relief illustration of these data are presented in Figures 12a and 12b, respectively. Water depths range from 10 meters in the eastern and western margins of the southern part of the survey area to 18.5 meters to the north. A small bathymetric high (values reaching up to -13m) is present between the -13.5m and -14m contours in the left-central part of the map, with the bathymetric expression of the church easily noted at UTM 2057160m N, 471940m E. The bell tower of the church and several other large structures are also clearly imaged on the bathymetry and sidescan records (Figure 13). The sidescan images were featureless in the deeper parts (>10 m) of the survey area, even in areas where we knew that a 50 gallon barrel was present on the lake floor. This result is puzzling as the sidescan images in the shallow water areas clearly imaged channel cuts and differences in reflectivity of the lake floor. Given the good images of the lake floor in shallow water and the good images of the bell tower, we conclude that the system was working and we suspect that the poor images in deeper

water may be due to a strong stratification of the water column which prevented the sound from reaching the bottom. Alternatively, there may be a thick layer of mud or suspended sediments in the deeper parts of the lake which, given the high frequency (200 kHz) of the sidescan transducers, may be masking the barrel and other objects on the lake floor.

Results and Discussion

The major cultural remains (church, Presbytery and the remains located north of the Presbytery) determined by the previous dive surveys covers an area of about 65 m in the north-south direction and 20 meters in the east-west direction, a total

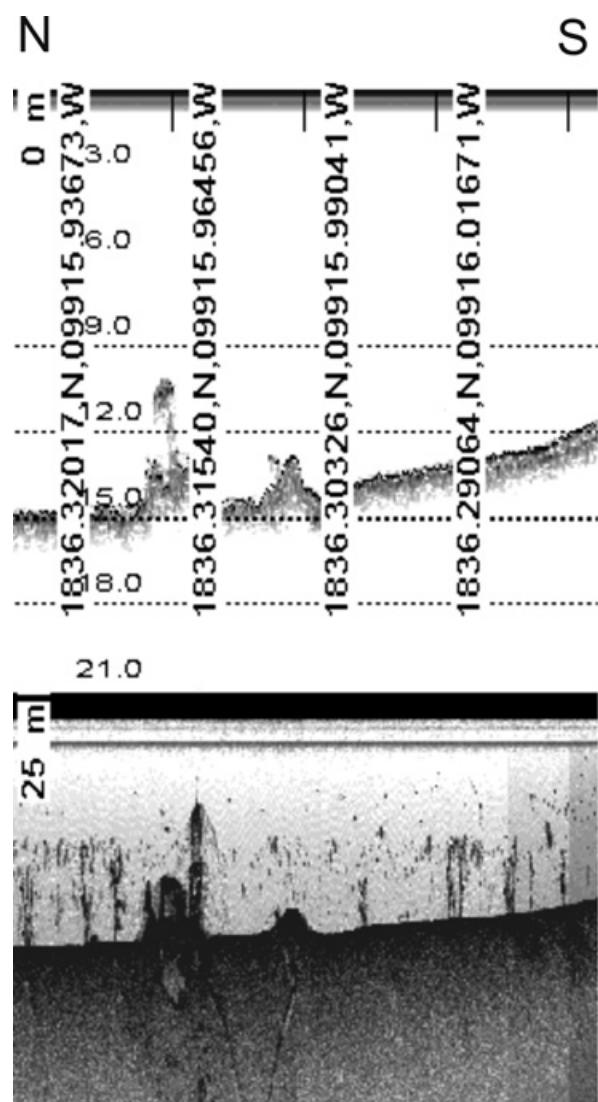


Figure 13. EA600 bathymetry profile (top) and associated side-scan sonar image (bottom) of the remains of the church. Note: the church tower on both profiles is aligned. The church tower is the highest structure extending from the lake floor on the left side of both images.

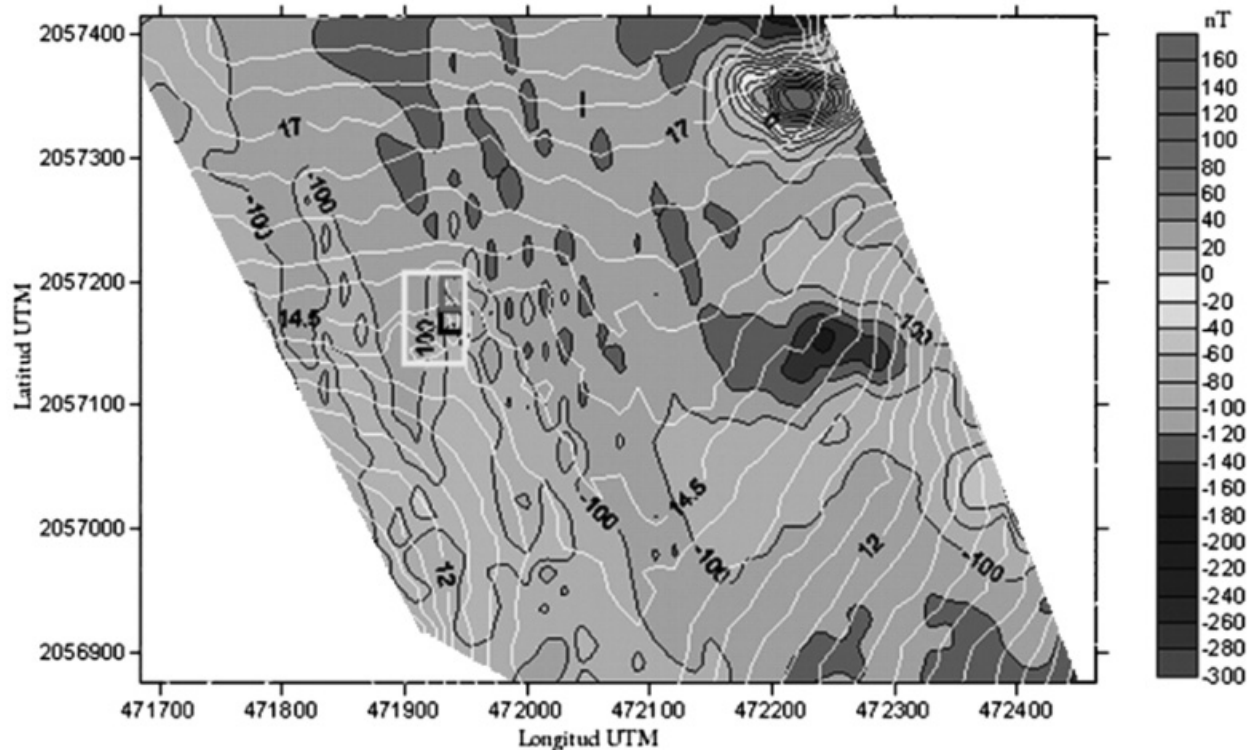


Figure 14. Filled magnetic contour map with bathymetric contours (white lines) superimposed. Small black box is the area (20m x 20m) of the remains of the church. Red box (45m x 20m) is the area of the remains of the Presbytery and the remains just to the north mapped by Virginia Urbietta. Big yellow box is the over-all area mapped during the two dive surveys.

area of 1300 m². To compare the magnetic anomalies with the cultural remains, this area is superimposed on the bathymetry and magnetic anomaly contours (Figure 14). Most notable is that the magnetic anomalies are markedly different in the area immediately north and east of the church, towards the deeper part of the survey area, than those observed in the rest of the survey area. Specifically, in the area immediately north and east of the church, the anomaly pattern consists of low-amplitude, short-period anomalies forming a “checkerboard” pattern. In marked contrast, no short period anomalies are observed in the eastern half of the survey area farther away from the church. Instead, that area contains only a few, very high amplitude (-180 to 160 nT), longer wavelength anomalies. [Concerning the very high amplitude anomaly located in the NE corner of the survey, given its very large amplitude and its location adjacent to a hotel that was in the process of being renovated at the time that the survey was conducted, we conclude that this anomaly most likely is not associated with artifacts of the submerged town. Consequently, this anomaly is not considered further in this paper.] South of the church some low amplitude, short period anomaly are observed but they do not form a checkerboard pattern. Immediately west of the church no short period anomalies

are observed. This spatial distribution of the magnetic anomalies suggests that the remains of the settlement were confined mainly to the area east of the church where the checkerboard pattern of anomalies is observed.

The above inference that the remains of the town are confined to the area east of the church is somewhat unexpected as settlements of this period commonly surrounded the church. To check the validity of this inference, the magnetic anomaly map was band pass filtered at eight different frequency bands (Figure 11). Based on the spatial distribution of the various wavelength components (and their amplitudes) comprising the magnetic anomalies, we delineate three distinct zones in the vicinity of the church. These zones are outlined in Panel II of Figure 11.

The first zone, Zone 1, corresponds to the area of the “checkerboard” magnetic anomaly pattern. It is best defined in Panel I, although the anomalies in Zone 1 have wavelength components in the 30 to 45 meter band (Panels I, II and III). Panel I indicates that the church is located on the western margin of this zone and that the zone extends approximately 120 meters east of the church, and roughly 70 meters north and south of the latitude of the church. Thus, this

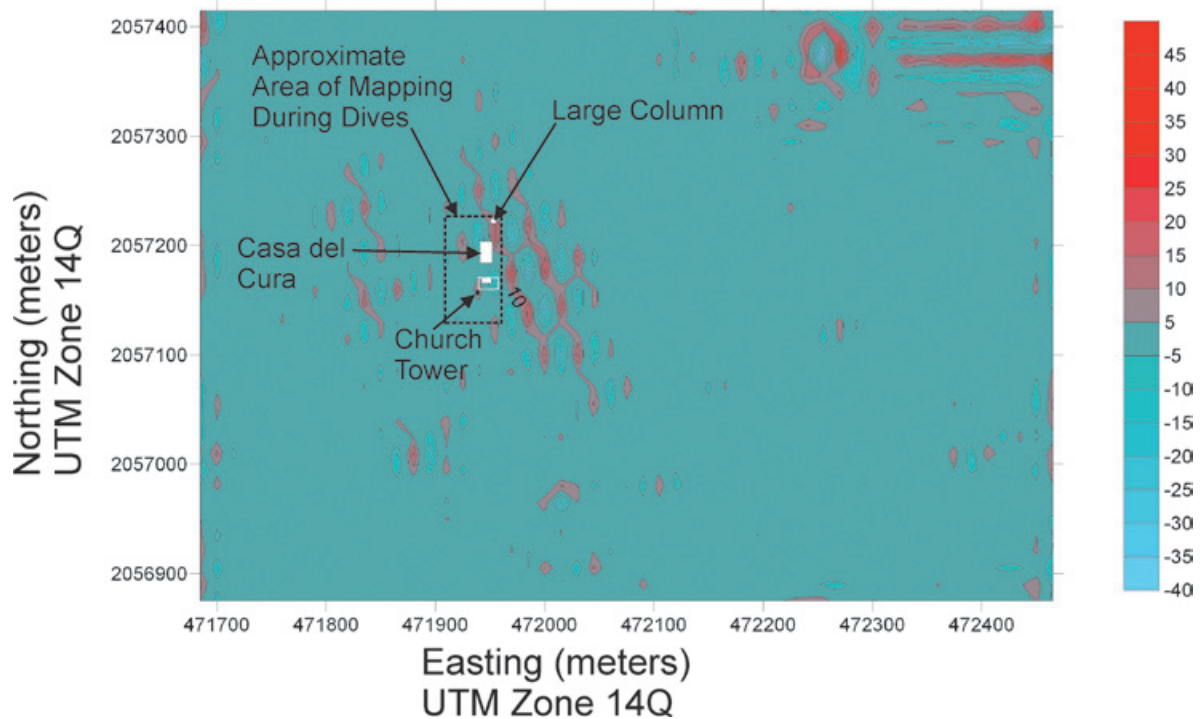


Figure 15. Major cultural remains mapped during the dive surveys superimposed on the band pass filtered magnetic anomaly map, the corner frequencies of the filter being 20, 25, 40, 45 meters (i.e. combination of panels I, II, and III, Figure 11) box is the over-all area mapped during the two dive surveys.

zone covers an area of roughly 16,800 m². The amplitudes of the wavelength components in this zone are the highest of the three zones, so much so that these anomalies are readily apparent on the unfiltered data (Figure 10). Amplitudes within the 20 to 35m, 25 to 40m and 30 to 45m band are -15 to 10nT, -20 to 15 nT and -10 to 5 nT, respectively. It is clear that these short wavelengths appear nowhere else in the survey area except in the area adjacent to the church. This strongly suggests that these anomalies can be attributed to the remains of the town.

The second zone, Zone 2, lies northwest of the church. Here, the component wavelengths of the anomalies are somewhat longer at the low end of the spectrum than those of Zone 1, lying in the 35 and 45 meter band (Panels II and III). Zone 2 also differs from Zone 1 in that the amplitudes of the wavelength components are less. Specifically, within the 25 to 40m and 30 to 45m bands the observed amplitudes are -10 to 10nT and -5 to 5nT, respectively. There is also a smaller area much further to the south at 2057000m N, 471900m E which exhibits similar component wavelengths, but with very low amplitudes (-5 to 5nT).

The third zone, Zone 3, is located immediately SW of the church. Here, the component wavelengths are significantly longer, lying in the

45 and 60 meter band (Panels IV, V and VI), than those observed in the other two areas. The amplitudes of the component wavelengths are also quite low, ranging from -5 to 5 nT.

Panel VII illustrates that there is no energy in all three zones for component wavelengths of between 50 and 65 meters. Panel VIII illustrates the long wavelength components (>60 meters) which are most likely related to the local geology and not to the remains of the town.

From the above analysis, we conclude that anomalies with wavelengths of between 30 and 45 meters found in Zones 1 and 2 most likely reflect the presence of cultural remains. The anomalies with wavelengths between 45 to 60 meters observed in Zone 3 may also reflect the presence of cultural remains; however, this is not entirely clear as we cannot relate such long wavelengths to any structure previously observed in the past dive investigations. However, it is quite possible that many more artifacts may be buried beneath the lake sediments.

For the sake of discussion, the major cultural remains mapped during the dive surveys are superimposed on the band pass filtered (30 to 45 m band) magnetic anomaly map (Figure 15). In contrast to what was inferred from the unfiltered magnetic anomaly map, the band pass filtered

map now shows that the anomalies are more or less centered about the church, as is more common for settlements of this period.

The church and the "Casa del Cura" are associated with anomalies roughly corresponding to their size. The amplitudes of these anomalies range from -15 to 15 nT. In general, the area within the dive site south and southwest of the church (corresponding to the cemetery, Figure 4) contains less anomalies than the area north of the church within the dive site. This is consistent with the amount of cultural remains found during the dives.

Of obvious interest to the underwater archaeologists working this site is the best location for future dives. Given the amplitudes of the anomalies illustrated in Figure 15 we propose that the area due east of the church tower (at 2057175m N, 471985m E) and the area immediately SE of that point are most likely to yield significant cultural remains. The anomalies in that area contain the shortest wavelength components and highest amplitudes (-25 to 20nT) of all of the areas adjacent to the church. The area NW of the church would be our second choice for a dive site as anomalies in that area still contains short wavelength components, although at lower amplitudes. The area SW of the church is also interesting as a dive site as this area contains wavelengths longer than 40 meters and we are at a loss to explain the source of these anomalies.

Conclusions

The main conclusions of this study are:

1. The unfiltered magnetic anomaly map constructed from the results of the new marine geophysical survey indicates that in the area immediately north and east of the church (Zone 1) the total field magnetic anomaly pattern consists of low-amplitude (< 25 nT), short-period anomalies forming a "checkerboard" pattern. In marked contrast, no similar anomaly pattern is observed in the eastern half of the survey area farther away from the church. Thus, we conclude that the checkerboard anomaly pattern signifies that this area contains many cultural remains.
2. The spectral analysis of the magnetic anomaly map reveals three areas around the church in which the character of the component wavelengths are distinct.
3. The analysis of the spatial wavelength components of the new magnetic anomaly map also reveals a checkerboard pattern east of the church: this area contains

anomalies with the shortest component wavelengths and the highest amplitudes (up to 25 nT). In addition, the analysis reveals that nearly the entire area surrounding the church contains anomalies with short wavelengths components. However, the amplitudes of the component wavelength are much smaller west of the church (Zones 2 and 3) than to the east of the church (Zone 1); consequently, these anomalies are not readily apparent in the unfiltered magnetic anomaly map. Thus, we conclude that the church was centrally located in the settlement as is common for that period.

4. The results suggest that the previous dive surveys covered only a small part of the total area containing cultural artifacts, and that many more artifacts remain to be discovered.
5. We recommend that future dive surveys focus first on the area of the checkerboard anomaly pattern located east of the church as this area appears from the magnetic data to have the greatest potential for discovering more archaeological remains.

Acknowledgements

We thank Cap. Ricardo B. Medrano Reyna, port captain of Tequesquitengo, for the use of the "Barracuda" and its crew during the survey. We also thank Alfredo Lowenstein and Virginia Urbieta for providing copies of their archaeological site plans. We thank Daniel Pérez Calderón, Francisco Ponce Núñez and Sandra Valle Hernández for their help during the survey and Esteban Hernández Quintero for providing the data from the Teoloyucan Magnetic Observatory. We also wish to thank the editor and an anonymous reviewer for their comments which added greatly to the clarity of the results. This work was funded in part by UNAM DGAPA grants IN108110 and IN114410, CONACYT grant 50235 and Instituto de Geofísica grant G111.

Bibliography

- Bandy W.L., Gangi A.F., Morgan F.D., 1990, Direct method for determining constant corrections to geophysical survey lines for reducing mistakes. *Geophysics*, 55, 7, 885-896.
- Breiner S., 1973, Applications Manual for Portable Magnetometers, Sunnyvale, California, Geometrics, U.S.A.
- Blakely R., 1996, Potential Theory in Gravity and Magnetic Application. Cambridge University Press, U.K.

- Crissman K., 2005, A horse-powered ferry: Burlington Bay, Lake Champlain, in *Beneath the Seven Seas*, edited by G.F. Bass, 218-219, Thames and Hudson Ltd, London.
- Cassavoy K.A., Crissman, K., 1988, The War of 1812: Battle for the Great Lakes, in *Ship and Shipwrecks of the Americas, A History Based on Underwater Archaeology*, edited by G.F. Bass, 169-188, Thames and Hudson Ltd, London.
- Cordell L., Phillips J.D., Godson R.H., 1992, U.S. Geological Survey Potential-Field geophysical software, Version 2.0, United States Geological Survey Open File Report, 92-18, 19 pp.
- Galindo Domínguez R.E., 2012, El pueblo sumergido del Lago de Tequesquitengo, Morelos. México. Siglo XIX. Historia, Arqueología y Geofísica Subacuática. Editorial Académica Española, Alemania.
- Galindo Domínguez R.E., 2011, Métodos geofísicos aplicados a la arqueología subacuática: el pueblo sumergido del lago de Tequesquitengo, Morelos. M.S. Tesis, Instituto de Geofísica, Universidad Nacional Autónoma de México, México D.F., 141 pp.
- Galindo Domínguez R.E., Bandy W.L., Mortera Gutiérrez C.A., Ortega Ramírez J., Ponce Núñez F., Valle Hernández S., Pérez Calderón D., 2009, Aplicaciones de prospección geofísica a la arqueología subacuática, in VII. Exploración, Memorias del Coloquio Interacción de diversas disciplinas científicas en las Ciencias de la Tierra, Posgrado en Ciencias de la Tierra-UNAM, México, 83-86 pp.
- Hildenbrand T.G., 1983, FFTFIL: A filtering program base on two-dimensional Fourier analysis of geophysical data, United States Geological Survey Open-File Report 83-237, 30 pp.
- International Association of Geomagnetism and Aeronomy, Working Group V-MOD. Participating members: C. C. Finlay, S. Maus, C. D. Beggan, T. N. Bondar, A. Chambodut, T. A. Chernova, A. Chulliat, V. P. Golovkov, B. Hamilton, M. Hamoudi, R. Holme, G. Hulot, W. Kuang, B. Langlais, V. Lesur, F. J. Lowes, H. Luhr, S. Macmillan, M. Manda, S. McLean, C. Manoj, M. Menvielle, I. Michaelis, N. Olsen, J. Rauberg, M. Rother, T. J. Sabaka, A. Tangborn, L. Toffner-Clausen, E. Thebault, A. W. P. Thomson, I. Wardinski Z. Wei, T. I. Zvereva, 2010, International Geomagnetic Reference Field: the eleventh generation. *Geophys. J. Int.*, 183, 3, 1216-1230. DOI: 10.1111/j.1365-246X.2010.04804.x.
- Kongsberg Maritime AS, 2004, EA 600 Single beam hydrographic echo sounder, Operator manual, Kongsberg Maritime AS, Norway.
- Kongsberg Maritime AS, 2007, Seatex SPH 20 NAV, Instruction Manual, Kongsberg Seatex AS, Norway.
- Lowenstein S.A., *et al.*, 1991, Proyecto Tequesquitengo, Boletín A.A.S.D.F. Comité Científico, Mexico D.F.
- Otaola J.A., Mendoza B., Pérez R., 1993, El sol y la tierra, una relación tormentosa, Fondo de Cultura Económica, 120 pp.

Variability of extreme precipitation in coastal river basins of the southern Mexican Pacific region

Nancy Pérez-Morga*, Thomas Kretzschmar, Tereza Cavazos, Stephen V. Smith and Francisco Munoz-Arriola

Received: September 20, 2012; accepted: February 05, 2013; published on line: June 28, 2013

Resumen

Se realizó un estudio sobre eventos extremos de sequía y humedad (± 1 desviación estándar), así como eventos de precipitación diaria mayores al percentil 95 (P95), asociados a tormentas tropicales y otros eventos, en tres cuencas hidrológicas costeras del sur de Oaxaca (Río Verde, Río Tehuantepec y la costa del sur de Oaxaca). El estudio está basado en registros de precipitación diaria de 47 estaciones bajo control de calidad durante el periodo de 1961-1990, con datos de tormentas tropicales para el Pacífico Oriental Tropical. El objetivo de este estudio fue evaluar eventos extremos (húmedos y secos), las tendencias de la contribución anual de la precipitación derivada del P95 y la relación de la precipitación de verano con El Niño-Oscilación del Sur y la Oscilación Decadal del Pacífico. Se realizó una regionalización basada en un análisis de componentes principales lo cual dió por resultado cuatro regiones de precipitación. Una correlación negativa significativa (al 95 % de confianza) fue encontrada sólo con el índice ONI en la región 3, la más cercana al Golfo de Tehuantepec. Los años húmedos ligados a eventos del P95 asociados con tormentas tropicales, fueron relacionados con anomalías negativas ($\geq -0.6^{\circ}\text{C}$) similares a condiciones de La Niña débil y neutrales. Mientras que los años secos fueron relacionados con anomalías positivas similares a condiciones neutrales ($\leq -0.5^{\circ}\text{C}$). La mayor contribución de precipitación del P95, asociada con tormentas tropicales, fue observada en la región 3. Sólo se encontró una tendencia positiva de esta contribución en la región 1: el bajo Río Verde.

Palabras clave: eventos de lluvia extrema, MSD, años secos, ciclones tropicales, ENSO, PDO.

Abstract

Extreme wet and dry years (± 1 standard deviation, respectively), as well as the top 95 percentile (P95) of daily precipitation events, derived from tropical cyclone (TC) and non-tropical cyclone (NTC) rainfall, were analyzed in coastal river basins in Southern Oaxaca, Mexico (Río Verde, Río Tehuantepec, and the Southern Coast). The study is based on daily precipitation records from 47 quality-controlled stations for the 1961 to 1990 period and TC data for the Eastern Tropical Pacific (EPAC). The aim of this study was to evaluate extreme (dry and wet) trends in the annual contribution of daily P95 precipitation events and to determine the relationship of summer precipitation with El Niño Southern Oscillation (ENSO) and the Pacific Decadal Oscillation (PDO). A regionalization based on a rotated principal component analysis (PCA) was used to produce four precipitation regions in the coastal river basins. A significant negative correlation (significance at the 95% level) was only found with ONI in rainfall Region 3, nearest to the Gulf of Tehuantepec. Wet years, mainly linked to TC-derived P95 precipitation events, were associated with SST anomalies ($\geq -0.6^{\circ}\text{C}$) similar to weak La Niña and Neutral cool conditions, while dry years were associated with SST positive anomalies similar to Neutral warm conditions ($\leq -0.5^{\circ}\text{C}$). The largest contribution of extreme P95 precipitation derived from TCs to the annual precipitation was observed in Region 3. A significant upward trend in the contribution of TC-derived precipitation to the annual precipitation was found only in Region 1, low Río Verde.

Key words: extreme rainfall events, MSD, dry years, tropical cyclones, ENSO, PDO.

Nancy Pérez-Morga*
 Thomas Kretzschmar
 Department of Geology
 Centro de Investigación Científica y de Educación Superior de Ensenada (CICESE)
 Carretera Ensenada-Tijuana Núm. 3918 Zona Playitas Ensenada, Baja California, 22860, México.
 *Corresponding author: pmorga@cicese.edu.mx;
 E-mail: tkretzsc@cicese.mx

Tereza Cavazos
 Department of Physical Oceanography, CICESE, Ensenada, B. C., Mexico.
 E-mail: tcavazos@cicese.mx

Stephen V. Smith
 349 Las Flores Drive, Chula Vista, CA 91910 USA.
 E-mail: svsmitt@cicese.mx

Francisco Munoz-Arriola
 Department of Biological Systems Engineering, University of Nebraska-Lincoln. 246 L. W. Chase Hall, Lincoln, NE 68583-0726
 E-mail: fmunoz@unl.edu

Introduction

Precipitation variability in the southern Mexican state of Oaxaca (Figure 1) has played a decisive role in the agriculture sector with social (Endfield *et al.*, 2004) and economic (Dilley, 1997; Endfield *et al.*, 2004) impacts, mainly during extreme events such as those associated with El Niño conditions or with the passage of tropical cyclones (TCs). Agriculture accounts for about 30% of the economic activity in Oaxaca and takes place mainly in the valleys, in the southern coastal plains, and the northeastern part of the state, with corn being one of the main crops (INEGI, 2012). Most maize in Oaxaca is planted during May and June to coincide with the onset of the rainy season (Dilley, 1997). Stress has been observed in maize growth (Dilley, 1997) coincident with the mid-summer drought (a relative minimum of precipitation between July and August known as "Canicula"; Mosiño and García, 1966; Magaña *et al.*, 1999; Curtis, 2004; Magaña and Caetano, 2005). For the 1978 to 1990 period the total August precipitation in the Oaxaca Valley predicted the yields on rain-fed maize (Dilley, 1997). During the August precipitation variability during this period was sensitive to interannual variations of the Southern Oscillation Index (SOI) and a synoptic index of summer 850 hPa-level temperatures (Dilley, 1997).

Precipitation in the early part of the rainy season (May–June) results from the northwards movement of the Inter-Tropical Convergence Zone (ITCZ) and easterly winds that bring moisture from the Gulf of Mexico; the latter part of the rainy season (July–September) is governed by the Mexican monsoon and increased TC frequency in the Gulf of Mexico and the Pacific, which are strongest during August (Dilley, 1997). This particular contribution for TCs over the annual precipitation has not been studied for the coast of Oaxaca. Between 1993 and 2007, one third of the major hurricanes in the Eastern Tropical Pacific (EPAC) had tracks that remained close to the Mexican west coast, with the highest peak intensity near Southern Mexico (Sánchez *et al.*, 2009). The ecological (Villegas-Romero *et al.*, 2009, Villegas-Romero *et al.*, 2004), social and economic impacts of TCs on the coast of Oaxaca are well documented by Bitrán (2002). Hurricane Pauline (in 1997) alone caused economic losses of around 450 million USD in Acapulco, in the neighbor state of Guerrero (Bitrán, 2002). Several parts of the basins in the southern coast of Oaxaca, such as Barra Coyula, Río Colotepec and Río Grande basins were also affected by this extreme event (CONABIO, 2012a).

A study regarding global trends shows an increase in daily extreme precipitation in

Southern Mexico over the past half century; one of the main problems in analyzing extreme climate events is the lack of high-quality, long-term climate data with adequate time resolution (Easterling *et al.*, 2000). Most studies of extremes have focused on Northwestern and Central Mexico (e.g., Magaña *et al.*, 2003; Cavazos *et al.*, 2008; Arriaga-Ramírez and Cavazos, 2010; Méndez and Magaña, 2010), while only a few studies have analyzed extreme events in Southern Mexico (Dilley, 1996; Peralta-Hernández, 2009). Peralta *et al.* (2009) in a regional study of Southern Mexico analyzed 23 extreme rainfall indices; they found an increase in extreme daily precipitation events over the 1960–2004 period, with a step-like jump in the early 1970's. The variability of extreme events was significantly related to ENSO (El Niño Southern Oscillation) and the PDO (Pacific Decadal Oscillation), with most daily heavy rainfall events occurring during La Niña and the positive phase of the PDO (Peralta *et al.*, 2009). In contrast, according to Pavía *et al.* (2006) El Niño events favor seasonal wet conditions in Southern Mexico, but during summers of a cold phase of the PDO.

Another study of the Oaxaca Valley associated droughts and reduced corn production to El Niño conditions (Dilley, 1997). ENSO warm events were associated with dry conditions in the valley owing to a southward displacement of the ITCZ during the low phase of the Southern Oscillation and diminished storm frequency in the Gulf of Mexico (Dilley, 1996). In other parts of the west coast of Mexico, this association of El Niño with dry conditions has also been found to occur during the warm phase of PDO in the Gulf of California continental watershed (Brito-Castillo *et al.*, 2003). On the other hand, a reduced number of TCs making landfall during El Niño years was also observed during 1961–1990 (Jauregui, 1995). According to these previous studies, a wet or dry summer depends on the phase of PDO and the ENSO condition. The current study focuses more on the positive and negative PDO phases and regions from the coast, to the Oaxaca Valley, and through the mountains of Oaxaca State. Study of the climate variability in this region is important due to its localization just in the north limit of the ITCZ, south of the North American monsoon and near the warm pool in the Gulf of Tehuantepec. In the case of extreme daily precipitation associated with TCs there are no studies in Oaxaca, while these events have been associated with weak La Niña to Neutral conditions in the monsoon region (Cavazos *et al.*, 2008).

The present study aims to understand the variability of extreme annual, seasonal and daily precipitation events in Southern Oaxaca (shown in Fig. 1), and their relationship to interannual

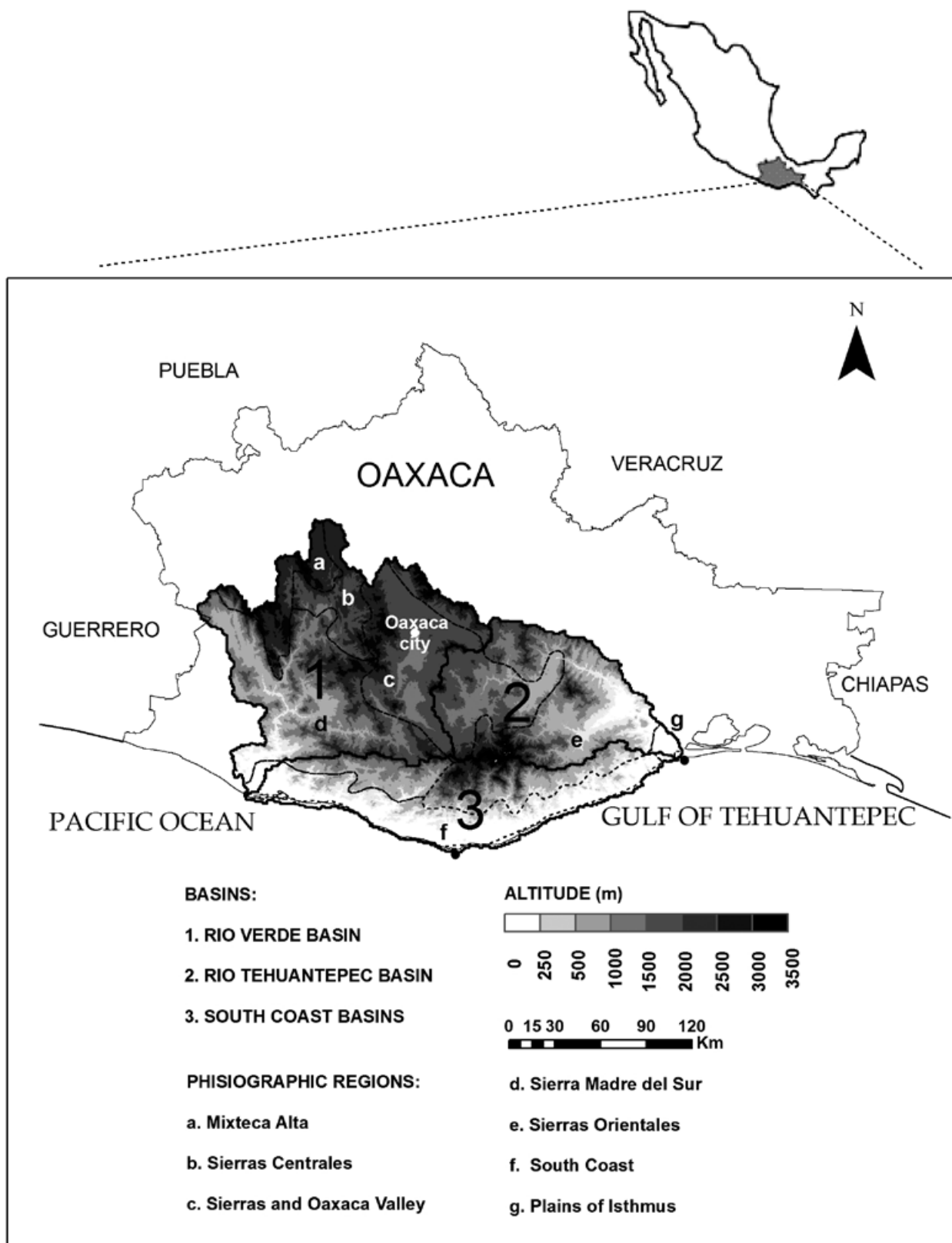


Figure 1. Study Area in Southern Oaxaca, Mexico. The black solid lines show the three basins, and the dashed lines, the physiographic characteristics (a-g).

and interdecadal phenomena such as ENSO and PDO. The study area reaches from the inland valley to the coastal areas, focusing on a regional scale that has not been addressed previously, and considering the summer precipitation when the TC season is predominant. This paper is organized into six sections (the first of which is the Introduction). Section 2 describes the region, section 3 the dataset used, and Section 4, the methods used to obtain regional extreme events (dry and wet years, and TC and Non-TC derived P95 daily rainfall events) and trends in the frequency of the extremes. The results of the regional extreme events at annual and seasonal timescales are presented in Section 5, and the discussion of the relationships with ENSO and PDO is presented in Section 6. The main conclusions of the study are presented in Section 7.

Study Region

The study area is located in the Southern Mexican Pacific region (Fig. 1), including the coastal hydrological basins of the state of Oaxaca: (1) Río Verde, (2) Río Tehuantepec, and (3) the Southern Coast region; this coastal region includes several smaller sub-basins (Río Colotepec, Río Copalita, Río Astata and others). The domain extends from the Pacific coast to the mountains, and covers an area of approximately 39,000 km². These basins are located between 15° 39' and 17° 35' N latitude and 95° 7' and 97° 55' W longitude (see Fig. 1) and are bounded to the north by the High Mixteca, by the Eastern Mountains to the northeastern, by Guerrero state to the West and by the Pacific Ocean to the South. The study area is bounded by the Gulf of Mexico and the Pacific Ocean, and near to the Gulf of Tehuantepec. The predominant climate is sub-humid and warm on the coast, and semiarid in the valley. The region's population totals to around 2,500,000 people. The study area includes several physiographic provinces shown in Fig. 1: the South coastal plains located up to 300 m above sea-level, the Sierra Madre del Sur (up to 2000 m elevation), the Oaxaca Valley (up to 1500 m), the Sierra Madre de Oaxaca (up to 2500 m), and the Isthmus plain (up to 400 m). The predominant vegetation consists of rain-fed and irrigated agriculture, oak, low deciduous trees, pine-oak, mountain mesophyll, and semi-evergreen seasonal forests.

The main economical activities in the state of Oaxaca are: commerce and services (47%), industrial and construction (41%), and agriculture (32%). Besides their use for water supply to agriculture and urban activities, some of the hydrological basins studied are also important carbon reservoirs and others function as coastal protection zones during extreme

events such as hurricanes (CONABIO, 2012 a). CONABIO (National Commission for Knowledge and Use of the Biodiversity) has classified some of the basins of the study as "priority for Mexico" based on environmental services (hydrological and maritime priority zones) and biodiversity (inland priority zones) (CONABIO, 2012 b).

Data

Daily-observed precipitation data were analyzed from 1950 to 2008 for a network of 184 stations across the study area (Fig. 2). The data were obtained from the Mexican Climatological Station Network Data (CLICOM) database of the Servicio Meteorológico Nacional (SMN) of the Mexican National Water Commission. A quality control protocol was adopted to identify errors and gaps; stations with less than 75% of complete and correct data were discarded. A threshold of 4 standard deviations above the climatological mean was used to identify daily outliers. Histogram analyses, using R-Climdex, an R statistical package of public domain (<http://cccma.seos.uvic.ca/ETCCDMI/software.shtml>), the median, a comparison with neighboring stations, and the type of related events, such as the passage of TCs, were used to determine the validity of the outliers, which were only rejected after manual inspection. Seventy per cent of the original 184 stations (i.e., 129) were accepted after the quality control.

A main parameter to accept or to discard a station was the continuity of the data series. The best period of the daily observations was 1961-1983; by early 1984 the continuity in the series quickly deteriorated; between 1983 and 1990, only 33% of the stations had complete data. The daily precipitation series showed continuing disruptions from 1990 to 2000.

Initially, the best 61 stations that covered thirty 33% of the original stations available in the study area were used for a Principal Components Analysis (PCA) of monthly precipitation of the 1961-1983 period to produce precipitation regions in the coastal river basins studied. A second analysis was carried out using only 47 stations (quality control with 70% of complete data series) to increase the time period of the analysis to 1961-1990 (Fig. 2). No significant differences in the regional distribution of the two data sets analyzed were found; therefore, the present article is based on the longer (1961-1990) period.

The variability of the extreme events was studied in each region derived from the PCA; first annual and seasonal anomalies of precipitation (for dry and wet years) were studied and after that daily P95 rainfall events derived from TCs

and Non-TCs (NTC) in the eastern Tropical Pacific were analyzed.

The classification of extreme daily rainfall events into TC-derived and non NTC extremes was done using a historical database of TC tracks of the EPAC from the Unysis data set (http://weather.unisys.com/hurricane/e_pacific/index.html).

The relationship between extreme events of precipitation and ENSO and PDO were analyzed through a correlation analysis with the PDO and the Oceanic El Niño Index (ONI), which is defined as 3-month running mean of ERSST.v3b SST anomalies in El Niño 3.4 region (5oN-5oS, 120o-170oW). An annual average of these values (based on 3-month running means) and a July-August-September (JAS) running mean were used for this analysis. This was obtained from the Climate Prediction Center (http://www.cpc.noaa.gov/products/analysis_monitoring/ensostuff/ensoyears.shtml). The PDO index (Mantua *et al.*, 1997) was obtained from <http://www.atmos.washington.edu/~mantua/TABLES2.html>.

Sea surface temperatures (SST) and their anomalies (SSTan) were used to show the conditions in wet and dry years. NOAA extended reconstructed SST v3 data was used and provided by the NOAA/OAR/ESRL PSD, Boulder, Colorado, USA, from their website at <http://www.esrl.noaa.gov/psd/>.

Methods

Principal analysis components (PCA)

A regionalization based on a rotated principal component analysis (PCA) was used to produce precipitation regions in Southern Oaxaca river basins. This regionalization was used to evaluate wet and dry years in the rainy period over May to October averages, and the P95 of daily precipitation rainfall events associated with TCs and Non-TCs.

An S-mode PCA was applied to monthly precipitation of the study area during the 1961-1983 period using 61 stations, and during the 1961-1990 period using only the 47 best stations after the quality control analysis. Gaps in the data were replaced with mean monthly climatological values before the analyses. The PCA was applied using a correlation matrix instead of a covariance matrix according to Comrie and Glenn (1998) for precipitation regionalizations. The selection of the number of principal components (PCs) to retain was based on a scree test (Cattel, 1966); four PCs were retained in both analyses, and the regionalization results were similar.

Orthogonal (varimax) and oblique (oblimin) rotations were tested; the oblimin rotation (with $\delta=0$) produced more consistent results, as in other precipitation regionalizations (White *et al.* 1991; Comrie and Glenn 1998; Englehart

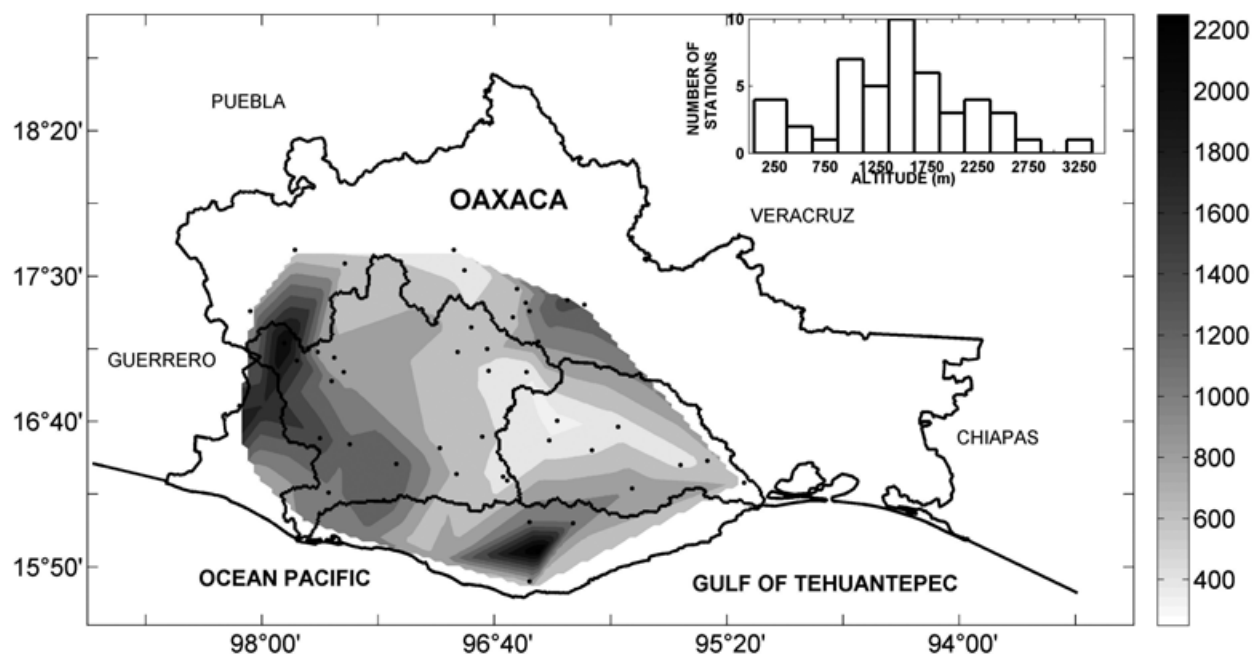


Figure 2. Spatial distribution of mean annual precipitation (mm/yr), station location and number of stations in function of topography for 47 out of 184 stations used in the study area during the 1961-1990 period.

and Douglas 2002; Guirguis and Avissar 2008; Arriaga-Ramírez and Cavazos, 2010). Four PCs were retained after rotation; these explained 97% of the total precipitation variance. The four regions were delineated using the contour $\gamma = 0.4$; 39 out of 47 stations met this criterion (Figure 2).

Extreme precipitation events

The precipitation regions derived from the PCA were used to analyze the variability of extreme precipitation events. First, regional wet and dry extreme events were analyzed at annual and seasonal scales, then extreme daily precipitation events derived from TC and Non-TC of eastern Pacific Tropical were also studied.

Extreme wet (dry) years were classified using standardized (Z) precipitation anomalies more than ± 1 standard deviation from Z; where the Z anomaly is defined as the annual mean precipitation of the stations in every region, minus the climatological mean for the 1961-1990 period divided by their standard deviation. Annual and seasonal anomalies were produced; as well as seasonal on the rainy season (May to October, winter (DJF), during the MSD period (JA) and at the start of the ITCZ (June) near the region.

An extreme daily precipitation event was defined when daily precipitation exceeded the 95th percentile (P95) value. Percentiles are obtained considering only wet days (precipitation > 1 mm). Extreme events were evaluated in individual stations and separated into summer events (June to October) and winter-spring events (November to May). The 5/7 month breakdown was used to evaluate the extreme events on the rainy season including the season of hurricanes, and to evaluate extreme events which were relationship with other processes (winter-spring events). This study exhibit only summer events. An extreme precipitation day derived from TCs was considered when a storm center was located within 5° (latitude) of the stations analyzed, as described in other studies (e.g., Cavazos et al., 2008).

The seasonal contribution from the P95 events was defined as the sum of all extreme event days from June to October divided by the annual precipitation. The seasonal contribution of TCs was calculated for each of the stations in each region derived from the PCA, and an annual average among the stations in each region was also calculated.

Linear trends in the annual contribution of the P95 rainfall events were evaluated with a non-parametric Mann-Kendall Test (Mann, 1945; Kendall, 1955) by normal approximation; an

adjustment was made for tied observations. The statistical significance level used for the trend analysis was 95% (i.e., $p < 0.05$). The slope of the trend was determined using Sen's slope estimator (Sen, 1968).

The Mid-Summer Drought (MSD).

As a manner to evaluate the MSD, a regional difference between June (the first summer maximum) and July (the first summer minimum) was calculated. Values above the regional mean of the 1961-1990 period were associated with a strong start of the MSD and values less than zero (negative differences) were years with a missing MSD.

Relationship between extreme events and ENSO and PDO.

The relationships between regional extreme events through precipitation anomalies at annual and seasonal scales, and through ENSO and PDO periods were analyzed by correlation analysis using the 95% level of statistical significance.

P95 daily extreme events associated with TCs and Non-TCs were evaluated over 1961-1990 period, identifying years with the largest frequency of events (> 1 standard deviation) and their relationship with ENSO conditions.

Results

Regional precipitation

The study area precipitation presents similar annual (Fig. 2) and summer (not shown) precipitation patterns, as expected in a region where the rainy season is mainly during the summer (May – Oct). These months represent and average of 91% of the annual precipitation throughout all stations. The highest precipitation is observed in the western part of the Río Verde Basin. Two areas of maximum precipitation are apparent, one over the NW of the Río Verde basin (reaching 2000 mm/yr), and another in the middle of the coastal basins (1600 mm/yr). The lowest precipitation is seen in the Río Tehuantepec Basin and in the Oaxaca Valley a (600 mm/yr) (Figs. 1 and 2). The mean annual precipitation for the 47 stations (Fig. 3) was 909 mm/yr. The precipitation time series (Fig. 3) show a relative dry period in 1961 and 1962, followed by a period with precipitation around the mean (with peaks in 1969, 1973 and 1981, El Niño and Neutral conditions). Finally, from 1982 to 1990 a relative dry period is observed. The time series does not contain a significant trend; however, the number of years with values over the annual mean increases during the cold phase of the PDO (Fig. 3).

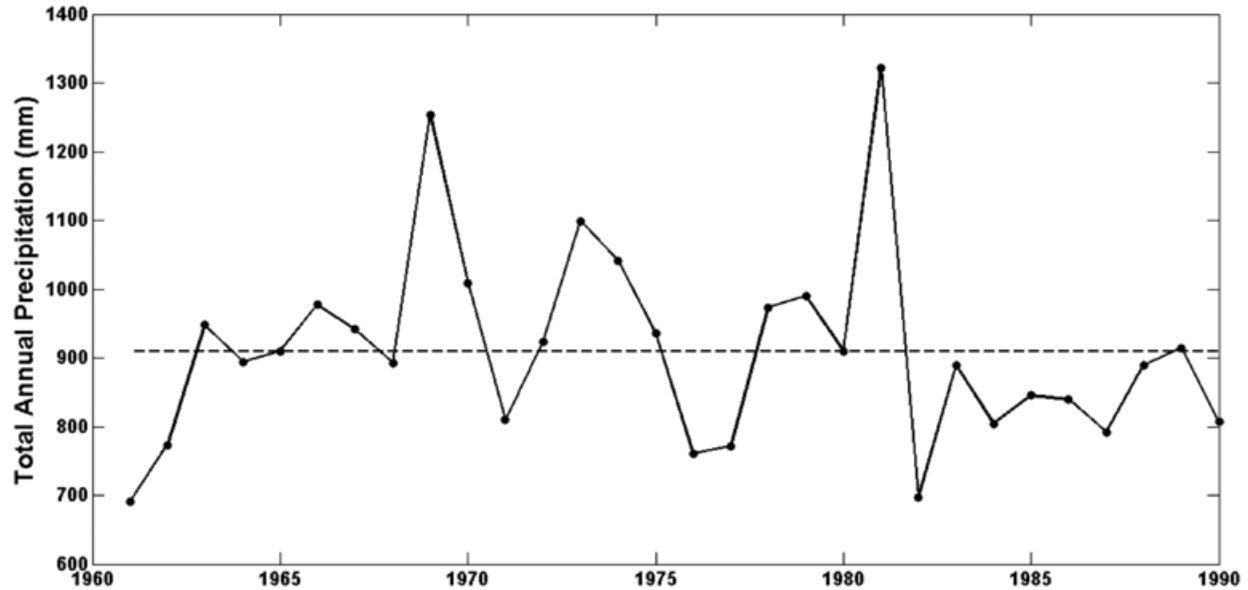


Figure 3. Mean total annual precipitation (mm) over the study area derived from 47 meteorological stations. The dash line indicates the mean annual precipitation during the period (909 mm).

PC-based precipitation regions

The four regions derived from the PCA (Fig. 4) show the monthly climatology for distinct regional precipitation patterns (Fig. 5). The percentage of variance explained by each PC region is as follows: PC1: 32.7, PC2: 29.8, PC3: 25.6, and PC4: 9.3. Río Verde basin presented three different patterns. PC1 coincides with the maximum annual precipitation (Fig. 2) and highest altitude (Fig. 1) including the Sierra Mixteca Alta and the South Coast Range; PC2, in the NE border of the Río Verde basin, covers the Sierras Orientales; and PC4 covers the sierras and the Oaxaca Valley. This last region does not follow the orography-precipitation pattern described above, and topography goes from 500 to 3000 m. Unfortunately, in PC4, the available weather stations are located only in the valley, so there is little or no data from the sierra area. Thus the valley, partly located in the orographic shadow of the mountains, presents the lowest precipitation of the four regions. The Tehuantepec basin covers the plains of the isthmus and belongs only to PC3. The South Coast sub-basins are characterized by two different patterns, PC1 and PC3.

The four regions are characterized by maximum precipitation in the summer (May-Oct) and considerably less rainfall during the rest of the year (Fig. 4 and 5). The main differences between the four regions are the summer precipitation regime distribution and the mean annual precipitation during the 1961-1990 period (Table 1). Low Río Verde (PC1) and the Isthmus

of Tehuantepec (PC3), experience an early summer start in May due to the establishment and northward movement of the ITCZ over the EPAC (García *et al.*, 1990, Cortéz-Vázquez, 1999; Valdés *et al.*, 2005, Amador *et al.*, 2006), and continues until July and August.

Table 1. Annual mean and June-July differences of precipitation for the 1961-1990 period.

	R1	R2	R3	R4
Annual mean (mm/y)	1257	869	646	546
June-July mean (mm)	51	22	44	54

A precipitation regime with a bimodal rainfall distribution is observed (Fig. 5a and 5c), with peaks in June and September and a minimum in July-August. After the "Canicula" (MSD) the precipitation increases in part due to the influence of TCs, which reach the maximum in September. The differences in the annual mean for each region are due to topography and location (Fig. 4). PC1 covers the coastal plains and areas with altitude around 2200 meters, and PC3 covers the coastal plains only (Fig. 4).

PC2 is in the NE limit of the Río Verde basin and goes into the Sierras Orientales. This region is influenced by the easterly trades from the Gulf of Mexico and TCs in the summer and fall (García *et al.*, 1990); the minimum in July is delayed until August with moisture enrichment from the Gulf of Mexico, and in September, a precipitation

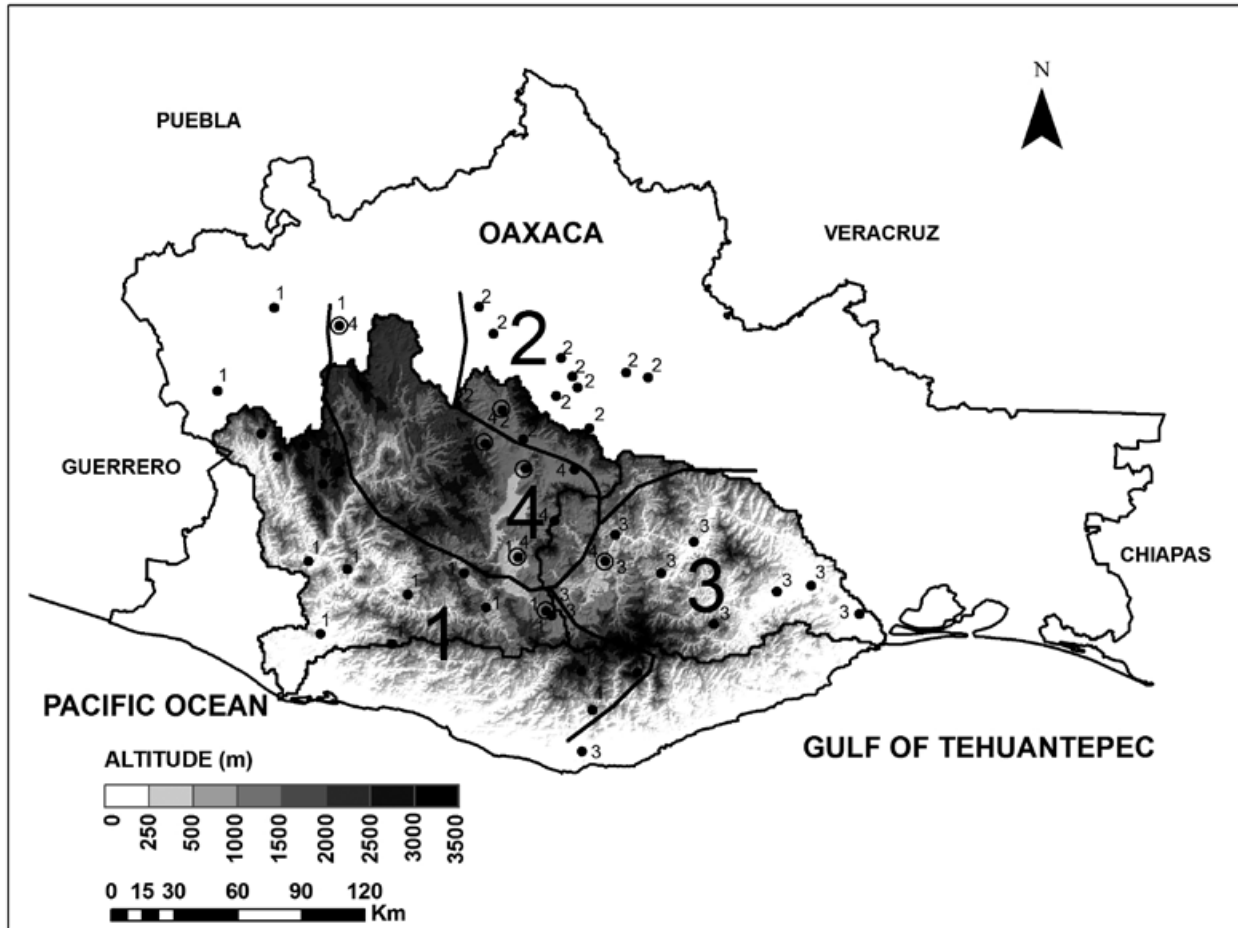


Figure 4. The four PC-derived precipitation regions delineated using the contour limit of $\gamma = 0.4$. The circles represent discarded stations.

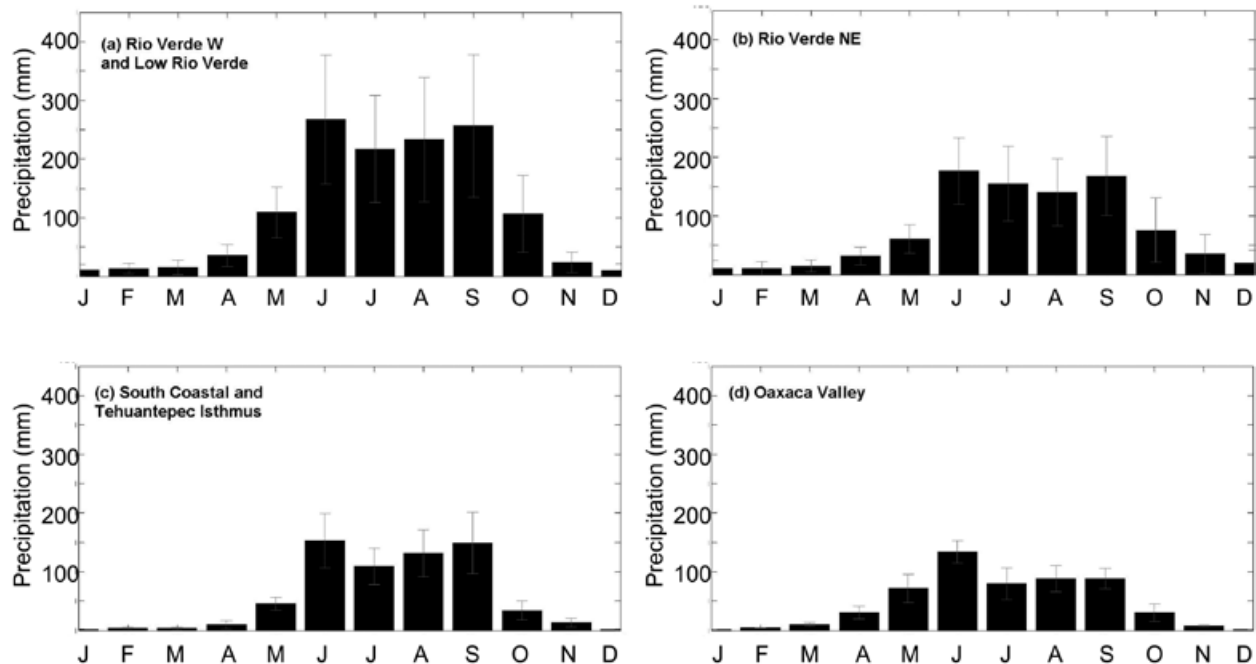


Figure 5. Mean monthly precipitation averaged over all stations in each of the regions. (a) to (d) from PC1 to PC4, respectively. One standard deviation is shown in error bars.

maximum is observed due to the hurricane period (Fig. 5 b).

PC4 has the lowest variance of the four regions. The annual mean rainfall is only 45 % of that observed in region 1. The maximum rainfall occurs in June, while in July the precipitation decreases and remains low during the next months, with a near-constant precipitation in the months of July, August and September and lacking the second peak of maximum precipitation observed in the other regions (Fig. 5 d). This trend could be due to the presence of the Southern range, acting as a barrier for the middle section of the Río Verde basin and presenting an intermountain rainfall pattern with a flat precipitation with a lesser influence of TCs.

Regional precipitation variability and its relationship to ENSO and PDO

The regional precipitation variability was evaluated through Z mean anomalies, but only the May to October mean is shown in Fig. 6. In the annual and the summer season, two major positive anomalies were observed: in 1969 (El Niño year under a PDO negative phase) and in 1981 (Neutral condition and PDO positive phase). Comparing the 4 PC regions only the PC3 region shows a high value in 1969 and PC1

in 1981. Both are strongly influenced by the ITCZ and their proximity to the Pacific Ocean. In other years, positive anomalies (> 1 standard deviation) were also observed: 1973, 1974, and 1979 in a particular region; but 1969 and 1981 were the years observed in the four regions. Dry periods were observed, from 1961 to 1965 (except 1963), from 1976 to 1977 and from 1982 to 1990 (except 1984).

Considering the June Z mean anomaly, the first peak in 1969 is only observed in the PC3 region, the Tehuantepec and South coast; but the one in 1981, a wet year, starts in June and is observed in all regions with highest relative values in PC2 and PC4, regions closest to the Gulf of Mexico. From July to August, the Z mean anomalies during the MSD period, 1969 wet year is observed in all regions, but precipitation in 1981 begins to decrease in all regions. Both anomalies disappear during September-October.

The results of the correlation between the Z mean anomalies in different periods with ONI and the PDO are shown in Table 2. No significant correlation was found between precipitation anomalies and PDO and SST anomalies (values not shown). The ONI index was significantly correlated (negative) only with precipitation anomalies in region 3 (Table 2).

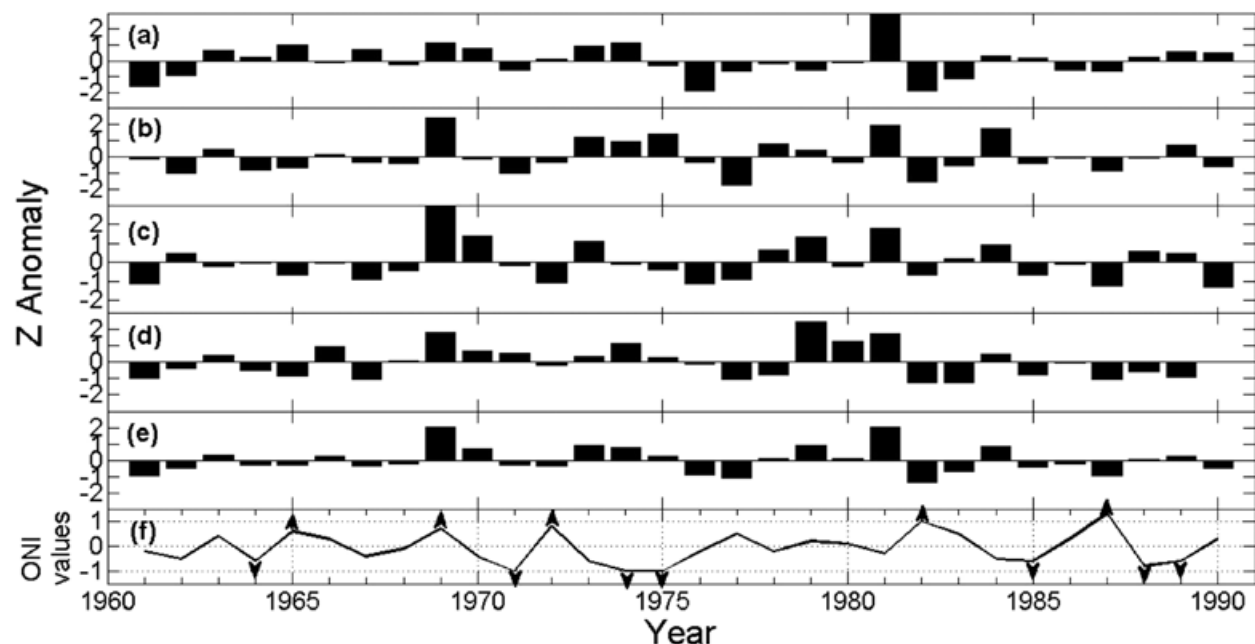


Figure 6. May to October standardized (Z) precipitation anomalies in the four PC-derived regions (a – d), (e) Z mean of the four regions. Annual El Niño Index (ONI) where El Niño is when ONI > 0.5 (up arrow), La Niña ONI < -0.5 (down arrow), and Neutral ONI between $-0.5-0.5$ (f).

Table 2. Correlations between Z precipitation anomalies in the four regions and ONI and PDO indexes. Correlations with 95 % confidence in bold face.

PCA derived Region	ONI (JAS)	PDO
Annual mean		
R1: Low Rio Verde y costa	-0.03	-0.02
R2: Golfo de México	-0.23	-0.17
R3: Tehuantepec y costa	-0.4	0.07
R4: Valle de Oaxaca (Rio Verde NE)	-0.1	-0.12
May to October mean		
R1: Low Rio Verde y costa	-0.2	-0.04
R2: Golfo de México	-0.32	0.03
R3: Tehuantepec y costa	-0.37	0.08
R4: Valle de Oaxaca (Rio Verde NE)	-0.18	-0.07
July to August mean		
R1: Low Rio Verde y costa	-0.1	0.17
R2: Golfo de México	-0.13	0.21
R3: Tehuantepec y costa	-0.39	0.19
R4: Valle de Oaxaca (Rio Verde NE)	-0.13	-0.01

the start of MSD and a particular ENSO condition was found (Fig. 7). There were strong MSD starts during La Niña and El Niño conditions. A lesser number of years without a MSD influence were observed (Fig. 7).

Extreme Events associated with TCs and Non-TCs.

The annual contribution of the extreme rainfall events, derived from the passage of TCs and Non-TCs in summer (June to October) is presented in Fig. 8 for the four regions; in some years the contribution of these events is zero. The total mean contribution of all extreme events to the annual precipitation in the four regions was low, only 23%, where 14% corresponds to extreme events related to TCs of the EPAC and 9% to Non-TCs. Thus the majority of the annual rainfall comes from less intense events. The thresholds to identify extreme events (P95 and P99) and the mean contribution of TCs and non-TCs per region are shown in Table 3. In both cases Region 3 (Isthmus of Tehuantepec and part of the South coast) is the region with the largest contribution of TC-derived and Non-TC-derived rainfall to the annual precipitation. For TCs a significant (at the 95 percent level) upward trend was found in region 1 (Fig 8a) and a significant downward trend in PC4, Oaxaca Valley (Fig, 8d). For Non-TC-derived rainfall, a significant downward trend was found in PC2 and in PC4. Frequent events of TCs and Non-TCs during the 1961 to 1990 period were evaluated and the years with values over the mean plus 1 standard deviation for TCs were: 1967, 1969, 1973, 1974, 1981 and 1983,

The MSD

An interannual variation of the MSD start was observed in all regions, but no relation between

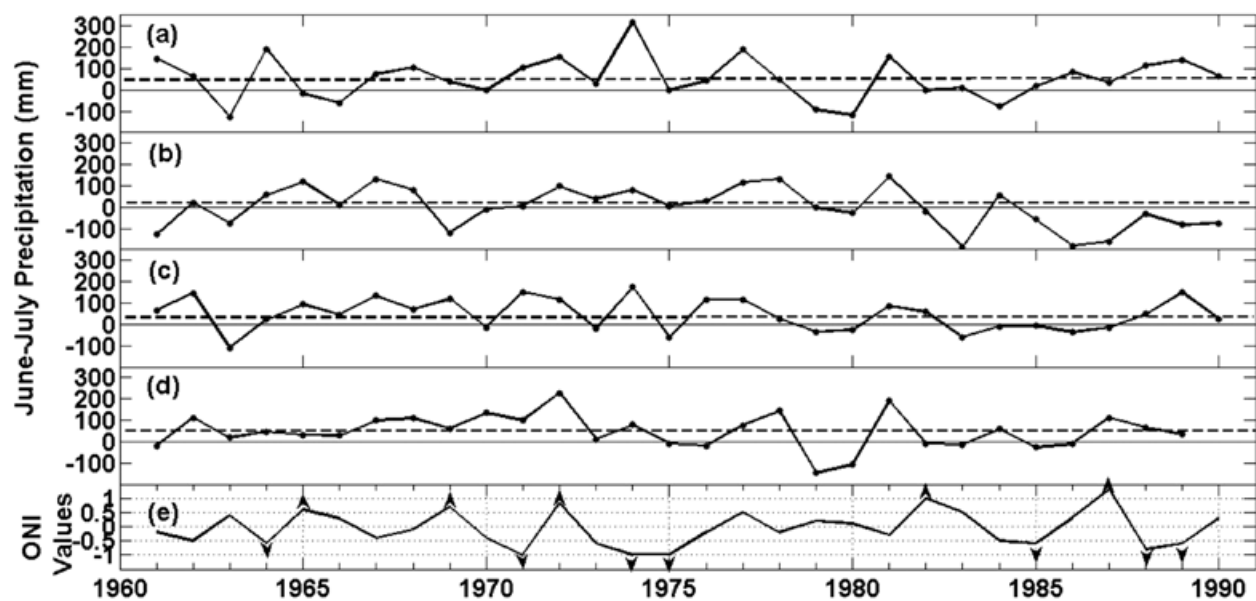


Figure 7. June minus July precipitation and ONI values. Dash line shows the mean monthly difference between June and July over 1961-1990 period in each region.

mainly during La Niña and neutral conditions and for Non-TCs: 1969, 1973 and 1981. These years coincide with the wet years previously analyzed in section 4.3 (except 1967 and 1983 for TCs), and in a similar way, the possible relationship between SSTan and these rainfall P95-derived extremes from TCs and Non-TCs will be explored in next section.

Table 3. Thresholds used P95 and P99 percentiles and the annual climatological mean of precipitation (1961-1990).

	R1	R2	R3	R4
P95 (mm)	40.5	33.4	51.5	35.8
P95 (mm)	63.5	55.3	86.3	58.2
TC (% Contribution mean)	12.7	14.4	18	8.9
TC (% Contribution mean)	7.8	9	14	6.5

SSTan associated with extreme precipitation events

SSTan behavior during extreme wet and dry years is described in Fig. 9. SSTan characteristics during wet years (1969, 1973 and 1981, Fig. 6 d) were compared with those during dry years (1961, 1976 and 1982, Fig. 6 d). Negative anomalies ($\geq -0.60^{\circ}\text{C}$) in the EPAC near the Equator during wet years are associated to weak La

Niña/Neutral negative conditions, while positive anomalies ($\leq 0.50^{\circ}\text{C}$) in the eastern Equatorial Pacific are observed during dry years associated to very weak El Niño to Neutral positive conditions.

Discussion

The rainfall regionalization (Fig. 4 and Fig. 5) in the study area is influence by orographic factors, but in the PC4 region, an underestimation of the mean precipitation is possible because of the lack of stations in the NW Sierras (Fig. 1 c) and Oaxaca Valley. Arbingast (1975) assigned this particularity in Oaxaca Valley to a decrease in precipitation due to orographic effects, observing a precipitation pattern following the isolines in the study area with low precipitation values in Oaxaca Valley. In central-northeastern Mexico, a rainfall regionalization was found consistent with topography and vegetation changes (Pineda-Martínez *et al.*, 2007). But topography is not the only cause of for the regional patterns. Other processes involved are related to the Pacific Ocean and the Gulf of Mexico. The ITCZ influences the establishment of the rainy season (Fig. 5) from May to July and August, but each region reaches different peaks and shows different precipitation distribution patterns due to TCs and the proximity of the Gulf of Tehuantepec and the Gulf of Mexico (Fig. 4 and Fig. 5). Dillely (1996) mentioned that orography and local convection determined the precipitation pattern in Oaxaca Valley, but this is also governed by synoptic factors of large scale like the easterlies,

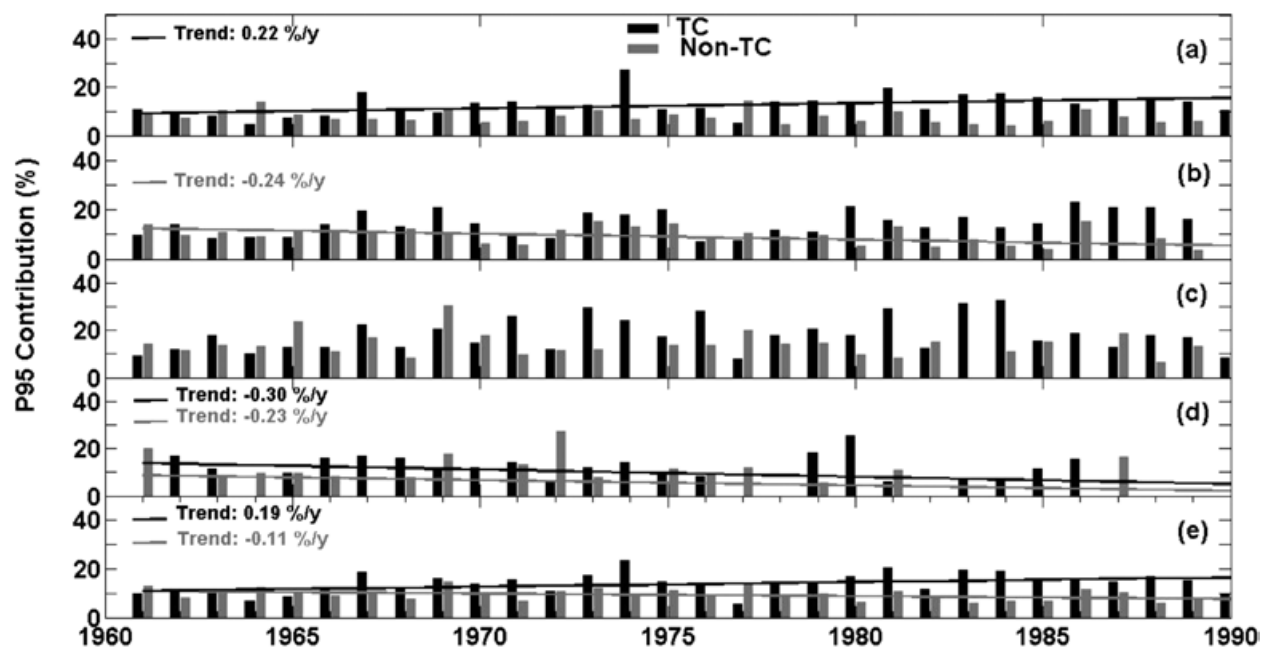


Figure 8. P95 contribution (%) from extreme daily precipitation events derived from TC (black) and Non-TC (gray) to the annual precipitation. (a) to (d) P95 contribution from PC1 to PC4, respectively. (e) Mean average contribution from the four regions. (a, b, d, e) Show the linear trend significative ($p < 0.05$).

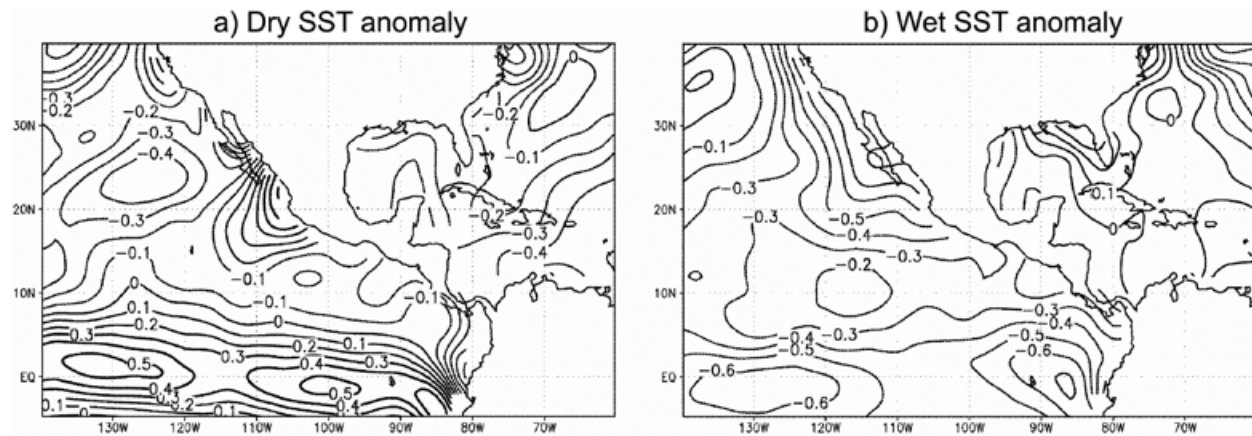


Figure 9. June to October mean SST anomalies for the extreme dry (a) and wet (b) years.

tropical storms, ENSO and the PDO. Here we find a significant, but low, correlation with ENSO (0.39, Table 2) only PC3 region. Cavazos and Hastenrath (1990), for example, observed that May-October precipitation, averaged over several stations in the state of Oaxaca from 1966 to 1987, correlates with the July-August average of the SO1 at 0.38. This trend is consistent with our results using the ONI index. The regionalization is also consistent with other climatic regionalizations for Mexico (García *et al.* 1990; Giddings *et al.* 2005).

Wet conditions in the negative phase of PDO have been observed in southern Mexico for the summer (Méndez *et al.*, 2010), however correlations between PDO and precipitation anomalies in each region was low and not significant, just a positive correlation (0.39) was found in PC1 over the winter period from December to February. Pavía *et al.* (2006) found that wet conditions during the summer in the coast of Oaxaca are also associated with a negative PDO phase and El Niño events, as the case in 1969. Méndez and Magaña (2010) explained that during the negative phase of the PDO, the Caribbean low-level jet weakens and the easterly wave activity increases, leading to more tropical convection over Mesoamerica. In the case of Oaxaca, more cases of wet years are observed during the negative phase of the PDO but no significant correlation appears. The time period evaluated was another problem, because only 3% of the initial 184 stations evaluated cover a PDO period completely and with an intermittent series of data, the rest of the stations do not cover a complete cycle of the PDO. In region 4, Oaxaca Valley, which has been related to drought conditions during El Niño events (Dilley, 1996), extreme dry years were related with the positive phase of PDO and weak El Niño/Neutral positive conditions, but no significant correlation was found during the complete period of study. Dilley (1996) found this

correlation for August from 1978 to 1990 period (after a PDO positive phase change). Figure 9a shows dry years associated to El Niño conditions over the equatorial Pacific. Méndez and Magaña, 2010, associate prolonged drought over central and southern Mexico to the interaction between easterly waves and the trade winds over the intra-Americas seas, in addition to low frequency modulators as Atlantic multidecadal oscillation or PDO. These results suggest that predictability of wet and dry years in the region is difficult, due to the influence of several large-scale teleconnections interacting at different time scales and the lack of long data series.

TCs in the eastern Tropical Pacific and their contribution to extreme events (P95) was larger than that of Non-TCs; other rainfall contribution to annual precipitation was possibly caused by local topography or by TCs in the Gulf of Mexico that in the present work were not evaluated. The years with more events in both cases coincided with negative SST anomalies in the equatorial Pacific (Fig. 9 b).

Dilley, 1996, analyzed storm frequency (from the Gulf of Mexico and the Pacific Ocean) correlations with Oaxaca precipitation and found these were strongest during August and in the areas between 0 and 25°N latitude into the Gulf of Mexico and in the Pacific Ocean. In September the highest correlations were found in the grid-cells on the Mexican coast adjacent to Oaxaca. The author mention that as easterly flow abates during September, easterly waves become less influential and those storms that are proximate to Oaxaca are the ones with the greatest effect on precipitation. These results coincide with region 3, the largest contribution of P95 rainfall-derived from TCs to the annual precipitation.

In general, during El Niño (La Niña) has been reported that precipitation decreases (increases)

es) in the Tehuantepec Isthmus (Magaña *et al.*, 2003) and a reduced number of tropical storms making landfall during El Niño years (1961-1990 period) has also been observed (Jauregui, 1995) coincident with our results. Region 4 was the lowest TC contribution. In 1997, during the passage of hurricane Pauline, the Southern Sierra worked as a natural barrier preventing the phenomenon to enter Mexican territory (CONABIO, 2012 a) farther away from the coastal regions. Nevertheless, still 6% of extreme events associated to TCs were retained in this region (Table 2).

The overall regional average of extreme events associated with TCs were related to La Niña and Neutral conditions, consistent with Peralta-Hernández *et al.* (2009), who reported that extreme rainfall events occur more frequently during periods of La Niña and during the positive phase of PDO. The only significant positive trend (0.29%/yr) in the contribution of extreme events to the annual precipitation was observed in region 1. This trend is also consistent with the observations of Peralta-Hernández *et al.* (2009), who found a positive trend in the largest and moderate extreme events in Southern Mexico. The influence of TCs at the lower Río Verde section of the Pastoría coastal lagoon (part of the mouth of region 1) has been analyzed through sediment core studies and has been traced as far back as the Holocene; but an increase in storms driven by more frequent El Niño conditions was found (Goman *et al.*, 2005). A diagram in figure 10 illustrates some of the main findings in this study.

Conclusions

Extreme wet and dry years as well as the top 95 percentile of daily precipitation events derived from tropical cyclone for the Eastern Tropical Pacific and non-tropical cyclone rainfall, were analyzed in coastal river basins in Southern Oaxaca, Mexico, for the 1961 to 1990 period. The aim of this study was to evaluate extreme, trends in the annual contribution of daily P95 precipitation events and to determine the relationship of summer precipitation with El Niño Southern Oscillation and the Pacific Decadal Oscillation.

Rainfall extremes in Oaxaca coastal basins were associated with tropical cyclones in the eastern Tropical Pacific, with less contribution of non-tropical cyclones; these were associated with weak La Niña and Neutral conditions. Dry events were associated with weak El Niño/Neutral positive conditions. An upward trend, significant for the hurricanes only was determined in region 1, the maximum annual precipitation of the study area; a downward trend was found in region 4, the Oaxaca Valley. The principal contribution of tropical cyclones and non-tropical cyclones was found in region 3, the closest to the Isthmus of Tehuantepec. A bimodal rainfall distribution, the topography and the influence of the Gulf of Mexico and Gulf of Tehuantepec distinguish this region.

Finally, from this study it is evident to investigate further the detailed nature of a few

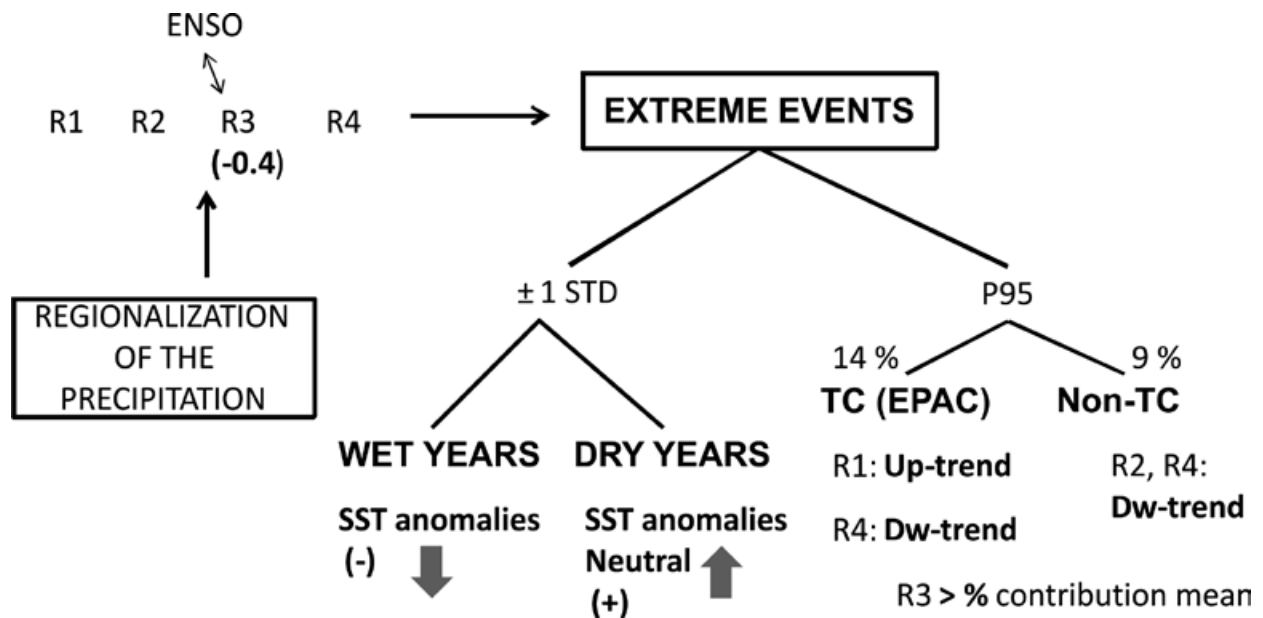


Figure 10. Diagram to illustrate some of the main findings in this study.

major events and the importance of a continuous monitoring of climate data, particularly in regions with gaps and lack of stations over inaccessible areas of high elevation. The study of the hydrology of the Oaxaca basins analyzed will be the next step to connect their variability with the climate patterns and extreme events studied in the present work.

Acknowledgments

The authors thank CONACYT and CICESE for their financial support to the first author N. Pérez-Morga through her PhD. studies.

Bibliography

- Arbingast S.A., Gill C.C., Blair C.P., Holz R.K., Buchanan J.R., Marin R., C.A., Ryan, R.H., Bonnie, M.E. and Weiler J.P., 1975, *Atlas of Mexico*, University of Texas.
- Arriaga-Ramírez S., Cavazos T., 2010, Regional trends of daily precipitation indices in northwest Mexico and Southwest United States. *J. Geophys. Res.*, 115, D14111, doi:10.1029/2009JDOI13248.
- Amador J.A., Alfaro E.J., Lizano O.G., Magaña V.O., 2006, Atmospheric forcing of the Eastern tropical Pacific: A review. *Prog. Oceanogr.*, 69, 101-142.
- Bitrán B.D., 2002, Características del impacto socioeconómico de los principales desastres ocurridos en México, en el periodo de 1980-99. CEPAL 8-25. México, D.F., 2002.
- Brito-Castillo L., Douglas A., Leyva-Contreras A., Lluch-Belda D., 2003, The effect of large-scale circulation on precipitation and streamflow in the Gulf of California continental watershed, *Int. J. Climatol.* 23, 751-768.
- Cattell R.B., 1966, The scree test for the number of factors. *Multivar. Behav. Res.*, 1, 245-276.
- Cavazos T., Hastenrath S., 1990, Convection and rainfall over Mexico and their modulation by Southern Oscillation. *Int. J. Climatol.*, 10, 377-386.
- Cavazos T., Turrent C., Lettenmaier D.P., 2008, Extreme precipitation trends associated with tropical cyclones in the core of the North American monsoon. *Geophys. Res. Lett.*, 35, L21703, doi:10.1029/2008GL035832.
- CONABIO, cited 2012 a: Natural Hazards hurricane Pauline case. Mexico: Federal Government. [Available online at http://www.conabio.gob.mx/conocimiento/cambios_veg/doctos/hp_s.html.]
- CONABIO, cited 2012 b: Priority Regions. Mexico: Federal Government. [Available on line at <http://www.conabio.gob.mx/conocimiento/regionalizacion/doctos/terrestres.html>.]
- Comrie A.C., Glenn E.C., 1998, Principal components-based regionalization of precipitation regimes across the Southwest United States and northern Mexico with an application to monsoon precipitation variability. *Clim. Res.*, 10, 201-215.
- Cortéz V.M., 1999, Marcha Anual de la Actividad Convectiva en México. *Atmósfera*, 12, 101-110.
- Curtis S., 2004, Diurnal cycle of rainfall and surface winds and the mid-summer drought of Mexico Central America. *Clim. Res.*, 27, 1-8.
- Dilley M., 1996, Synoptic controls on precipitation in the Valley of Oaxaca, Mexico. *Int. J. Climatol.*, 16, 1019-1031.
- Dilley M., 1997, Climatic factors affecting annual maize yields in the Valley of Oaxaca, Mexico. *Int. J. Climatol.*, 17, 1549-1557.
- Easterling D.R., Evans J.L., P. Ya. Groisman, Karl T.R., Kunkel K.E., Ambenje P., 2000, Observed Variability and trends in extreme climate events: A brief review. *Bull. Amer. Meteorol. Soc.*, 81, 417-425.
- Endfield G.H., Fernández-Tejedo I., O'Hara S.L., 2004, Drought and disputes, deluge and dearth: climatic variability and human response in colonial Oaxaca, Mexico. *J. Hist. Geogr.*, 30, 249-276.
- Englehart P.J., Douglas A.V., 2002, Mexico's summer rainfall patterns: an analysis of regional models and changes in their teleconnectivity. *Atmósfera*, 15, 147-164.
- García E., Vidal R., Hernández M.E., 1990, Las regiones Climáticas de México. In García de Fuentes, Ana. Editora. Atlas Nacional de México, UNAM, Instituto de Geografía. 2, IV, 10. Map at 1:12,000,000. México, D.F.
- Giddings L., Soto M., Rutherford B.M., Maarouf A., 2005, Standardized Precipitation Index Zones for México. *Atmósfera*, 33-56.
- Goman M., Joyce A., Mueller R., 2005, Stratigraphic evidence for anthropogenically induced coastal environmental change from Oaxaca, Mexico. *Quaternary Res.*, 63, 250- 260.

- Guirguis K.J., Avissar R., 2008, A precipitation Climatology and Dataset Intercomparison for the Western United States. *J. of Hydrometeorology*, 9, 825-841.
- INEGI cited 2012: CENSO de Población y Vivienda 2010. Mexico: Federal Government. [Available on line at <http://www.inegi.org.mx/est/contenidos/proyectos/ccpv/cpv2010/principales2010.aspx>]
- Jauregui E., 1995, Rainfall fluctuation and tropical storm activity. *Erdkunde*, 39-47.
- Kendall M.G., 1955, Rank correlation methods. Charles Griffin, 196 pp.
- Magaña V.O., Amador J.A., Medina S., 1999, The Midsummer Drought over Mexico and Central America. *J. Climate*, 12, 1577-1588.
- Magaña V.O., Vázquez J.L., Pérez J.L., Pérez J.B., 2003, Impact of El Niño on precipitation in Mexico. *Geofísica Internacional*, 42, 3, 313-330.
- Magaña V.O., Caetano E., 2005, Temporal evolution of summer convective activity over the Americas warm pools. *Geophys. Res. Lett.*, 32, L02803, doi:10.1029/2004GL021033.
- Mann H.B., 1945, Non-parametric tests against trend. *Econometrica*, 13, 245-259.
- Mantua N.J., Hare S.R., Zhang Y., Wallace J.M., Francis R.C., 1997, A Pacific interdecadal climate oscillation with impacts on salmon production. *Bull. Amer. Meteor. Soc.*, 78, 1069-1079.
- Méndez M., Magaña V.O., 2010, *Regional Aspects of Prolonged Meteorological Droughts over Mexico and Central America*. *J. Climate*, 23, doi: 10.1175/2009JCLI3080.1.
- Méndez G.J., Ramírez A., Cornejo O.E., Zarate L.A., Cavazos T., 2010, Teleconexiones de la Oscilación Decadal del Pacífico (PDO) a la precipitación y temperatura en México. *Investigaciones Geográficas, Boletín del Instituto de Geografía, UNAM*. ISSN 0188-4611, 73, 57-70.
- Mosiño A.P., García E., 1966, Evaluación de la sequía intraestival en la República Mexicana. Conferencia Regional Latinoamericana. Ciudad de México, 9-15 de agosto. *Unión Geográfica Internacional*, 3, 500-516.
- Mosiño A.P., García E., 1974, The climate of Mexico. *World Survey of Climatology. Climates of North America*. R. A. Bryson and F. K. Hare. Eds., Elsevier. 11, 345-404.
- Pavía E.G., Graef F., Reyes J., 2006, Notes and Correspondence PDO-ENSO effects in the Climate of Mexico, *J. Climate*, 19, 6433-6438.
- Peralta-Henández A.R., Balling R.C. Jr., Barba-Martínez L.R., 2009, Comparative analysis of indices of extreme rainfall events: variations and trends from Southern México. *Atmósfera*, 22, 2, 219-228.
- Pineda-Martínez L.F., Carbajal N., Medina-Roldán E., 2007, Regionalization and classification of bioclimatic zones in the central-northeastern region of Mexico using principal component analysis (PCA), *Atmósfera*, 20, 2, 133-145.
- Sánchez O., Raga G.B., Zavala-Hidalgo J., 2009, Is the ocean responsible for the intense tropical cyclones in the Eastern Tropical Pacific? Elsevier Editorial System (tm) for Dynamics of Atmospheres and Oceans. DYNAT-D-09-00016.
- Sen P.K., 1968, Estimates of the regression coefficient based on Kendall's Tau, *J. Amer. Statist. Assoc.*, 63, 1379-1389.
- Valdés M.A., Cortéz V.M., Pastrana F.J., 2005, Un Estudio Explorativo de los Sistemas convectivos de Mesoescala de México. *Investigaciones Geográficas, Boletín del Instituto de Geografía, U.N.A.M.*, Abril, 056, 26-42.
- Villegas-Romero I., Oropeza-Mota J.L., Martínez-Ménes M., Mejía-Sáenz E., 2004, Producción de agua y sedimentos por impacto de ciclones tropicales en la cuenca hidrográfica del río La Sabana, Guerrero. *Terra Latinoamericana*, Julio- Septiembre, 323-333.
- Villegas-Romero I., Oropeza-Mota J.L., Martínez-Ménes M., Mejía-Sáenz E., 2009, Path and relation rain-runoff caused by hurricane Pauline in the Sabana River, Guerrero, México, *Agrociencia*, 43, 4.
- White D., Richman M., Yarna B., 1991, Climate regionalization and rotation of principal components. *Int. J. Climatol.*, 11, 1-25, doi:551.582.2:551.501.45:551.577.21(748).

Parallel Algorithms for Computational Models of Geophysical Systems

Antonio Carrillo-Ledesma, Ismael Herrera* and Luis M. de la Cruz

Received: October 10, 2012; accepted: February 05, 2013; published on line: June 28, 2013

Resumen

Los modelos matemáticos de muchos sistemas geofísicos requieren el procesamiento de sistemas algebraicos de gran escala. Las herramientas computacionales más avanzadas están masivamente paralelizadas. El software más efectivo para resolver ecuaciones diferenciales parciales en paralelo intenta alcanzar el *paradigma de los métodos de descomposición de dominio*, que hasta ahora se había mantenido como un anhelo no alcanzado. Sin embargo, un grupo de cuatro algoritmos –los *algoritmos DVS*– que lo alcanzan y que tiene aplicabilidad muy general se ha desarrollado recientemente. Este artículo está dedicado a presentarlos y a ilustrar su aplicación a problemas que se presentan frecuentemente en la investigación y el estudio de la Geofísica.

Palabras clave: computational-geophysics, computational-PDEs, non-overlapping DDM, BDDC; FETI-DP.

Abstract

Mathematical models of many geophysical systems are based on the computational processing of large-scale algebraic systems. The most advanced computational tools are based on massively parallel processors. The most effective software for solving partial differential equations in parallel intends to achieve the *DDM-paradigm*. A set of four algorithms, the *DVS-algorithms*, which achieve it, and of very general applicability, has recently been developed and here they are explained. Also, their application to problems that frequently occur in Geophysics is illustrated.

Key words: computational-geophysics, computational-PDEs, non-overlapping DDM, BDDC, FETI-DP.

A. Carrillo-Ledesma
I. Herrera*
L. M. de la Cruz
Instituto de Geofísica
Universidad Nacional Autónoma de México
Ciudad Universitaria
Delegación Coyoacán, 04510
México D.F., México
*Corresponding author: iherrera@geofisica.unam.mx

1. Introduction

Mathematical models of many systems of interest, including very important continuous systems of Earth Sciences and Engineering, lead to a great variety of partial differential equations (PDEs) whose solution methods are based on the computational processing of large-scale algebraic systems. Furthermore, the incredible expansion experienced by the existing computational hardware and software has made amenable to effective treatment problems of an ever increasing diversity and complexity, posed by scientific and engineering applications [PITAC, 2006].

Parallel computing is outstanding among the new computational tools and, in order to effectively use the most advanced computers available today, massively parallel software is required. Domain decomposition methods (DDMs) have been developed precisely for effectively treating PDEs in parallel [DDM Organization, 2012]. Ideally, the main objective of domain decomposition research is to produce algorithms capable of '*obtaining the global solution by exclusively solving local problems*', but up-to-now this has only been an aspiration; that is, a strong desire for achieving such a property and so we call it '*the DDM-paradigm*'. In recent times, numerically competitive DDM-algorithms are *non-overlapping*, *preconditioned* and necessarily incorporate *constraints* [Dohrmann, 2003; Farhat *et al.*, 1991; Farhat *et al.*, 2000; Farhat *et al.*, 2001; Mandel, 1993; Mandel *et al.*, 1996; Mandel and Tezaur, 1996; Mandel *et al.*, 2001; Mandel *et al.*, 2003; Mandel *et al.*, 2005; J. Li *et al.*, 2005; Toselli *et al.*, 2005], which pose an additional challenge for achieving the *DDM-paradigm*.

Recently a group of four algorithms, referred to as the '*DVS-algorithms*', which fulfill the *DDM-paradigm*, was developed [Herrera *et al.*, 2012; L.M. de la Cruz *et al.*, 2012; Herrera and L.M. de la Cruz *et al.*, 2012; Herrera and Carrillo-Ledesma *et al.*, 2012]. To derive them a new discretization method, which uses a non-overlapping system of nodes (the *derived-nodes*), was introduced. This discretization procedure can be applied to any boundary-value problem, or system of such equations. In turn, the resulting system of discrete equations can be treated using any available DDM-algorithm. In particular, two of the four *DVS-algorithms* mentioned above were obtained by application of the well-known and very effective algorithms BDDC and FETI-DP [Dohrmann, 2003; Farhat *et al.*, 1991; Farhat *et al.*, 2000; Farhat *et al.*, 2001; Mandel *et al.*, 1993; Mandel *et al.*, 1996; Mandel and Tezaur, 1996; Mandel *et al.*, 2001; Mandel *et al.*, 2003; Mandel *et al.*, 2005; J. Li *et al.*, 2005; Toselli *et al.*, 2005]; these will be referred to as the *DVS-BDDC* and *DVS-FETI-DP* algorithms. The other

two, which will be referred to as the *DVS-PRIMAL* and *DVS-DUAL* algorithms, were obtained by application of two new algorithms that had not been previously reported in the literature [Herrera *et al.*, 2011; Herrera *et al.*, 2010; Herrera *et al.*, 2009; Herrera *et al.*, 2009; Herrera, 2008; Herrera, 2007]. As said before, the four *DVS-algorithms* constitute a group of preconditioned and constrained algorithms that, for the first time, fulfill the *DDM-paradigm* [Herrera *et al.*, 2013; L.M. de la Cruz *et al.*, 2012].

Both, BDDC and FETI-DP, are very well-known [Dohrmann, 2003; Farhat *et al.*, 1991; Farhat *et al.*, 2000; Farhat *et al.*, 2001; Mandel *et al.*, 1993; Mandel *et al.*, 1996; Mandel and Tezaur, 1996; Mandel *et al.*, 2001]; and both are highly efficient. Recently, it was established that these two methods are closely related and its numerical performance is quite similar [Mandel *et al.*, 2003; Mandel *et al.*, 2005]. On the other hand, through numerical experiments, we have established that the numerical performances of each one of the members of *DVS-algorithms* group (*DVS-BDDC*, *DVS-FETI-DP*, *DVS-PRIMAL* and *DVS-DUAL*) are very similar too. Furthermore, we have carried out comparisons of the performances of the standard versions of BDDC and FETI-DP with *DVS-BDDC* and *DVS-FETI-DP*, and in all such numerical experiments the *DVS* algorithms have performed significantly better.

Each *DVS-algorithm* possesses the following conspicuous features:

- It fulfills the *DDM-paradigm*;
- It is applicable to symmetric, non-symmetric and indefinite matrices (i.e., neither positive, nor negative definite); and
- It is preconditioned and constrained, and has update numerical efficiency.

Furthermore, the uniformity of the algebraic structure of the matrix-formulas that define each one of them is remarkable.

This article is organized as follows. In Section 2 the basic definitions for the *DVS* framework are given; here we define the set of '*derived-nodes*', internal, interface, primal and dual nodes, the '*derived-vector-space*', among others. Section 3 is devoted to define the new set of vector spaces that conforms the *DVS* framework; the Euclidean inner product, is also defined here. In Section 4 the '*transformed-problem*' on the *derived-nodes* is explained in detail, and this is our starting point to define the *DVS* algorithms. Section 5 presents a summary of the four *DVS-algorithms*: *DVS-BDDC*, *DVS-FETI-DP*, *DVS-PRIMAL* and *DVS-DUAL*. In Section 6 we give the numerical procedures

we use to fulfilling the DDM-paradigm, and we explain in detail the implementation issues. Finally, in Section 7 we show some numerical results obtained after the application of the DVS-algorithms in the solution of several boundary values problems of interest in Geophysics. We studied examples for a single-equation, for the cases of symmetric, non-symmetric and indefinite problems. We also present results for an elasticity problem, where a system of PDE equations is solved.

2. DVS Framework: A Summary

The 'derived-vector-space framework (DVS-framework)' is applied to the discrete system of equations that is obtained after the partial differential equation, or system of such equations, has been discretized. The procedure is independent of the method of discretization that is used. Thus, the DVS-framework's starting point is a system of linear algebraic equations that is referred to as the 'original problem':

$$\underline{\underline{\hat{A}}}\underline{\underline{\hat{u}}} = \underline{\underline{\hat{f}}} \quad (2.1)$$

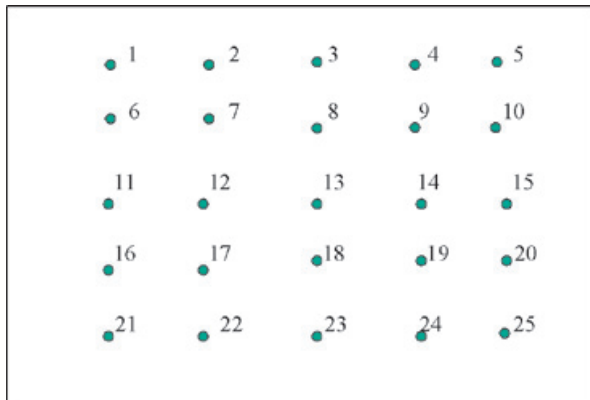


Figure 1. The 'original nodes'.

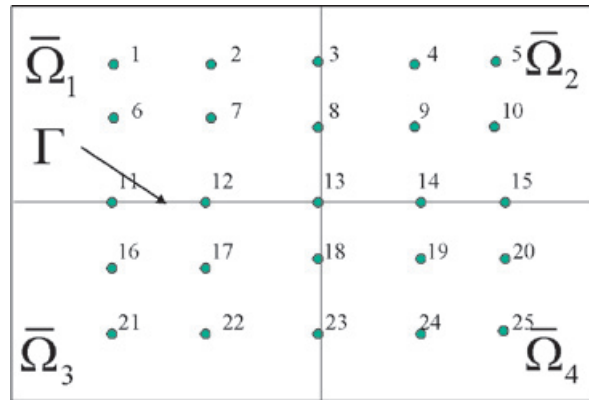


Figure 2. The original nodes in the coarse-mesh.

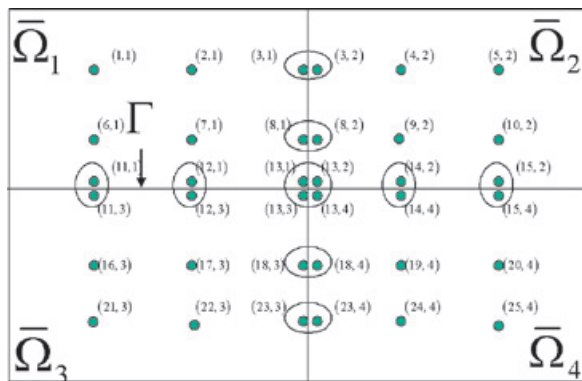


Figure 3. The mitosis.

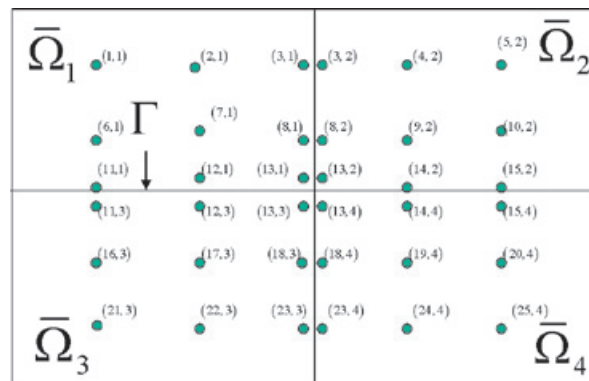


Figure 4. The derived-nodes distributed in the coarse-mesh

However, in the DVS setting one does not work with the set of nodes originally used for discretizing the problem the 'original-nodes' (Figure 1). Instead, one uses an auxiliary set of nodes: the 'derived-nodes'. Each one of such nodes has the property that it belongs to one and only one subdomain of the coarse mesh.

Indeed, generally after a coarse-mesh has been introduced, some original-nodes belong to more than one subdomain of the coarse-mesh (Figure 2), which is inconvenient for achieving the DDM-paradigm. Therefore, in the DVS-framework, each original-node that belongs to more than one subdomain is divided into as many new nodes – the derived-nodes (Figure 3) – as subdomains it belongs to. Then, the derived-nodes so obtained are distributed into the coarse-mesh subdomains so that each derived-node is assigned to one and only one subdomain of the coarse-mesh (Figure 4). Once this has been done, a convenient notation is to label each derived-node by a pair of natural numbers: the first one indicating the original-node from which it derives and the second one, the subdomain to which it is assigned.

The real-valued functions defined in the set of *derived-nodes* constitute a vector-space: the '*derived-vector-space*', W . This space becomes a finite-dimensional Hilbert-space when it is supplied with the inner-product that is usually introduced when dealing with real-valued functions defined in a set of nodes; this is referred to as the *Euclidean inner-product*.

Afterwards, a new problem (referred to as the '*transformed problem*') is defined in the *derived-vector-space*, which is equivalent to the original system of discrete equations. Thereafter, all the numerical and computational work is carried out in the *DVS-space*.

Before leaving this Section, we dwell a little further on the meaning of a *coarse-mesh*. By it, we mean a partition of Ω into a set of non-overlapping subdomains $\{\Omega_1, \dots, \Omega_E\}$, such that for each $\alpha=1, \dots, E$, Ω_α is open and:

$$\Omega_\alpha \cap \Omega_\beta = \emptyset \text{ and } \Omega \subset \bigcup_{\alpha=1}^E \bar{\Omega}_\alpha \quad (2.2)$$

Where $\bar{\Omega}_\alpha$ stands for the closure of Ω_α . The set of '*subdomain-indices*' will be

$$\hat{E} \equiv \{1, \dots, E\} \quad (2.3)$$

\hat{N}^α , $\alpha=1, \dots, E$, will be used for the subset of *original-nodes* that correspond to nodes pertaining to $\bar{\Omega}_\alpha$. As usual, nodes will be classified into '*internal*' and '*interface-nodes*': a node is *internal* if it belongs to only one partition-subdomain closure and it is an *interface-node*, when it belongs to more than one. For the application of *dual-primal* methods, *interface-nodes* are classified into '*primal*' and '*dual*' nodes. We define:

$\hat{N}_I \subset \hat{N}$ as the set of *internal-nodes*;

$\hat{N}_\Gamma \subset \hat{N}$ as the set of *interface-nodes*;

$\hat{N}_\pi \subset \hat{N}_\Gamma \subset \hat{N}$ as the set of *primal-nodes*¹; and

$\hat{N}_\Delta \subset \hat{N}$ as the set of *dual-nodes*.

The set of *primal-nodes* is required to be a subset of \hat{N}_Γ and, in principle, could be otherwise

chosen arbitrarily. However, the algorithms considered by *domain decomposition methods* are iterative-algorithms and their rate of convergence depends crucially on the selection of the set \hat{N}_π . Thus, criteria for selecting \hat{N}_π have been studied extensively (see [Toselli *et al.*, 2005], for detailed discussions of this topic). Each one of the following two families of node-subsets is disjoint :

$\{\hat{N}_I, \hat{N}_\Gamma\}$ and $\{\hat{N}_I, \hat{N}_\pi, \hat{N}_\Delta\}$. Furthermore, these node subsets fulfill the relations:

$$\hat{N} = \hat{N}_I \cup \hat{N}_\Gamma = \hat{N}_I \cup \hat{N}_\pi \cup \hat{N}_\Delta \text{ and } \hat{N}_\Gamma = \hat{N}_\pi \cup \hat{N}_\Delta \quad (2.4)$$

Throughout our developments the *original matrix* \hat{A} is assumed to be non-singular (i.e., it defines a bijection of \hat{W} into itself). The following assumption ('*axiom*') is also adopted in throughout the *DVS-framework*: "When the indices $p \in \hat{N}^\alpha$ and $q \in \hat{N}^\beta$ are *internal original-nodes*, while $\alpha \neq \beta$, then $p \in \hat{N}^\alpha$ and $q \in \hat{N}^\beta$ are unconnected". We recall that unconnected means:

$$\hat{A}_{pq} = \hat{A}_{qp} = 0 \quad (2.5)$$

3. The Derived-Vector Space (DVS)

In order to have at hand a sufficiently general framework, we consider functions defined on the set X of *derived-nodes* whose value at each *derived-node* is a *dD-Vector*. The numerical applications that will be discussed in this paper correspond to two possible choices of d : when the application refers to a single partial differential equation (PDE), $d=1$, and for the problems of elasticity that will be considered, which are governed by a three-equations system, $d=3$.

Independently of the chosen value for d , the set of such functions constitute a vector space, W , referred to as the '*derived-vector space*'. When $\underline{u} \in W$, we write $u(p, \alpha)$ for the value of \underline{u} at the *derived-node* (p, α) . We observe that, in general, $u(p, \alpha)$ itself is a *d-Vector* and we adopt the notation $u(p, \alpha, i)$, $i=1, \dots, d$. For the i -th component of $u(p, \alpha)$. When $d=1$ the index i is irrelevant and, in such a case, will be deleted throughout.

For every pair of functions, $\underline{u} \in W$ and $\underline{v} \in W$, the '*Euclidean inner product*' is defined to be

¹In order to mimic standard notations, we should have used Π instead of the *low-case* π . However, the modified definitions given here yield some convenient algebraic properties.

$$\underline{u} \cdot \underline{w} = \sum_{(p,\alpha) \in X} u(p,\alpha) \odot w(p,\alpha) \quad (3.1)$$

Here, $u(p, \alpha) \odot w(p, \alpha)$ stands for the inner-product of the dD -Vectors involved; thus,

$$u(p,\alpha) \odot w(p,\alpha) \equiv \sum_{i=1}^n u(p,\alpha,i) w(p,\alpha,i) \quad (3.2)$$

A fundamental property of the *derived-vector space* W , is that it constitutes a finite dimensional *Hilbert-space* with respect to the *Euclidean inner-product*.

Let $W' \subset W$ be a linear subspace and assume $M \subset X$ is a subset of *derived-nodes*. Then, the notation $W'(M)$ will be used to represent the vector subspace of W' , whose elements vanish at every *derived-node* that does not belong to M . Furthermore, corresponding to each *local subset of derived-nodes*, X^α , there is a '*local subspace of derived-vectors*', W^α , which is defined by

$$W^\alpha \equiv W(X^\alpha) \quad (3.3)$$

Clearly, when $\underline{u} \in W^\alpha \subset W$, $\underline{u}(p, \beta) = 0$ whenever $\beta \neq \alpha$. We observe that

$$W = W^1 \oplus \dots \oplus W^E \quad (3.4)$$

A *derived-vector* $\underline{u} \in W$ is said to be *continuous* when $\underline{u}(p, \alpha)$ is independent of α . The set of *continuous vectors* constitute the linear subspace, W_{12} .

The orthogonal complement (with respect to the Euclidean inner-product) of $W_{12} \subset W$ is $W_{11} \subset W$. Then $W = W_{11} \oplus W_{12}$. Two projection-matrices $\underline{a}: W \rightarrow W$ and $\underline{j}: W \rightarrow W$ are here introduced; they are the projection-operators, with respect to the *Euclidean inner-product* on W_{12} and W_{11} , respectively. When $\underline{u} \in W$, one has

$$\underline{u} = \underline{u}_{11} + \underline{u}_{12} \text{ with } \begin{cases} \underline{u}_{11} \equiv \underline{j}\underline{u} \in W_{11} \\ \underline{u}_{12} \equiv \underline{a}\underline{u} \in W_{12} \end{cases} \quad (3.5)$$

the vectors $\underline{j}\underline{u}$ and $\underline{a}\underline{u}$ are said to be the '*jump*' and the '*average*' of \underline{u} , respectively. Therefore, W_{11} is the '*zero-average*' subspace, while W_{12} is the '*zero-jump*' subspace.

Original-nodes are classified into '*internal*' and '*interface-nodes*': a node is *internal* if it belongs to only one subdomain-closure of the *coarse-mesh*, and it is an *interface-node* when it belongs to more than one of such closure-subdomains. Some

subspaces, significant for our developments, are listed next:

$$\begin{aligned} W_I &\equiv W(I); \\ W_\Gamma &\equiv W(\Gamma); \\ W_\pi &\equiv W(\pi); \\ W_\Delta &\equiv W(\Delta); \text{ and} \\ W_\Pi &\equiv W(\Pi). \end{aligned}$$

At present, numerically competitive algorithms need to incorporate *restrictions* and to this end, in the *DVS-framework*, a '*restricted subspace*' $W_r \subset W$ is selected. In the developments that follow, it is assumed that:

$$W_r \equiv W_I + \underline{a}W_\pi + W_\Delta \quad (3.6)$$

The matrix \underline{a}^r will be the projection-operator on W_r . We observe that when $\underline{u} \in (W_I + W_\Delta)$, one has $\underline{a}^r \underline{u} = \underline{u}$. We also notice that

$$W = W_I \oplus W_\Gamma = W_I \oplus W_\pi \oplus W_\Delta \quad (3.7)$$

4. The Transformed Problem

The *transformed-problem* consists in finding $\underline{u} \in W$ such that

$$\underline{a}^r \underline{A}' \underline{u} = \underline{f} \text{ and } \underline{j}\underline{u} = 0 \quad (4.1)$$

Where:

$$\underline{A}' \equiv \sum_{\alpha=1}^E \underline{A}^\alpha \quad (4.2)$$

and

$$\underline{\hat{A}}^\alpha \equiv \left(\underline{\hat{A}}_{pq}^\alpha \right) \text{ with } \underline{\hat{A}}_{pq}^\alpha \equiv \frac{\hat{A}_{pq} \delta_{pq}^\alpha}{s(p,q)} \quad (4.3)$$

together with

$$m(p,q) \equiv \sum_{\alpha=1}^E \delta_{pq}^\alpha \text{ and } s(p,q) \equiv \begin{cases} 1, \text{ when } m(p,q) = 0 \\ m(p,q), \text{ when } m(p,q) \neq 0 \end{cases} \quad (4.4)$$

The function $m(p, q)$ is said to be the '*multiplicity*' of the pair (p, q) . The '*derived-nodes*' are created after a *coarse-mesh* has been

introduced, by dividing the *original-nodes* as explained in the Overview (Section 2), and then with each '*derived-node*' we associate a unique pair of numbers (p, α) such that $\alpha \in \hat{E}$ and $p \in \hat{N}^\alpha$. In what follows, we identify *derived-nodes* with such pairs.

Then, in order to incorporate the constraints, we define

$$W_r \equiv W(\mathbf{I}) + W(\Delta) + aW(\pi) \quad (4.5)$$

then, the matrix $\underline{\underline{A}}: W_r \rightarrow W_r$ defined by

$$\underline{\underline{A}} \equiv \underline{\underline{a}}^r \underline{\underline{A}}^t \underline{\underline{a}}^r \quad (4.6)$$

has the property that

$$\underline{\underline{A}} \underline{\underline{A}} \underline{\underline{a}} = \underline{\underline{a}} \underline{\underline{A}}^t \underline{\underline{a}} \quad (4.7)$$

Hence, Eq. (4.1) is replaced by

$$\underline{\underline{A}} \underline{\underline{A}} \underline{\underline{u}} = \underline{\underline{f}} \text{ and } \underline{\underline{j}} \underline{\underline{u}} = 0 \quad (4.8)$$

For matrices and vectors the following notation is adopted:

$$\underline{\underline{A}} \equiv \begin{pmatrix} \underline{\underline{A}}_{\Pi\Pi} & \underline{\underline{A}}_{\Pi\Delta} \\ \underline{\underline{A}}_{\Delta\Pi} & \underline{\underline{A}}_{\Delta\Delta} \end{pmatrix}; \begin{cases} \underline{\underline{u}} \equiv \begin{pmatrix} \underline{\underline{u}}_\Pi \\ \underline{\underline{u}}_\Delta \end{pmatrix} \text{ for any } \underline{\underline{u}} \in W \\ \underline{\underline{u}} \equiv \begin{pmatrix} \underline{\underline{u}}_1 \\ \underline{\underline{u}}_\pi \end{pmatrix} \text{ for any } \underline{\underline{u}} \in W(\Pi) \end{cases} \quad (4.9)$$

where the matrices

$$\begin{aligned} \underline{\underline{A}}_{\Pi\Pi}: W_r(\Pi) \rightarrow W_r(\Pi), \quad \underline{\underline{A}}_{\Pi\Delta}: W_r(\Delta) \rightarrow W_r(\Pi) \\ \underline{\underline{A}}_{\Delta\Pi}: W_r(\Pi) \rightarrow W_r(\Delta), \quad \underline{\underline{A}}_{\Delta\Delta}: W_r(\Delta) \rightarrow W_r(\Delta) \end{aligned} \quad (4.10)$$

furthermore,

$$\begin{aligned} \underline{\underline{A}}_{\Pi\Pi} &\equiv \begin{pmatrix} \left(\underline{\underline{A}}^t\right)_\Pi & \left(\underline{\underline{A}}^t\right)_{\text{I}\pi} \underline{\underline{a}}^r \\ \underline{\underline{a}}^r \left(\underline{\underline{A}}^t\right)_{\pi\Delta} & \underline{\underline{a}}^r \left(\underline{\underline{A}}^t\right)_{\pi\pi} \underline{\underline{a}}^r \end{pmatrix}, \quad \underline{\underline{A}}_{\Pi\Delta} \equiv \begin{pmatrix} \left(\underline{\underline{A}}^t\right)_{\text{I}\Delta} \\ \underline{\underline{a}}^r \left(\underline{\underline{A}}^t\right)_{\pi\Delta} \end{pmatrix} \\ \underline{\underline{A}}_{\Delta\Pi} &\equiv \begin{pmatrix} \left(\underline{\underline{A}}^t\right)_{\Delta\text{I}} & \left(\underline{\underline{A}}^t\right)_{\Delta\pi} \underline{\underline{a}}^r \end{pmatrix}, \quad \underline{\underline{A}}_{\Delta\Delta} \equiv \left(\underline{\underline{A}}^t\right)_{\Delta\Delta} \end{aligned} \quad (4.11)$$

The matrix $\underline{\underline{A}}: W \rightarrow W$ will be referred to as the '*transformed-matrix*'. We observe that $\underline{\underline{A}} = \underline{\underline{A}}^t$ when $\pi = \emptyset$.

In turn, the *transformed problem* of (4.8) can be reduced, see [Herrera *et al.*, 2010; Herrera *et al.*, 2009; Herrera, 2008; Herrera, 2007; Farhat *et al.*, 2000] for details, into the following problem, which is expressed in terms of the values of the solution at *dual-nodes*, exclusively: "Find $\underline{\underline{u}}_\Delta \in W(\Delta)$ that satisfies

$$\underline{\underline{a}} S \underline{\underline{u}}_\Delta = \underline{\underline{f}}_\Delta \text{ and } \underline{\underline{j}} \underline{\underline{u}}_\Delta = 0 \quad (4.12)''$$

Here, $\underline{\underline{f}}_\Delta \in aW(\Delta)$ and the '*Schur-complement matrix with constraints*' are defined by

$$\underline{\underline{f}}_\Delta \equiv \underline{\underline{f}}_\Delta - \underline{\underline{A}}_{\Delta\Pi} \left(\underline{\underline{A}}_{\Pi\Pi} \right)^{-1} \underline{\underline{f}}_\Pi \quad (4.13)$$

and

$$\underline{\underline{S}} \equiv \underline{\underline{A}}_{\Delta\Delta} - \underline{\underline{A}}_{\Delta\Pi} \left(\underline{\underline{A}}_{\Pi\Pi} \right)^{-1} \underline{\underline{A}}_{\Pi\Delta} \quad (4.14)$$

respectively.

5. The DVS-Algorithms

Generally two kinds of approaches are distinguished: primal –these are direct approaches, which do not resort to Lagrange multipliers- and dual –indirect approaches that use Lagrange multipliers-. However, when DDMs are formulated using a setting as general as that supplied by the *DVS-framework*, such a distinction is irrelevant. The feature that is conspicuous for different options is the information that the algorithm seeks. Indeed, four algorithms will be obtained by seeking successively for the vectors: $\underline{\underline{u}}_\Delta$, $\underline{\underline{S}}^{-1} \underline{\underline{j}} S \underline{\underline{u}}_\Delta$, $\underline{\underline{j}} S \underline{\underline{u}}_\Delta$, and $\underline{\underline{S}} \underline{\underline{u}}_\Delta$. However, in the presentation that follows we stick to the '*primal vs. dual-algorithms*' classification.

5.1 Primal Formulations

The DVS Version of BDDC

This is a primal algorithm which seeks directly for $\underline{\underline{u}}_\Delta$. Pre-multiplying Eq. (4.12) by $\underline{\underline{a}} S^{-1}$, one gets:

$$\underline{\underline{a}} S^{-1} \underline{\underline{a}} S \underline{\underline{u}}_\Delta = \underline{\underline{a}} S^{-1} \underline{\underline{f}}_\Delta \text{ and } \underline{\underline{j}} \underline{\underline{u}}_\Delta = 0 \quad (5.1)$$

In [Farhat *et al.*, 2000], it was shown that Eq. (5.1) is equivalent to Eq. (4.12). This equation is the DVS-version of BDDC.

The DVS-Primal Algorithm

For this algorithm, the *sought-information* is:

$$\underline{\underline{v}}_{\Delta} \equiv -\underline{\underline{S}}^{-1} \underline{\underline{jS}} \underline{\underline{u}}_{\Delta} \quad (5.2)$$

Applying to $\underline{\underline{aS}}$ Eq. (5.2) it is seen that $\underline{\underline{aS}} \underline{\underline{v}}_{\Delta} = 0$. Furthermore,

$$\underline{\underline{j}} \left(\underline{\underline{S}}^{-1} \underline{\underline{f}}_{\Delta} + \underline{\underline{v}}_{\Delta} \right) = \underline{\underline{j}} \left(\underline{\underline{S}}^{-1} \underline{\underline{aS}} + \underline{\underline{S}}^{-1} \underline{\underline{jS}} \right) \underline{\underline{u}}_{\Delta} = \underline{\underline{j}} \underline{\underline{u}}_{\Delta} = 0 \quad (5.3)$$

Therefore

$$\underline{\underline{j}} \underline{\underline{v}}_{\Delta} = -\underline{\underline{jS}}^{-1} \underline{\underline{f}}_{\Delta} \text{ and } \underline{\underline{aS}} \underline{\underline{v}}_{\Delta} = 0 \quad (5.4)$$

Eq. (5.4) does not define an iterative algorithm. In order to obtain such an algorithm, we project on $\underline{\underline{jS}}^{-1} \underline{\underline{W}}_{\Delta}$, to obtain:

$$\underline{\underline{S}}^{-1} \underline{\underline{jS}} \underline{\underline{j}} \underline{\underline{v}}_{\Delta} = -\underline{\underline{S}}^{-1} \underline{\underline{jS}} \underline{\underline{jS}}^{-1} \underline{\underline{f}}_{\Delta} \text{ and } \underline{\underline{aS}} \underline{\underline{v}}_{\Delta} = 0 \quad (5.5)$$

This algorithm is referred to as the 'DVS-primal algorithm'. The solution is given by

$$\underline{\underline{u}}_{\Delta} = \underline{\underline{a}} \left(\underline{\underline{v}}_{\Delta} + \underline{\underline{S}}^{-1} \underline{\underline{f}}_{\Delta} \right) \quad (5.6)$$

We observe that we could have written $\underline{\underline{u}}_{\Delta} = \underline{\underline{v}}_{\Delta} + \underline{\underline{S}}^{-1} \underline{\underline{f}}_{\Delta}$ instead of Eq. (5.6). However, the application of the projection operator $\underline{\underline{a}}$ is important when $\underline{\underline{v}}_{\Delta}$ and $\underline{\underline{S}}^{-1} \underline{\underline{f}}_{\Delta}$ are not computed with exact arithmetic, as it is the case when using numerical methods, because when it is applied it replaces $\underline{\underline{v}}_{\Delta} + \underline{\underline{S}}^{-1} \underline{\underline{f}}_{\Delta}$ by the continuous-vector closest (with respect to the Euclidean distance) to it.

5.2 Dual Formulations

The DVS Version of FETI-DP

For this algorithm the *sought-information* is defined to be: $\underline{\underline{\lambda}}_{\Delta} \equiv -\underline{\underline{jS}} \underline{\underline{u}}_{\Delta}$. This algorithm can be easily derived from the *DVS-primal* formulation that has just been presented. We observe that $\underline{\underline{v}}_{\Delta} = \underline{\underline{S}}^{-1} \underline{\underline{\lambda}}_{\Delta}$, $\underline{\underline{\lambda}}_{\Delta} = \underline{\underline{S}} \underline{\underline{v}}_{\Delta}$, in view of Eq. (5.2), and $\underline{\underline{a}} \underline{\underline{\lambda}}_{\Delta} = 0$. This permits transforming Eq. (5.5) into

$$\underline{\underline{S}} \underline{\underline{jS}} \underline{\underline{jS}}^{-1} \underline{\underline{\lambda}}_{\Delta} = \underline{\underline{S}} \underline{\underline{jS}} \underline{\underline{jS}}^{-1} \underline{\underline{f}}_{\Delta} \text{ and } \underline{\underline{a}} \underline{\underline{\lambda}}_{\Delta} = 0 \quad (5.7)$$

Applying $\underline{\underline{S}}^{-1}$ to the first of these equations, it is obtained:

$$\underline{\underline{jS}} \underline{\underline{jS}}^{-1} \underline{\underline{\lambda}}_{\Delta} = \underline{\underline{jS}} \underline{\underline{jS}}^{-1} \underline{\underline{f}}_{\Delta} \text{ and } \underline{\underline{a}} \underline{\underline{\lambda}}_{\Delta} = 0 \quad (5.8)$$

As for Eq. (5.6), it becomes:

$$\underline{\underline{u}}_{\Delta} = \underline{\underline{aS}}^{-1} \left(\underline{\underline{f}}_{\Delta} - \underline{\underline{j}} \underline{\underline{\lambda}}_{\Delta} \right) \quad (5.9)$$

The DVS-Dual Algorithm

In this algorithm, the *sought-information* is: $\underline{\underline{\mu}}_{\Delta} \equiv \underline{\underline{Su}}_{\Delta}$. Then, $\underline{\underline{u}}_{\Delta} = \underline{\underline{S}}^{-1} \underline{\underline{\mu}}_{\Delta}$. Replacing this in Eq. (5.1), one gets:

$$\underline{\underline{aS}}^{-1} \underline{\underline{a}} \underline{\underline{\mu}}_{\Delta} = \underline{\underline{Sa}} \underline{\underline{S}}^{-1} \underline{\underline{f}}_{\Delta} \text{ and } \underline{\underline{jS}}^{-1} \underline{\underline{\mu}}_{\Delta} = 0 \quad (5.10)$$

Finally, multiplying by $\underline{\underline{S}}$ the first of these equalities, it is obtained:

$$\underline{\underline{Sa}} \underline{\underline{S}}^{-1} \underline{\underline{a}} \underline{\underline{\mu}}_{\Delta} = \underline{\underline{Sa}} \underline{\underline{S}}^{-1} \underline{\underline{f}}_{\Delta} \text{ and } \underline{\underline{jS}}^{-1} \underline{\underline{\mu}}_{\Delta} = 0 \quad (5.11)$$

When $\underline{\underline{\mu}}_{\Delta}$ is known, $\underline{\underline{u}}_{\Delta}$ can be recovered by means of

$$\underline{\underline{u}}_{\Delta} = \underline{\underline{aS}}^{-1} \left(\underline{\underline{f}}_{\Delta} + \underline{\underline{\mu}}_{\Delta} \right) \quad (5.12)$$

A comment similar to that made immediately after Eq. (5.6), goes here: we have applied the projection matrix $\underline{\underline{a}}$, in Eq. (5.12) because we are assuming that exact arithmetic generally will not be used.

6. Numerical Procedures Fulfilling the DDM-Paradigm

Summarizing, the preconditioned *DVS-algorithms* with constraints are:

$$\underline{\underline{aS}}^{-1} \underline{\underline{aS}} \underline{\underline{u}}_{\Delta} = \underline{\underline{aS}}^{-1} \underline{\underline{f}}_{\Delta} \text{ and } \underline{\underline{j}} \underline{\underline{u}}_{\Delta} = 0; \text{ DVS - BDDC} \quad (6.1)$$

$$\underline{\underline{jS}} \underline{\underline{jS}}^{-1} \underline{\underline{\lambda}}_{\Delta} = \underline{\underline{jS}} \underline{\underline{jS}}^{-1} \underline{\underline{f}}_{\Delta} \text{ and } \underline{\underline{a}} \underline{\underline{\lambda}}_{\Delta} = 0; \text{ DVS - FETI - DP} \\ \text{where } \underline{\underline{u}}_{\Delta} = \underline{\underline{aS}}^{-1} \left(\underline{\underline{f}}_{\Delta} - \underline{\underline{j}} \underline{\underline{\lambda}}_{\Delta} \right) \quad (6.2)$$

$$\underline{\underline{S}}^{-1} \underline{\underline{jS}} \underline{\underline{j}} \underline{\underline{v}}_{\Delta} = \underline{\underline{S}}^{-1} \underline{\underline{jS}} \underline{\underline{jS}}^{-1} \underline{\underline{f}}_{\Delta} \text{ and } \underline{\underline{aS}} \underline{\underline{v}}_{\Delta} = 0; \text{ DVS - PRIMAL} \\ \text{where } \underline{\underline{u}}_{\Delta} = \underline{\underline{aS}}^{-1} \left(\underline{\underline{f}}_{\Delta} - \underline{\underline{jS}} \underline{\underline{v}}_{\Delta} \right) \quad (6.3)$$

$$\underline{\underline{Sa}} \underline{\underline{S}}^{-1} \underline{\underline{a}} \underline{\underline{\mu}}_{\Delta} = \underline{\underline{Sa}} \underline{\underline{S}}^{-1} \underline{\underline{aS}} \underline{\underline{jS}}^{-1} \underline{\underline{f}}_{\Delta} \text{ and } \underline{\underline{jS}}^{-1} \underline{\underline{\mu}}_{\Delta} = 0; \text{ DVS - DUAL} \\ \text{where } \underline{\underline{u}}_{\Delta} = \underline{\underline{aS}}^{-1} \left(\underline{\underline{f}}_{\Delta} + \underline{\underline{\mu}}_{\Delta} \right) \quad (6.4)$$

6.1 Comment on the DVS Numerical Procedures

The outstanding uniformity of the formulas given in Eqs. (6.1) to (6.4) yields clear advantages for code development, especially when such codes are built using object-oriented programming techniques. Such advantages include:

- I. The construction of very robust codes. This is an advantage of the *DVS-algorithms*, which stems from the fact the definitions of such algorithms exclusively depend on the discretized system of equations, obtained after discretization of the partial differential equations considered (referred to as the *original problem*), but which is otherwise independent of the problem that motivated it. In this manner, for example, essentially the same code was applied to treat 2-D and 3-D problems; indeed, only the part defining the geometry had to be changed, and that was a very small part of it;
- II. The codes may use different local solvers, which can be direct or iterative solvers;
- III. Minimal modifications are required for transforming sequential codes into parallel ones; and
- IV. Such formulas also permit developing codes which fulfill the *DDM-paradigm*; i.e., in which "the solution of the global problem is obtained by exclusively solving local problems".

This last property makes the DVS-algorithms very suitable as a tool to be used in the construction of massively-parallelized software, so much needed for efficiently programming the most powerful parallel computers available at present. In the next Subsection, procedures for constructing codes possessing Property IV are explained with some detail.

All the DVS-algorithms of Eqs. (6.1) to (6.4) are iterative and can be implemented with recourse to Conjugate Gradient Method (CGM), when the matrix is definite and symmetric, or some other iterative procedure such as GMRES, when that is not the case. At each iteration step, depending on the *DVS-algorithm* that is applied, one has to compute the action on a *derived-vector* of one of the following matrices: $\underline{\underline{a}}\underline{\underline{S}}^{-1}\underline{\underline{a}}$, $\underline{\underline{j}}\underline{\underline{S}}\underline{\underline{j}}\underline{\underline{S}}^{-1}$, $\underline{\underline{S}}^{-1}\underline{\underline{j}}\underline{\underline{S}}\underline{\underline{j}}$ or $\underline{\underline{S}}\underline{\underline{a}}\underline{\underline{S}}^{-1}\underline{\underline{a}}$. Such matrices in turn are different permutations of the matrices $\underline{\underline{S}}$, $\underline{\underline{S}}^{-1}$, $\underline{\underline{a}}$ and $\underline{\underline{j}}$. Thus, to implement any of the preconditioned *DVS-algorithms*, one only needs to separately develop codes capable of computing

the action of each one of the matrices $\underline{\underline{S}}$, $\underline{\underline{S}}^{-1}$, $\underline{\underline{a}}$ or $\underline{\underline{j}}$ on an arbitrary *derived-vector*, of $\underline{\underline{W}}$.

Therefore, next we present numerical procedures for computing the application of each one of the matrices $\underline{\underline{S}}$, $\underline{\underline{S}}^{-1}$, $\underline{\underline{a}}$ and $\underline{\underline{j}}$, which fulfill the *DDM-paradigm*. It will be seen that only $\underline{\underline{a}}$ requires exchange of information between *derived-nodes* belonging to different subdomains; actually, between *derived-nodes* that are descendants of the same *original-node* (the exchange of information is minimal). As for $\underline{\underline{j}} = \underline{\underline{I}} - \underline{\underline{a}}$, once the action of $\underline{\underline{a}}$ has been computed, no further exchange of information is required.

6.2 Application of $\underline{\underline{S}}$

From Eq. (4.13), we recall the definition of the matrix $\underline{\underline{S}} \equiv \underline{\underline{A}}_{\underline{\underline{\Delta\Delta}}} - \underline{\underline{A}}_{\underline{\underline{\Delta\Pi}}} \left(\underline{\underline{A}}_{\underline{\underline{\Pi\Pi}}} \right)^{-1} \underline{\underline{A}}_{\underline{\underline{\Pi\Delta}}}$. In order to evaluate the action of $\underline{\underline{S}}$ on any *derived-vector*, we need to successively evaluate the action of the following matrices $\underline{\underline{A}}_{\underline{\underline{\Pi\Delta}}}$, $\underline{\underline{A}}_{\underline{\underline{\Pi\Pi}}}^{-1}$, $\underline{\underline{A}}_{\underline{\underline{\Delta\Pi}}}$ and $\underline{\underline{A}}_{\underline{\underline{\Delta\Delta}}}$. Nothing special is required except for $\left(\underline{\underline{A}}_{\underline{\underline{\Pi\Pi}}} \right)^{-1}$. A procedure for evaluating the action of this matrix, which fulfills the *DDM-paradigm* is explained next.

We have

$$\underline{\underline{A}}_{\underline{\underline{\Pi\Pi}}} \equiv \begin{pmatrix} \underline{\underline{A}}_{\underline{\underline{\Pi\Pi}}} & \underline{\underline{A}}_{\underline{\underline{\Pi\pi}}} \\ \underline{\underline{A}}_{\underline{\underline{\pi\Pi}}} & \underline{\underline{A}}_{\underline{\underline{\pi\pi}}} \end{pmatrix} = \begin{pmatrix} \underline{\underline{A}}_{\underline{\underline{\Pi\Pi}}} & \underline{\underline{A}}_{\underline{\underline{\Pi\pi}}} \underline{\underline{a}}^r \\ \underline{\underline{a}}^r \underline{\underline{A}}_{\underline{\underline{\pi\Pi}}} & \underline{\underline{a}}^r \underline{\underline{A}}_{\underline{\underline{\pi\pi}}} \underline{\underline{a}}^r \end{pmatrix} \quad (6.5)$$

Let $\underline{\underline{v}} \in \underline{\underline{W}}$, be an arbitrary *derived-vector*, and write

$$\underline{\underline{w}} \equiv \left(\underline{\underline{A}}_{\underline{\underline{\Pi\Pi}}} \right)^{-1} \underline{\underline{v}} \quad (6.6)$$

Then, $\underline{\underline{w}} = \underline{\underline{w}}_1 + \underline{\underline{w}}_\pi \in \underline{\underline{W}}$ is characterized by

$$\begin{aligned} \sigma_{\pi\pi} \left(\underline{\underline{A}}_{\underline{\underline{\Pi\Pi}}} \right) \underline{\underline{w}}_\pi &= \left\{ \underline{\underline{v}}_\pi - \underline{\underline{A}}_{\underline{\underline{\pi\Pi}}} \left(\underline{\underline{A}}_{\underline{\underline{\Pi\Pi}}} \right)^{-1} \underline{\underline{v}}_1 \right\}, \text{subjected to } \underline{\underline{j}}_\pi^r \underline{\underline{w}}_\pi = 0 \\ \underline{\underline{w}}_1 &= \left(\underline{\underline{A}}_{\underline{\underline{\Pi\Pi}}} \right)^{-1} \left\{ \underline{\underline{v}}_1 - \underline{\underline{A}}_{\underline{\underline{\Pi\pi}}} \underline{\underline{w}}_\pi \right\} \end{aligned} \quad (6.7)$$

and can be obtained iteratively. Here,

$$\sigma_{\pi\pi}(\underline{\underline{A}}_{\Pi\Pi}) \equiv \left\{ \underline{\underline{A}}_{\pi\pi} - \underline{\underline{A}}_{\pi\Delta} \left(\underline{\underline{A}}_{\Delta\Delta} \right)^{-1} \underline{\underline{A}}_{\Delta\pi} \right\} \quad (6.8)$$

and, with $\underline{\underline{a}}^\pi$ as the projection-matrix into $W_r(\pi)$, $\underline{\underline{j}}^\pi \equiv \underline{\underline{I}} - \underline{\underline{a}}^\pi$.

We observe that fulfilling the *DDM-paradigm* when computing the action of $\left(\underline{\underline{A}}_{\Pi\Pi} \right)^{-1}$ is straightforward because

$$\left(\underline{\underline{A}}_{\Pi\Pi} \right)^{-1} = \sum_{\alpha=1}^E \left(\underline{\underline{A}}_{\Pi\Pi}^\alpha \right)^{-1} \quad (6.9)$$

is parallelizable. Once $\underline{\underline{v}}_\pi \in W_r(\pi)$ has been obtained, to derive $\underline{\underline{v}}_1$ one can apply:

$$\underline{\underline{v}}_1 = \left(\underline{\underline{A}}_{\Pi\Pi} \right)^{-1} \left(\underline{\underline{w}}_1 - \underline{\underline{A}}_{\Pi\pi} \underline{\underline{v}}_\pi \right) \quad (6.10)$$

this completes the evaluation of $\underline{\underline{S}}$.

6.3 Application of $\underline{\underline{S}}^{-1}$

We define

$$\Sigma \equiv \text{I} \cup \Delta \quad (6.11)$$

and observe that

$$\Sigma \cup \pi = X \text{ and } \Sigma \cap \pi = \emptyset \quad (6.12)$$

Therefore, the matrix $\underline{\underline{A}}^{-1}$ can be written as:

$$\underline{\underline{A}}^{-1} = \begin{pmatrix} \left(\underline{\underline{A}}^{-1} \right)_{\Pi\Pi} & \left(\underline{\underline{A}}^{-1} \right)_{\Pi\Delta} \\ \left(\underline{\underline{A}}^{-1} \right)_{\Delta\Pi} & \left(\underline{\underline{A}}^{-1} \right)_{\Delta\Delta} \end{pmatrix} = \begin{pmatrix} \left(\underline{\underline{A}}^{-1} \right)_{\Sigma\Sigma} & \left(\underline{\underline{A}}^{-1} \right)_{\Sigma\pi} \\ \left(\underline{\underline{A}}^{-1} \right)_{\pi\Sigma} & \left(\underline{\underline{A}}^{-1} \right)_{\pi\pi} \end{pmatrix} \quad (6.13)$$

Furthermore, $\underline{\underline{S}} : W_\Delta \rightarrow W_\Delta$ fulfills

$$\underline{\underline{S}}^{-1} = \left(\underline{\underline{A}}^{-1} \right)_{\Delta\Delta} \quad (6.14)$$

Another property that is relevant for the following discussion is:

$$W_r(\Sigma) = W(\Sigma) \quad (6.15)$$

for any $\underline{\underline{v}} \in W$, let us write

$$\underline{\underline{w}} \equiv \underline{\underline{A}}^{-1} \underline{\underline{v}} \quad (6.16)$$

then, $\underline{\underline{w}}_\pi$ fulfills

$$\sigma_{\pi\pi}(\underline{\underline{A}}) \underline{\underline{v}}_\pi = \underline{\underline{w}}_\pi - \underline{\underline{A}}_{\pi\Sigma} \left(\underline{\underline{A}}'_{\Sigma\Sigma} \right)^{-1} \underline{\underline{w}}_\Sigma, \text{ subjected to } \underline{\underline{j}}^r \underline{\underline{v}}_\pi = 0 \quad (6.17)$$

Here, $\underline{\underline{j}}^r \equiv \underline{\underline{I}} - \underline{\underline{a}}^r$, where the matrix $\underline{\underline{a}}^r$ is the projection operator on W_r , while

$$\sigma_{\pi\pi}(\underline{\underline{A}}) \equiv \underline{\underline{A}}_{\pi\pi} - \underline{\underline{A}}_{\pi\Sigma} \left(\underline{\underline{A}}'_{\Sigma\Sigma} \right)^{-1} \underline{\underline{A}}_{\Sigma\pi} \quad (6.18)$$

Furthermore, we observe that

$$\left(\underline{\underline{A}}'_{\Sigma\Sigma} \right)^{-1} = \sum_{\alpha=1}^E \left(\underline{\underline{A}}_{\Sigma\Sigma}^\alpha \right)^{-1} \quad (6.19)$$

In order to use Eq. (6.19) as a means of parallelizing the DVS-algorithms, however, the detailed discussion of such procedures will be presented separately [Herrera *et al.*, 2013; L.M. de la Cruz *et al.*, 2013]. It is necessary that the local matrices, $\underline{\underline{A}}_{\Sigma\Sigma}^\alpha$, be invertible. This is granted when invertible $\underline{\underline{A}}$ in W_r , which generally is achieved by taking a sufficiently large number of *primal-nodes*.

Eq. (6.17) is solved iteratively. Once $\underline{\underline{v}}_\pi$ has been obtained, we apply:

$$\underline{\underline{v}}_\Sigma = \left(\underline{\underline{A}}'_{\Sigma\Sigma} \right)^{-1} \left(\underline{\underline{w}}_\Sigma - \underline{\underline{A}}_{\Sigma\pi} \underline{\underline{v}}_\pi \right) \quad (6.20)$$

This procedure permits obtaining $\underline{\underline{A}}^{-1} \underline{\underline{w}}$ in full; however, we only need $\left(\underline{\underline{A}}^{-1} \right)_{\Delta\Delta} \underline{\underline{w}}$. We observe that

$$\left(\underline{\underline{A}}^{-1} \right)_{\Delta\Delta} \underline{\underline{w}} = \left(\underline{\underline{A}}^{-1} \underline{\underline{w}}_\Delta \right)_\Delta \quad (6.21)$$

The vector $\underline{\underline{A}}^{-1} \underline{\underline{w}}_\Delta$ can be obtained by the general procedure presented above. Thus, take $\underline{\underline{w}} \equiv \underline{\underline{w}}_\Delta \in W_\Delta \subset W$ and

$$\underline{\underline{v}} \equiv \underline{\underline{A}}^{-1} \underline{\underline{w}}_\Delta \quad (6.22)$$

Therefore,

$$\underline{\underline{v}}_1 + \underline{\underline{v}}_\Delta = \underline{\underline{v}}_\Sigma = - \left(\underline{\underline{A}}'_{\Sigma\Sigma} \right)^{-1} \underline{\underline{A}}_{\Sigma\pi} \underline{\underline{v}}_\pi = - \left(\underline{\underline{A}}'_{\Sigma\Sigma} \right)^{-1} \underline{\underline{A}}_{\Sigma\pi} \underline{\underline{a}}^r \underline{\underline{v}}_\pi. \quad (6.23)$$

6.4 Application of $\underline{\underline{a}}$ and $\underline{\underline{j}}$.

We use the notation

$$\underline{\underline{a}} = \left(a_{(i,\alpha)(j,\beta)} \right) \quad (6.24)$$

then [Herrera *et al.*, 2010]:

$$a_{(i,\alpha)(j,\beta)} = \frac{1}{m(i)} \delta_{ij}, \forall \alpha \in Z(i) \text{ and } \forall \beta \in Z(j) \quad (6.25)$$

while $\underline{\underline{j}} = \underline{\underline{I}} - \underline{\underline{a}}$ therefore,

$$\underline{\underline{j}} \underline{\underline{w}} = \underline{\underline{w}} - \underline{\underline{a}} \underline{\underline{w}}, \text{ for every } \underline{\underline{w}} \in W \quad (6.26)$$

Therefore, only the evaluation of $\underline{\underline{a}} \underline{\underline{u}}$ requires exchange of information between subdomains. In general, such numbers are very small; for example in application to single-equation problem, when an orthogonal grid is used, they are at most: 4, for problems in 2D, and 8 for problems in 3D.

As for the right hand-sides of Eqs. (4.14), all they can be obtained by successively applying to $\underline{\underline{f}}_{-\Delta}$ some of the operators that have already been discussed. Recalling Eq. (4.14), we have

$$\underline{\underline{f}}_{-\Delta} \equiv \left(R \hat{\underline{\underline{f}}} \right)_{\Delta} - \underline{\underline{A}}_{\Delta \Pi} \underline{\underline{A}}_{\Pi \Pi}^{-1} \left(R \hat{\underline{\underline{f}}} \right)_{\Pi} \quad (6.27)$$

The computation of $R \hat{\underline{\underline{f}}}$ does not present any difficulty and the evaluation of the actions of $\left(\underline{\underline{A}}_{\Pi \Pi} \right)^{-1}$ and $\underline{\underline{A}}_{\Delta \Pi}$ were already analyzed.

7. Numerical Results

Taking into account the general description of the DVS-framework given of Section 2, it can be seen that each one of the DVS-algorithms is uniquely defined by:

1. The original-matrix;
2. The partition of the set of original-nodes, which is induced by the *coarse-mesh* that is applied; and
3. The set of constraints.

In turn, the original-matrix is determined by the partial differential equation, or system of such equations, the discretization method chosen and the *fine-mesh* adopted. As explained in Section 2, the partition of the set of original-nodes depends when the *fine-mesh* has already been defined, on

the *coarse-mesh* (i.e., the domain decomposition) used. The *coarse-mesh* is constituted by a family of non-overlapping subdomains $\{\Omega_1, \dots, \Omega_E\}$ of Ω , the domain of definition of the boundary-value problem to be solved. In all the examples that are presented in this article, the *constraints* are fully determined by the *primal-nodes* and consist in requiring continuity of the *derived-vectors* at them.

Several codes were developed to treat the examples, which were written in C++ language, using the MPI library for the communications. In the computational implementations, the methods of solution used to treat the *original-problems* are: CGM, when such a linear system is symmetric and positive-definite and GMRES when the discrete system is non-symmetric or indefinite. Both are applied with a tolerance of 10^{-6} . Each *DVS-algorithm* was applied to each one of the examples considered, except for that referring to elasticity.

The results obtained for Examples 1 to 5 are summarized in Tables 1 to 5, respectively. In them, the acronym *dof* stands for to the number of degrees of freedom of the *original problem*, but it should be mentioned that the procedures used to treat such examples are such that the nodes that lie on the external boundary do not contribute to the *dof*. The notation to indicate the meshes that were adopted is as follows: In 2D cases, we use $(n \times m) \times (q \times r)$, where $(n \times m)$ refers to the *coarse-mesh*, while $(q \times r)$ to the *fine-mesh*; and similarly, in 3D cases, we use $(n \times m \times p) \times (q \times r \times s)$, where $(n \times m \times p)$ define the *coarse-mesh* and $(q \times r \times s)$ the *fine-mesh*. The constrains are imposed on the primal nodes, in all of our experiments the primal nodes were located at vertex in 2D and at edges in 3D of the subdomains, this coinciding with the algorithm "D" in [Toselli *et al.*, 2005].

Each Table contains at most ten columns. The first four indicate respectively: 1) the meshes used, 2) the number of subdomains of the *coarse-mesh*, 3) the *dof*, and 4) the number of *primal-nodes* used. The figures appearing in columns 5 to 9 correspond to the number of iterations that were required for convergence of each one of the algorithms applied. Columns 9 and 10 were only included in Table 3. For Example 3, in order to cover a wide range of values of the Peclet-number, the diffusion coefficient in Eq. (7.3), ν , was varied and the tenth column in Table 3 indicates the different values of ν for which the corresponding boundary-value problem was solved. Furthermore, the results obtained when the DVS-algorithms were applied were compared with those obtained in [Da Conceição *et al.*, 2006] for the same problem, using the standard version of BDDC.

7.1 Application of the DVS-algorithms to a Single-Equation

The applicability of the *DVS-algorithms* is wide, as previously said it can be applied to general equation systems. In Section 3, it was announced that in this paper we present examples for which d , the number of equations of the system, is one and three. In this Subsection the examples for which $d=1$ will be discussed, leaving for the next Subsection the treatment of static-elasticity models, for which $d=3$.

Four boundary value problems corresponding to a single-equation will be presented. The first two are symmetric and positive definite boundary-value problems, whose definition involves the Laplace differential operator. The other two correspond to advection-diffusion transport, and the corresponding boundary-value problems are non-symmetric and indefinite. The discretization methods used in this Subsection are based on central finite differences (CFD), which are directly applicable to the symmetric problems. To apply CFD to the advection-diffusion problems it was necessary to stabilize the advection-diffusion differential-operator and to this end artificial diffusion was incorporated.

Despite the simplicity of the examples presented in this Subsection, they are very important because a wide range of geophysical systems give rise to similar problems [Herrera and Pinder, 2012]. The diversity of physical interpretations of the boundary-value problems here discussed is enormous. All the differential operators involved can be classified as advection-diffusion operators, since Laplace operator is obtained from the general advection-diffusion differential-operator when the transport-velocity vanishes. Transport processes of heat and solutes occur in a great diversity of geophysical systems. However, the physical processes governed by such differential-equations go far beyond transport phenomena.

Example 1. Poisson equation in two-dimensions.

$$\begin{aligned} -\Delta u &= 2\pi^2 n^2 \sin(\pi nx) \sin(\pi ny), \quad (x, y) \in [-1, 1] \times [-1, 1], \quad n = 100 \\ u &= 0 \text{ on } \partial\Omega \end{aligned} \quad (7.1)$$

We can see from Table 1, that the four algorithms perform very well as the number of subdomains and the degrees of freedom (dof) are increased. In this example, the DVS-DUAL algorithm presents the best performance, requiring only 11 iterations from 12x12 until 30x30 subdomains, and the same number of dof. All other algorithms show similar behavior. The numerical solution of this example can be seen in the Figure 5.

Example 2. Similar to Example 1, but it is formulated in a 3D domain.

$$\begin{aligned} -\Delta u &= 3\pi^2 n^2 \sin(\pi nx) \sin(\pi ny) \sin(\pi nz), \\ (x, y, z) &\in [-1, 1] \times [-1, 1] \times [-1, 1], \quad n = 100 \\ u &= 0 \text{ on } \partial\Omega \end{aligned} \quad (7.2)$$

In Table 2, we observe a similar performance of the algorithms as in the two-dimensional case. One more time the DVS-DUAL algorithm presents a little better behavior with respect all others.

Example 3. The boundary-value problem treated is:

$$\begin{aligned} -v\Delta u + \underline{b} \cdot \nabla u &= 0; \quad (x, y) \in [0, 1] \times [0, 1], \quad \underline{b} \equiv (1, 3) \\ u(x, y) &= \begin{cases} 0, & (x, y) \in \psi_1 \\ 1, & (x, y) \in \psi_2 \end{cases} \end{aligned} \quad (7.3)$$

This is an advection-diffusion transport problem in 2D, for which the differential operator is not self-adjoint.

This example is very interesting because it contains diffusion and advection terms, which are common in several complex geophysics phenomena. In this example, the Péclet number is defined as $Pe = \|\underline{b}\| L / \nu$, where L is a characteristic length (in this case $L = 1$). We also define a local Péclet number as $Pe_h = \|\underline{b}\| h / \nu$. Using these definitions, fixing the global partition to $h=1/512$, and the varying the viscosity from 0.01 to 0.0001, we have that the Péclet number varies from 316 to 316,227, and the local Péclet number varies from 0.617 to 617. In this case the linear system is non-symmetric, therefore we choose the GMRES method with a tolerance of 10^{-6} .

In Table 3 presents the results that the *DVS-algorithms* yielded and compares them with those obtained in [Da Conceição *et al.*, 2006]. We observe that, with fixed *coarse* and *fine meshes*, as the viscosity coefficient is reduced, so that the Péclet number increases, generally the iterations required for convergence reduce. Increasing the Péclet number implies that the effect of the advection term enlarges, and the numerical solution generally becomes unstable. However, the performance of the discretization strategy based on CFD combined with stabilization of the numerical-scheme by means of artificial viscosity is resilient to Péclet-number variations. For comparison purposes, the examples presented here were chosen to be the same as those

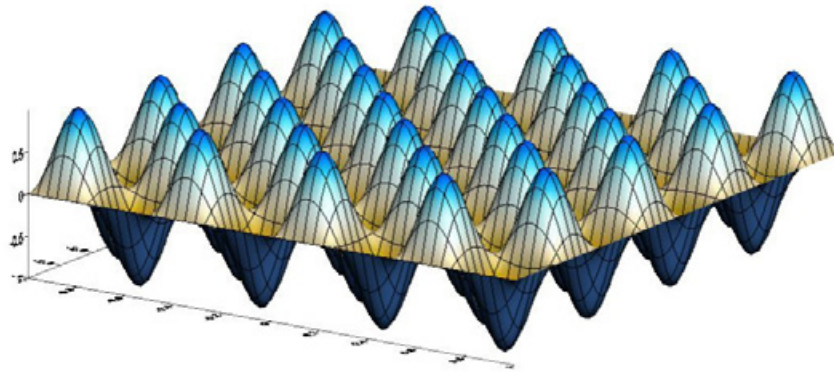


Figure 5. The numerical solution for the 2D case, here we use $n=4$.

Table 1. Number of iterations made by the four DVS algorithms. The primal nodes were located at the vertices of subdomains.

PARTITION	SUBDOMAINS	DOF	PRIMALS	DVS-BDDC	DVS-FETI-DP	DVS-PRIMAL	DVS-DUAL
(2x2) X (2x2)	4	9	1	1	1	1	1
(4x4) X (4x4)	16	225	9	1	5	5	4
(6x6) X (6x6)	36	1,225	25	8	8	8	7
(8x8) X (8x8)	64	3,969	49	10	10	10	9
(10x10) X (10x10)	100	9,801	81	11	11	12	10
(12x12) X (12x12)	144	20,449	121	12	11	12	11
(14x14) X (14x14)	196	38,025	169	12	12	12	11
(16x16) X (16x16)	256	65,025	225	13	11	13	11
(18x18) X (18x18)	324	104,329	289	13	11	13	11
(20x20) X (20x20)	400	159,201	361	13	11	13	11
(22x22) X (22x22)	484	233,289	441	13	12	14	11
(24x24) X (24x24)	576	330,625	529	13	12	13	11
(26x26) X (26x26)	676	455,625	625	13	12	14	11
(28x28) X (28x28)	784	613,089	729	13	12	14	11
(30x30) X (30x30)	900	808,201	841	13	12	14	11

Table 2. Number of iterations made by the four DVS algorithms. The primal nodes were located at edge.

PARTITION	SUBDOMAINS	DOF	PRIMALS	DVS-BDDC	DVS-FETI-DP	DVS-PRIMAL	DVS-DUAL
(2x2x2) X (2x2x2)	8	27	7	1	1	1	1
(3x3x3) X (3x3x3)	27	512	80	4	4	4	3
(4x4x4) X (4x4x4)	64	3,375	351	5	4	4	3
(5x5x5) X (5x5x5)	125	13,824	1,024	6	5	6	5
(6x6x6) X (6x6x6)	216	42,875	2,375	7	6	7	5
(7x7x7) X (7x7x7)	343	110,592	4,752	7	6	7	5
(8x8x8) X (8x8x8)	512	250,047	8,575	8	6	8	5
(9x9x9) X (9x9x9)	729	512,000	14,336	8	6	8	6
(10x10x10) X (10x10x10)	1,000	970,299	22,599	9	6	9	6

presented in [Da Conceição *et al.*, 2006], where the standard BDDC algorithm was applied with the same set of constraints; namely, the same set of subdomains and vertex nodes were chosen to be *primal*. As can be seen in Table 3, when the comparison criterion is based on the number

of iterations required for convergence, the observed performance of the *DVS-algorithms* in these examples is slightly better than that of the standard BDDC algorithm. Finally, an illustration of the kind of numerical solution obtained is shown in Figure 7.

Table 3. Comparison of the DVS-algorithms against the BDDC implemented in [Mandel *et al.*, 1996].

PARTITION	SUB-DOMAINS	DOF	PRIMALS	DVS-FETI-DP	DVS-BDDC	DVS-PRIMAL	DVS-DUAL	BDDC	ν
(8x8) X (64x64)	64	261,121	49	12	11	11	11	12	0.01
(8x8) X (64x64)	64	261,121	49	8	8	8	7	9	0.001
(8x8) X (64x64)	64	261,121	49	7	7	7	7	9	0.0001
(8x8) X (64x64)	64	261,121	49	7	7	7	7	9	0.00001
(16x16) X (32x32)	256	261,121	255	19	17	17	18	20	0.01
(16x16) X (32x32)	256	261,121	255	14	14	13	13	17	0.001
(16x16) X (32x32)	256	261,121	255	13	13	13	13	15	0.0001
(16x16) X (32x32)	256	261,121	255	13	13	13	13	16	0.00001
(32x32) X (16x16)	1,024	261,121	961	33	29	29	31	33	0.01
(32x32) X (16x16)	1,024	261,121	961	26	25	25	25	30	0.001
(32x32) X (16x16)	1,024	261,121	961	25	25	25	25	28	0.0001
(32x32) X (16x16)	1,024	261,121	961	25	25	25	26	29	0.00001
(64x64) X (8x8)	4,096	261,121	3,969	53	52	53	59	52	0.01
(64x64) X (8x8)	4,096	261,121	3,969	46	46	46	47	53	0.001
(64x64) X (8x8)	4,096	261,121	3,969	45	47	45	47	53	0.0001
(64x64) X (8x8)	4,096	261,121	3,969	45	47	45	48	54	0.00001

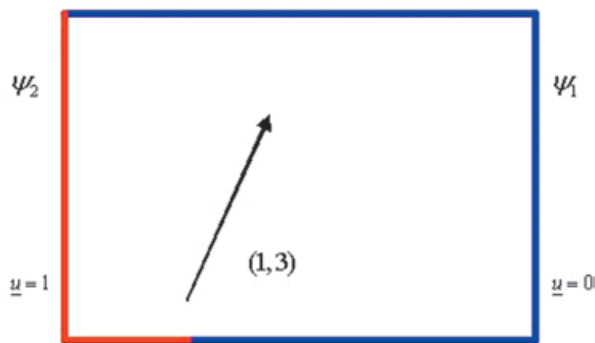


Figure 6. $\partial\Omega$.

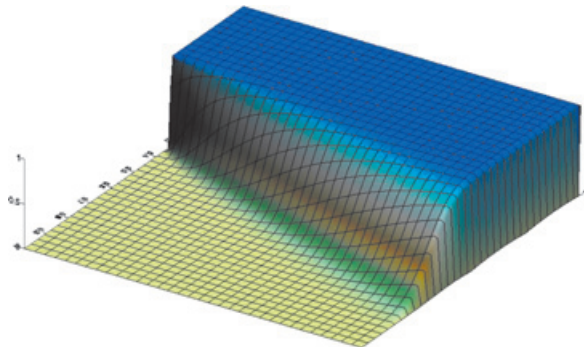


Figure 7. The numerical solution for $\nu=0.01$.

The relative-residual decay for a coarse mesh (16X16) and several fine meshes is presented in Figure 8. We consider in these computations $b=(1,3)$ and $\nu=0.00001$, in such a way that $Pe=3.16e+5$. We observe that the best convergence is obtained when the fine mesh is increased, and the convergence slows when the dof occurring in the subdomains is reduced.

Example 4. The boundary-value problem treated is:

$$-\Delta u + \underline{b} \cdot \nabla u = 0; \quad (x, y, z) \in [0,1] \times [0,1] \times [0,1], \quad \underline{b} = (1,1,1)$$

$$u(x, y, z) = \exp(x + y + z) \text{ on } \partial\Omega \quad (7.4)$$

This is an advection-diffusion transport problem in 3D, for which the differential operator is not self-adjoint.

The diffusion and advection-diffusion differential-operator appears in the equations

of the examples presented above. They are very important in natural and industrial phenomena. For example, the flow and transport of solutes in subsurface groundwater, the movement of aerosol and trace gases in the atmosphere, mixing of fluids in processes of crystal growth, among many other important applications [Tood, 1980; Pinder *et al.*, 2006; Herrera *et al.*, 1969; Herrera *et al.*, 1973; Herrera *et al.*, 1977; Herrera G.S. *et al.*, 2005; L.M. de la Cruz *et al.*, 2006]. In all our examples, we have shown that the *DVS-algorithms* obtain the numerical solution efficiently on parallel machines. In this respect, we remark that for advection-diffusion problems the matrices of the discrete linear systems are non-symmetric.

7.2 Application to a System-Equations

We use the *DVS-framework* to solve a Dirichlet boundary value problem, where displacements are zero over the boundary of the elastic body that occupies the domain Ω of the physical space.

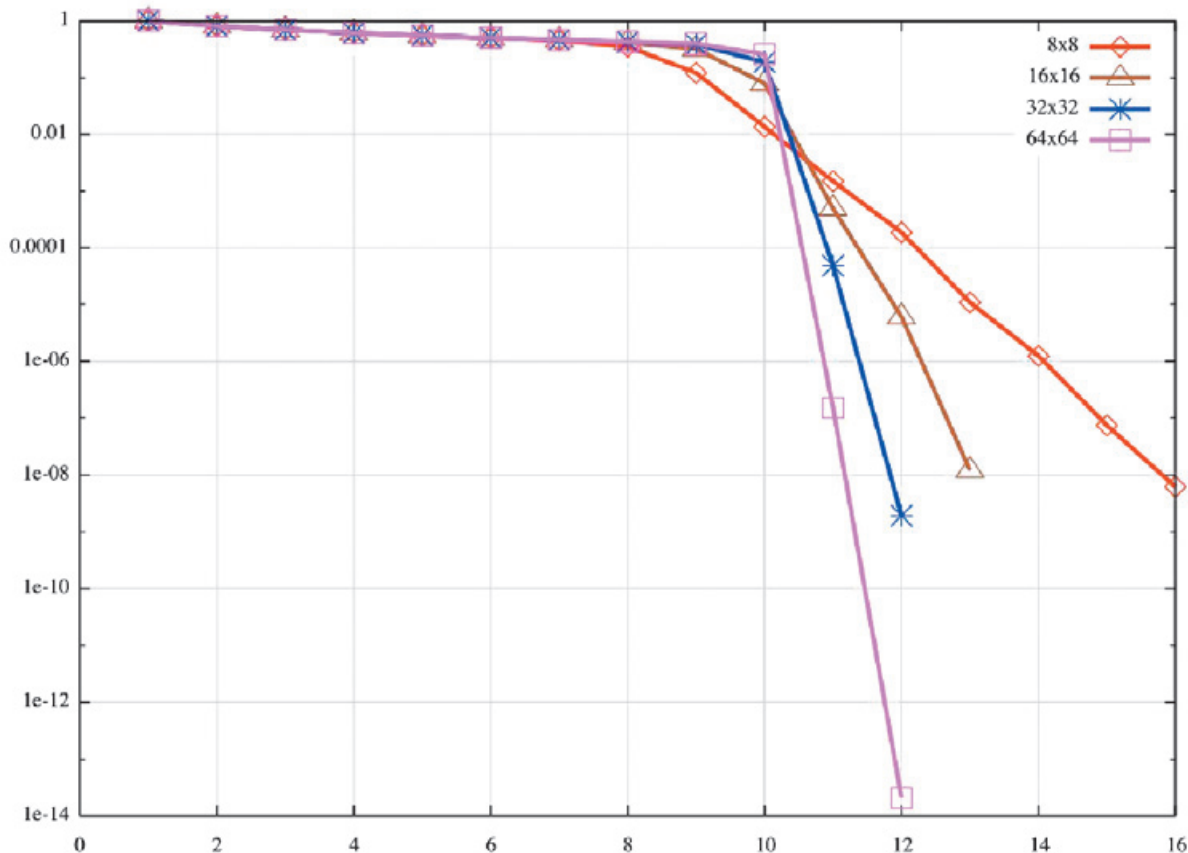


Figure 8. Relative residual decay for the local mesh (16X16).

Table 4. Number of iterations made by the four DVS algorithms. The primal nodes were located at edges of the subdomains.

PARTITION	SUBDOMAINS	DOF	PRIMALS	DVS-BDDC	DVS-FETI-DP	DVS-PRIMAL	DVS-DUAL
(2x2x2) X (2x2x2)	8	27	7	4	3	3	4
(3x3x3) X (3x3x3)	27	512	80	7	5	6	5
(4x4x4) X (4x4x4)	64	3,375	351	9	6	7	6
(5x5x5) X (5x5x5)	125	13,824	1,024	10	7	8	7
(6x6x6) X (6x6x6)	216	42,875	2,375	11	7	9	8
(7x7x7) X (7x7x7)	343	110,592	4,752	12	8	10	8
(8x8x8) X (8x8x8)	512	250,047	8,575	13	8	11	8
(9x9x9) X (9x9x9)	729	512,000	14,336	14	8	11	9
(10x10x10) X (10x10x10)	1,000	970,299	22,599	15	9	12	9

Over each one of such subdomains is solved a local problem by FEM, using linear functions as basis. On each node α of the mesh is defined a vector valued function \underline{u}_α with each component identified as $u_{\alpha i}$ for $i=1, 2, 3$.

Because our operators are symmetric and positive definite, we use CGM as an iterative procedure to solve those linear systems of equations that we have defined in the DVS framework.

The code used in the previous section, which was originally developed to solve a single equation

using finite differences, was adapted for solving systems of equations with FEM. We added the corresponding functionality in order to be able to solve systems of equations, in this case the elasticity problem.

Example 5. A system of partial differential equations in three-dimensions has also been treated. This is the system of differential equations of static elasticity; namely:

$$(\lambda + \mu)\nabla\nabla\cdot\underline{u} + \mu\Delta\underline{u} = \underline{f}_\Omega, \text{ in } \Omega \quad (7.5)$$

Table 5. Results for DVS Algorithms.

PARTITION	SUBDOMAINS	DOF	PRIMALS	DVS-BDDC	DVS-FETIDP	DVS-PRIMAL	DVS-DUAL
(5x5x5) X (5x5x5)	125	41,472	1,024	8	7	9	9
(6x6x6) X (6x6x6)	216	128,625	2,375	8	8	10	10
(7x7x7) X (7x7x7)	343	331,776	4,752	8	8	11	11
(8x8x8) X (8x8x8)	512	750,141	8,575	8	8	12	12

which was subject to the following Dirichlet boundary conditions:

$$\underline{u} = 0, \text{ on } \partial\Omega \quad (7.6)$$

The domain of study for our numerical experiments is a homogeneous isotropic linearly elastic unitary cube. In all of our experiments the primal nodes were located at edges of the subdomains, which is enough for \underline{A}' not being singular.

We consider constant coefficients λ and μ equal to one. With these conditions we have a problem that has analytical solution, and is written as follows:

$$\underline{u} = (\sin\pi x \sin\pi y \sin\pi z, \sin\pi x \sin\pi y \sin\pi z, \sin\pi x \sin\pi y \sin\pi z) \quad (7.7)$$

The Tables 5, summarizes the numerical results obtained using the DVS methods with a tolerance of 10^{-7} .

8. Conclusions

Mathematical models of many geophysical systems lead to a great variety of partial differential equations (PDEs) whose solution methods are based on the computational processing of large-scale algebraic systems [Herrera and Pinder, 2012]. Parallel computing is outstanding among the new computational tools and, in order to effectively use the most advanced computers available today, massively parallel software is required. Domain decomposition methods (DDMs) have been developed precisely for effectively treating PDEs in parallel [DDM Organization, 2012]. What domain decomposition methods ideally intend to do has been summarized in this paper in the "*DDM-paradigm*": to develop algorithms that '*obtain the global solution by exclusively solving local problems*'.

In conclusion, in this paper:

1. We have presented a *non-overlapping discretization* method (the *DVS-discretization*)

-in the sense that it uses a system of nodes such that each one of them belongs to one and only one subdomain of the *coarse-mesh*- applicable to a wide class of well-posed boundary problems associated with elliptic systems of equations. In particular, the differential operators may be symmetric, non-symmetric or indefinite (non-positive-definite);

2. Four algorithms –the *DVS-algorithms* [Herrera *et al.*, 2011]-, which were derived using the *DVS-discretization* and achieve the *DDM-paradigm* have been explained. Two of them are the result of using the BDDC and FETI-DP algorithms after applying *DVS-discretization* to the boundary value problem considered. The other two are obtained when two new algorithms, which had not been reported previously in the literature, were used instead;

3. Numerical procedures that permit achieving the *DDM-paradigm* with each one of the *DVS-algorithms* have been also presented;

4. Codes were developed and applied to several boundary values problems that occur in the modeling of certain geophysical phenomena, such as transport of solutes by both, free-fluids and fluids in a porous medium. We also present results for a static elasticity problem, which thereby illustrates the application of the algorithms to systems of differential equations; and

5. Besides their attractive parallelization properties, in the numerical examples the *DVS-algorithms* exhibited significantly improved numerical performance with respect to standard versions of BDDC and FETI-DP.

Acknowledgement

The authors express their gratitude to Alberto Rosas-Medina e Iván Contreras-Trejo, both PhD students of the Earth-Sciences Graduate Program at UNAM, for having permitted us to reproduce some numerical results of their research work.

Luis M. de la Cruz wishes to acknowledge the support from the project PAPIIT-UNAM TB100112 to develop this research.

Bibliography

- Da Conceição D.T. Jr., 2006, Balancing domain decomposition preconditioners for non-symmetric problems, Instituto Nacional de Matemática Pura e Aplicada, Agência Nacional do Petróleo PRH-32, Rio de Janeiro, May. 9.
- DDM Organization, 2012, Proceedings of 21 International Conferences on Domain Decomposition Methods. www.ddm.org.
- De la Cruz L.M., Herrera I., 2013, Generic and Parallel Software based on DVS algorithms for engineering, Submitted at Advances in Engineering Software.
- De la Cruz L.M., Ramos E., 2006, Mixing with time dependent natural convection, *Int. Comm. in Heat and Mass Transfer*, 33, 2, pp 191-198.
- Dohrmann C.R., 2003, A preconditioner for substructuring based on constrained energy minimization, *SIAM J. Sci. Comput.* 25, 1, 246-258.
- Farhat Ch., Roux F., 1991, A method of finite element tearing and interconnecting and its parallel solution algorithm, *Internat. J. Numer. Methods Engrg.* 32:1205-1227.
- Farhat C., Lesoinne M. LeTallec P., Pierson K., Rixen D., 2001, FETI-DP a dual-primal unified FETI method, Part I: A faster alternative to the two-level FETI method, *Int. J. Numer. Methods Engrg.* 50, pp 1523-1544.
- Farhat C., Lesoinne M., Pierson K., 2000, A scalable dual-primal domain decomposition method, *Numer. Linear Algebra Appl.*, 7, pp 687-714.
- Herrera I., Rosas-Medina A., 2013, The Derived-Vector Space Framework and Four General Purposes Massively Parallel DDM Algorithms, *Engineering Analysis with Boundary Elements*, in press.
- Herrera I., De la Cruz L.M., Carrillo-Ledesma A., Rosas-Medina A., Contreras I., 2012, Foundations of the DVS-framework: Theory and algorithms, Memoria No. 8 del Grupo de Modelación Matemática y Computacional del Instituto de Geofísica, UNAM.
- Herrera I., Carrillo-Ledesma A., Rosas-Medina A., 2012, Four general purposes massively parallel DDM algorithms, available as Memoria No.7 del Grupo de Modelación Matemática y Computacional del Instituto de Geofísica, UNAM.
- Herrera I., Carrillo-Ledesma A., Rosas-Medina A., 2011, A brief overview of non-overlapping domain decomposition methods, *Geofísica Internacional*, 50, 4, pp 445-463.
- Herrera I., Yates R.A., 2009, The multipliers-free dual primal domain decomposition methods for non-symmetric Matrices, *NUMER. METH. PART D. E.* 2009, DOI 10.1002/Num. 20581.
- Herrera I., Yates R.A., 2010, The multipliers-free domain decomposition methods, *NUMER. METH. PART D. E.* 26: 874-905 July 2010, DOI 10.1002/num. 20462.
- Herrera I., Yates R., 2009, Unified multipliers-free theory of dual-primal domain decomposition methods, *NUMER. METH. PART D. E.* Eq. 25:552-581, May 2009, (Published on line May 13, 08) DOI 10.1002/num. 20359.
- Herrera I., 2008, New formulation of iterative substructuring methods without Lagrange Multipliers: Neumann-Neumann and FETI, *NUMER METH PART D E* 24, 3, pp 845-878, DOI 10.1002 NO. 20293.
- Herrera I., 2007, Theory of differential equations in discontinuous piecewise-defined-functions, *NUMER METH PART D E*, 23, 3, pp 597-639, DOI 10.1002, 20182.
- Herrera I., Pinder G.F., 2012, *Mathematical modeling in science and engineering: An axiomatic approach*, Wiley, 243 p.
- Herrera I., Figueroa V. G.E., 1969, A correspondence principle for the theory of leaky aquifers, *Water Resources Research*, 5, 4, P. 900.
- Herrera I., Rodarte L., 1973, Integrodifferential equations for systems of leaky aquifers and applications, Part 1: The nature of approximate Theories, *Water Resources Research*, 9, 4, pp. 995-1005.
- Herrera I., Yates R., 1977, Integrodifferential equations for systems of leaky aquifers. Part 3. A numerical method of unlimited applicability, *Water Resources Research*, 13, 4, pp. 725-732.
- Herrera G.S., Pinder G.F., 2005, Space-time optimization of groundwater quality sampling networks, *Water Resources Research*, 41, W12407, 15 pp.
- Li J., Widlund O., 2005, FETI-DP, BDDC and block Cholesky methods, *Int. J. Numer. Methods Engrg.*, 66, 250-271.

- Mandel J., 1993, Balancing domain decomposition, *Commun. Numer. Methods Engrg.* 233-241.
- Mandel J., Brezina M., 1996, Balancing domain decomposition for problems with large jumps in coefficients, *Math. Comput.* 65, pp 1387-1401.
- Mandel J., Tezaur R., 1996, Convergence of a substructuring method with Lagrange multipliers, *Numer. Math* 73, 4, 473-487.
- Mandel J., Tezaur R., 2001, On the convergence of a dual-primal substructuring method, *SIAM J. Sci. Comput.*, 25, pp 246-258, 2001.
- Mandel J., Dohrmann C.R., 2003, Convergence of a balancing domain decomposition by constraints and energy minimization, *Numer. Linear Algebra Appl.*, 10, 7, 639-659, 2003.
- Mandel J., Dohrmann C.R., Tezaur R., 2005, An algebraic theory for primal and dual substructuring methods by constraints, *Appl. Numer. Math.*, 54: 167-193.
- Pinder G.F., Celia M.A., 2006, *Subsurface hydrology*, Wiley, 468 p.
- PITAC, 2005, *Computational Science: Ensuring america's competitiveness*, Report to the President of the United States, President Information, Technology Advisory Committee, Executive Office of the President of the United States, June.
- Todd D.K., 1980, *Groundwater hydrology*, 2nd ed. Wiley.
- Toselli A., Widlund O., 2005, *Domain decomposition methods-algorithms and Theory*, Springer Series in Computational Mathematics, Springer-Verlag, Berlin, 450 p.